Silver and/or mercury doped thioarsenate and thiogermanate glasses : Transport, structure and ionic sensibility

Rayan Zaiter

SILVER AND/OR MERCURY DOPED THIOARSENATE AND THIOGERMANATE GLASSES : TRANSPORT, STRUCTURE, AND IONIC SENSIBILITY

Verres Thioarsénate et Thiogermanate Dopés à l'Argent et/ou au Mercure : Transport, Structure et Sensibilité Ionique

---

THESIS

Presented to

Université du Littoral Côte d'Opale

To obtain

Doctoral degree at the Université du Littoral Côte d'Opale

Discipline : Chemistry of Materials

By

Rayan ZAITER

Doctoral School : Sciences de la Matière, du Rayonnement et de l'Environnement

Laboratoire de Physico-Chimie de l'Atmosphère

Defended on **11 December 2018**

Members of the jury :

David Le Coq, Associate professor (HDR), University of Rennes1	President of jury
Annie Pradel, Research director, CNRS, University of Montpellier 2	Rapporteur
Laurent Cormier, Research director, CNRS, University of Paris 6	Rapporteur
Eugène Bychkov, University professor, University of Littoral Côte d'Opale	Director of thesis
Pascal Masselin, Associate professor (HDR), University of Littoral Côte d'Opale	Examiner
Mohammad Kassem, Associate professor, University of Littoral Côte d'Opale	Examiner
Mariana Milochova, Independent researcher, University of Littoral Côte d'Opale	Invited member

Acknowledgements

Here in is the last phase of writing my thesis. In fact, it is not the easiest part, but certainly the closest to my heart. Indeed, all of this work would not have been possible without the support of some very special people.

This work was realized at the Laboratoire de Physico-Chimie de l'Atmosphère (LPCA) at the University of Littoral Côte d'Opale (ULCO).

First, I would like to express my heartfelt appreciation to Mr. Eugène BYCHKOV, my thesis director, for his confidence, giving me the opportunity to do my PhD in LPCA. Without his support and honorable contribution, this thesis would not have been a reality.

I would also like to thank my supervisor, Mr. Mohammad KASSEM, for his guidance and insight. He has been truly a good mentor throughout my 3 years of PhD. His devotion to working is inspiring.

I would like to extend my sincere gratitude to Mrs. Mariana MILOCHOVA for her care, help, patience and guidance in my work with chemical sensors.

Many thanks to Mr. Danielle FONTANARI, Mr. Anton SOKOLOV, Mr. Arnaud CUISSET for the RMC/DFT and AIMD calculations, and to Mr. Marc FOURMENTIN for his help in the Scanning Electron Microscopy measurements.

I would like to express my gratitude to the members of the jury who have accepted to evaluate my thesis work. Thanks to Mrs. Annie PRADEL, research director in CNRS at the University of Montpellier 2, Mr. David LE COQ, associate professor (HDR) at the University of Rennes 1, Mr. Laurent CORMIER, research director in CNRS at the University of Paris 6, and Mr. Pascal MASSELIN, associate professor (HDR) at the University of Littoral Côte d'Opale.

I would like to reiterate my gratitude to the staff of LPCA for welcoming me especially the Functional Materials (MF) team, and to my colleagues. Special thanks to those whom their friendship has truly honored me and made the long distances with my family tolerable.

At the end, I should like to express my sincere thanks to my parents, my sisters, my brother and to all my family for their support and encouragement over the years.

Table of contents

GENERAL INTRODUCTION

"*The deepest and most interesting unsolved problem in solid state theory is probably the theory of the nature of glass and the glass transition… This could be the breakthrough in the coming decade.*"

Philip W. Anderson, 1995

Extensive studies of chalcogenide glass systems over the last decades resulted in their numerous applications in data and energy storage, optics and photonics, imaging and chemical sensing. Vitreous chalcogenide alloys are also useful model systems to relate the glass composition and local structure at the short- and intermediate-range scale to various phenomena, in particular, to ion transport in chalcogenide glass/ceramics, widely studied for all-solid-state lithium and sodium batteries. A vast majority of the published research in this field is focused on superionic chalcogenide materials with high mobile ion content. Much less attention was payed to cation-diluted glasses and to the origin of the ion transport in disordered solids.

Furthermore, the research undertaken in this thesis is in a way the result of integration between the National and European policies on one hand, and special skills of the « Glasses and Sensors » team of the Laboratoire de Physico-Chimie de l'Atmosphère (LPCA) of the Université du Littoral Côte d'Opale (ULCO), on the other hand. During several years, our team has focused on developing potentiometric chemical sensors with membranes based on chalcogenide glasses to detect heavy metal ions (Cu^{2+}, Hg^{2+} Fe^{3+}, Cd^{2+}, Pb^{2+}, Tl^{+} and Ag^{+}). The recommendations in terms of the discharge limits of heavy metals are regularly amended. Therefore, it is necessary to develop new and more efficient sensors.

Mercury ion (Hg^{2+}) is undoubtedly one of the extremely hazardous metal ions widely spread in air, water, soil and biota. Thus, we have opted to search for new glasses for the detection of Hg^{2+} ions in aqueous solutions. This work is therefore a part of a strong environmental context in which fundamental research on chalcogenide glasses to be carried out is of a particular scientific interest. The development of new sensors in this case dedicated for the detection of mercury, requires a systematic study to determine all the relationships between composition, structure, ionic and/or electronic transport properties in the bulk material.

The manuscript is organized in four chapters:

Chapter I comprises some generalities on glasses and specifically chalcogenide glasses. The synthesis of $AgY\text{-}As_2S_3$ (Y = Br, I), $HgS\text{-}GeS_2$, $AgI\text{-}HgS\text{-}As_2S_3$ and $AgI\text{-}HgS\text{-}GeS_2$ systems has been described. Macroscopic properties including density, mean atomic volume and thermal properties have been presented and discussed.

Chapter II focuses on the electrical conductivity of the $AgY\text{-}As_2S_3$ (Y = Br, I), $HgS\text{-}GeS_2$, $AgI\text{-}HgS\text{-}As_2S_3$ and $AgI\text{-}HgS\text{-}GeS_2$ systems. These studies were performed using dc conductivity measurements and complex impedance spectroscopy. The results obtained allows us to understand the origin of the ion transport mechanism in disordered solids and especially in the cation-diluted glasses.

Chapter III concerns the structural analysis of $AgY\text{-}As_2S_3$ (Y = Br, I), $HgS\text{-}GeS_2$, $AgI\text{-}HgS\text{-}As_2S_3$ and $AgI\text{-}HgS\text{-}GeS_2$ glasses. These studies were conducted using different techniques. Raman spectroscopy, RMC/DFT and AIMD modelling, high energy X-ray diffraction, neutron diffraction and small-angle neutron scattering measurements have been carried out to interpret the origin of conductivity changes, but also to elucidate the structural aspects at the short- and intermediate-range orders.

Chapter IV presents a preliminary study of chemical sensors based on chalcogenide glasses for the detection of Hg^{2+} ions. Electrodes with different membrane compositions were tested in order to define the sensitivity and detection limit. These measurements were done to understand and explain the significant differences in sensitivity and detection limit exhibited by sensors.

Chapter I :

The quasi-binary AgI-As_2S_3, AgBr-As_2S_3, HgS-GeS_2 and the pseudo-ternary AgI-HgS-As_2S_3, AgI-HgS-GeS_2 systems

I.1 Generalities on glasses

It is thought that the first glass was developed in the Mitannian or Hurrian region of Mesopotamia (~5000 BCE). Being an unlimited, innovative and versatile material, the glass has plenty of applications in daily life. It is used in construction, transport, optics, etc… owing to its unique characteristics: hardness, chemical resistance, color and shape varieties, property modification, low-cost production and others. Hereinafter, we present some generalities about glasses.

Glasses are non-crystalline solids described as amorphous materials depending on their structural aspect, in which three-dimensional periodicity is absent [1], **Figure I.1**. The corresponding physical state is the glassy state and the binding forces between atoms are very similar to those in the crystal. Although the long-range order is absent in glasses, the short-range order will generally be present and is translated by an arrangement of the close neighbors with respect to a given atom; the arrangement is variable depending on the site considered.

The glasses are produced via rapid cooling from the molten state, during which crystallization does not have time to occur, and undergo a second-order transition at the so-called glass transition temperature T_g, **Figure I.2**. This transition, which corresponds to the accessibility of new configurational energy states or degrees of freedom, marks the onset of softening and is accompanied by an increase in the heat capacity and thermal expansion coefficient. Thus, their thermal behavior can be described by a substantial change in the physical properties (specific volume, enthalpy and thermal and electrical conductivities).

For a long time, the glass transition temperature was treated as the temperature at which the liquid viscosity reaches 10^{12} Pa s which has not been confirmed for many glasses. It is now more common to define T_g from a calorimetric experiment in such a way that the enthalpy relaxation time is always the same, 100 s at T_g [2].

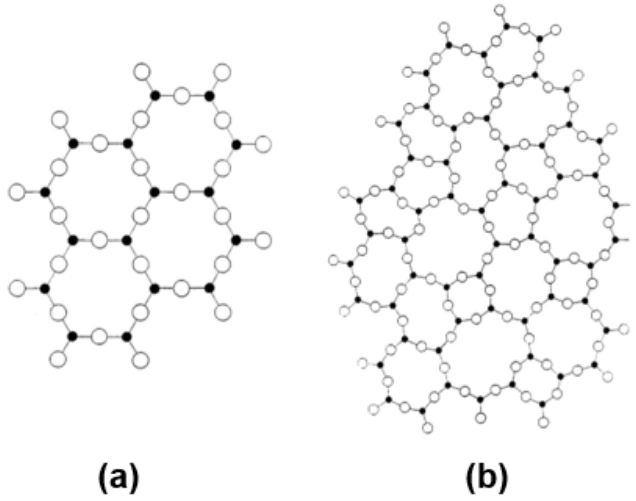

Figure I.1. Examples of (a) crystalline and (b) amorphous SiO_2 structure [3].

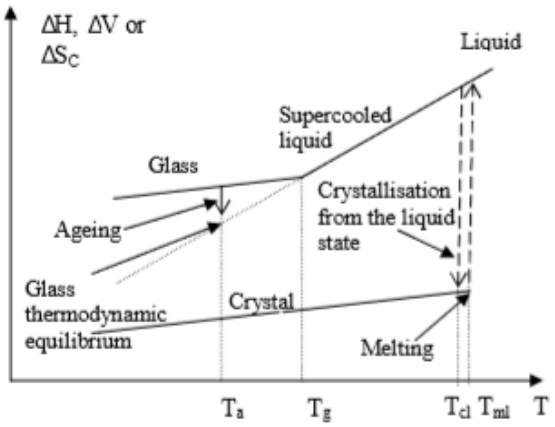

Figure I.2. Enthalpic diagram showing the glass transition and the crystallization from the liquid state and the melting state.

There are four components that can intervene in the composition of glasses: network formers, network modifiers, intermediate compounds and doping salts [4].

- Network formers

These are covalent compounds that are easily vitrified and have the capacity to form the glass-network alone. The best known examples are the chalcogenides or the oxides of silicon, boron, phosphorus, germanium or arsenic. The structure of such network formers is formed by a sequence of triangles or tetrahedrons linked together in a mono-, bi- or tri-dimensional network.

- Network modifiers

These are alkaline, alkaline-earth or metal oxides or chalcogenides, e.g. Na_2O, Cu_2O, Ag_2S, etc. They cannot form glasses alone but are easily incorporated into the glass-network formed by the network formers where they induce, after dissociation, structural changes in the glass-network. The modifier's anions (e.g. O^{2-}, $S^{2-,}$ I^-) are incorporated into the glass-network which becomes negatively charged while the cations (e.g. Li^+, Ag^+, Na^+, Cu^{2+}) are distributed in the interstitial sites of the glass-network and are at the origin of ionic conduction phenomenon in glasses.

- Intermediate compounds

These compounds are usually incorporated in the formers' network, thus modifying its structure. They can act as both network formers and modifiers, according to the glass composition. Examples of such compounds include titanium, zirconium or aluminum oxides or chalcogenides.

- Doping salts

For these compounds, the vitreous matrix (network former + network modifier) acts as a solvent. They may include halides, sulfates, or phosphates containing the same cation as the modifier. The doping salt can affect the optical properties of the glasses, e.g., the addition of heavy elements such as lead or mercury will push the IR transmission limit to longer wavelengths. The addition of high mobile elements such as silver or lithium will induce an increase in the ionic conductivity by increasing in the number of mobile carriers and by redistributing of the negative sites that can be used for the movement of the cations.

I.2 Chalcogenide glasses

I.2.1 Generalities

Chalcogenide glasses are likely to form when the chalcogen elements of group VIA of the periodic table {sulfur (S), selenium (Se) and tellurium (Te)} are associated covalently with one or more elements belonging to other groups of the periodic table such as elements of group VA {arsenic (As), antimony (Sb), bismuth (Bi), phosphorus (P)}, elements of group IVA {germanium (Ge), silicon (Si)}, elements of group IIIA {gallium (Ga), indium (In), thallium (Tl)}, and/or halogens salts of group VIIA {Fluorine (F), chlorine (Cl), bromine (Br) or iodine (I)}. In massive systems, for example, Ge and As are unambiguously the best network formers; they are associated to chalcogen elements [5] in a large number of binary and ternary compounds. Ga and Si, elements of columns 13 and 14, form relatively narrow glassy domains. Also, one should not to forget that the size of the vitreous domains depends intrinsically on the speed of quenching used and as a consequence, we will only be interested in the so-called « classical quenching », i.e. quenching of the molten material in water or other types of fast quenching. Compared to oxide glasses, the chalcogenide ones are denser and exhibit weaker bonds. The chalcogen elements have an s^2p^4 electronic configuration, two of its valence p-electrons form covalent bonds with the nearest neighbor atoms, while the remaining two valence p-electrons form a non-bonding lone pair (LP)

orbital at the top of the valence bond; these LP electrons are suggested to be responsible for the reversible switching properties of chalcogenide glasses [6].

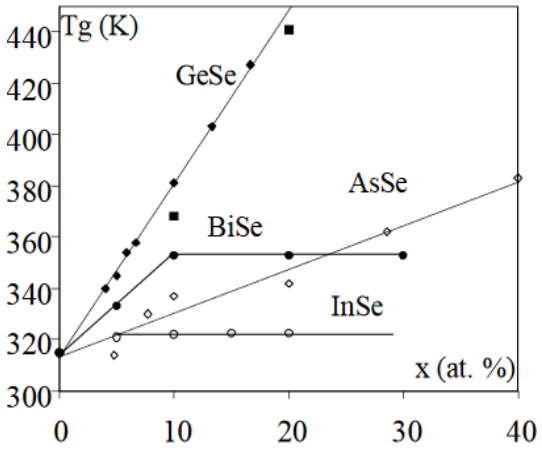

Figure I.3. Variation T_g of the Se binary based glass alloys as a function of the concentration of the added element *x*.

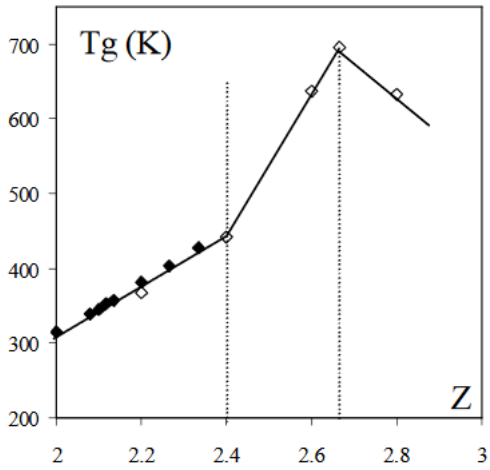

Figure I.4. Variation of T_g as a function of the average coordination number Z of the binary glasses Se_xGe_{1-x}.

The thermal stability of these glasses is unambiguously related to their composition. For example, the arsenic selenide glass As_2Se_3 presents, upon heating, a crystallization feature T_c in addition to the glass transition one, T_g. This same crystallization feature is absent for the arsenic sulfide glass As_2S_3. The T_g values depends on the connectivity, and thus on the rigidity of the vitreous network. **Figure I.3** shows the variation of the T_g as a function of the different systems $Se_{1-x}Ge_x$, $Se_{1-x}As_x$, $Se_{1-x}Bi_x$ and $Se_{1-x}In_x$ [5], [7], [8]. The addition of an element *i* (*i* = Ge, As, Bi, In, etc.) with coordination number greater than 2 to a linear polymeric structure, e.g., Se vitreous matrix, results in an increase of T_g with *x*; a behavior that is mainly related to network connectivity. It has been established that the glassy covalent networks exhibit two topological thresholds. When describing the glass structures by means of virtual atoms bonded together with an average coordination number given by:

$$Z = \sum_i x_i Z_i, \qquad (1)$$

(x_i is the at.% content and Z_i the coordination number of the element *i*), the glassy network must change from a floppy to a rigid type for Z = 2.4 (Phillips constraints theory), then it transforms from a two-dimensional layered structure 2D to a three-dimensional network arrangement 3D for

Z = 2.7 (Tanaka model). These two thresholds are well-observed in the graph presenting the variation of T_g with Z for germanium selenide glasses, Se_xGe_{1-x} [9] (**Figure I.4**).

To be brief, the nature of chalcogen bonds that are present in the network is determinant for the local organization of glass. As the chalcogen atomic number Z increases (S → Te), the bonds associated with the chalcogen lose some of their covalent character in favor of a metallic one as in the case of Te. The differences of character between bonds (directional for covalent bonds and isotropic for metallic ones) are important, since they do not only affect the stability of the glass, but also its corresponding properties, e.g., electrical ones. The covalent glasses tend to be more stable and resistive rather than the metallic glasses. A typical example for As_2Ch_3 glasses (where Ch = S, Se or Te) is shown in **Figure I.5**, where the substitution of one chalcogen by another lead to a staggering variation of the electrical resistivity ρ and energy gap E_g. The gradual substitution of sulfur by selenium in the $As_2S_{3-x}Se_x$ compound decreases drastically the electrical resistivity. This decrease is even more prominent for the $As_2S_{3-x}Te_x$ compound where the sulfur is substituted by tellurium. The decrement in ρ values is accompanied by a corresponding decrease in the E_g values. However, the decrease in ρ is not only due to a decrease in E_g.

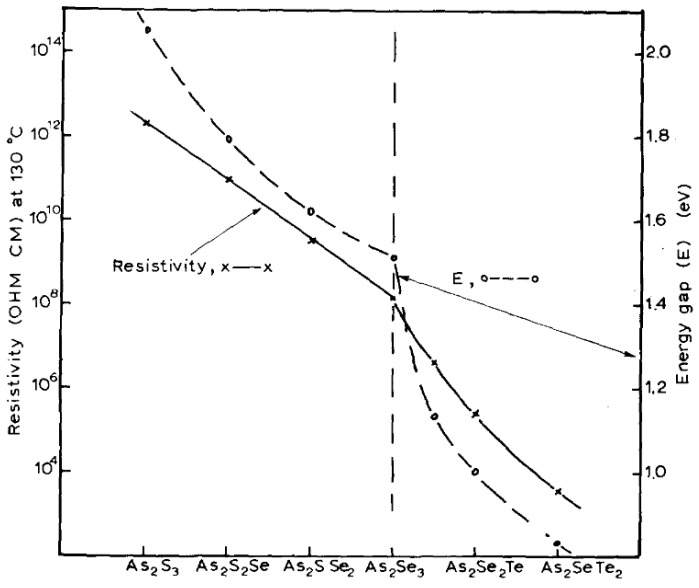

Figure I.5. Resistivity and energy band gap E, measured optically for various glasses [10].

I.2.2 Basic material properties and interests

Chalcogenide glasses, extensively studied since the 1970s, provide numerous applications in the fields of electronics, imaging, photonics and sensors [11]. The existence of a broad range of glass-forming systems with wide-spaced composition and good resistance towards crystallization makes it possible to alter their optical, electrical, magnetic, chemical, thermal and other properties. The unique set of properties such as nonlinearity, photosensitivity and infrared transparency, allowed the usage of chalcogenide films and glasses as electron-beam resists [12] as well as the creation of three-dimensional optical nanostructures by direct laser writing. In addition, the intrinsic properties of chalcogenides render them attractive materials for use in infrared-transmitting optical fibers, as waveguides for optical sensors and telecommunications [13], and as phase-change memories in CD/DVD-RW discs [14]. Finally, the chemical stability and durability in aggressive environments [15] of these glasses allow an advanced application in the field of environmental monitoring and industrial process control, especially when doped with metals [16]. As a result, chalcogenide glasses have been used as sensible membranes in ion selective electrodes (ISE) for the detection of heavy metal cations and toxic anions in solution [17]–[19].

Chalcogenide glasses are also interesting because of their use as model systems to investigate glass networks, and structural roles with respect to materials properties, etc. [20], [21]. For example, silver-halide doped glasses were used as model systems to investigate the ionic-conductivity in materials [20], [21]. Remarkable effect on the conductivity has been observed when chalcogenide glasses are doped with small amounts of Ag [22]. Owen found that the dc conductivity of As_2S_3 increases by > 4 orders of magnitude when < 1 at. % Ag is introduced [23]. Kawamoto et al. have reported that sulfide glasses containing large amount of Ag can be obtained in wide regions of the systems Ge-S-Ag and As-S-Ag [24]. Hence, intensive studies has been devoted to investigate the system Ag_2S-As_2S_3 because of its interesting electrical properties [20], [24], [25].

I.3 Synthesis of glasses

In our continuous quest for the discovery of new glasses, destined for sensible membrane application in chemical sensors, we have opted for the two binary systems: AgY-As_2S_3 (Y = Br, I) and HgS-GeS_2, and the two ternary systems: AgI-HgS-GeS_2 and AgI-HgS-As_2S_3. For those systems, the arsenic sulfide As_2S_3 and the germanium sulfide GeS_2 glasses act as network formers. The silver iodide (AgI) and the silver bromide (AgBr) compounds have been chosen because of

their ionic conductivity, since a good conduction is a necessary condition for the proper functioning of the developed sensors. Finally, the mercury sulfide HgS allows both the integration of Hg^{2+} ions in the vitreous system and the ionic exchange with the aqueous solution, and hence renders the sensible membrane specific to mercury detection. However, its presence is not mandatory for the eventual development of a specific chemical sensor for mercury detection as seen from ref. [26]. The objective of the current work is (i) to synthesize and define the glassy domain of the new systems as a first step, and (ii) to study their physico-chemical properties as a second step.

The synthesis of chalcogenide glasses is always a delicate process because the presence of oxides, moisture and other impurities may cause undesirable effects on both the vitrification levels and the desired sample properties. Consequently, the synthesis is carried out in silica tubes under vacuum using high purity starting materials. Before their use, the silica tubes are cleaned with aqua regia (mixture of acids, 1/3 HNO_3 and 2/3 HCl) for several hours, rinsed with distilled water, alcohol before being dried in the stove.

I.3.1 Purification of sulfur

The starting materials are initially of high purity (5-6 N). However, due to their oxidation upon contact with air, a preliminary mandatory purification step is required. The purification process is carried out by introducing the sulfur pellets (99.999% pure, Acros Organics) into a silica set-up, comprised of a filter and a tube, that is then heated at 130°C under vacuum in order to eliminate volatile impurities such as water and sulfur oxides, and later for the removal of less volatile impurities such as carbon and trace metals via a distillation step up to 450 °C. The volatilization of oxides by purification is based on the fact that the vapor pressure of oxides is significantly greater than their corresponding elements [27].

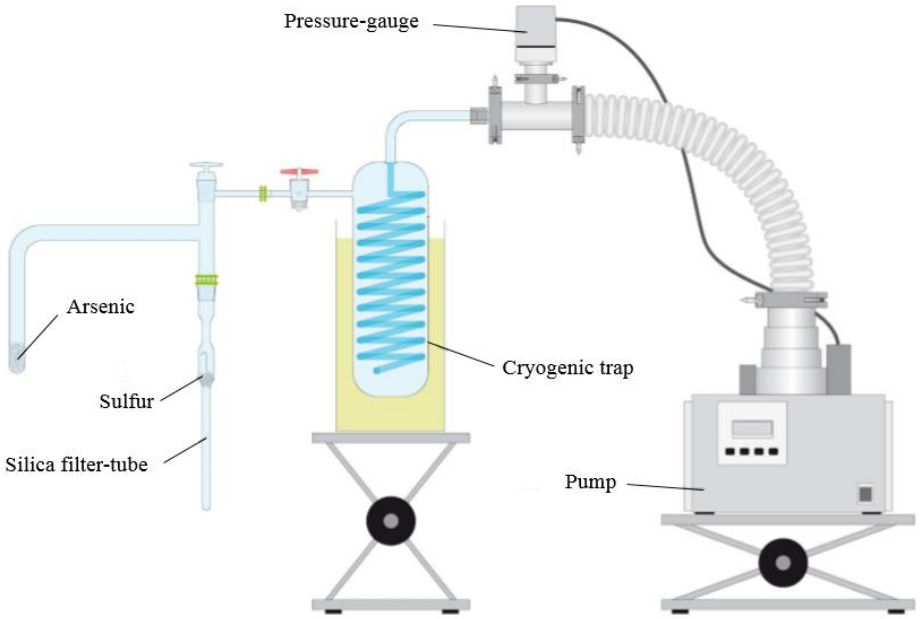

Figure I.6. The experimental setup used for the synthesis of the As_2S_3 glass.

I.3.2 Synthesis of the starting materials

I.3.2.a As_2S_3

The synthesis of As_2S_3 is accomplished from arsenic (99.9999% pure, Cerac) and the previously purified sulfur pellets. The experimental setup used for the synthesis is shown in **Figure I.6**. The starting materials are introduced into an assembly constituted of a pyrex part for the purification of arsenic and a silica tube containing a filter for the distillation of the elements and the synthesis of glasses. Arsenic is introduced into the pyrex setup while sulfur is introduced into the silica filter. The entire assembly is placed under high vacuum of 10^{-6} mbar. Arsenic is heated up to 320 °C to remove the oxide layer on the surface. Initially black, it becomes gray after this procedure. Then, it is transferred to the filter part with sulfur. The reaction tube containing the mixture of arsenic and sulfur, obtained by sealing, is placed in the furnace to be heated and distilled at 850 °C for 24 hr. The purpose of this procedure is to eliminate all the impurities having boiling temperatures higher than that of the glass. When the distillation is done, the cold part of the tube is sealed and placed in a rocking furnace at 800 °C to homogenize the melt. Air quenching is carried out from 650 °C to room temperature to obtain this glass.

I.3.2.b GeS

GeS was synthesized by mixing, in stoichiometric ratio, germanium (Aldrich, 99.999%) and sulfur pellets (Aldrich, 99.999%) in a silica tube. It was then heated under vacuum up to 995 °C, homogenized in the furnace, and finally quenched in air at 600 °C.

I.3.2.c AgBr

The synthesis of AgBr was carried out, via a precipitation process in the absence of light, by mixing 4.2×10^{-2} M of potassium bromide KBr solution with 2.9×10^{-2} M of silver nitrate $AgNO_3$ solution. Both solutions were heated separately under agitation. Then the heated KBr solution was added in several times to the heated $AgNO_3$ solution under agitation. Few minutes after the last addition, the agitation was stopped and the heating temperature was decreased. After 48 hours, 2 ml of nitric acid HNO_3 (0.1 M) was added, the solution was then mixed and the temperature was left in order to evaporate the maximum amount of water. Once this was achieved, the remaining liquid was decanted and the remaining AgBr precipitate was rinsed with distilled water several times. The precipitate was then left overnight in distilled water under agitation, before being filtered and dried at 110-120 °C.

I.3.2.d AgI

The AgI was synthesized via the same precipitation process as AgBr. The potassium iodide KI solution (6×10^{-2} M) was added to the silver nitrate $AgNO_3$ solution (5.9×10^{-2} M). After 2-3 h of incubation, the resulting mixture was decanted and the resulting silver iodide precipitate was rinsed with distilled water several times. The precipitate was then stirred with distilled water-overnight in order to remove all traces of ions related to potassium nitrate, before being filtered and dried at 110-120 °C in the stove.

I.3.3 Synthesis of the quasi-binary and pseudo-ternary glasses

The synthesis of a glass is based on an essential element: the rapid cooling of a molten liquid, a process called quenching. The glasses were prepared, via this classical quenching method, by mixing the starting compounds mentioned above. Sample compositions (typically 3 g of the total mass), in required proportions, were sealed under vacuum (10^{-6} mbar) in silica tubes of 1mm thickness (8 mm ID/10 mm OD) and heated at ≈800-850 °C for As_2S_3-based glasses and at 900-995 °C for GeS_2-based ones for 24 h before being quenched into a cold salt–water mixture. Glasses

at the limit of the glass-forming region were typically 1.5 g of the total mass. Silica tubes of 0.5 mm thickness (5 mm ID/6 mm OD) were used in order to maximize the heat exchange surface/mass ratio.

I.4 Characterization

I.4.1 Density d and mean atomic volume V_{ma}

Density is an important macroscopic property which is related to other physical properties of the material. It is measured by a hydrostatic method using toluene as immersion fluid and germanium as a standard. The density change is related to the atomic mass of the elements present in the composition. In general, the higher the atomic masses of the elements added to the composition, the higher is the density. Meanwhile, the mean atomic volume, calculated from both density and mean atomic mass values of each glass composition, represents the volume "occupied" by one mole of atoms in a certain composition. Changes in the line-slope of one or both parameters, i.e. d or V_{ma}, as a function of glass composition could be related to possible structural changes of the glass network.

I.4.2 Vitreous domain analyzed by XRD

To verify the glassy state of the samples and detect the presence of crystals, X-ray diffraction (XRD) was performed, and a Bruker D8 Advance diffractometer at room temperature was used. This later is equipped with a copper anticathode emitting K_α radiation, a LinxEye detector, a goniometer θ/θ and a rotating sample holder (to avoid preferential orientations). The general conditions of acquisition correspond to an angular range of 2θ from 10° to 80° with a step of 0.02° and a counting time of one second. This powerful analytical tool, based on the diffraction of X-rays by matter and usually used to study in details the crystallized material (e.g. minerals, metals, ceramics…), is not really adapted to analyze amorphous materials (e.g. liquids, polymers, glasses). Due to the absence of long-range order in amorphous materials, the diffraction pattern obtained via XRD lack the Bragg peaks while the diffraction pattern of crystalline materials do not. The crystalline phases were identified by comparing the positions of the Bragg peaks obtained with those of reference compounds in the JCPDS database (Joint Committee on Powder Diffraction Standards).

I.4.3 Thermal properties analyzed by DSC

The differential scanning calorimetry (DSC) is an analytical technique that measures the characteristic temperatures and heat flows associated with different thermal phenomena that may occur during heating or cooling materials. Three characteristic temperatures exist: glass transition temperatures (T_g), the crystallization temperatures (T_x) and the melting temperatures (T_m). The T_g is obtained from the intersection of two linear portions [32] adjoining the transition bend of a DSC thermogram and is associated to the transition of the material from the glassy state to the viscous state. Beyond this temperature, the viscosity decreases continuously and progressively. This allows for the atoms to re-organize and the atomic structure to re-arrange. Hence, the crystallization phase represented by an exothermic peak. In contrast, the melting temperature is determined by an endothermic peak.

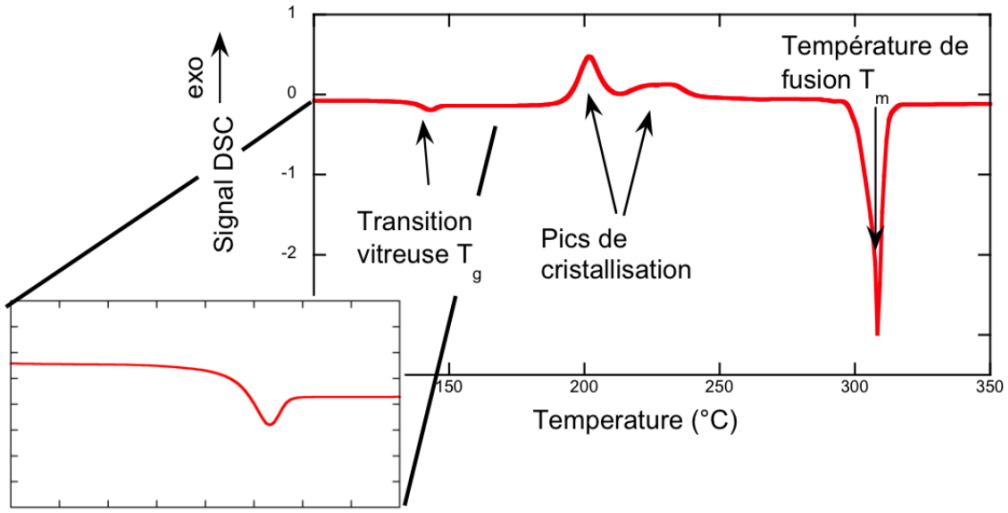

Figure I.7. Typical DSC graph for a chalcogenide glass showing the characteristic transformations (glass transition, crystallization and melting temperatures) *[28]*.

The parameter which defines the tendency to form glasses has been proposed by Hruby and is given by the following relation:

$$K_H = \frac{T_x - T_g}{T_m - T_x} \qquad \text{(I. 1)}$$

The difference T_x-T_g informs us about the stability of the glass facing crystallization. The higher the difference, the greater is the stability of the glass, and the shaping of the material by heating above its glass transition temperature is feasible.

In our case, the thermal phenomena in glasses was studied using a DSC Q200 TA Instruments. Samples weighing between 3 and 15 mg are sealed in aluminum capsules and are heated with a slope of 10 °C.min^{-1} in a range of 10 to 550 °C max under nitrogen flow. A typical DSC curve obtained under these conditions is shown in **Figure I.7**.

I.5 Searching for new glassy systems

I.5.1 Quasi-binary AgBr-As_2S_3

I.5.1.a Glass forming-region

The $(AgBr)_x(As_2S_3)_{1-x}$ system reveal a quite-extended glass-forming region up 60 mol% of AgBr.

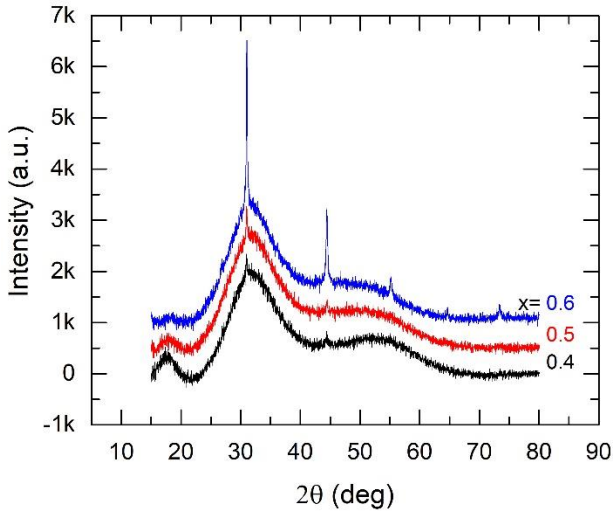

Figure I.8. XRD pattern of the system $(AgBr)_x(As_2S_3)_{1-x}$ with x = 0.4, 0.5 and 0.6.

The XRD patterns of the x = 0.4, 0.5 and 0.6 compositions are shown in **Figure I.8**. The first crystallization peaks appear clearly for x > 0.4, the indexation of the peaks using JCPDC reveals that the crystallites correspond to bromargyrite AgBr (00-006-0438). This result was obtained for glasses synthesized in a large mass quantity (≈3-10 g), **Figure I.9(b)**. The Bragg peaks do not show or their intensity becomes negligible for the small x = 0.6 composition (0.3g) at the limit of the glass forming range, **Figure I.9(a)**. Hence, the extended rage $x = 0.0 \rightarrow x = 0.6$.

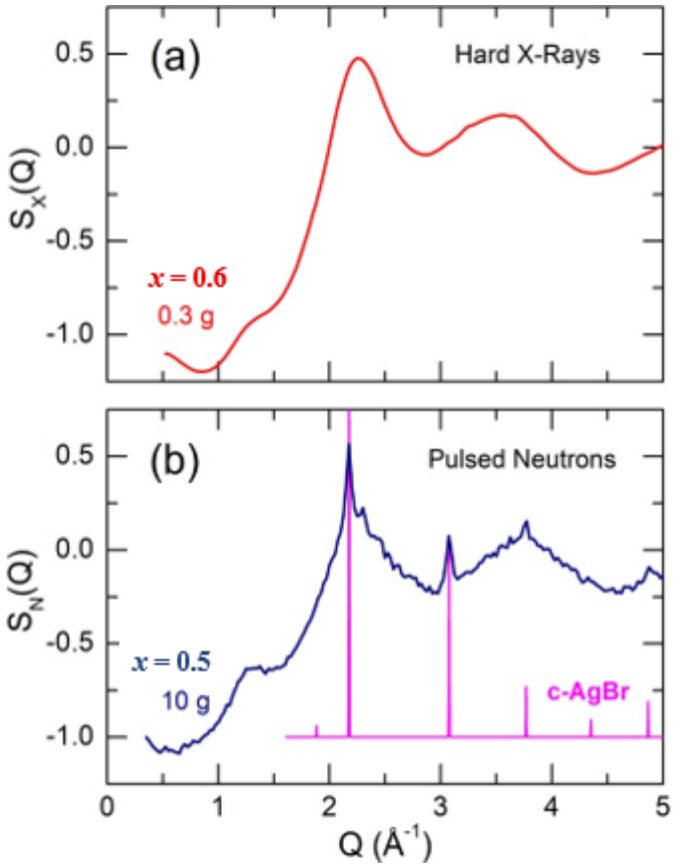

Figure I.9. A low-Q part of (a) the X-ray $S_X(Q)$ and (b) neutron $S_N(Q)$ structure factors for AgBr-rich thioarsenate glasses. A small x = 0.6 glass sample (0.3 g) was used for high-energy X-ray diffraction experiments. A much larger x = 0.5 sample (10 g) was measured using pulsed neutrons. Characteristic Bragg peaks of cubic AgBr, space group $Fm\bar{3}m$ [29], are also shown.

I.5.1.b Density and mean atomic volume

The density and the mean atomic volume of the glassy samples in the $(AgBr)_x(As_2S_3)_{1-x}$ system are shown in **Figure I.10**. The density values are also listed in **Table I.1**. The density increases monotonically with x from 3.15 ($x = 10^{-4}$) to 4.44 g cm^{-3} (x = 0.6) **(Figure I.10(a))**. This behavior is expected since the density of the crystalline silver bromide (d_{AgBr} = 6.47 g cm^{-3}) [30] is higher than that of the g-As_2S_3 host glass ($d_{g\text{-}As2S3}$ = 3.18 g cm^{-3}) or crystalline orpiment c-As_2S_3 ($d_{c\text{-}As2S3}$ = 3.46 g cm^{-3}). The mean atomic volume decreases with x **(Figure I.10(b))**. The extrapolation to x = 1 gives density and mean atomic volume values that correspond to the crystalline AgBr.

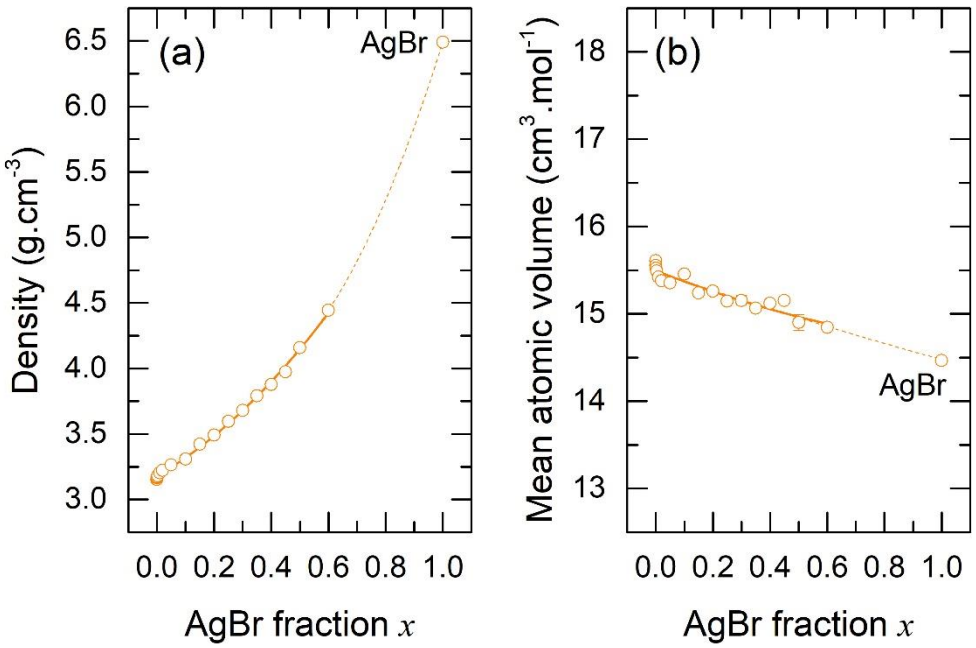

Figure I.10. (a) Density and (b) mean atomic volume of the $(AgBr)_x(As_2S_3)_{1-x}$ alloys as a function of the silver bromide content.

I.5.1.c Thermal properties

Table I.1 summarizes the characteristic temperatures T_g and T_x of the investigated glassy samples. Typical DSC traces of the $(AgBr)_x(As_2S_3)_{1-x}$ glasses are plotted in **Figure I.11**. Samples with low AgBr content ($x \leq 0.3$) show a single endothermic step-like feature corresponding to glass transition indicating a homogeneous glass nature at the macroscopic and mesoscopic scale. However, those with high AgBr content (x = 0.35, 0.4 and 0.45) show two glass transition temperatures related to glass inhomogeneity and the probable presence of phase separation.

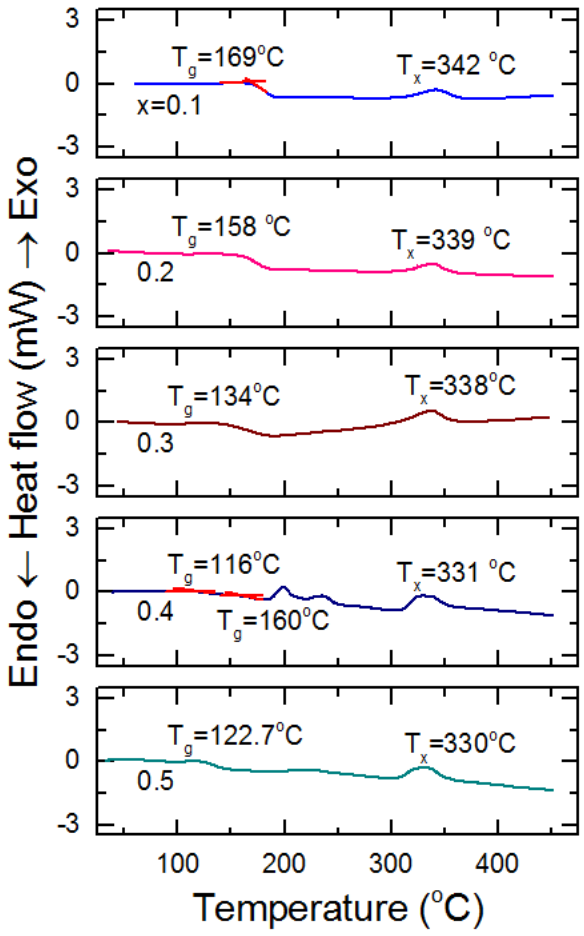

Figure I.11. DSC curves of the glass system $(AgBr)_x(As_2S_3)_{1-x}$ with $0.1 \leq x \leq 0.5$. The curves are obtained between the temperature ranges 25 and 450 °C.

The evolution of T_g for the investigated samples as a function of the AgBr content is plotted in **Figure I.12**. The addition of AgBr to the host glass shows an overall decrease in T_g from 193 °C (x = 10^{-4}) to 108 °C (x = 0.6) owing to the initial framework disorder. T_g of AgBr-poor glasses decreases by ~35 °C from 193 °C (x = 10^{-4}) to 158 °C (x = 0.2), while that of AgBr-rich glasses changes by ~50°C from 158 °C (x = 0.2) to 108 °C (x = 0.6). The stagnation or even the slight increase of T_g values after x = 0.45 is attributed to the partial crystallization and inhomogeneity of the glassy samples. Similar non-monotonic changes in the glass transition temperatures were observed for both Ag_2S-As_2S_3 and Ag_2S-Sb_2S_3 sulfide glass systems doped with AgI [31]. In contrast, the changes were monotonic for the silver-halide doped As_2Se_3 selenide glasses [32], [33]. For all the glasses, the T_g is followed by a broad and weak exothermic crystallization peaks; T_x decreases from 356 °C to 152 °C with increasing x. The glass-forming ability increases with

continuous addition of AgBr (ΔT increases – **Table I.1**) up to the x = 0.3 glass composition with this later being the most stable. However, at x > 0.3, the trend is reversed as the sharp decrease in T_x values (T_x = 152 °C for x = 0.6) lead to a corresponding decrease of the ΔT values which reflects a deterioration in the glass-forming ability for AgBr-rich glasses **(Table I.1)**. This increased and decreased glass-forming ability for AgBr-poor and AgBr-rich glasses respectively, suggests different atomic structural organization between the two regions.

Table I.1. Density, glass transition temperature (T_g) and crystallization temperature (T_x) of the binary glass system $(AgBr)_x(As_2S_3)_{1-x}$. Glass forming and thermal stability criteria are also given: $\Delta T = T_x - T_g$.

Composition	Density ($g.cm^{-3}$)	T_g (°C) (±2)		T_x (°C) (±2)			ΔT (°C)
		T_{g1}	T_{g2}	T_{x1}	T_{x2}	T_{x3}	
0.0001	3.152(9)	193	-	353	-	-	160
0.0003	3.164(4)	191	-	354	-	-	163
0.001	3.171(3)	190	-	353	-	-	163
0.003	3.180(0)	185	-	356	-	-	171
0.01	3.202(5)	180	-	356	-	-	176
0.02	3.222(9)	178	-	355	-	-	177
0.05	3.264(8)	173	-	349	-	-	176
0.1	3.307(1)	169	-	342	-	-	173
0.15	3.422(3)	159	-	342	-	-	183
0.2	3.490(5)	158	-	339	-	-	181
0.25	3.595(9)	150	-	338	-	-	188
0.3	3.678(6)	134	-	338	-	-	204
0.35	3.792(1)	123	161	237	332	-	114
0.4	3.876(2)	116	160	200	331	331	84
0.45	3.974(8)	100	120	156	239	345	56
0.5	4.158(5)	119	-	216	330	-	97
0.6	4.443(4)	118	-	152	204	329	34

The bimodal distribution of glass transition temperatures can be attributed to phase separation effects in a similar way to the Ag_2S-As_2S_3 glasses where T_g varied by ~20 °C in the concentration range 4–20 at.% Ag [34]. Similar behavior was exhibited for other Ag-containing glasses [35]; high T_g values were assigned to the Ag-poor phase while the low ones corresponded to the Ag-rich phase.

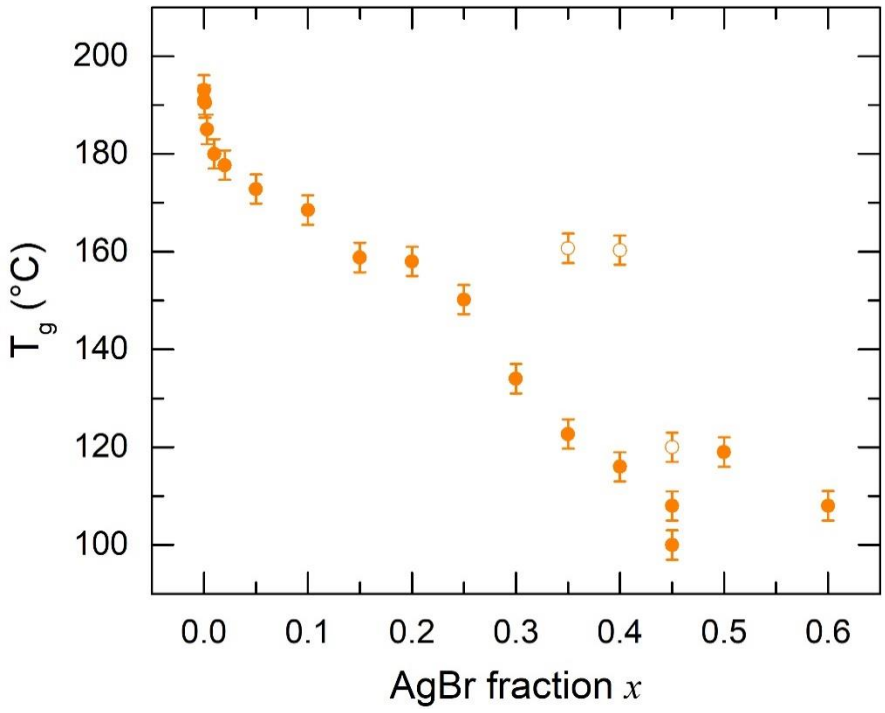

Figure I.12. Variation of the glass transition temperature T_g as a function of different compositions in the quasi-binary system $(AgBr)_x(As_2S_3)_{1-x}$.

As had been shown in Ag_2S-As_2S_3 [36] and Ag-AsS_2 [37] glasses, the addition of Ag has a profound impact on the glass morphology. At low Ag concentration, the Ag-poor phase is the dominant one. It also contains large Ag-rich domains with inclusions of Ag-poor phase of various sizes. However, for high Ag concentrations, the situation changes drastically and the Ag-rich phase becomes the dominant one. This behavior was considered as a characteristic of a percolation threshold with the Ag-poor phase being responsible for the conductivity at low Ag concentrations and vice-versa for the Ag-rich phase. This transition has been considered as the basic mechanism of the abrupt change of the ionic conductivity.

I.5.2 Quasi-binary AgI-As_2S_3

I.5.2.a Glass-forming region

In contrast to the previously reported limited glass-forming range of the $(AgI)_x(As_2S_3)_{1-x}$ system (glasses up to $x \leq 0.2$ [38]), we were able via an aggressive/time consuming quenching technique to extend the glass-forming range up to the $x = 0.4$ glass composition, **Figure I.13**.

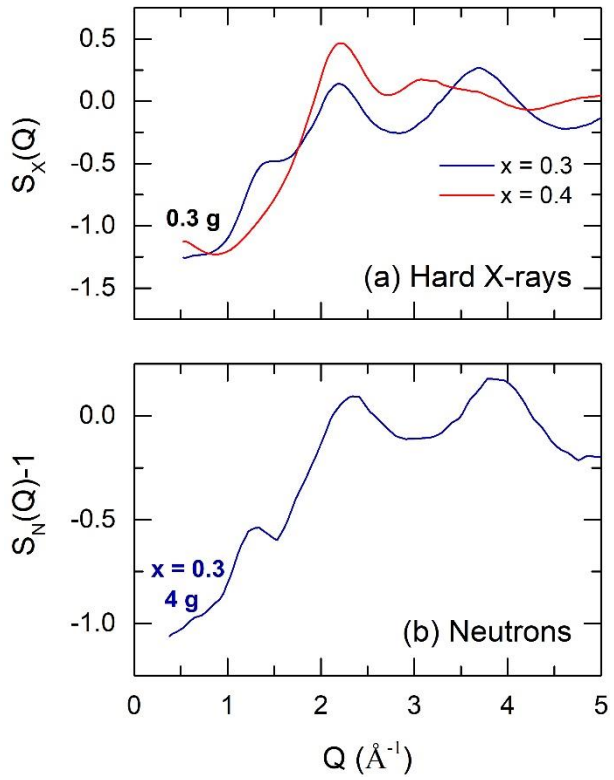

Figure I.13. A low-Q part of (a) the X-ray $S_X(Q)$ and (b) neutron $S_N(Q)$ structure factors for AgI-rich thioarsenate glasses. A small x = 0.3 and 0.4 glass sample (0.3 g) was used for high-energy X-ray diffraction experiments. A much larger x = 0.3 sample (4 g) was measured using pulsed neutrons.

I.5.2.b Density and thermal properties

The density and the mean atomic volume of the $(AgI)_x(As_2S_3)_{1-x}$ glasses are presented in **Figure I.14**. The density increases monotonically with the silver iodide content x, while the mean atomic volume remains essentially invariant. The measured density values vary between 3.13(9) g.cm^{-3} (x = 10^{-4}) and 4.03(6) g.cm^{-3} (x = 0.4). This observed trend, which is related to silver iodide, is well expected since the density of the two crystalline forms of silver iodide ($d_{\alpha\text{-AgI}}$ = 6.12 g cm^{-3} and $d_{\beta\text{-AgI}}$ = 5.68 g cm^{-3}) [30] is higher than that of the As_2S_3 host glass ($d_{\text{g-As2S3}}$ = 3.18 g cm^{-3}) or the crystalline orpiment As_2S_3 ($d_{\text{c-As2S3}}$ = 3.46 g cm^{-3}) [39]. The extrapolation to x = 1 gives a density value which corresponds to the crystalline silver iodide form, α-AgI.

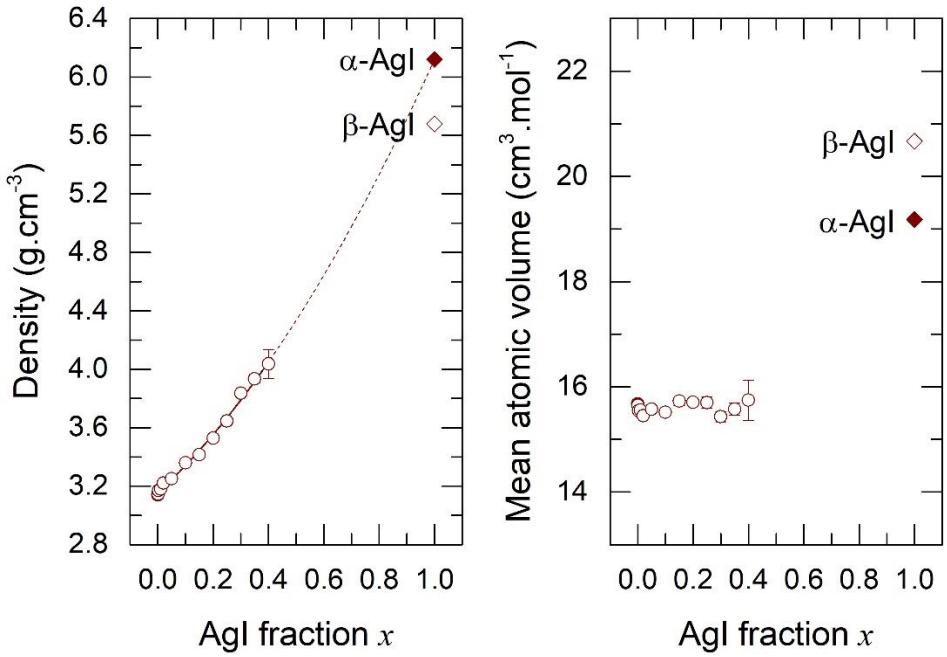

Figure I.14. (a) Density and (b) mean atomic volume of the $(AgI)_x(As_2S_3)_{1-x}$ alloys as a function of the silver iodide content x.

I.5.2.c Thermal properties

Typical DSC traces of the $(AgI)_x(As_2S_3)_{1-x}$ glasses are plotted in **Figure I.15** and the evolution of T_g as a function of the AgI content is plotted in **Figure I.16**. The addition of AgI to the host glass causes an overall decrease in T_g from 188 °C (x = 10^{-4}) to 110 °C (x = 0.4). Meanwhile, glasses with x = 0.35 and 0.4 compositions do not present a unique T_g value. This indicates a non-homogeneous nature of the glass and the presence of phase-separation, confirmed via both HE-XRD (high energy X-ray diffraction) and SEM (scanning electron microscopy) measurements. Two regions were distinguished, (i) AgI-poor and (ii) AgI-rich region that are to be presented in Chapter III. A slight red shift in T_x is also noticed, **Figure I.15**. Furthermore, ΔT increases monotonically with x from 164 °C (x = 0.1) to 231 °C (x = 0.4; taking the lowest value in T_g) indicating an enhancement in the glass-forming ability, **Figure I.17**.

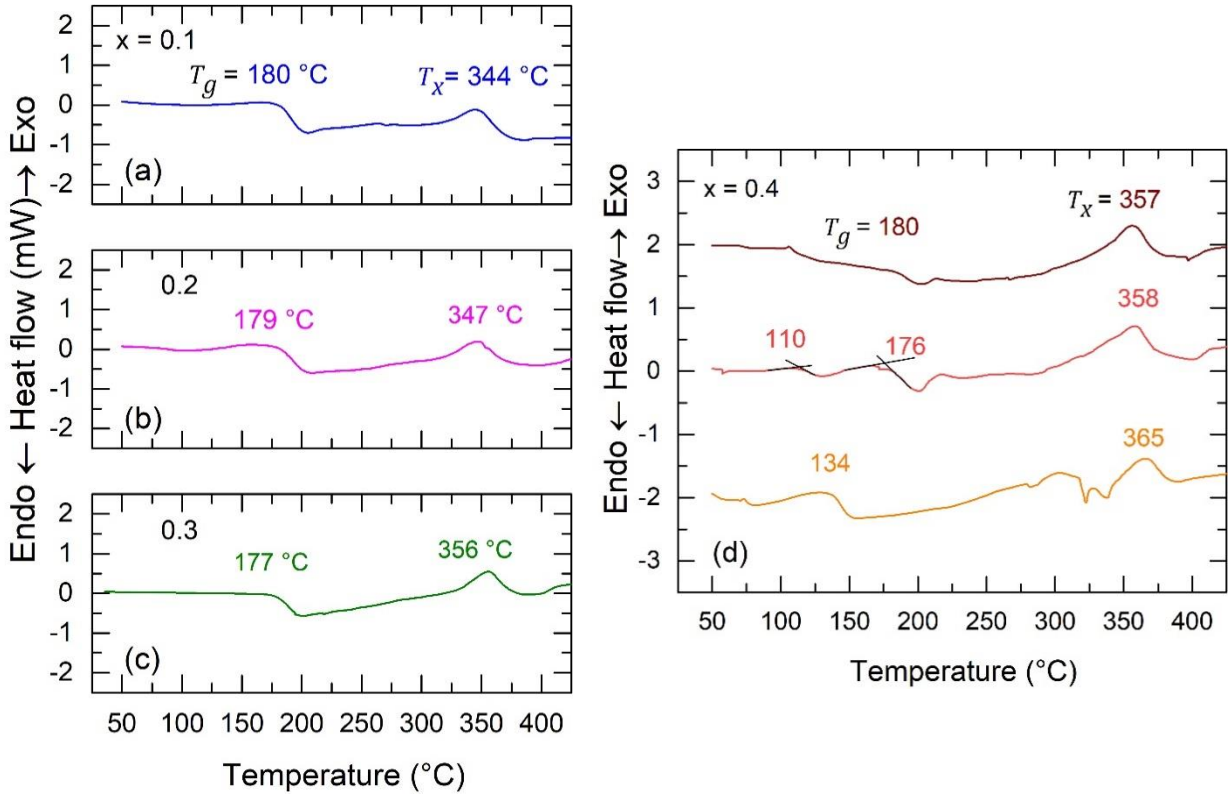

Figure I.15. DSC curves of the glass system $(AgI)_x(As_2S_3)_{1-x}$ with $0.1 \leq x \leq 0.4$. The curves are obtained between the temperature ranges 25 and 450 °C.

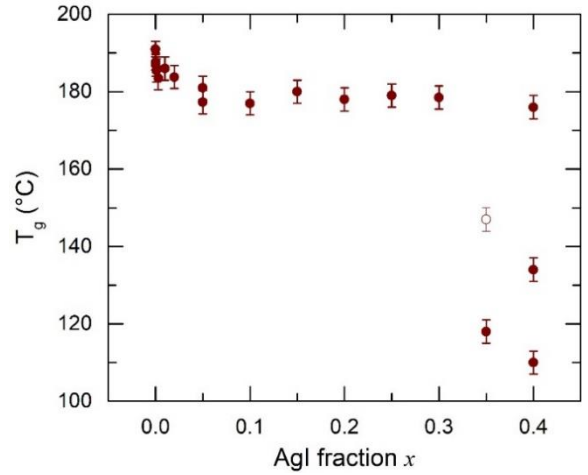

Figure I.16. Variation of the glass transition temperature T_g as a function of AgI content in the quasi-binary system $(AgI)_x(As_2S_3)_{1-x}$.

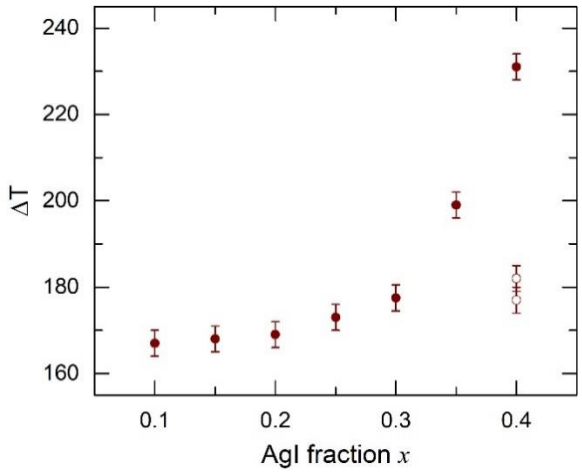

Figure I.17. Evolution of the ΔT parameter as a function of AgI fraction content in the quasi-binary system $(AgI)_x(As_2S_3)_{1-x}$.

I.5.3 Quasi-binary HgS-GeS_2

I.5.3.a Glass forming-region

The $(HgS)_x(GeS_2)_{1-x}$ samples containing less than 60 mol% HgS ($x < 0.6$) appear to be vitreous, **Figure I.18**. The $x = 0.6$ composition synthesized in large quantities (3 g) is crystalline. However, when synthesized in small quantities (1.5 g), it appears to be glassy. The Bragg peaks were those of the Hg_4GeS_6 crystalline compound.

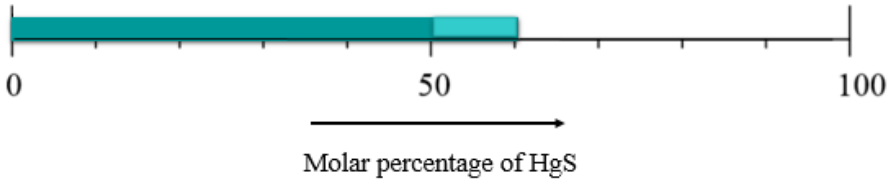

Figure I.18. The vitreous domain of the quasi-binary system $(HgS)_x(GeS_2)_{1-x}$: ■, with crystallites and ■, without crystallites.

I.5.3.b Density and thermal properties

The density of the glassy samples in the $(HgS)_x(GeS_2)_{1-x}$ system increases monotonically with x, while the mean atomic volume decreases **(Figure I.19)**. The density increase is expected since the two crystalline forms of mercury sulfide have significantly higher density ($d_{\alpha\text{-HgS}} = 8.17$ g cm^{-3} and $d_{\beta\text{-HgS}} = 7.70$ g cm^{-3} [30]) than the GeS_2 host glass ($d_{\text{g-GeS2}} = 2.72$ g cm^{-3}) or crystalline GeS_2 ($d_{\text{g-GeS2}} = 3.03$ g cm^{-3}).

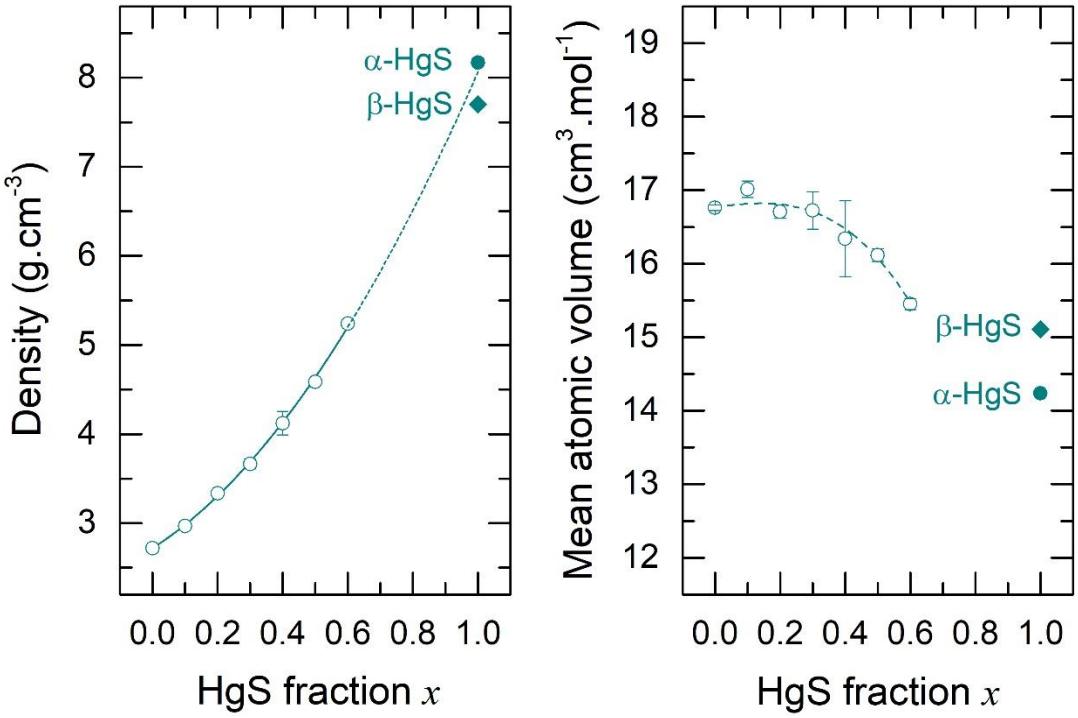

Figure I.19. (a) Density and (b) mean atomic volume of the $(HgS)_x(GeS_2)_{1-x}$ alloys as a function of the mercuric sulfide content *x*.

DSC traces of the $(HgS)_x(GeS_2)_{1-x}$ are plotted in **Figure I.20**. All the samples show a single endothermic peak corresponding to the glass transition temperature, T_g. The unique glass transition indicates a homogeneous glass nature on both mesoscopic and macroscopic scale. T_g in the mercury thiogermanate glasses decreases with increasing *x* from 380 °C to 285 °C **(Figure I.21)** in a similar manner to the mercury thioarsenate $(HgS)_x(As_2S_3)_{1-x}$ glasses [40]. The reduced connectivity in the mercury thiogermanate glasses seems to be responsible for the observed changes. **Figure I.21** reproduces the glass transition temperature in vitreous $HgS\text{-}GeS_2$ as a function of the germanium atomic fraction together with the thermal properties of Ge_yS_{1-y} binaries, $y \leq 0.45$ [41]. In the latter system, the excessive sulphur species at $y \leq 0.33$ form S-S dimers and/or short oligomeric sulphur chains replacing bridging sulphur in $CS\text{-}GeS_{4/2}$ and $ES\text{-}GeS_{4/2}$ structural units, thus reducing the network connectivity, and therefore decreasing the glass transition temperature [41]. The T_g composition dependence in $HgS\text{-}GeS_2$ mimics this trend. Finally, a sharp and intense exothermic crystallization peak T_x re-appears for the $x = 0.4$ composition which then rapidly shifts to lower temperatures ($x = 0.5$ and 0.6) reflecting a reduced glass-forming ability.

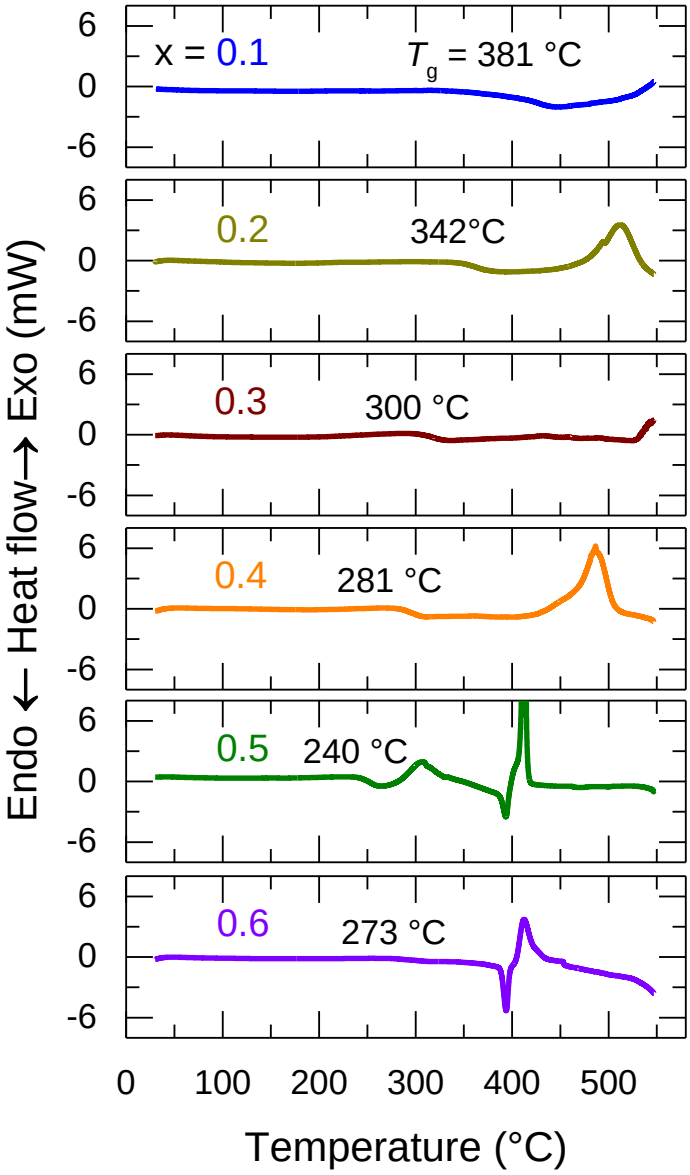

Figure I.20. DSC traces of the $(HgS)_x(GeS_2)_{1-x}$ glasses, $0.1 \leq x \leq 0.6$, obtained in the temperature range from 30 to 550 °C.

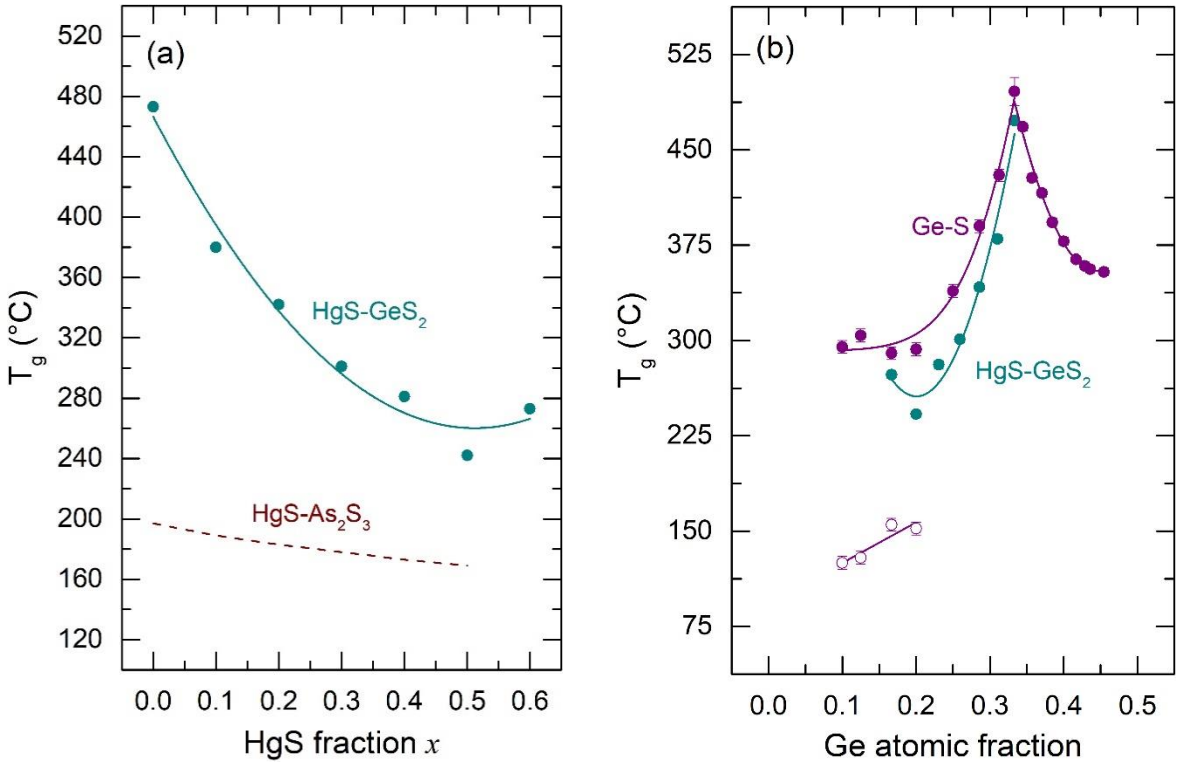

Figure I.21. Composition dependence of the glass transition temperature T_g in the quasi-binary system $(HgS)_x(GeS_2)_{1-x}$; (a) comparison with $(HgS)_x(As_2S_3)_{1-x}$ (the dashed line) [40], (b) comparison with Ge–S binaries. The solid lines are drawn as a guide to the eye.

I.5.4 Pseudo-ternary $(AgI)_x(HgS)_{0.5-x/2}(GeS_2)_{0.5-x/2}$

Silver-containing chalcogenide and chalcohalide glasses in the thiogermanate systems have already been investigated, e.g. GeS_2-Ag_2S and GeS_2-Ag_2S-AgI [42], [43], Ge-Se-AgI [44], Ge-S-I [45], [46], Ge-S-Ag [47], [48], Ga_2S_3-GeS_2-AgI [49], GeS_2-CdS-Ag_2Se [50], Ag_2S-Tl_2S-GeS-GeS_2 [51]. Moreover, Monchev *et al*. [52], [53] have studied the $(AgI)_x(GeS_2)_{1-x}$ system and have determined the boundaries of the glass-forming region with AgI content up to 20 mol%. Indeed, the introduction of the doping salt such as silver halides [44] influences largely the properties of chalcohalide glasses. For example, the high halide concentrations improve the ionic conductivity, because they provide a good medium for the migration of Ag^+ ions [42]. Glasses with low AgI content are more stable, as they are close to the energetically stable stoichiometric GeS_2 glass. Meanwhile, higher AgI concentrations suppress the glass-forming ability and reduce the thermal stability of the glasses. This is explained by the fact that AgI addition modifies the Ge-S glassy

network, which in return has a significant impact on the glass-forming ability. The microhardness experiments, performed on the Ge-S-AgI glasses for S/Ge ratio = 1.5 and 2, shows that microhardness decreases with increasing AgI content [53] and this is probably related, from a macroscopic point of view, to the very low microhardness of the AgI (~167×10^6 Pa) [54]. This network "plasticizing effect" upon AgI doping had already been reported by Ibanez for various bulk glasses [43]. As a result, the increment in AgI content reduces the concentration of Ge-S structural that possess high hardness and hence the decrease in the hardness of the glasses.

I.5.4.a Glass-forming region

Figure I.22 shows the glass-forming domain of the pseudo-ternary AgI-HgS-GeS_2 alloys is relatively narrow and centered around the $(AgI)_x(HgS)_{0.5-x/2}(GeS_2)_{0.5-x/2}$ composition line. The glass-forming region of the $(AgI)_x(HgS)_{0.5-x/2}(GeS_2)_{0.5-x/2}$ system, obtained in our synthesis and quenching conditions, extends up to 60 mol% of AgI (x = 0.6).

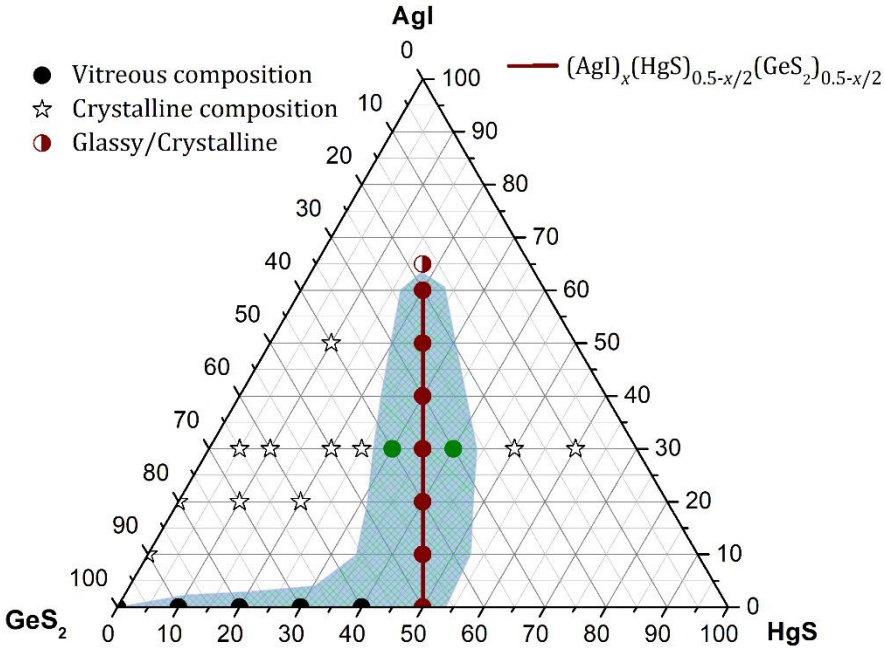

Figure I.22. Glass-forming region in the AgI-HgS-GeS_2 pseudo-ternary system.

I.5.4.b Density and mean atomic volume

The density and the mean atomic volume of the glassy samples of the $(AgI)_x(HgS)_{0.5-x/2}(GeS_2)_{0.5-x/2}$ are presented in **Figure I.23** listed in **Table I.2**. The density increases with increasing the AgI content from 4.59 (x = 0) to 5.55 g cm^{-3} (x = 0.6). This trend is well-expected since the two

crystalline forms of silver iodide ($d_{\alpha\text{-AgI}}$ = 6.12 g cm^{-3} and $d_{\beta\text{-AgI}}$ = 5.68 g cm^{-3} [30]) are higher than that of the host glass $(HgS)_{0.5}(GeS_2)_{0.5}$ ($d_{(HgS)0.5(GeS2)0.5}$ = 4.58 g cm^{-3}). The extrapolation to x = 1 gives a density value which corresponds to the crystalline silver iodide form, α-AgI **(Figure I.23(a))**. The mean atomic volume increases monotonically with x **(Figure I.23(b))**.

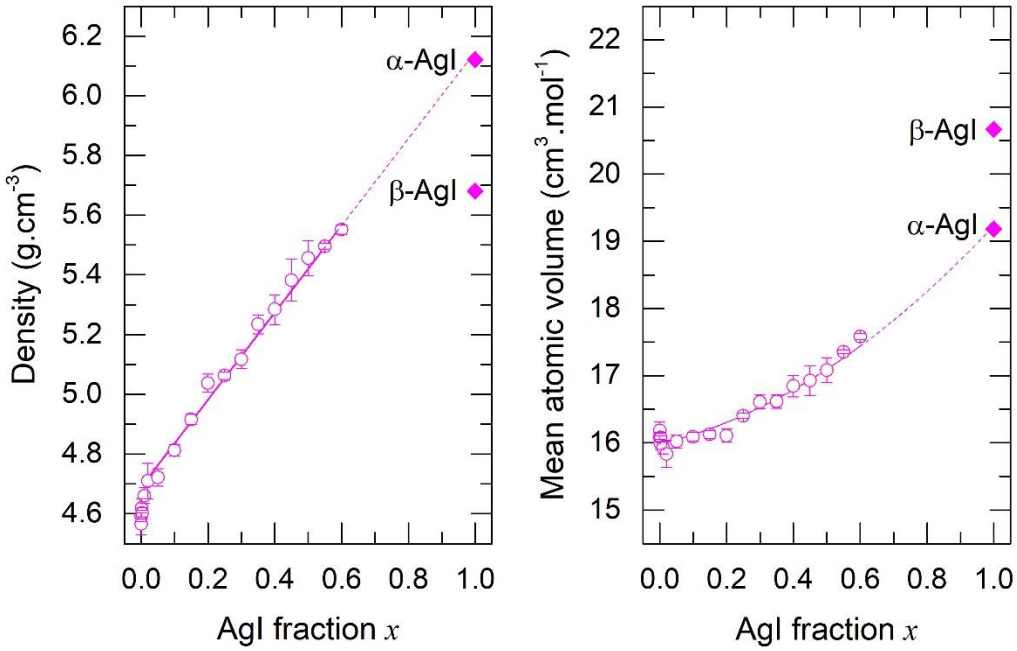

Figure I.23. (a) Density and (b) mean atomic volume of the $(AgI)_x(HgS)_{0.5-x/2}(GeS_2)_{0.5-x/2}$ alloys as a function of the silver iodide content.

I.5.4.c Thermal properties

Table I.2 summarizes the measured glass transition T_g and crystallization T_x temperatures of the $(AgI)_x(HgS)_{0.5-x/2}(GeS_2)_{0.5-x/2}$ glasses. The obtained glasses were homogenous for all the glass compositions, $0 \leq x \leq 0.6$ as only a single glass transition is observed. **Figure I.24,** displaying T_g evolution as a function of x, shows an overall decrease of T_g with increasing x content. However, four different T_g decreasing-rates can be easily seen with increasing x, displayed in four regions: (i) the T_g of the AgI-poor glasses decreases sharply by ~26 °C from 232 °C (x = 0.0) to 206 °C (x = 0.1), (ii) T_g of AgI-intermediate glasses changes slightly by ~12 °C till 194 °C (x = 0.3), (iii) T_g of AgI-rich glasses changes linearly till 165 °C (x = 0.5); however, (iv) T_g of high-AgI rich glasses ($x \geq 0.5$) form a plateau. We should note that glasses in the latter region are sensitive to crystallization, i.e., appearance of AgI micro- or nano-crystals because it is the limit of glass

formation. In the literature, β-AgI transforms to α-AgI at 147 °C [55]. Therefore, most probably the peaks observed in the temperature range 147-167 °C are due to glass transition which is, however, partly covered by the β-α AgI transition. Changes in glass transition temperatures was previously seen in AgI-doped Ag_2S-As_2S_3 and Ag_2S-Sb_2S_3 alloys as well as the corresponding AgI-As_2S_3 host glasses [31]; the T_g decreases from 144 °C (36 mol% AgI) to 85 °C (70 mol% AgI). Similar trend was also observed for $(HgI_2)_x(Ag_2S)_{0.5-x/2}(As_2S_3)_{0.5-x/2}$ glasses with increasing mercury iodide content [55].

Two crystallization features at T_{x1} and T_{x2} appear for all glass compositions and a new high-T crystallization appears at T_{x3} for the x = 0.55 and 0.6 glass compositions. Silver iodide additions decrease the overall resistance of binary $(HgS)_{0.5}(GeS_2)_{0.5}$ host matrix towards crystallization; T_{x1} decreases from 287 (x = 0.0) to 233 (x = 0.6). Meanwhile, the empirical parameter, $\Delta T = T_x - T_g$, usually used to characterize the glass-forming ability presents values that are systematically below 100 °C indicating that those glass are thermally unstable, **Table I.2**.

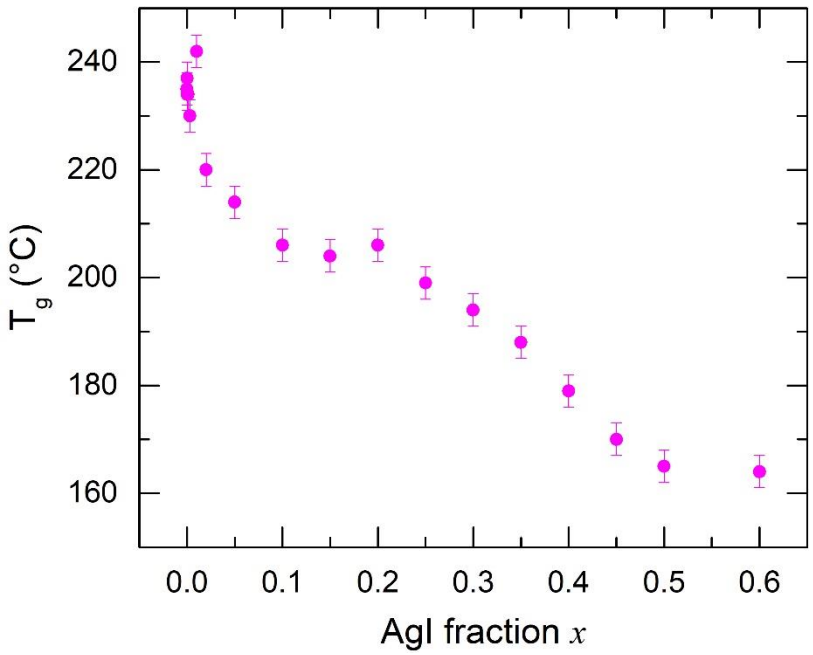

Figure I.24. Variation of the glass transition temperature T_g as a function of different compositions in the pseudo-ternary system $(AgI)_x(HgS)_{0.5-x/2}(GeS_2)_{0.5-x/2}$.

Table I.2. Density, glass transition temperature (T_g) and crystallization temperature (T_x) of the binary glass system $(AgI)_x(HgS)_{0.5-x/2}(GeS_2)_{0.5-x/2}$. Glass forming and thermal stability criteria are also given: $\Delta T = T_x - T_g$.

Composition (x)	Density (g.cm^{-3})	T_g (°C) (±2)		T_x (°C) (±2)		ΔT (°C)
		T_{g1}	T_{x1}	T_{x2}	T_{x3}	
0	4.623(6)	235	287	411		52
0.0001	4.566(4)	237	310	415		73
0.0003	4.395(8)	234	351	421		54
0.001	4.619(3)	234	284	410		50
0.003	4.601(9)	230	289	410		59
0.01	4.660(5)	242	283	402		41
0.02	4.709(7)	220	258	403		38
0.05	4.721(5)	214	277	406		63
0.1	4.812(7)	206	248	398		42
0.15	4.915(8)	204	264	404		60
0.2	5.037(3)	206	253	397		47
0.25	5.062(7)	199	263	355		64
0.3	5.117(5)	194	235	365		41
0.35	5.234(6)	188	236	353		48
0.4	5.284(1)	179	232	360		53
0.45	5.382(1)	170	223	357		63
0.5	5.456(3)	165	230	340		65
0.55	5.495(7)	164	225	348	400	61
0.6	5.551(4)	164	233	350	391	69

I.5.5 Pseudo-ternary $(AgI)_{0.5-x/2}(HgS)_{0.5-x/2}(As_2S_3)_x$

I.5.5.a Glass-forming region

The glass-forming region of the pseudo-ternary system AgI-HgS-As_2S_3 have been reported recently [38]. The vitreous domain is very large covering more than half of the diagram as depicted in **Figure I.25**. The vitreous domain is located in the As_2S_3–rich region and a minimum of 20 mol% As_2S_3 of is required. The structures of these glasses, studied using Raman spectroscopy, show that the A– and B–series, i.e. $(AgI)_{0.5-x/2}(HgS)_{0.5-x/2}(As_2S_3)_x$ and $(AgI)_{0.3}(HgS)_y(As_2S_3)_{0.7-y}$ respectively, form a hybrid Hg-S chain/As-S pyramidal network. The Raman reveals an additional silver related vibration mode at ≈226 cm^{-1} that appears for the AgI-rich vitreous glasses of the A–series at $x >$ 0.2. The amplitude of this mode changes non-monotonically with AgI or HgS content and reveals a maximum amplitude at x = 0.3 [39]. The same ≈226 cm^{-1} mode appears in B–series glasses and

the maximum amplitude occurs at y = 0.35 composition. This maximum amplitude corresponds to the equimolar Hg/Ag fraction, [Hg]/[Ag] ≈ 1. This latter suggests that the ≈226 cm^{-1} mode is related to a structural motif in the glass involving two species, Ag and Hg, and more precisely the presence of mixed interconnected $(AgI_{2/2}S_{2/2})_n$ and $(HgS_{2/2})_m$ chains in the glass network. To this end, i.e., to depict the continuous presence of this ≈226 cm^{-1} vibrational mode, we have synthesized an additional D–series in the $(AgI)_{0.5-x/2}(HgS)_{0.5-x/2}(As_2S_3)_x$ composition range corresponding to the equimolar Hg/Ag fraction, [Hg]/[Ag] ≈ 1. The XRD patterns show that the D-series alloys are amorphous in the composition range, $0.0 \leq x \leq 0.4$.

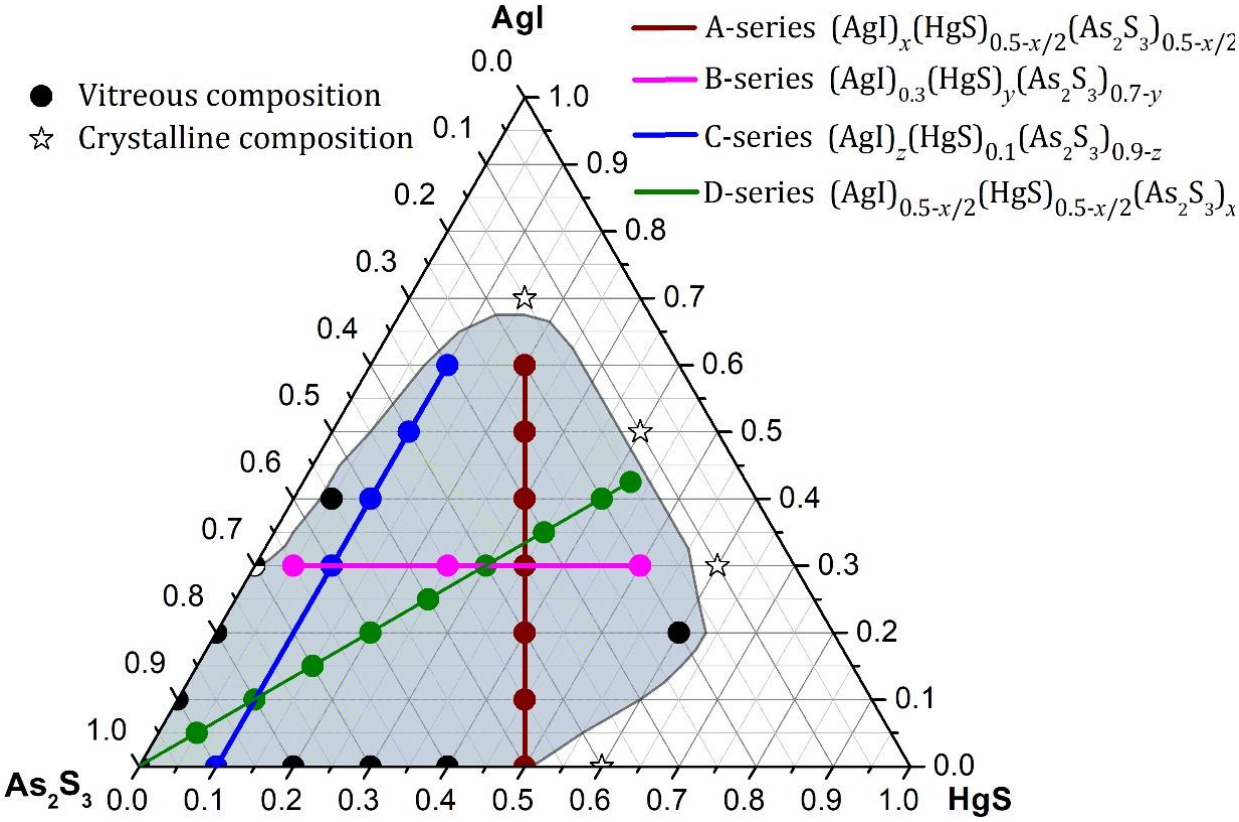

Figure I.25. Glass-forming region in the AgI-HgS-As_2S_3 pseudo-ternary system with the four series: A-series: $(AgI)_x(HgS)_{0.5-x/2}(As_2S_3)_{0.5-x/2}$; B-series: $(AgI)_{0.3}(HgS)_y(As_2S_3)_{0.7-y}$; C-series: $(AgI)_z(HgS)_{0.1}(As_2S_3)_{0.9-z}$ and D-series: $(AgI)_{0.5-x/2}(HgS)_{0.5-x/2}(As_2S_3)_x$.

I.5.5.b Density and mean atomic volume

The glass density and the mean atomic volume of the D-series are presented in **Figure I.26**. The density values are also listed in **Table I.3**. The density increases with increasing the AgI content from 3.16 (x = 10^{-4}) to 5.57 g cm^{-3} (x = 0.4). This observed trend is related to silver iodide and mercuric sulfide and is well expected because the densities of the crystalline forms of each ($d_{\alpha\text{-HgS}}$ = 8.17 g cm^{-3}, $d_{\beta\text{-HgS}}$ = 7.70 g cm^{-3} [30], [56] and $d_{\alpha\text{-AgI}}$ = 6.12 g cm^{-3}, $d_{\beta\text{-AgI}}$ = 5.68 g cm^{-3} [30]) together with the densities of the LT and HT-AgHgSI, 6.68 and 6.67 g cm^{-3} respectively [57], are higher than that of the As_2S_3 host glass ($d_{g\text{-}As2S3}$ = 3.18 g cm^{-3}) or crystalline orpiment As_2S_3 ($d_{c\text{-}As2S3}$ = 3.46 g cm^{-3}) [58]. The mean atomic volume remains invariant for low AgI content, and only exhibits a slight but gradual increase at high AgI fraction. The extrapolation to *AgI fraction* = 0.5 gives density and mean atomic volume values that correspond to the crystalline AgHgSI.

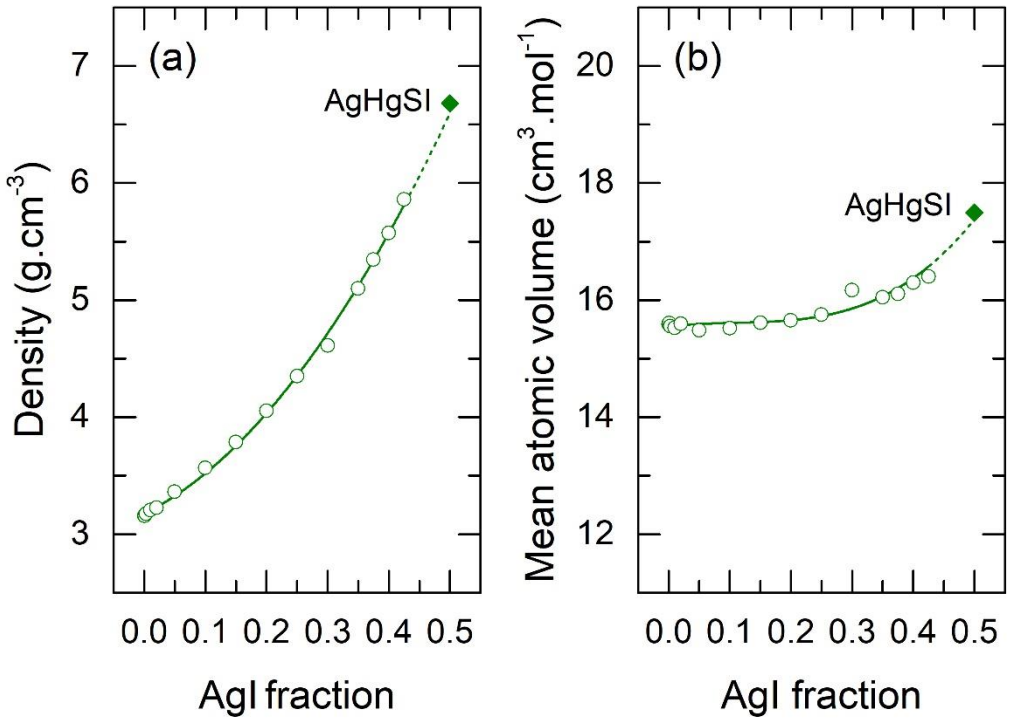

Figure I.26. (a) Density and (b) mean atomic volume of the $(AgI)_{0.5-0.5x}(HgS)_{0.5-0.5x}(As_2S_3)_x$ alloys as a function of the silver iodide content.

I.5.5.c Thermal properties

Table I.3 lists the characteristic temperatures for the D-series. A single glass transition is observed for all the samples indicating a homogeneous glass nature on macroscopic and mesoscopic scale. **Figure I.27** shows the evolution of T_g as a function of the AgI content. The addition of AgI and HgS in equimolar ratio [HgS]/[AgI] = 1 to the host glass As_2S_3 causes an overall decrease in T_g from 199 °C (x = 0.0001) to 122 °C (x = 0.4). The absence of crystallization temperature (T_x), except for the two glass compositions x = 0.35 (T_x = 251 °C) and 0.4 (T_x = 240 °C), confirms that these glasses are thermally stable; i.e. ΔT is very high (**Table I.3**).

Table I.3. Density d, mean atomic volume V_a and glass transition temperature (T_g) of the ternary glass system $(AgI)_{0.5-x/2}(HgS)_{0.5-x/2}(As_2S_3)_x$.

AgI Fraction	d (g.cm^{-3})	V_a (cm^3 mol^{-1})	T_g (±2) (°C)	T_x (±2) (°C)	ΔT
0	3.18(1)		198		
0.0001	3.15(7)	15.58(7)	199		
0.0003	3.15(8)	15.58(6)	200		
0.001	3.15(6)	15.60(7)	198		
0.003	3.17(4)	15.55(3)	190		
0.01	3.20(5)	15.52(3)	188		
0.02	3.22(6)	15.59(4)	184		
0.05	3.36(4)	14.48(1)	173		
0.1	3.56(6)	15.51(9)	161		
0.15	3.78(6)	15.61(2)	152		
0.2	4.05(3)	15.65(3)	144		
0.25	4.35(1)	16.75(0)	138		
0.35	5.10(1)	16.04(9)	128	251	123
0.4	5.57(2)	16.30(1)	122	240	118

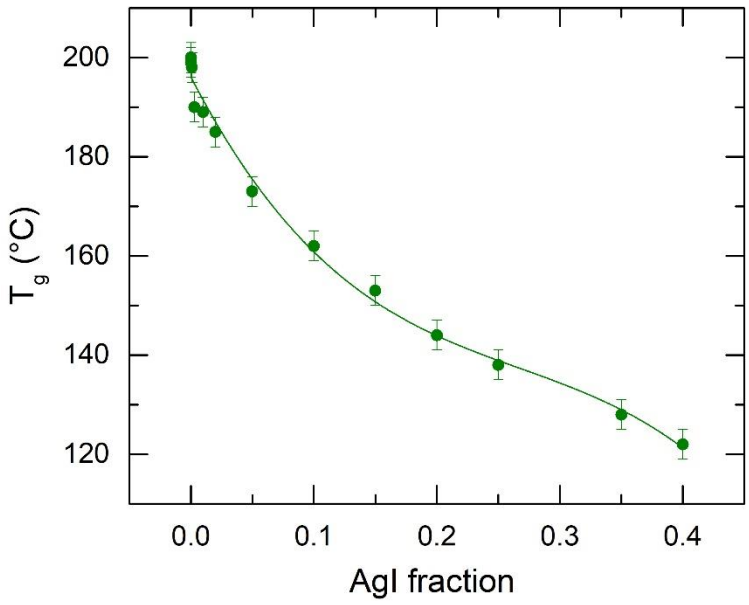

Figure I.27. Evolution of the glass transition temperature T_g as a function of the AgI content for the D-series glasses, $(AgI)_{0.5-x/2}(HgS)_{0.5-x/2}(As_2S_3)_x$.

I.6 Conclusions

In this first chapter, the physical and thermal characteristics of the glassy systems AgY-As_2S_3 (Y = Br, I), HgS-GeS_2, AgI-HgS-As_2S_3 and AgI-HgS-GeS_2 have been measured and analyzed.

We have first determined the vitreous domain for the different systems. The two silver halide thioarsenate $(AgY)_x(As_2S_3)_{1-x}$ (Y = Br, I) families reveal quite extended glass-forming regions: $x_{max} \leq 0.6$ for the AgBr-glasses and $x_{max} \leq 0.4$ for their AgI-counterparts. Secondly we have studied the density and thermal properties of the glasses. In terms of density, the results show that the change is monotonic with the increase of silver halide content, mainly related to the densities of silver halides in the glass compositions. The characteristic glass temperatures determined by DSC have also been presented. The overall decrease of the glass transition temperatures with the addition of the silver halide can be explained by the fragmentation/depolymerization of the glass network. Silver halide thioarsenate glasses exhibit two T_g at intermediate and high silver concentrations. This inhomogeneity is explained in terms of phase-separation.

We have finalized the study of the AgI-HgS-As_2S_3 system by studying the $(AgI)_{0.5-x/2}(HgS)_{0.5-x/2}(As_2S_3)_x$ series. The glass-forming region extends up to 40 mol% AgI. The density increases

monotonically with AgI content and the glasses are all homogeneous as only a single T_g is exhibited.

We have carried out a study on novel chalcogenide glasses in the AgI-HgS-GeS_2 system. In this study, silver iodide, one of the best cationic conductors, has been added to the quasi-binary $(HgS)_{0.5}(GeS_2)_{0.5}$ matrix. The thermal parameters and glass forming stability criteria decrease as AgI content increases.

I.7 References

[1] N. F. Mott and E. A. Davis, *Electronic processes in non-crystalline materials*. Oxford; New York: Clarendon Press; Oxford University Press, 1979.

[2] C. A. Angell, "Glass-Formers and Viscous Liquid Slowdown since David Turnbull: Enduring Puzzles and New Twists," *MRS Bull.*, vol. 33, no. 05, pp. 544–555, May 2008.

[3] W. H. Zachariasen, "The atomic arrangement in glass," *J. Am. Chem. Soc.*, vol. 54, no. 10, pp. 3841–3851, Oct. 1932.

[4] J. L. Souquet and W. G. Perera, "Thermodynamics applied to ionic transport in glasses," *Solid State Ion.*, vol. 40, pp. 595–604, Aug. 1990.

[5] Z. Borisova, *Glassy Semiconductors*. Springer Science & Business Media, 2013.

[6] M. Kastner, "Bonding Bands, Lone-Pair Bands, and Impurity States in Chalcogenide Semiconductors," *Phys. Rev. Lett.*, vol. 28, no. 6, pp. 355–357, Feb. 1972.

[7] A. N. Sreeram, D. R. Swiler, and A. K. Varshneya, "Gibbs-DiMarzio equation to describe the glass transition temperature trends in multicomponent chalcogenide glasses," *J. Non-Cryst. Solids*, vol. 127, no. 3, pp. 287–297, Feb. 1991.

[8] J. M. Saiter, J. Ledru, G. Saffarani, and S. Benazeth, *Mater. Lett.*, p. 451, 1994.

[9] J. M Saiter, "Physical Ageing in Chalcogenide Glasses," *J. Optoelectron. Adv. Mater.*, vol. 3, pp. 685–694, Sep. 2001.

[10] J. T. Edmond, "Measurements of electrical conductivity and optical absorption in chalcogenide glasses," *J. Non-Cryst. Solids*, vol. 1, no. 1, pp. 39–48, Dec. 1968.

[11] B. J. Eggleton, B. Luther-Davies, and K. Richardson, "Chalcogenide photonics," *Nat. Photonics*, vol. 5, no. 3, pp. 141–148, Mar. 2011.

[12] M. Vlcek and H. Jain, "Nanostructuring of chalcogenide glasses using electron beam lithography," *J. Optoelectron. Adv. Mater.*, vol. 8, no. 6, Dec. 2006.

[13] M.-L. Anne *et al.*, "Chalcogenide Glass Optical Waveguides for Infrared Biosensing," *Sensors*, vol. 9, no. 9, pp. 7398–7411, Sep. 2009.

[14] A. V. Kolobov and J. Tominaga, "Chalcogenide glasses as prospective materials for optical memories and optical data storage," *J. Mater. Sci. Mater. Electron.*, vol. 14, no. 10–12, pp. 677–680.

[15] Z. U. Borisova, *Glassy Semiconductors*, Plenum Press New York. Springer, Boston, MA, 1981.

[16] Y. G. Vlasov and E. A. Bychkov, “Ion-selective chalcogenide glass electrodes,” *Ion-selective electrode reviews*, vol. 9, no. 1, pp. 5–91, Jan. 1987.

[17] Y. G. Vlasov and E. A. Bychkov, “Chalcogenide glass chemical sensors: Relationship between ionic response, surface ion exchange and bulk membrane transport,” *J. Electroanal. Chem.*, vol. 378, no. 1, pp. 201–204, Nov. 1994.

[18] Y. G. Vlasov, E. A. Bychkov, and A. V. Legin, “Chalcogenide glass chemical sensors: Research and analytical applications,” *Talanta*, vol. 41, no. 6, pp. 1059–1063, Jun. 1994.

[19] A. V. Legin, E. A. Bychkov, and Y. G. Vlasov, “Analytical applications of chalcogenide glass chemical sensors in environmental monitoring and process control,” *Sens. Actuators B Chem.*, vol. 24, no. 1, pp. 309–311, Mar. 1995.

[20] E. Bychkov, V. Tsegelnik, Y. Vlasov, A. Pradel, and M. Ribes, “Percolation transition in Ag-doped germanium chalcogenide-based glasses: conductivity and silver diffusion results,” *J. Non-Cryst. Solids*, vol. 208, no. 1–2, pp. 1–20, Nov. 1996.

[21] Y. Onodera, T. Usuki, T. Nasu, and S. Kohara, “Structure of silver bromide doped chalcogenide glasses,” *Solid State Ion.*, vol. 262, pp. 469–471, Sep. 2014.

[22] K. Arai, T. Kuwahata, H. Namikawa, & S. Saito, *Jap. J. Appl. Phys.*, vol. 11, pp. 1080–1089, 1972.

[23] A. E. Owen, “Electronic Conduction Mechanisms in Glasses: I,” *Glass Ind.*, vol. 48, no. 11, pp. 637–42, 658, 1967.

[24] Y. Kawamoto, N. Nagura, and S. Tsuchihashi, “Dc Conductivity of Ge-S-Ag and As-S-Ag Glasses,” *J. Am. Ceram. Soc.*, vol. 57, no. 11, pp. 489–491, Nov. 1974.

[25] M. Ohto, M. Itoh, and K. Tanaka, “Optical and electrical properties of Ag-As-S glasses,” *J. Appl. Phys.*, vol. 77, no. 3, pp. 1034–1039, Feb. 1995.

[26] M. Miloshova *et al.*, “Tracer and surface spectroscopy studies of sensitivity mechanism of mercury ion chalcogenide glass sensors,” *Sens. Actuators B Chem.*, vol. 57, no. 1–3, pp. 171–178, Sep. 1999.

[27] A. B. Seddon, “Chalcogenide glasses: a review of their preparation, properties and applications,” *J. Non-Cryst. Solids*, vol. 184, pp. 44–50, May 1995.

[28] J.-B. Vaney, “Contribution à l’étude des propriétés thermoélectriques de vitrocéramiques et verres de chalcogénures semi-conducteurs,” Université de Lorraine, 18-Sep-2014.

[29] S. Hull and D. A. Keen, “Pressure-induced phase transitions in AgCl, AgBr, and AgI,” *Phys. Rev. B*, vol. 59, no. 2, pp. 750–761, Jan. 1999.

[30] D. R. Lide, Ed., *CRC Handbook of Chemistry and Physics 78th Edition: A Ready-Reference Book of Chemical and Physical Data*, 78 edition. Boca Raton; New York: CRC Press, 1997.

[31] J. M. Reau, B. Tanguy, J. J. Videau, J. Portier, and P. Hagenmuller, “Transport properties of rapidly quenched glasses in the Z_2S_3−Ag_2S−AgI (Z=As, Sb) systems,” *Solid State Ion.*, vol. 28, pp. 792–798, Sep. 1988.

[32] Y. Onodera, T. Furukawa, S. Hashimoto, T. Usuki, Y. Amo, and Y. Kameda, “Vitrification and transport properties in AgBr-doped chalcogenide systems,” *Solid State Ion.*, vol. 177, no. 26, pp. 2597–2599, Oct. 2006.

[33] T. Usuki *et al.*, “Structural and electrical properties of AgI dispersed As-chalcogenide glasses,” *J. Non-Cryst. Solids*, vol. 312, pp. 570–574, Oct. 2002.

[34] E. Bychkov, D. L. Price, and A. Lapp, “Universal trend of the Haven ratio in glasses: origin and structural evidences from neutron diffraction and small-angle neutron scattering,” *J. Non-Cryst. Solids*, vol. 293, pp. 211–219, Nov. 2001.

[35] P. Boolchand and W. J. Bresser, “Mobile silver ions and glass formation in solid electrolytes,” *Nature*, vol. 410, no. 6832, pp. 1070–1073, Apr. 2001.

[36] A. Pradel, N. Kuwata, and M. Ribes, “Ion transport and structure in chalcogenide glasses,” *J. Phys. Condens. Matter*, vol. 15, no. 16, p. S1561, 2003.

[37] F. Kyriazis *et al.*, “Effect of silver doping on the structure and phase separation of sulfur-rich As–S glasses: Raman and SEM studies,” *J. Non-Cryst. Solids*, vol. 355, no. 37, pp. 2010–2014, Oct. 2009.

[38] S. Khaoulani, M. Kassem, S. Fourmentin, and E. Bychkov, “The AgI-HgS-As_2S_3 glassy system: Macroscopic properties and Raman scattering studies,” *J. Alloys Compd.*, vol. 685, pp. 752–760, Nov. 2016.

[39] “Refinement of the crystal structures of realgar, AsS and orpiment, As_2S_3*,” *Z. Für Krist.*, vol. 136, no. 1–2, pp. 48–65, 2010.

[40] M. Kassem, S. Khaoulani, A. Cuisset, D. L. Coq, P. Masselin, and E. Bychkov, “Mercury thioarsenate glasses: a hybrid chain/pyramidal network,” *RSC Adv.*, vol. 4, no. 90, pp. 49236–49246, Oct. 2014.

[41] E. Bychkov, M. Miloshova, D. L. Price, C. J. Benmore, and A. Lorriaux, “Short, intermediate and mesoscopic range order in sulfur-rich binary glasses,” *J. Non-Cryst. Solids*, vol. 352, no. 1, pp. 63–70, Jan. 2006.

[42] E. Robinel, B. Carette, and M. Ribes, “Silver sulfide based glasses (I). Glass forming regions, structure and ionic conduction of glasses in GeS_2-Ag_2S and GeS_2-Ag_2S-AgI systems,” *J. Non-Cryst. Solids*, vol. 57, no. 1, pp. 49–58, Aug. 1983.

[43] A. Ibanez, E. Philippot, S. Benazeth, and H. Dexpert, “Characterization of germanium surrounding in Ge-S, GeS_2-Ag_2S and GeS_2-Ag_2S-AgI glassy systems by Ge K-edge X-ray absorption study,” *J. Non-Cryst. Solids*, vol. 127, no. 1, pp. 25–35, Jan. 1991.

[44] V. Boev, M. Mitkova, E. Lefterova, T. Wagner, S. Kasap, and M. Vlček, “Glass formation in the Ge–Se–AgI ternary,” *J. Non-Cryst. Solids*, vol. 266, no. Part 2, pp. 867–871, May 2000.

[45] J. Heo and J. D. Mackenzie, “Chalcohalide glasses: I. Synthesis and properties of Ge-S-Br and Ge-S-I glasses,” *J. Non-Cryst. Solids*, vol. 111, no. 1, pp. 29–35, Sep. 1989.

[46] J. Heo and J. D. Mackenzie, “Chalcohalide glasses: III. Vibrational spectra of Ge-S-I glasses,” *J. Non-Cryst. Solids*, vol. 113, no. 2, pp. 246–252, Dec. 1989.

[47] T. Kawaguchi, “Photoinduced surface deposition of Ag on Ag-rich Ag–Ge–S films: Optimal Ag content and film thickness for applications in optical recording devices,” *Appl. Phys. Lett.*, vol. 72, no. 2, pp. 161–163, Jan. 1998.

[48] L. Červinka, L. Tichý, and J. Bergerová, “X-ray analysis of the structure of Ge–S–Ag glasses,” *J. Non-Cryst. Solids*, vol. 232, no. Supplement C, pp. 335–340, Jul. 1998.

[49] S. L. Kuznetsov, M. D. Mikhailov, I. M. Pecheritsyn, and E. Y. Turkina, “Structural chemical processes at the synthesis of chalcogenide glasses,” *J. Non-Cryst. Solids*, vol. 213, no. Supplement C, pp. 68–71, May 1997.

[50] V. S. Vassilev and Z. G. Ivanova, “On the glass formation in the Ge-S-Cd and GeS_2-Cd-I systems,” *J. Phys. Chem. Solids*, vol. 58, no. 4, pp. 573–576, Apr. 1997.

[51] M. Bokova, I. Alekseev, and E. Bychkov, “Mixed cation effect in Ag_2S–Tl_2S–GeS–GeS_2 glasses: Conductivity and tracer diffusion studies,” *Solid State Ion.*, vol. 273, no. Supplement C, pp. 55–58, May 2015.

[52] B. Monchev, T. Petkova, P. Petkov, and J. Philip, “Thermal Behavior of Novel $(GeS_2)_{1-x}(AgI)_x$ Glasses,” *SpringerLink*, pp. 353–356, 2009.

[53] B. Monchev, T. Petkova, P. Petkov, and S. Vassilev, “Novel chalcohalide glasses from the Ge–S–AgI system and some physicochemical features,” *J. Mater. Sci.*, vol. 42, no. 23, pp. 9836–9840, Dec. 2007.

[54] L. Gmelin, *Gmelin Handbook of Inorganic and Organometallic Chemistry*. Springer-Verlag, 1974.

[55] R. Boidin *et al.*, “Study of the pseudo-ternary Ag_2S-As_2S_3-HgI_2 vitreous system,” *J. Solid State Chem.*, vol. 199, pp. 264–270, Mar. 2013.

[56] D. Rodic, V. Spasojevic, A. Bajorek, and P. Onnerud, “Similarity of structure properties of $Hg_{1-x}Mn_xS$ and $Cd_{1-x}Mn_xS$ (structure properties of HgMnS and CdMnS),” *J. Magn. Magn. Mater.*, vol. 152, no. 1–2, pp. 159–164, 1996.

[57] V. Tomashyk, *Quaternary Alloys Based on II - VI Semiconductors*. CRC Press, 2014.

[58] D. J. E. Mullen and W. Nawacki, “Refinement of the crystal structures of realgar, AsS and orpiment, As_2S_3*,” *Z. Für Krist.*, vol. 136, no. 1–2, pp. 48–65, 2010.

Chapter II :

Conductivity of the glassy systems: AgI-As_2S_3, AgBr-As_2S_3, HgS-GeS_2, AgI-HgS-As_2S_3 and AgI-HgS-GeS_2

II.1 Introduction

An ion-selective electrode sensor based on chalcogenide glasses must have a good electrical conductivity in order to be able to measure the potential difference. This conductivity, whether it is ionic and/or electronic, is generated by the movement of ions and/or the movement of electrons respectively. Thus, it is not only important to know the conductivity of the material but also to measure the contribution of ions and/or electrons to the total conductivity.

The principle of electrical conduction entails the migration of mobile charge carriers under the influence of an electric field. Generally, the total electrical conductivity " σ " is the set of partial conductivities " σ_j " associated with each charge-carrying species capable of moving within homogeneous and isotropic solid [1], i.e.,

$$\sigma = \sum_j \sigma_j = \sum_j c_j \, q_j \, \mu_j \qquad \text{(II. 1)}$$

where q_j is the charge, c_j is the concentration and μ_j is the mobility of the charge-carrying species. Indeed, the partial conductivity corresponds to the charge carrier "j", which is defined by the transport number "t_j", i.e.,

$$t_j = \frac{\sigma_j}{\sigma} \qquad \text{(II. 2)}$$

Since all materials are mixed electrical conductors, then all the charge carriers are divided into two subsets, one which contains the electronic charge carriers, and the other the ionic charge carriers. The electronic " σ_e " and ionic " σ_i " conductivities are grouped by the equation:

$$\sigma = \sigma_i + \sigma_e = (t_e + t_i)\sigma \qquad \text{(II. 3)}$$

Furthermore, the materials for which " t_i " is greater than 0.99 are considered to be purely ionic conductors, while those with " t_e " greater than 0.99 are considered to be purely electronic conductors [2].

II.1.1 Electronic conductivity

II.1.1.a Generalities

Before going deep in the transport properties of chalcogenide glasses, we will begin this chapter by recalling some general notions about the electronic transport in disordered materials. The rules determining the electronic properties of crystalline and amorphous solids are often very different.

Perfect crystals are the basis for the development of the theory of solid-state physics, which exploits in particular the translational invariance in their atomic networks. In fact, real crystalline materials contain imperfections (such as impurities or dangling bonds at point defects or microvoids), that we consider as a disorder of low amplitude and can be treated by improving/ adjusting/ complexifying the starting models.

In the case of disordered solids such as glasses, the invariance by translation, seen as a notion of long-range order, seems to be no longer the same; yet a certain notion of order, at short- range, remains well-presented. So, it's no longer possible to develop theories based on the interaction of Bloch waves to describe the electronic properties of the materials. As a result, the first question related to electronic transport in disordered materials (liquid metals and semiconductors, glasses, amorphous films produced by evaporation, sputtering or any other technique) is which of the concepts appropriate to crystalline solids can be used in non-crystalline materials. Mott and Davis [3] have shown that the first concept, equally valid for both types of materials, is the electronic density of states $N(E)$. In general, the available evidence suggests that the $N(E)$ form in a liquid or non-crystalline solid does not differ greatly from that in the crystal, except for some details such as localized states in the forbidden energy range or energy gap in semiconductors. Anderson [4] gave a quantitative criterion for electron localization **(Figure II.1,2)**. This localization results in an exponential decrease of the wave function with distance. Physically, we can explain simply this feature as follows: localization of a wave function would result from the sum of the destructive interferences created by the elements of the surrounding disorder [3].

Gubanov [5] and then Banyai [6] suggested that near the edges of conduction or valence bands in most non-crystalline materials the states are localized. The concept of localized states is very simple; they are simply 'traps' for injected carriers. Moreover, at the bottom of a conduction band or top of a valence band, such localized states must necessarily occur in a disordered material.

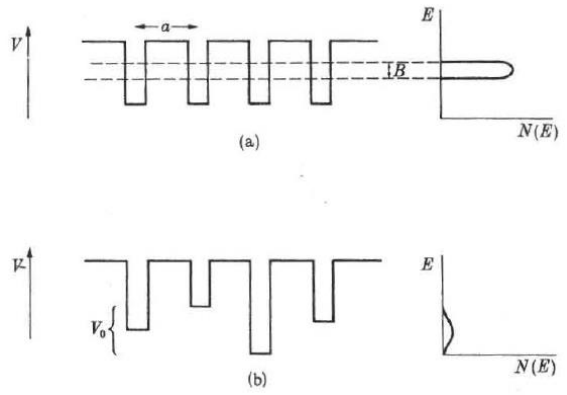

Figure II.1. (a) Potential wells for a crystalline lattice (b) Potential wells for the Anderson lattice. The density of states $N(E)$ is also shown.

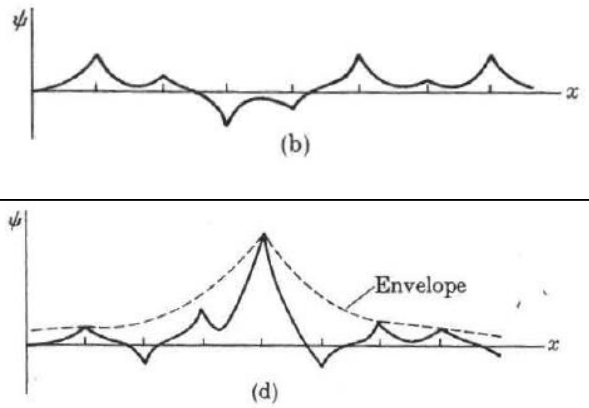

Figure II.2. Form of the wavefunction in the Anderson model: (b) the states are non-localized (extended); (d) strong localization.

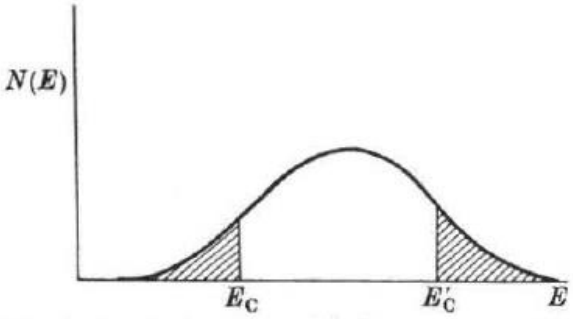

Figure II.3. Density of states in the Anderson model when the states are non-localized in the center of the band. Localized states are shown shaded. E_C, E'_C separate the ranges of energy where states are localized and non-localized (extended).

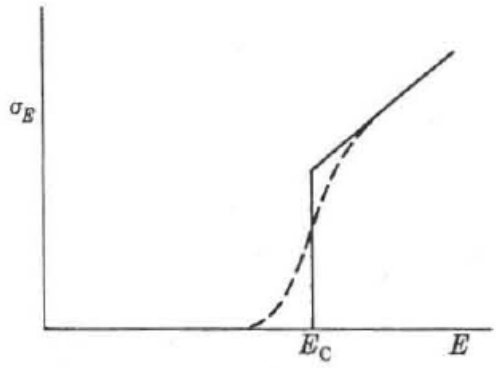

Figure II.4. Conductivities σ_E at T=0 K as a function of E: the full line is dc electronic conductivity σ_{dc} and the dashed line is ac electronic conductivity $\sigma_{ac}(\omega)$.

In any non-crystalline material, localized and delocalized states cannot coexist with same energy. The electrical conductivity at a given energy level E, expressed in the Kubo-Greenwood formula [3], has the characteristic of being zero at T= 0 K for the localized states (because proportional to the recovery of the waveform functions of the states to this energy), but not zero in the case of delocalized states. As this conductivity can be both null and non-zero, there must be an energy E_C separating two domains: one in which all the states are localized and one that only includes delocalized states. The energy E_C separating the delocalized states (high electronic mobility) and

the localized states (low electronic mobility), first pointed out by Mott [7] **(Figure II.3)**, is called a 'mobility edge' by Cohen, Fritzsche and Ovshinsky [8].

For energies below the mobility edge, an electron moves by hopping. Its mobility at 0 K vanishes, even though the wave functions of neighboring states overlap. As the energy E is just above E_C, $E \cong E_C$, the conductivity has a finite value, called the 'minimum metallic conductivity' **(Figure II.4)**.

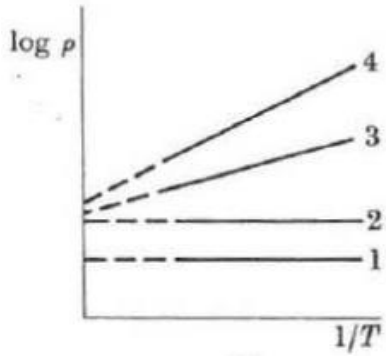

Figure II.5. Plots of resistivity log ρ vs. $1/T$ $(\rho = 1/\sigma)$ for values of V_0/B increasing from curves 1 to 4, where V_0 is a random potential in the Anderson model and B is the crystalline linewidth, see **Figure II.1** for details. Curve 2 shows the value of ρ for E_F at E_C, so that $1/\rho(T)$ for this curve is the minimum metallic conductivity σ_{min}.

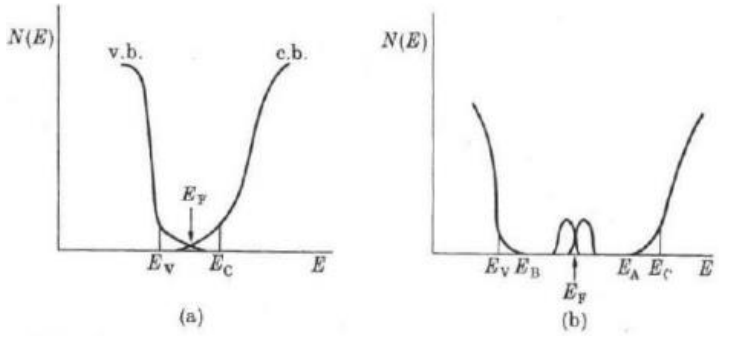

Figure II.6. Density of states in amorphous non-crystalline semiconductor: (a) model of Cohen-Fritsche-Ovshinsky [8], and (b) model of Mott [7] with states in the gap due to dangling bonds acting as deep donors below acceptors; E_V and E_C are the energies separating localized and extended states in the valence and conduction bands, respectively; $\Delta E = E_C - E_A$ and $\Delta E' = E_B - E_V$ are the bandwidths of localized electronic states in the conduction and valence bands.

For T > 0 K and electron excitation above the mobility edge, the electronic conductivity has an exponential form **(Figure II.5)**:

$$\sigma = \sigma_{min} \exp[-(E_c - E_F)/kT] \qquad \text{(II.4)}$$

where E_F is the Fermi energy. The minimum metallic conductivity was calculated by Mott [7], $\sigma_{min} \approx 10^2 - 10^3$ S. cm^{-1} depending on model parameters. Two most common models of amorphous semiconductors are presented in **Figure II.6**. The Cohen-Fritzsche-Ovshinsky model [8] suggests a pseudo-gap for non-crystalline materials when the localized states of the valence and conduction bands are overlapping in the semiconductor band gap. In contrast, Mott [7] assumes a real energy

gap for amorphous semiconductors with $N(E) = 0$ both above and below limiting energies E_B and E_A, which correspond to highest localized electronic states in the valence band and lowest localized electronic states in the conduction band. Electron excitation into localized states at E_A also leads to an exponential temperature dependence of the hopping conductivity:

$$\sigma = \sigma_{hop} \exp[-(E_A - E_F)/kT] \quad \text{(II.5)}$$

but the pre-exponential factor $\sigma_{hop} << \sigma_{min}$, at least by a factor of $\sigma_{hop}/\sigma_{min} = 10^{-2} – 10^{-3}$ [3].

II.1.1.b Case of chalcogenide glasses

Pure chalcogenide glasses, i.e. without metal, are electronic conductors [13-15] and their conductivity varies with increasing the atomic number of the chalcogen element present in the glass [16,17]. This phenomenon, observed by Tanaka *et al.* [14], show that the conductivity increases due to the metal bonding appearing when passing from sulfur, to selenium and then tellurium. The electronic conductivity obtained at room temperature (298 K) for the As-S binary system is very low (in the order of 10^{-18} to 10^{-13} S.cm^{-1} depending on the composition). These materials have electrical properties almost identical to those of the insulating materials (dielectric materials) [15]. The maximum conductivity value, recorded for the stoichiometric As_2S_3 composition, was 5×10^{-16} S.cm^{-1}, which also shows a lower activation energy of ≈1.1 eV in [3]. Typical conductivities of some chalcogenide glasses are presented in **Figure II.7** [3]. Replacing sulfur by selenium in As_2S_3 increases the conductivity up to 8.0×10^{-9} and to 2.5×10^{-4} S.cm^{-1} for As_2Te_3. The corresponding activation energies were 0.7 and 0.3 eV, respectively [16], [17].

The addition of metallic elements such as thallium (Z = 81) to the glass composition, further increases of the glass electronic conductivity [18], except Tl-rich (> 17 at.%) vitreous alloys, showing ionic conductivity [19]–[21]. Meanwhile, the addition of lighter elements such as lithium (Z = 3) [22], silver (Z = 47) [23] or sodium (Z = 23) enhances the ionic conductivity due to the contribution of the mobile ions, hence the ionic transport phenomenon.

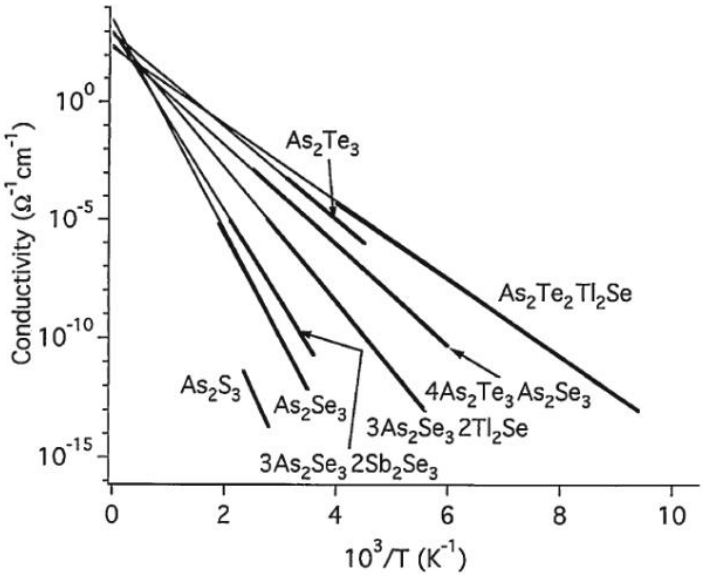

Figure II.7. Variation of conductivity as a function of temperature for several chalcogenide glasses.

II.1.2 Ionic conductivity

The ion migration phenomenon in solids forms the basis for a wide variety of electrochemical applications, ranging from power generators and chemical sensors to ionic switches. In this part, we describe briefly the mechanisms of ion transport in crystals and glasses.

II.1.2.a Mechanisms of ion transport in crystals

In solid electrolytes, ions are in perpetual random movement in all possible directions (Brownian motion) from a lattice point to a vacancy or interstitial site, or from one interstitial site to another, even in the absence of electric field. By this random movement, the concentration of ions and defects are rendered uniform throughout the solid, and this process is referred to as diffusion. When an electric field is applied on the solid, the ions still randomly move about, but migrate as a whole along the direction of the electric field manifesting as ionic conduction. Thus diffusion and migration of ions via defects constitute the basic processes of ionic conduction in crystalline ionic solids [24]. During diffusion and ionic conduction, ions move through the lattice via some jumping process, a direct cation-anion exchange is ruled out and the ion transport mediated through defects. The ion transport is thus governed by the jump probability of an ion into a defect and is hence proportional to:

i) The probability for the ion to jump into the defect in a given direction in unit time, which is the jump frequency and,

ii) The probability that a given site has a defect on a nearest neighbor site, i.e., the product of the number of nearest neighbor sites and the mole fraction of the defects.

II.1.2.b Mechanism of ion transport in glasses

Since its discovery in the 19th century [25], the ion transport in glasses has been widely studied in order to understand the transport mechanisms and to find its potential applications. Alkali oxide glasses were more particularly studied to understand the ion transport in glassy materials [26]–[28].

For temperatures lower than the T_g, the conductivity obeys the classical Arrhenius law:

$$\sigma(\text{or } \sigma T) = \sigma_0 \exp(-E_a/kT), \tag{II.6}$$

When only one type of carriers is concerned:

$$\sigma = Ze.n.\mu, \tag{II.7}$$

where n is the concentration of mobile ions, Ze the charge number and μ the mobility).

The mobility can be obtained from the diffusion coefficient using the Nernst-Einstein equation:

$$\mu kT = ZeD, \tag{II.8}$$

In the case of models involving independent jumps of the carriers:

$$D = \alpha\lambda^2\nu_0 \, exp\left(-\frac{E_m}{kT}\right) \tag{II.9}$$

where α is the degree of freedom, λ the average jump distance, ν_0 the attempt frequency of the ions and E_m the migration energy. From Eqs. (II.8) and (II.9)

$$\mu = \frac{\alpha\lambda^2\nu_0 Ze}{kT} \, exp\left(-\frac{E_m}{kT}\right) \tag{II.10}$$

The most general expression of the concentration of mobile carriers will be:

$$n = N_0 \exp(-\frac{E_C}{kT}) \quad \text{(II.11)}$$

where N_0 is the total number of the modifier cations and E_C the energy related to the creation of mobile carriers. Combining Eqs. (II.7), (II.10) and (II.11):

$$\sigma = \frac{(Ze)^2 \alpha \lambda^2 \nu_0 N_0}{kT} \exp\left(-\frac{E_m + E_c}{kT}\right) \quad \text{(II.12)}$$

Therefore, one obtains Eq. (II.6) . The measured activation energy E_a is the sum of two terms, the creation energy of mobile carriers E_c (directly linked to n) and the migration energy of the ions E_m (directly linked to μ).

Whether μ or n contributes mainly to the variations of σ depends on whether E_m or E_c contribute mainly to these variations. Thus, a number of theories have been proposed to determine which of the two parameters influences most the conductivity.

1. **The strong electrolyte theory**

This model, proposed in 1954 and called « The Anderson-Stuart model » [29], assumed that the charge carriers effective density is independent of ion concentration or temperature, while the charge carriers mobility varies as a function of these parameters.

According to this model, the activation energy E_a is the result of two contributions: an electrostatic force which accounts for the M^+-O^- binding energy E_b and the strain energy E_s, arising from the elastic bending of the glass when the ion passes through.

$$E_a = E_b + E_S \quad \text{(II.13)}$$

$$E_a = \frac{1}{\gamma}\left(\frac{ZZ_0e^2}{r + r_0} - \frac{ZZ_0e^2}{\lambda/2} + 4\pi G r_D (r - r_D)\right) \quad \text{(II.14)}$$

where γ is a covalency parameter, Z_0 and r_0 are the charge and the radius of O^{2-} ion, λ is the jump distance, r is the cation radius, r_D is the doorways radius and G is the elastic modulus. This model

has explained the variation of activation energy as a function of composition in alkali silicate glasses.

2. The weak electrolyte theory

Ravaine and Souquet proposed this model in 1977 [30]. It postulates that μ_i is independent of the ionic concentration and has a low temperature dependence while n_i depends strongly on the two parameters at once. It is suggested that there are two distinct populations of ions: the mobile population and the immobile population. The concentration of the mobile ions n_i is one of the key parameters to control the ionic-conductivity magnitude of ionic/superionic solids. The weak electrolyte signifies a situation in which the number of free ions is relatively smaller than it should be. According to the weak electrolyte theory, the free ions are the mobile population, while the rest of the ions belong to the category of immobile population. Meanwhile, the immobile ions can begin to move in the vitreous electrolytic system if an energy equivalent to the activation energy is present. In the simple case of glasses obtained by dissolving a modifier oxide M_2O in a network forming oxide, the dissociation equation of the dissolved oxide can be written as:

$$M_2O \leftrightarrow M^+ + MO^- \qquad \text{(II.15)}$$

M^+ ions originally belong to the immobile population. From the dissociation reaction, the non-bridging oxide ions are created. Correlating the ionic conductivity and the thermodynamic activity, Ravaine and Souquet observed a significant increase in conductivity for a number of silica-based glasses based, resulting in the increase of the M_2O activity. On the basis of this hypothesis, the activation energy can be written as:

$$E_a = \frac{\Delta H}{2} + E_m \qquad \text{(II.16)}$$

where ΔH is the enthalpy of the dissociation reaction, E_m is the « true » activation energy involved in the ion transport. In this case, the conductivity is mainly due to the dissociation of mobile ions, hence $\frac{\Delta H}{2} \geq E_m$.

II.1.2.c Ion transport in chalcogenide glasses

The investigation of ion transport in glasses is a topic of interest to link together structure and electrical properties in glasses.

Dopant content

To improve the ionic conductivity, the classical idea is to dissolve a salt in the host-glass. The dissolved salts are generally alkaline or silver halides; ≈40-50 mol% of halide can be introduced in a glass [23], [31], [32]. The cation, alkali or silver ion, will be responsible for the conduction in this glass [31], [33]. For example, in the case of silver halide doped glasses, the Ag^+ conductivity reaches a limiting value of about 1 S m^{-1} whatever the host glass used [23]. Two assumptions were suggested to explain this behavior: (i) the existence of α-AgI micro-domains [34], [35] or (ii) the migration of Ag^+ by simple rotation around the iodide anions when the I^- ions come close together at high silver content [23]. The second assumption is more consistent with an activation energy of 0.3 eV, much larger than that of α-AgI (0.05 eV).

In systems such as $(AgX)_x(As_2Se_3)_{1-x}$ (X = I, Br, Cl) [36], [37], $LiPO_3$-LiX (X = I, Br, Cl), and AgX-$AgPO_3$ (X = I, Br, Cl) [38], the conductivity increases with increasing the radius of the ionic halide. In these later, i.e. glasses based on $AgPO_3$, the Raman spectra do not show any significant changes with the variation of composition; the structure of the glass remains unchanged while the halides do not fit in the polyphosphate chains but constitute a « subnetwork » in the glassy matrix [39]. This causes the appearance of two types of Ag^+ ions of different mobility:

- Ag^+ ions of the vitreous support coordinated with the oxygen and halogen atoms;
- Ag^+ ions whose environment consists only of the halogen atoms with a coordination close to that of the Ag^+ in the crystalline α-AgI.

Ag^+ ions of the second type are more mobile than those of the first type. Therefore, this insures a conduction following a mechanism comparable to that proposed for the crystalline components containing AgI [39].

Ion transport over a wide composition range

It is indispensable to start first by summarizing state-of-the-art of ion transport studies in chalcogenide glassy systems over a wide composition range in order to emphasize the established facts and open questions.

One of the first reports dealing with conductivity studies over a wide composition range in mobile cation content was devoted to Na_2S-B_2S_3 glasses [40]. Nevertheless, the most studied systems

appear to be silver sulfide and silver selenide vitreous alloys since they have excellent chemical stability and suitable ^{110m}Ag and ^{108m}Ag tracers for long-term diffusion experiments. Conductivity and tracer diffusion studies of silver and copper chalcogenide glasses over 3 to 5 orders of magnitude in Ag/Cu content [41]–[43] have shown two drastically different ion transport regimes above the percolation threshold at $x_c \approx 30$ ppm: (i) critical percolation, and (ii) modifier-controlled ion motion, **Figure II.8**. The critical percolation transport was shown to be closely related to the connectivity of the glassy host reflected by the average coordination number $\langle n_0 \rangle$. The nature of mobile species (Ag^+ or Cu^+ cations), the chemical form of dopants (halides or chalcogenides) or of the host matrix (sulfide or selenide) appear to be much less important in a remarkable contrast to the modifier-controlled regime. However, the effect of the dopant chemical form has not been studied in details since the majority of the published results were related to selenide glassy systems [42]–[44] having the enhanced electronic conductivity, mostly of *p*-type, $\sigma_e > 10^{-12}$ S cm^{-1}, and masking the ionic transport at low cation content, $x < 0.3$ at.% or $100x_c$. The most extended mobile cation concentration range was studied in silver thioarsenate system Ag_2S-As_2S_3, from 4 ppm to 33.3 at.% Ag [45], [46]. Vitreous arsenic sulfide host As_2S_3 has very low electronic conductivity, $\sigma_e \approx 2\times10^{-16}$ S cm^{-1} at room temperature [3], allowing the reliable ionic conductivity measurements of extremely diluted glasses to be compared with ^{110m}Ag tracer diffusion results [45], [46]. We have chosen glassy As_2S_3 for silver halide AgY (Y = Br, I) doping to verify whether chemically different silver compounds will induce similar or contrasting Ag^+ ion transport in the critical percolation and modifier-controlled domains. We did not expect any surprises for glasses with high silver content since the widely accepted viewpoint predicts an increase of ionic conductivity going from sulfide to halides: $\sigma_{Ag_2S-As_2S_3} < \sigma_{AgBr-As_2S_3} < \sigma_{AgI-As_2S_3}$. The open question was what happens for diluted or extremely diluted vitreous alloys.

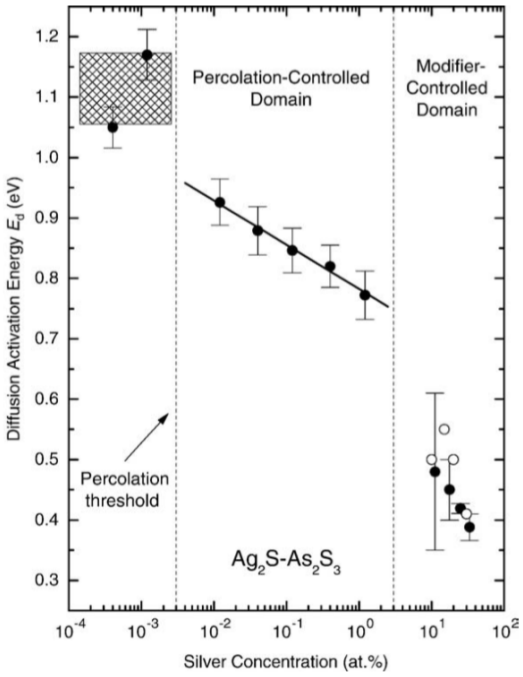

Figure II.8. Diffusion activation energy E_d plotted as a function of silver concentration for the quasi-binary Ag_2S–As_2S_3 glasses.

II.1.2.c.1 Critical percolation regime in Ag^+ ion-conducting glasses

It was shown earlier [41], [45], [46] that the ionic conductivity and tracer diffusion coefficient in the critical percolation domain ($x_c < x \leq$ 1–3 at.% Ag) follow simple power-law dependencies as a function of the mobile ion content *x* and temperature T:

$$\sigma_i(x,T) = \sigma_i(1,T)x^{t(T)}, \tag{II.17}$$

$$D_{Ag}(x,T) = D_{Ag}(1,T)x^{T_0/T-1}, \tag{II.18}$$

with the temperature dependent power-law exponent $t(T)$ can be written as

$$t(T) = t_0 + T_0/T, \tag{II.19}$$

where $\sigma_i(1,T)$ and $D_{Ag}(1,T)$ are the ionic conductivity and tracer diffusion coefficient, respectively, of a hypothetical-controlled phase at x = 1, t_0 is the critical exponent at $T = \infty$ and T_0 is the critical fictive temperature which reflects the interconnectivity of the infinite percolation clusters. The conductivity or diffusion activation energy, $E(x)$, also shows a dependence on T_0

$$E(x) = E_0 - kT_0\, ln(x/x_c), \tag{II.20}$$

where E_0 is the activation energy at the percolation threshold x_c and $ln(x/x_c)$ is the term related to the number of conduction pathways frozen below T_g.

A structural hypothesis [47] suggests the following simple pattern. (1) At $x < x_c$, the majority of silver ions reside in isolated domains. These domains are the allowed volumes of the glass [41], [42] of 30 to 50 Å in diameter defined by local mean-square displacements of Ag^+ ions [48]. Consequently, the glass below x_c behaves as an electronic insulator. (2) In the critical percolation region above the percolation threshold, $x_c < x \leq \approx 1000 x_c$, the previously isolated allowed volumes containing Ag^+ ions become connected forming infinite percolation clusters embedded in an insulating glassy host. The percolative ion transport depends on the number and interconnectivity of infinite percolation clusters. The latter is related to the connectivity of the host matrix reflected by the average coordination number

$$\langle n_0 \rangle = \sum_i x_i N_{ij}, \tag{II.21}$$

where x_i and N_{ij} are the atomic fraction and the local coordination number of species i in the glassy host. The average coordination number $\langle n_0 \rangle$ appears to be a key factor determining the critical fictive temperature T_0, derived either from the conductivity and/or diffusion isotherms, Eqs. (II.17)-(II.19), or from the slope $\partial E(x)/\partial \ln x$, Eq. (II.20). A simple relationship was found between the critical fictive temperature T_0 and $\langle n_0 \rangle$,

$$T_0 \propto \langle n_0 \rangle - 2, \tag{II.22}$$

indicating that percolative transport is absent for chain structures, $T_0 = 0$ at $\langle n_0 \rangle = 2$, which is identical to the classical models[20,21] stating the absence of percolation for 1D networks.

The Haven ratio H_R is an important parameter, reflecting correlation effects in ionic motion and defined as [49]

$$H_R = \frac{D^*}{D_{\sigma_i}}, \tag{II.23}$$

where D^* is the tracer diffusion coefficient and D_{σ_i} the conductivity diffusion coefficient, calculated from the ionic conductivity σ_i using the Nernst-Einstein relation

$$D_{\sigma_i} = \frac{kT\sigma_i}{x(ze)^2}, \tag{II.24}$$

where ze is the charge of the mobile cation and x its concentration.

The Haven ratio in the critical percolation regime decreases monotonically with increasing x or decreasing the Ag-Ag interatomic separation distance $r_{\mathrm{Ag-Ag}}$ [41]–[43]

$$H_R = 1 - \frac{const}{r_{\mathrm{Ag-Ag}}}. \tag{II.25}$$

The observed change from uncorrelated ionic migration, H_R = 1 in the Ag dilution limit: $r_{\mathrm{Ag-Ag}}$ $\rightarrow \infty$, to a correlated ionic motion ($H_R \approx 0.5$) suggests a random distribution of mobile cations when the Ag-Ag separation distance is a hyperbolic function of x

$$r_{\mathrm{Ag-Ag}} = 2\left(\frac{3}{4\pi}\frac{V_a}{N_A x}\right)^{1/3}, \tag{II.26}$$

where V_a is the mean atomic volume and N_A the Avogadro's number. Interionic interactions of Ag^+ cations, increasing with decreasing $r_{\mathrm{Ag-Ag}}$, led to correlation effects in the ionic diffusion.

It was also suggested that neither the nature of mobile cations (Ag^+ or Cu^+) nor the dopant chemical form (metal halide or chalcogenide) plays any important role in the critical percolation, as well as the chemical form of the host matrix. This hypothesis has not been checked in details since the majority of the studied glasses in the critical percolation domain having identical average coordination of the glassy host, $\langle n_0 \rangle$ = 2.40, belong to selenide systems: AgI-As_2Se_3, CuI-As_2Se_3, Cu_2Se-As_2Se_3 [42]–[44]. The only exception was the silver thioarsenate family, Ag_2S-As_2S_3 [45]. Enhanced *p*-type electronic conductivity of selenide glasses [3] is masking the ionic contribution at low x. A complete set of tracer diffusion measurements was also hardly to be realized since the short half-life of the ^{64}Cu tracer ($t_{½}$ = 12.7 hours) restricts seriously the duration of diffusion anneals and the accessible diffusion coefficients. The best solution to verify the conductivity invariance in the critical percolation domain is to work with silver halide thioarsenate systems AgY-As_2S_3 (Y = Br, I).

II.1.2.c.2 Modifier-controlled ion transport

At higher silver content, the conductivity isotherm at 298 K reveals a positive deviation from the hypothetical percolation controlled regime. The conductivity isotherms are thought to obey an exponential law in this region:

$$\sigma_i(x) = \sigma_i(0)e^{ax}, \quad \text{(II.27)}$$

this exponential increase in the ionic conductivity assumes a straight-line behavior on a semi-logarithmic scale and was often observed by many investigators [50]–[53]. In some cases, at higher silver or alkali content, saturation effects were observed [23], [54], [55]. Souquet [56] analyzed this type of behavior in terms of the weak-electrolyte theory [30].

It is suggested that the ionic conductivity is no longer caused by percolation. In this modifier-controlled domain far away from the percolation threshold $x >> x_c$, the once isolated silver clusters are now predominant covering the whole glass volume and forming the preferential conduction pathways. Hence, the ion transport parameters are no longer dependent on the host matrix structural organization but depend mostly on the connectivity of the cation-related network.

After presenting the different particularities at low and high Ag concentrations in Ag-doped chalcogenide glasses, we would like to check whether different chemical forms in the AgY-As_2S_3 (Y = Br, I) glasses behave identically or differently in the two regimes.

II.2 Electrical measurements

II.2.1 Impedance spectroscopy

Impedance spectroscopy is a technique that allows the measurement of the total conductivity of a sample, i.e. both ionic and electronic conductivities. The method is based on the variation of the imaginary part of the impedance of the sample and its real part as a function of frequency.

II.2.1.a Principle

When one applies an alternating voltage U to a sample, an alternating current I which is out of phase with respect to the voltage, will be created.

$$U = U_0 \exp(i\omega t) \quad \text{(II.28)}$$

$$I = I_0 \exp i(\omega t + \varphi) \quad \text{(II.29)}$$

U_0 and I_0 are the amplitudes of the voltage and current, ω is the angular frequency and φ is the phase difference between current and voltage.

The electrical impedance $Z(\omega)$ of a circuit element (here the sample studied is between the two electrodes) is the ratio between the alternating voltage and the resulting current:

$$Z(\omega) = \frac{U}{I} \quad \text{(II.30)}$$

Combining the equations (II.28) and (II.29), we can write:

$$Z(\omega) = \frac{U_0}{I_0} \exp(-i\varphi) = |Z| \cos\varphi - i\,|Z| \sin\varphi \quad \text{(II.31)}$$

$$Z(\omega) = Z' - i.Z'' \quad \text{(II.32)}$$

The real component of the complex impedance, $Z' = |Z| \cos\varphi$ is called "effective resistance", while the imaginary component, $Z'' = |Z| \sin\varphi$, is known under the name of "reactance". The plot of the impedance vector Z in the complex plane based on the frequency ω gives a characteristic curve of the system studied **(Figure II.9)**. If several impedances Z_k are in series, the total impedance Z will be the sum of the impedances such that: $Z = \Sigma Z_k$

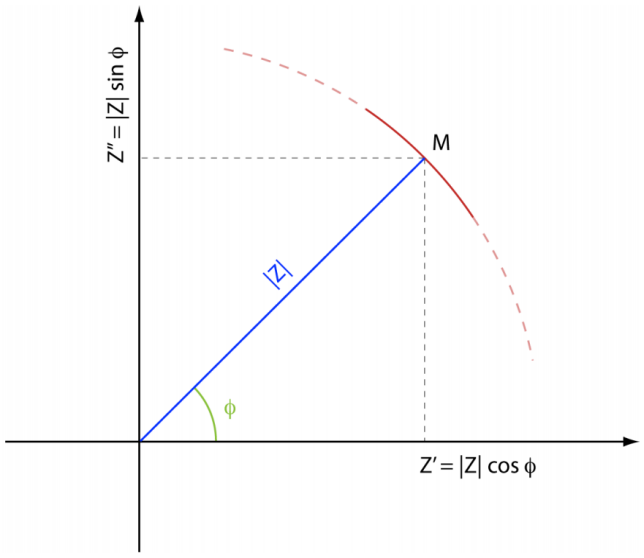

Figure II.9. Real (Z') and imaginary (Z'') part of the impedance vector in the complex plane.

II.2.1.b Typical example of impedance spectrum

A typical spectrum of complex impedance (Z'' = f (Z')) obtained at different temperatures is shown in **Figure II.10**. This type of diagram is called Cole-Cole plot.

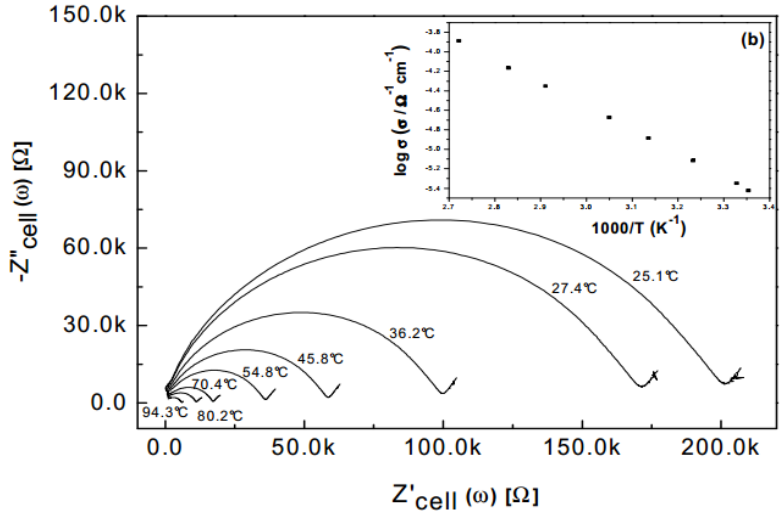

Figure II.10. (a) Complex impedance spectrum of (-Z"cell (ω) vs. Z'cell (ω)) for a solid sample obtained at different temperatures. (b) Arrhenius plot (log σ vs. 1000/T) corresponding to the same sample.

These curves, in the form of a semicircle, are used to determine the resistance R of the material as a function of the temperature. The total conductivity values σ are then obtained using the relationship $\sigma = \frac{1}{R} \times \frac{L}{S}$ where $\frac{L}{S}$ is the geometrical factor of the sample (L = thickness, S = surface). Finally, the values obtained are plotted according to the function $\ln(\sigma) = f(\frac{1}{T})$.

II.2.1.c Impedance measurements

The impedance measurements were performed using an impedance meter whose frequency range extends from 100 Hz to 15 MHz. The conductivity cell used is shown in **Figure II.11**. In the cell, the sample is positioned between a conductive rod and a copper plate which is itself connected to a further rod. The absence of pressure on the sample allows us to avoid the variations related to the geometric factor when approaching the glass transition temperature. Gold was deposited on each face of the sample to establish the blocking electrodes in the electrochemical cell, Au/glass /Au. The temperature measurement is provided by a thermocouple placed near the sample.

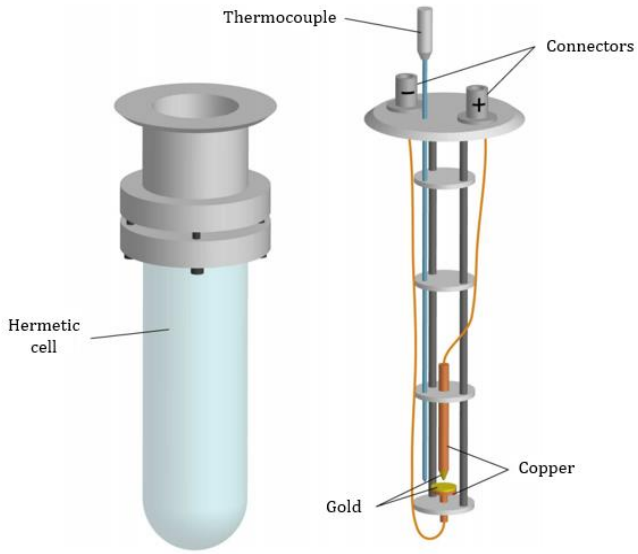

Figure II.11. Conductivity cell used during complex impedance measurements.

II.2.2 DC conductivity measurement

The conductivity measurements were performed using a Hewlett Packard 4339B high resistivity meter with a continuous current source (or voltage) and an applied voltage of 100 Volts. These measurements apply Ohm's Law:

$$\sigma = I \times l/U \times S \qquad \text{(II.33)}$$

where l is the length of the sample, S is the surface of its cross-section, U is the voltage and I is the current. The temperature was monitored using a thermocouple with an accuracy of ±1 °C. The temperature range used ranges from 20 to 155–185 °C depending on the sample composition, but the maximum temperature is below the T_g of the glasses.

II.2.3 Sample preparation

The quenched samples were cut as rectangular plates and polished using silicon carbide SiC powder (9.3 µ grain size). The sample sides were ground parallel and gold was deposited on opposite sides. The typical thickness of the samples was in the range of 1 to 5 mm.

II.3 Experimental results

II.3.1 Conductivity of the binary glassy systems

II.3.1.a AgY-As_2S_3 (Y = Br, I) binary system

Typical Cole-Cole impedance plots, at various temperatures (25, 50, and 75 °C), are displayed for both (a) AgBr–As_2S_3 (x = 0.5) and (b) AgI–As_2S_3 (x = 0.3) glasses, respectively **(Figure II.12 (a) & Figure II.12 (b))**. The room temperature plot shows, in both cases, an almost semi-circle attached to a polarization-tail. The semi-circle, related to electronic-conduction in glasses, decreases progressively with (a) increasing temperature due to the decrease of the sample resistance and (b) with increasing x **(Figure II.12 (a)**, **inset)** indicating an enhancement of ionic-conduction due to increase of mobile ion concentration. The polarization in the low-frequency, at the glass/Au-electrode interface, is related to diffusion-dependent transport phenomena in the materials, and hence indication of ionic character.

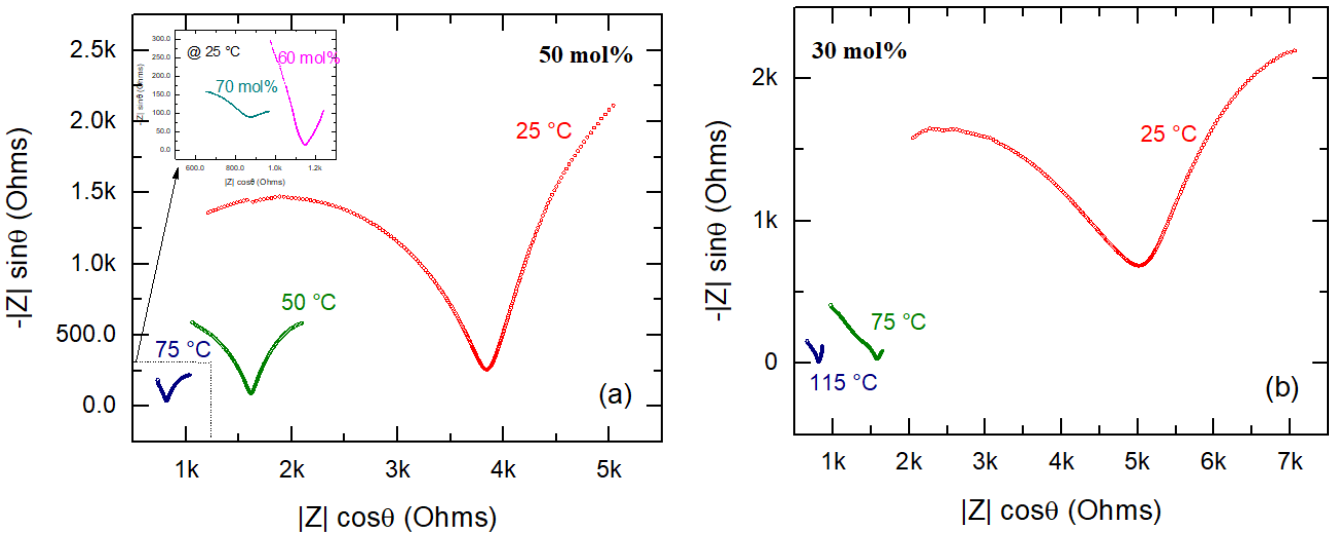

Figure II.12. Nyquist plot of impedance of (a) $(AgBr)_x(As_2S_3)_{1-x}$ for x = 0.5 at 25, 50 and 75 ˚C, and x = 0.6 and 0.7 at 25 °C and (b) $(AgI)_x(As_2S_3)_{1-x}$ for x = 0.3 at 25, 75 and 115 °C.

II.3.1.a.1 Electric transport

Typical conductivity temperature dependencies for the AgY-As_2S_3 (Y = Br or I) glasses are shown in **Figure II.13**. The total electrical conductivity, σ, determined either by the complex impedance method ($\sigma \geq 10^{-8}$ S cm^{-1}) or from the dc conductivity measurements ($\sigma < 10^{-8}$ S cm^{-1}), does not show any significant hysteresis and obeys the Arrhenius law

$$\sigma = \frac{\sigma_0}{T} \exp\left(-\frac{E_a}{kT}\right), \qquad \text{(II.34)}$$

where σ_0 is the conductivity pre-exponential factor, E_a the activation energy, k the Boltzmann constant and T the temperature.

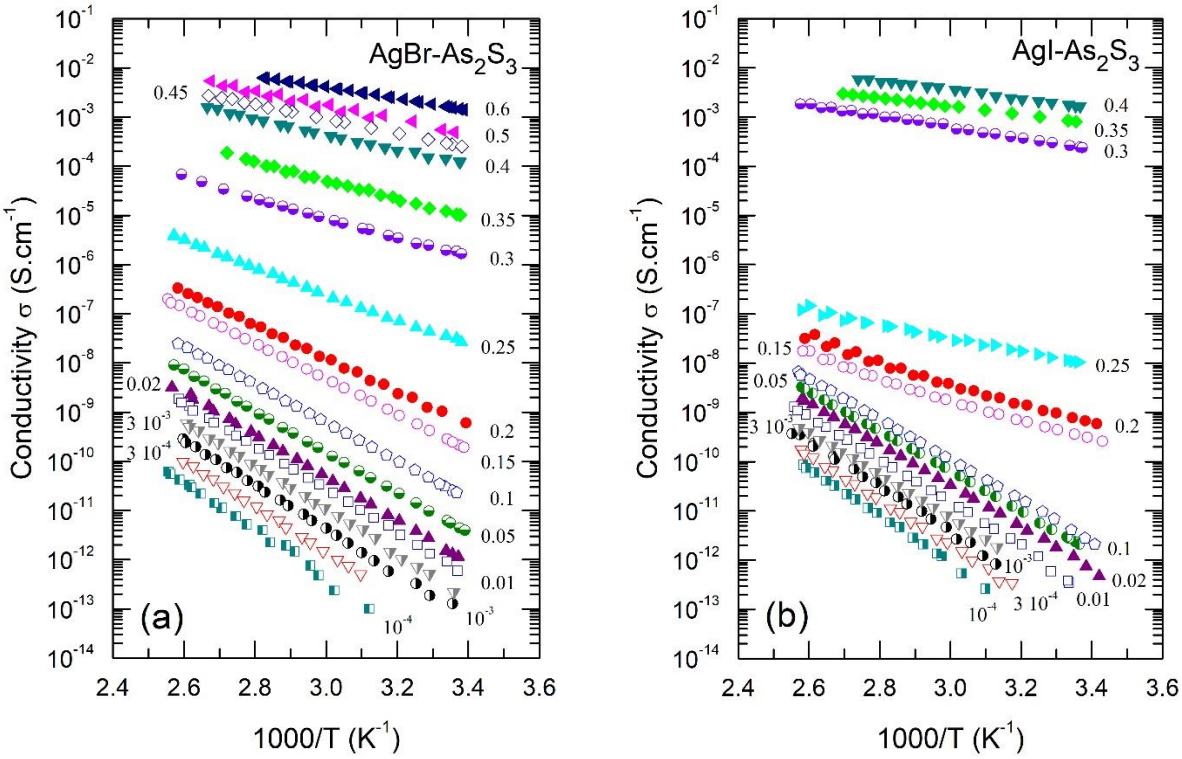

Figure II.13. Temperature dependences of the total electrical conductivity σ for the quasi-binary (a) $(AgBr)_x(As_2S_3)_{1-x}$ and (b) $(AgI)_x(As_2S_3)_{1-x}$ glass systems. The numbers indicate the AgY molar fraction x.

The room temperature conductivity σ_{298}, σ_0 and E_a were calculated from a least-square fit of the data to Eq. (II.34). The results are summarized in **Table II.1** and **Table II.2** and shown in **Figure II.14** and **Figure II.15**. The room-temperature conductivity **(Figure II.14)** increases by ≈13 orders of magnitude with increasing silver halide content from the values which are typical for insulating sulfide glasses (10^{-16} S cm^{-1}) [3] to those characteristic of superionic vitreous alloys (10^{-3} S cm^{-1}) [57], [58]. The maximum room-temperature conductivity is 1.6×10^{-3} S cm^{-1} for the AgBr-rich glasses (x = 0.6, x = 18.75 at.% Ag) and 1.7×10^{-3} S cm^{-1} for the AgI-rich alloys containing 10.53 at.% Ag (x = 0.4).

Table II.1. Electric characteristics of the glass system $(AgBr)_x(As_2S_3)_{1-x}$.

x	[Ag] (at.%)	r_{Ag-Ag} (Å)	$\log \sigma_{298}$ (S cm^{-1})	E_a(eV)	$\log \sigma_0$ (S cm^{-1} K)
10^{-4}	0.002	109.0	-14.13	1.005	5.3
3×10^{-4}	0.006	75.5	-13.50	0.950	5.0
10^{-3}	0.020	50.5	-12.98	0.923	5.1
3×10^{-3}	0.060	35.0	-12.59	0.921	5.4
0.01	0.201	23.3	-12.13	0.898	5.5
0.02	0.405	18.5	-11.87	0.888	5.6
0.05	1.031	13.5	-11.28	0.850	5.6
0.10	2.128	10.6	-10.59	0.799	5.4
0.15	3.297	9.2	-9.60	0.744	5.4
0.20	4.545	8.2	-9.11	0.703	5.2
0.25	5.882	7.5	-7.54	0.561	4.4
0.30	7.317	7.0	-5.76	0.426	3.9
0.35	8.861	6.6	-4.96	0.403	4.3
0.40	10.53	6.2	-3.90	0.338	4.3
0.45	12.33	5.9	-3.56	0.318	4.3
0.50	14.29	5.6	-3.30	0.318	4.6
0.60	18.75	5.1	-2.80	0.255	4.0

Table II.2. Electric characteristics of the glass system $(AgI)_x(As_2S_3)_{1-x}$.

x	[Ag] (at.%)	r_{Ag-Ag} (Å)	$\log \sigma_{298}$ (S cm^{-1})	E_a (eV)	$\log \sigma_0$ (S cm^{-1} K)
10^{-4}	0.002	92.2	-13.78	0.986	5.4
3×10^{-4}	0.006	63.9	-13.34	0.938	5.0
10^{-3}	0.020	42.8	-13.08	0.947	5.4
3×10^{-3}	0.060	29.6	-12.70	0.892	4.8
0.01	0.201	19.8	-12.45	0.917	5.5
0.02	0.405	15.6	-11.98	0.866	5.1
0.05	1.031	11.5	-11.64	0.837	6.0
0.10	2.128	9.0	-11.43	0.849	5.4
0.15	3.297	7.8	-9.49	0.460	0.7
0.20	4.545	7.0	-9.17	0.457	1.0
0.25	5.882	6.4	-8.03	0.326	0.0
0.30	7.317	6.0	-3.60	0.253	3.2
0.35	8.861	5.6	-3.09	0.200	2.8
0.40	10.53	5.3	-2.77	0.208	3.2

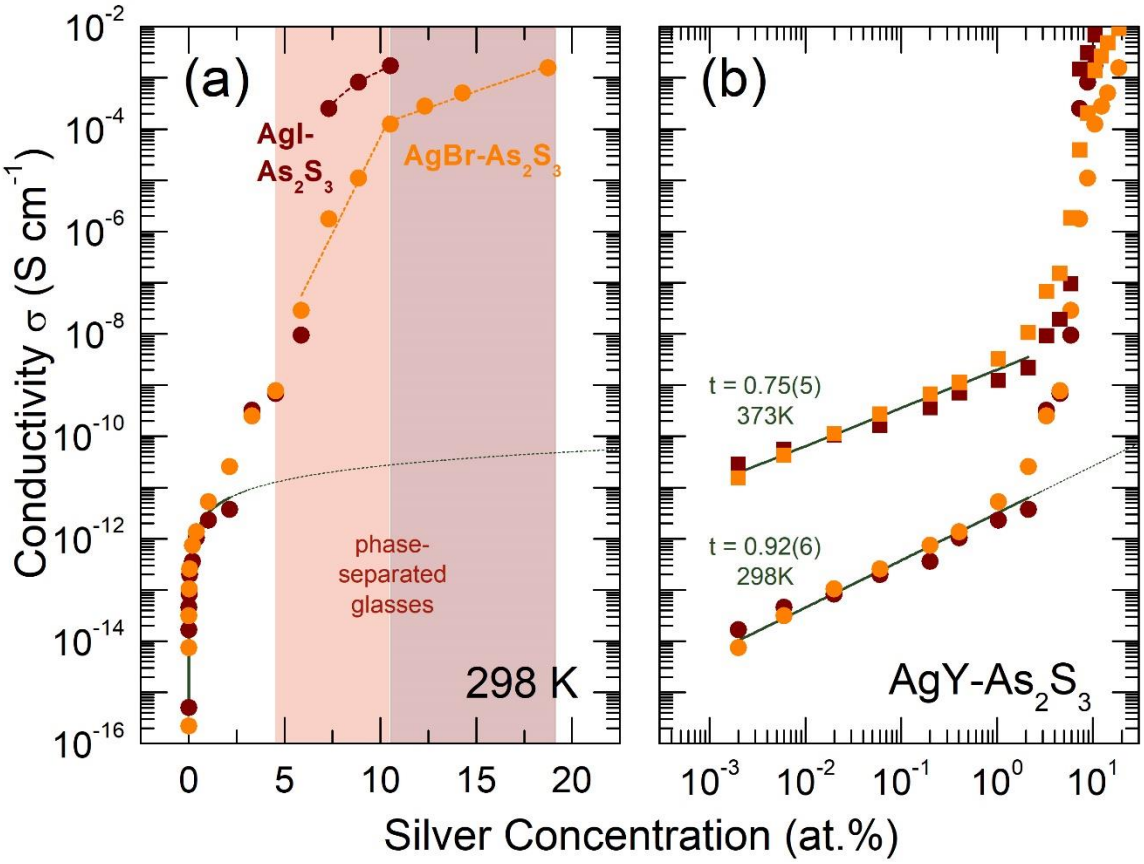

Figure II.14. (a) Room-temperature conductivity of (●, orange) $AgBr\text{-}As_2S_3$ and (●, brown) $AgI\text{-}As_2S_3$ glasses plotted on a semi-logarithmic scale, and (b) conductivity isotherms of silver halide thioarsenate glasses at (●●, solid circles) 298 K and (■■, solid squares) 373 K plotted on a log-log scale. The solid lines represent a least-square fit of the experimental data points in the critical percolation domain to Eq. (II.17); the thin short dashed lines show hypothetical conductivity data beyond the percolation domain; the bold dashed lines in the modifier-controlled domain are drawn as a guide to the eye. An approximate composition region of phase-separated glasses is highlighted in red.

This enormous change in conductivity is accompanied by a drastic decrease of the activation energy from 1.0 to 0.2 eV, **Figure II.15(a)**. In contrast, the pre-exponential factor σ_0 in both systems remains rather invariant up to 4 at.% Ag ($AgBr\text{-}As_2S_3$) or 2 at.% Ag ($AgI\text{-}As_2S_3$), $\sigma_0 \approx 2\times10^5$ S cm^{-1} K, and then drops to $\approx 2\times10^4$ S cm^{-1} K for AgBr-rich glasses or to $\approx10^3$ S cm^{-1} K for their AgI counterparts, **Figure II.15(b)**. We should also note that phase-separated glasses in the $AgI\text{-}As_2S_3$ system, $0.15 \leq x \leq 0.25$, are characterized by unusually low values of σ_0 = 1 – 10 S cm^{-1} K. In addition, the phase-separated glasses in the two systems show non-monotonic changes at intermediate silver concentrations, $4 \leq x \leq 10$ at.% Ag, both in σ_{298} and E_a, **Figure II.14** and **Figure II.15**.

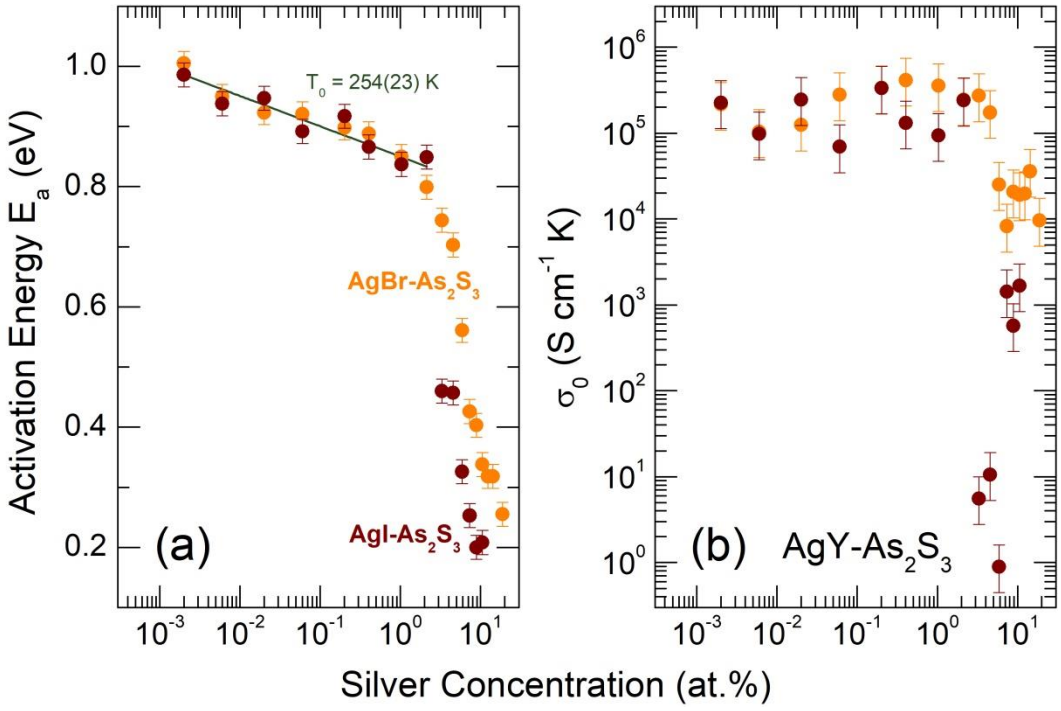

Figure II.15. (a) Conductivity activation energy E_a and (b) conductivity pre-exponential factor σ_0 of (●, orange) AgBr-As_2S_3 and (●, brown) AgI-As_2S_3 glasses. The solid line represents a least-square fit of the E_a experimental data points in the critical percolation domain to Eq. (II.20).

Figure II.13-15 clearly show two drastically different composition trends in conductivity parameters: (i) the critical percolation below 2 at.% Ag, and (ii) the modifier-controlled regime at higher silver content, x > 7-10 at.% Ag. The exact starting concentration of the modifier-controlled domain is difficult to establish because of phase-separation.

II.3.1.a.1.1 Critical percolation domain, $x_c < x \leq 2$ at.% Ag

The conductivity isotherms of AgY-As_2S_3 glasses at 298 and 373 K are consistent with the expected critical percolation behavior, revealing the power-law composition dependences, Eq. (II.17), over 3 orders of magnitude in silver content x and two orders of magnitude in σ, **Figure II.14(b)**. The critical exponent $t(T)$ decreases with increasing temperature in accordance with Eq. (II.19): $t(298\text{K})$ = 0.92±0.06 and $t(373\text{K})$ = 0.75±0.05. The conductivity activation energy follows Eq. (II.20) and shows a linear decrease of $E_a(x)$ on a logarithmic concentration scale, **Figure II.15(a)**. However, the most important result of the conductivity study is a *chemically-invariant* critical percolation since the conductivity parameters of AgY-As_2S_3 (this work) and Ag_2S-As_2S_3 (Ref. [41]) glasses appear to be identical within experimental uncertainty. The maximum conductivity difference between the three systems does not exceed ±0.3 $\log \sigma_i$ units.

This conductivity invariance indicates also that the measured electrical conductivity in the AgY-As_2S_3 glasses is essentially ionic as it was verified for the Ag_2S-As_2S_3 system using ^{110m}Ag tracer [46]. Nevertheless, we are planning silver tracer diffusion measurements to validate this conclusion and to study correlation effects of ionic transport.

Figure II.16 shows the average values of the critical exponent $t(T)$ calculated for these three thioarsenate families and plotted as a function of reciprocal temperature. A perfect fit of the experimental data points to Eq. (II.19) is observed with $t_0 \cong 0$ as for other chalcogenide systems [41]–[44]. The derived average critical temperature T_0 = 264±4 K appears to be very similar to that calculated from $E_a(x)$ using Eq. (II.20), T_0 = 254±23 K. The individual critical temperatures for each thioarsenate as well as selenoarsenate family with $\langle n_0 \rangle$ = 2.40 are mutually consistent with these average values and follow the host connectivity, Eq. (II.22), **Figure II.17**.

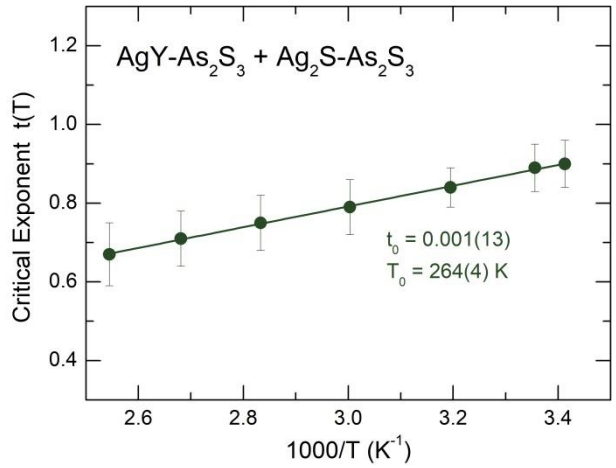

Figure II.16. Average values of the critical exponent t(T) calculated for AgY- and Ag_2S-As_2S_3 glasses at $x \leq 2$ at.% Ag and plotted as a function of reciprocal temperature. The derived t_0 and T_0 parameters are also shown.

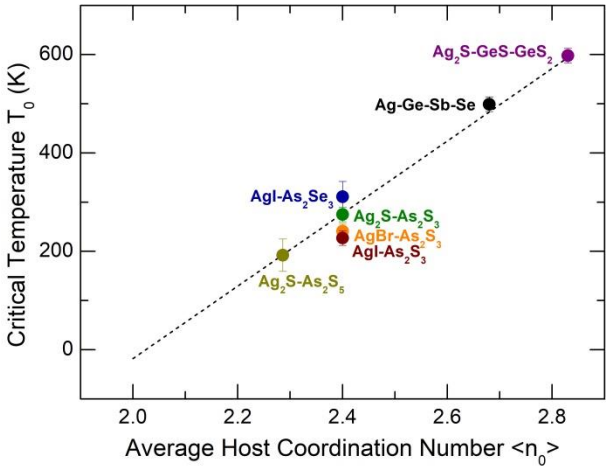

Figure II.17. Critical fictive temperature T_0 plotted as a function of the average local coordination number $\langle n_0 \rangle$ of the host matrix for a number of chalcogenide and chalcohalide glasses. All data points, except for AgY-As_2S_3 (this work), were taken from ref. [43].

II.3.1.a.1.2 Modifier-controlled region, x > 7-10 at.% Ag

The ionic conductivity diverges from chemically-invariant behavior in the modifier-controlled domain at higher x. **Figure II.18** shows the room-temperature conductivity isotherms of the investigated silver halide thioarsenate glasses and their selenoarsenate AgY-As_2Se_3, telluroarsenate AgI-As_2Te_3 and thioantimonate AgY-Sb_2S_3 counterparts [36], [37], [43], [59],

[60], as well as of Ag_2S-As_2S_3 vitreous alloys [45], [46]. Most of the data were only obtained in the modifier-controlled domain because of enhanced electronic conductivity of selenide and especially telluride glasses. In the AgI-As_2Te_3 system, we have used the ion transport numbers t_{Ag^+}, obtained from a combined conductivity and ^{108m}Ag tracer diffusion study [59], to calculate the ionic conductivity up to 0.3 at.% Ag.

As expected, the modifier-controlled ionic conductivity varies strongly when changing the chemical form of silver reaching 4 orders of magnitude between $\sigma_{Ag_2S-As_2S_3}(x)$ and $\sigma_{AgI-As_2S_3}(x)$. The nature of halide species also appears to be important; substitution of AgCl by AgBr increases the ionic conductivity by a factor of 4 to 30. The AgBr/AgI change is accompanied by further increase in σ_i, $40 \leq \sigma_{AgI-host}(x)/\sigma_{AgBr-host}(x) \leq 200$. A clear effect is observed changing the chalcogen: $\sigma_{AgI-As_2S_3}(x) > \sigma_{AgI-As_2Se_3}(x) > \sigma_{AgI-As_2Te_3}$. Vitreous silver halide thioantimonates are also less conducting than their thioarsenate counterparts.

The ionic conductivity increases exponentially at intermediate silver concentrations Eq. (II.27). Nevertheless, one observes a saturation trend at higher x, and the room-temperature ionic conductivity seems to be limited by $\sigma_{298} \approx 10^{-2}$ S cm^{-1}. This or similar conductivity level was reached at $x \approx 10$ at.% Ag for AgI-As_2S_3, $x \approx 20$ at.% Ag for AgI-As_2Se_3, and $x \approx 30$ at.% Ag for AgI-As_2Te_3 glasses.

The phase-separated glasses exhibit a non-monotonic behavior at intermediate concentrations; and here the question arises regarding the change of slope in this region. The first hypothesis suggests that it could be related to phase-separation as has been evidenced by the SEM (to be presented in chapter 3) and DSC measurements. For low silver concentrations ($0.3 \leq x < 0.4$), the Ag-poor phase is the dominant phase and the Ag-rich phase appears in the form of spherical droplets. However, for high silver concentrations ($x \geq 0.4$), the situation changes drastically and the Ag-rich phase becomes the dominant phase. Nevertheless, the homogenous vitreous alloys, i.e., AgI-As_2Se_3 or AgI-As_2Te_3, reveal smooth conductivity isotherms [37], [59]; they present a change in slope but it's much smoother. So, in this case, is it an equation of structural changes of Ag-related sub-network.

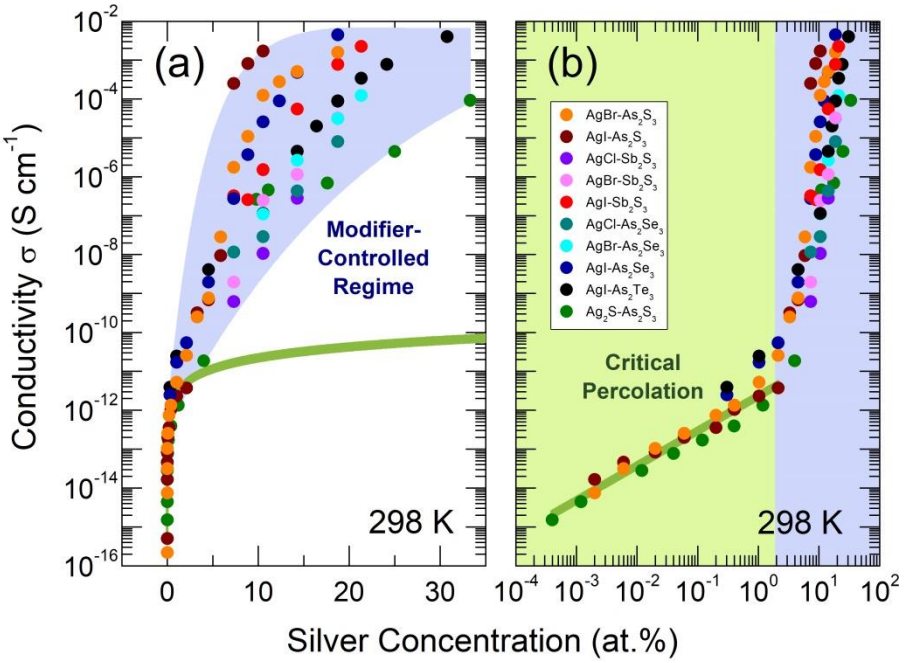

Figure II.18. Room-temperature ionic conductivity isotherms of $AgY\text{-}As_2S_3$ (Y = Br, I) (this work), $AgY\text{-}As_2X_3$ (Y = Cl, Br, I; X = Se, Te) [36], [37], [59], $AgY\text{-}Sb_2S_3$ (Y = Cl, Br, I) [60] and $Ag_2S\text{-}As_2S_3$ glasses [45], [46]; (a) a linear concentration scale, (b) a log-log plot. The bold green solid line shows chemically-invariant power-law composition dependence of $\sigma_{298}(x)$, Eq. (II.17), for three families of silver thioarsenate glasses in the critical percolation domain. The modifier-controlled domain is highlighted in light blue.

The preliminary analysis of the diffraction data reveals the presence of mixed cation-related structural units. As a fact of matter, this scenario is reinforced with the present studies on the structures of silver (I) halide and copper (I) halide coordination polymers [61], [62]. These compounds are built up of different AgX or CuX substructures (X = Cl, Br, I) such as 4- and 6-membered rings, or single and double chains, which are connected into one-, two- or three-dimensional coordination polymers by the N-donor ligands [62]. In fact, the situation changes systematically; for example, at low AgBr contents, the Ag and Br atoms form coplanar $(AgBr)_2$ dimers that are connected by the ethylenediamine ligands via μ-N,N'- coordination into corrugated layers **(Figure II.19)** [61]. Whereas, for rich AgBr compounds, a 3D AgBr substructure forms consisting of helical AgBr chains connected by peripheral Ag–Br contacts into a 3D network that contains large channels [61]. Yet, for the moment it is not possible to estimate the Ag-Ag correlations in our glasses, i.e., the existence of edge-sharing or corner- sharing units, forming 1D chains, 2D sheets or tunnels, etc., in the glass network. This enigma is clarified in Chapter 3.

Basically, we can deduce two conclusions from the presence of mixed interconnected tetrahedral structures. (i) The silver ion distribution in the glass network is no longer random; Ag-rich chalcogenide and oxide glasses [63]–[68] reported experimental Ag-Ag correlations values, r_{Ag-Ag}^{exp} = 3-4 Å, that are far below the expected Ag-Ag random correlations values, r_{Ag-Ag}^{random} = 6-7 Å. (ii) The silver-related motifs form preferential conduction pathways ensuring high Ag^+ mobility in the glass. In other words, the ion transport characteristics are directly related to specific structural parameters, r_{Ag-Ag} and N_{Ag-Ag}. Bychkov *et al*. [69] reported different N_{Ag-Ag} values between Ag-As-S (N_{Ag-Ag} = 2.0–2.5) and Ag-As-Se (N_{Ag-Ag} = 2.7-3.1) glasses and suggested that the quasi-2D conduction pathways in the sulfide case is responsible for the enhanced Ag^+ ion transport.

Finally, the situation has turned out to be as follows: the transport characteristics for AgY-As_2S_3 (Y = Br, I) glasses appear to be similar in the percolation domain with close values of T_0 but different in the modifier-controlled one.

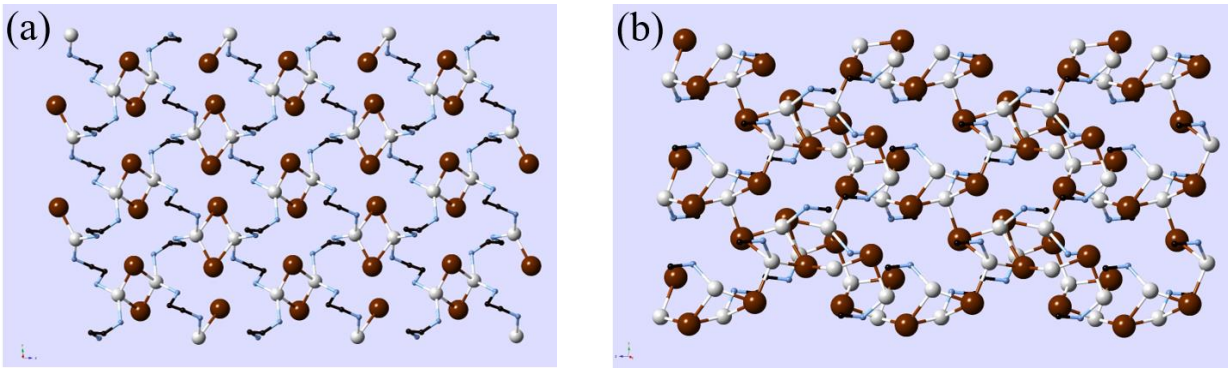

Figure II.19. Crystal structures of the (a) 1:1 and (b) 2:1 AgBr hybrid coordination polymer poly[(AgBr)(μ_2-en-N,N')] with N-donor ligand (ethylenediamine).

II.3.1.b HgS-GeS_2 binary system

Typical temperature dependencies of the *dc* conductivity for the HgS-GeS_2 glasses are shown in **Figure II.20**. They do not show any significant hysteresis and obey the Arrhenius law (Eq. (II.34). The results are listed in **Table II.3** and displayed in **Figure II.21**.

Table II.3. Conductivity parameters for the HgS-GeS_2 glasses: the room-temperature conductivity σ_{298}, the activation energy E_σ, and the pre-exponential factor σ_0.

x	[Hg] (at.%)	σ_{298} (S cm^{-1})	E_σ (eV)	σ_0 (S cm^{-1} K)
0.0	0.00	6.61×10^{-15}	0.910(5)	6.92×10^{3}
0.1	3.45	4.01×10^{-13}	0.805(8)	4.77×10^{3}
0.2	7.14	7.06×10^{-13}	0.729(13)	4.36×10^{2}
0.3	11.11	1.42×10^{-13}	0.773(11)	4.91×10^{2}
0.4	15.39	2.42×10^{-14}	0.873(6)	4.10×10^{3}
0.5	20.00	4.50×10^{-15}	0.964(6)	2.59×10^{4}

Uncertainties in the last digit(s) of the parameter are given in parentheses.

Both $\sigma_{dc}(x,T)$ temperature dependence, **Figure II.20**, and the conductivity isotherm $\sigma_{298}(x)$, **Figure II.21(a)**, show that the mercury thiogermanate glasses are electronic insulators, $4.5\times10^{-15} \leq \sigma_{298}(x) \leq 7.0\times10^{-13}$ S cm^{-1}, with a maximum at the x = 0.2 composition. The change in conductivity activation energy, **Figure II.21(b)**, upon the addition of HgS to the GeS_2 host glass is rather small, ΔE_σ = 0.21 eV. The extremity compositions, x = 0.0 and x = 0.5, gives a mean activation energy value of ~0.94 eV with a minimum value of 0.73 eV at the x = 0.2 composition. In a similar manner, a minimum for the pre-exponential factor σ_0 is present around the x = 0.2 composition and the σ_0 values ranges between 10^2 and 10^4 S cm^{-1} K, indicating that the electronic transport in the $(HgS)_x(GeS_2)_{1-x}$ glasses involves the extended electronic states in the top of the valence band and/or the bottom of the conduction band [3]. The non-monotonic changes of the conductivity parameters, as a function of the mercury sulfide content x, with a maximum (σ_{298})/minimum (E_σ) at x ≈0.2, is probably structure dependent. Similar changes of conductivity parameters were observed for both room temperature $\sigma_{298}(x)$ and E_σ values in the thiogermanate glassy system $(PbS)_x(GeS)_{0.3-x}(GeS_2)_{0.7}$, but not for the σ_0 values **(Figure II.21)**. Although the optical gap of the semiconducting lead sulfide (E_g= 0.3 eV) is narrow compared to the wide gaps of the electronic insulators GeS (E_g= 1.58 eV) and GeS_2 (E_g= 3.2 eV), the conductivity in the thiogermanate glasses does not exhibit continuous changes as reported earlier for the thioarsenate PbS-As_2S_3 glasses where the changes were monotonic [70]–[72]. A non-monotonic behavior was also seen in the mercury thioarsenate $(HgS)_x(As_2S_3)_{1-x}$ glasses, $0.0 \leq x \leq 0.5$. The two composition domains below (region 1) and above (region 2) the $x_0 \approx 0.3$ threshold was attributed to the HgS dimorphism and the dual structural role of mercury in the glasses [73]. The crystalline HgS

presents two polymorphic forms; the red cinnabar α-HgS (2-fold coordinated mercury, E_g= 2.0 eV) [74] and the black metacinnabar β-HgS (4-fold coordinated mercury, E_g= 0.5 eV) [74]. In mercury-poor glasses (region 1, $x < x_0$, fraction of 4-fold coordinated mercury $f_{Hg}^{4F} < 0.1$), the $HgS_{4/4}$ units seem to be distributed randomly in the hybrid Hg−S chain/As−S pyramidal network and do not affect structural, thermal, or electronic properties. An agglomerated mixed $(HgS_{2/2})_m(HgS_{4/4})_{m'}$ subnetwork is formed in HgS-rich vitreous alloys (region 2, $x > x_0$, fraction of 4-fold coordinated mercury $f_{Hg}^{4F} > 0.1$), leading to a fragmentation of the host network, reduced thermal stability and crystallization, as well as changes in electronic properties.

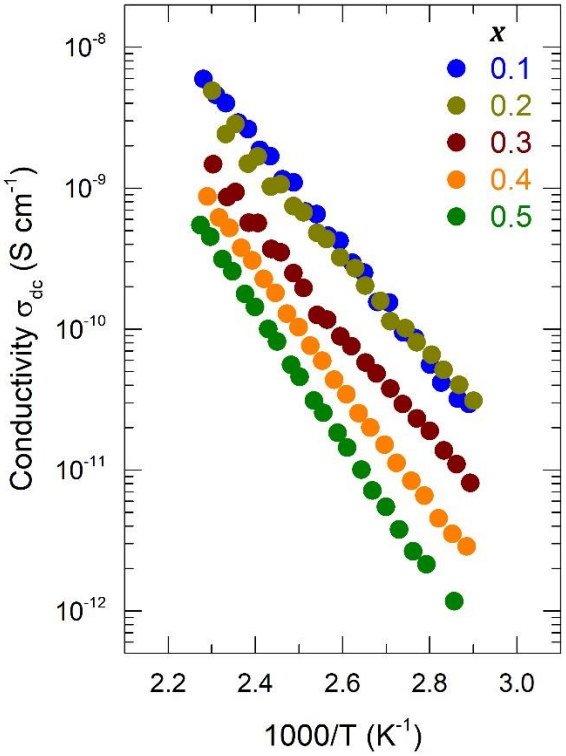

Figure II.20. Temperature dependences of the total electrical conductivity σ for the quasi-binary $(HgS)_x(GeS_2)_{1-x}$ glass system. The numbers indicate the HgS molar fraction x.

The fact that the change is monotonic for PbS-As_2S_3 and non-monotonic for PbS-GeS-GeS_2 suggests that the origin of change in electrical properties of HgS-GeS_2 glasses is not related to HgS dimorphism; PbS is not polymorph, yet different electronic behavior is seen when different host glasses are involved. The electronic changes are probably related to modification of the thiogermanate GeS_2 host matrix itself. HgS additions leads to changes in the molar ratio Ge/S of the thiogermanate matrix and hence affects non-monotonically the electric transport characteristics as was seen recently for the $(Tl_2S)_{10}(GeS)_x(GeS_2)_{90-x}$ glasses [21].

Conductivity was also measured for the x = 0.55 and 0.6 compositions of the $(HgS)_x(GeS_2)_{1-x}$ samples and rather high conductivity values were obtained, $\sigma_{298}(x) \approx 10^{-6}$–$10^{-7}$ S cm^{-1}. Such values are not consistent with those of the glassy mercury thiogermanate electronic insulators and can be attributed to the formation of conducting microscopic inclusions at high modifier concentrations [75]. Halyan et al. [76], revealed also the existence of these aggregates in the 54%HgS-46%GeS_2 glassy alloy.

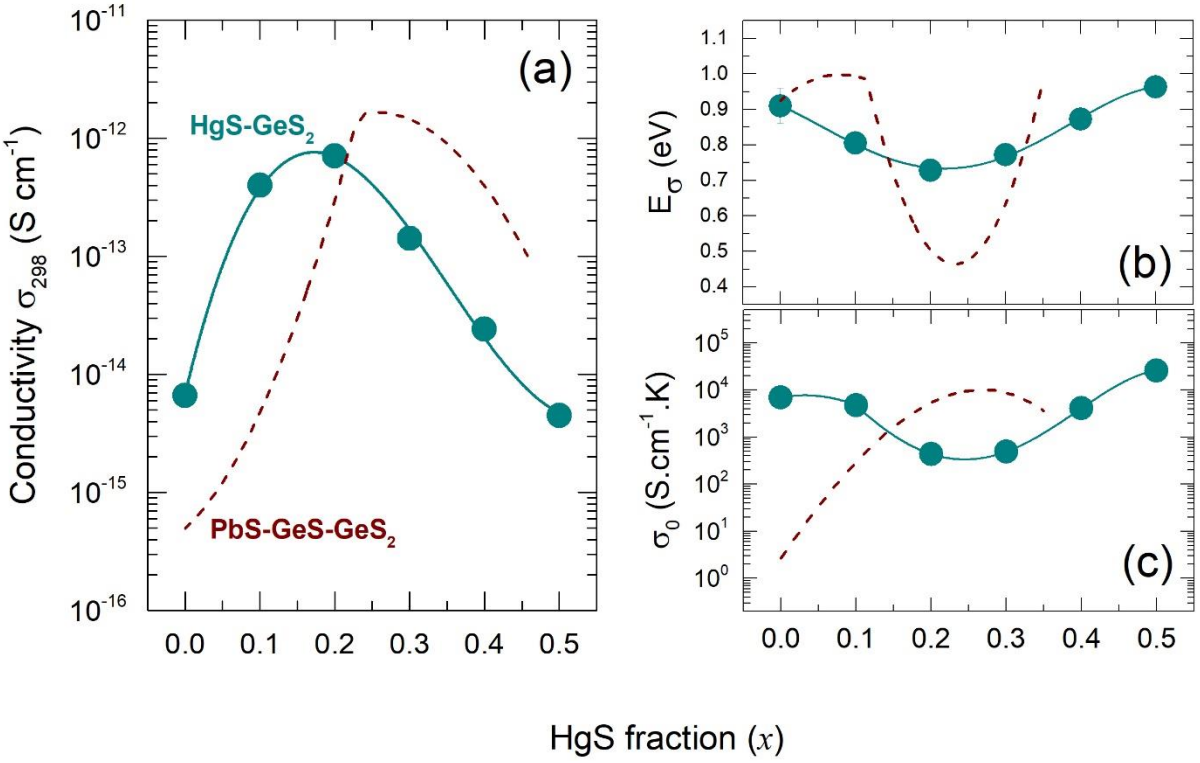

Figure II.21. (a) Room-temperature conductivity σ_{298}, (b) conductivity activation energy E_a and (c) pre-exponential factor σ_0 for the quasi-binary $(HgS)_x(GeS_2)_{1-x}$ glass system. The solid lines are drawn as a guide to the eye. The average conductivity parameters for PbS-GeS-GeS_2 [77] are shown by the dashed lines.

II.3.2 Conductivity of the ternary glassy systems

II.3.2.a AgI-HgS-As_2S_3 ternary system

We have mentioned earlier (Chapter I) that both macroscopic properties and Raman scattering studies were performed on the A– and B–series glasses, i.e. $(AgI)_{0.5-x/2}(HgS)_{0.5-x/2}(As_2S_3)_x$ and $(AgI)_{0.3}(HgS)_y(As_2S_3)_{0.7-y}$, of the pseudo-ternary AgI-HgS-As_2S_3 alloys [78]. In a similar manner, the electrical properties for the A–series glasses were also studied and drastic changes in ionic conductivity σ_i with silver iodide additions were recorded. The ionic transport increases by 13

orders of magnitude with increasing silver content from ~0.002 to ~23 at.%, and the activation energy decreases from 1.05 to 0.35 eV. Two distinctly different ion transport regimes above the percolation threshold concentration, $x_c \approx 30$ ppm, were distinguished, i.e., a critical percolation regime at low silver content (≤ 2-5 at.% Ag) and a modifier-controlled domain (≥ 8 at.% Ag).

In this system, we have synthesized and studied the additional D–series in the $(AgI)_{0.5-x/2}(HgS)_{0.5-x/2}(As_2S_3)_x$ composition range corresponding to the equimolar Hg/Ag fraction, [Hg]/[Ag] ≈ 1, and the motive for this is well stated in Chapter I. The total electrical conductivity σ values are temperature dependent, do not show significant hysteresis effects, and obey the Arrhenius law of Eq. (II.34), **Figure II.22**. The conductivity parameters (σ_{298}, E_a and σ_0) are summarized in **Table II.4** and displayed in **Figure II.23** and **Figure II.24**. σ_{298} increases by ≈10 orders of magnitude with increasing silver content from the values which are typical of insulating glasses (~10^{-16} S cm^{-1}) to the values which are characteristic of super ion-conducting vitreous alloys (~10^{-3} S cm^{-1}) [57], **Figure II.23(a)**. The activation energy decreases from ~1.0 to 0.45 eV **(Figure II.24(a))** while the pre-exponential factor σ_0 values **(Figure II.24(b))** fluctuates between 10^4 and 10^6 S cm^{-1} K.

Table II.4. Electric characteristics of the glass system $(AgI)_{0.5-x/2}(HgS)_{0.5-x/2}(As_2S_3)_x$.

AgI fraction	[Ag] (at.%)	r_{Ag-Ag} (Å)	log σ_{298} (S cm^{-1})	E_a (eV)	log σ_0 (S cm^{-1} K)
10^{-4}	0.002	135.2	-13.78	0.919	4.2
3×10^{-4}	0.006	93.7	-13.31	0.867	3.8
10^{-3}	0.020	62.8	-13.16	0.891	4.3
3×10^{-3}	0.060	43.4	-12.72	0.887	4.7
0.01	0.202	29.0	-12.31	0.881	5.1
0.02	0.410	22.9	-11.95	0.865	5.1
0.05	1.064	16.6	-11.04	0.837	5.6
0.10	2.273	12.9	-9.99	0.781	5.7
0.15	3.659	11.1	-9.09	0.701	5.2
0.20	5.263	9.8	-7.97	0.686	6.1
0.25	7.143	8.9	-7.07	0.630	6.1
0.30	9.38	8.2	-5.75	0.542	5.9
0.35	12.07	7.5	-5.81	0.466	5.9
0.40	15.39	6.9522	-4.89	0.374	5.3

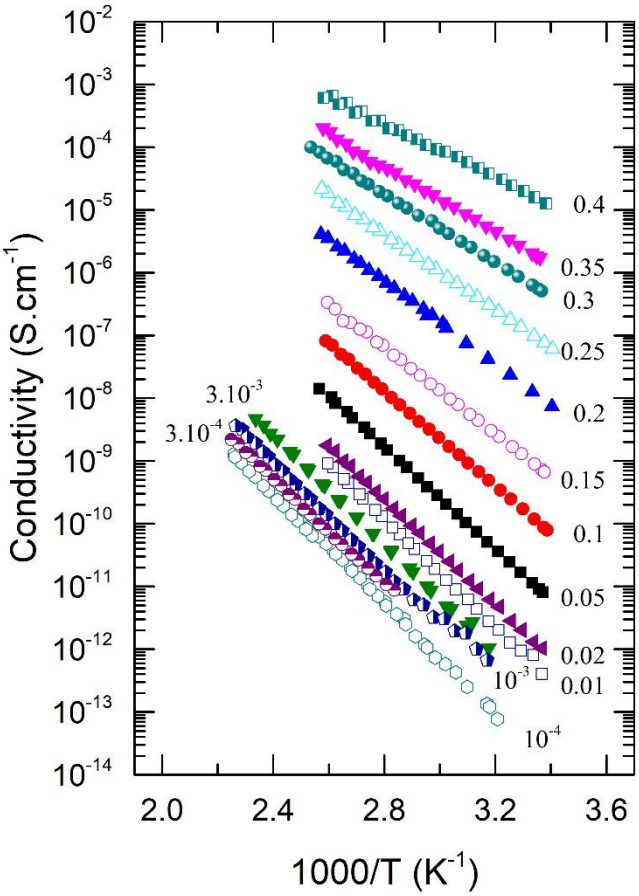

Figure II.22. Temperature dependences of the total electrical conductivity σ for the pseudo-ternary $(AgI)_{0.5-x/2}(HgS)_{0.5-x/2}(As_2S_3)_x$ glass system. The numbers indicate the AgI molar fraction.

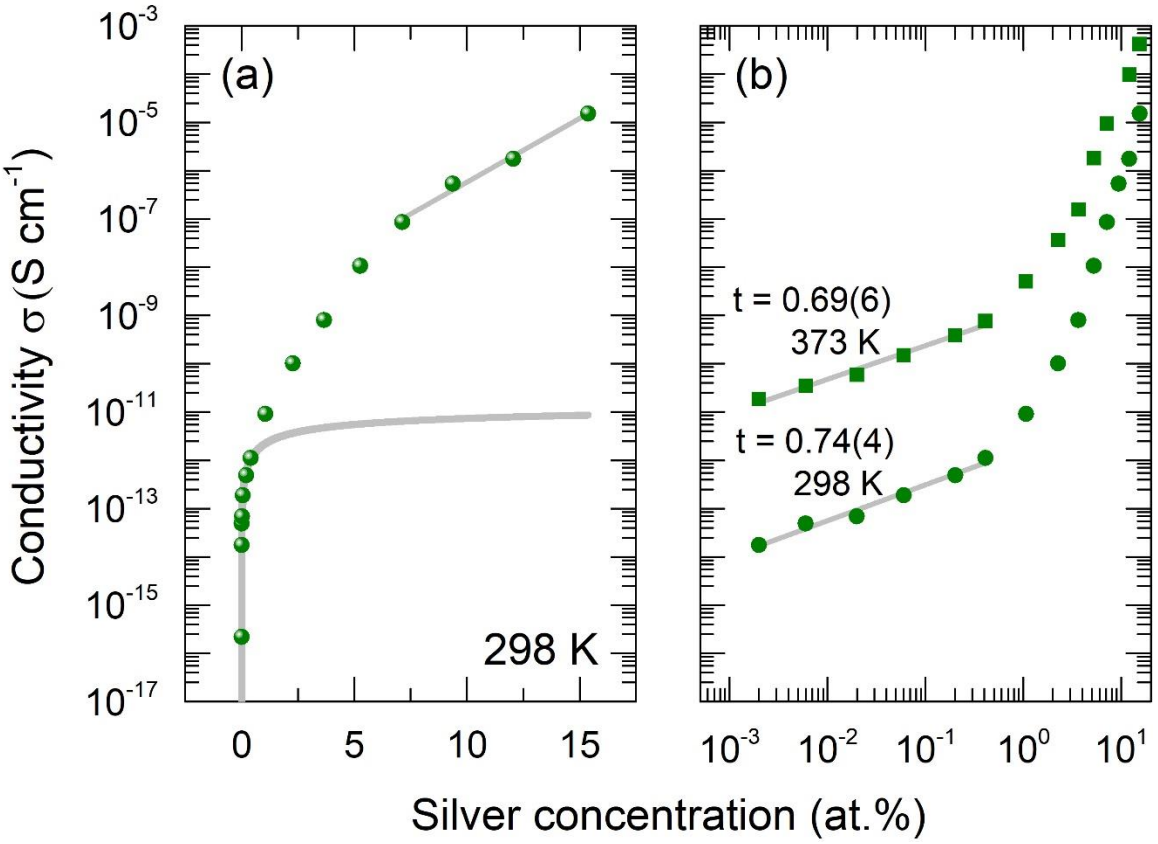

Figure II.23. (a) Room-temperature conductivity of AgI-HgS-As_2S_3 glasses plotted on a semi-logarithmic scale, and (b) conductivity isotherms of silver iodide mercury thioarsenate glasses at (●, solid circles) 298 K and (■, solid squares) 373 K plotted on a log-log scale. The solid lines represent a least-square fit of the experimental data points in the critical percolation domain to Eq. (II.17), showing hypothetical conductivity data beyond the percolation domain; the bold lines in the modifier-controlled domain are drawn as a guide to the eye.

The conductivity isotherms exhibit at least two concentration regions with distinctly different variations in electrical conductivity, **Figure II.23**: (i) the critical percolation below 2 at.% Ag, and (ii) the modifier-controlled regime at higher silver content, x > 7 at.% Ag. This tendency is similar to AgY-As_2S_3 (Y = Br, I) (this work), alkali ion-conducting chalcogenide and oxide glasses [79], [80].

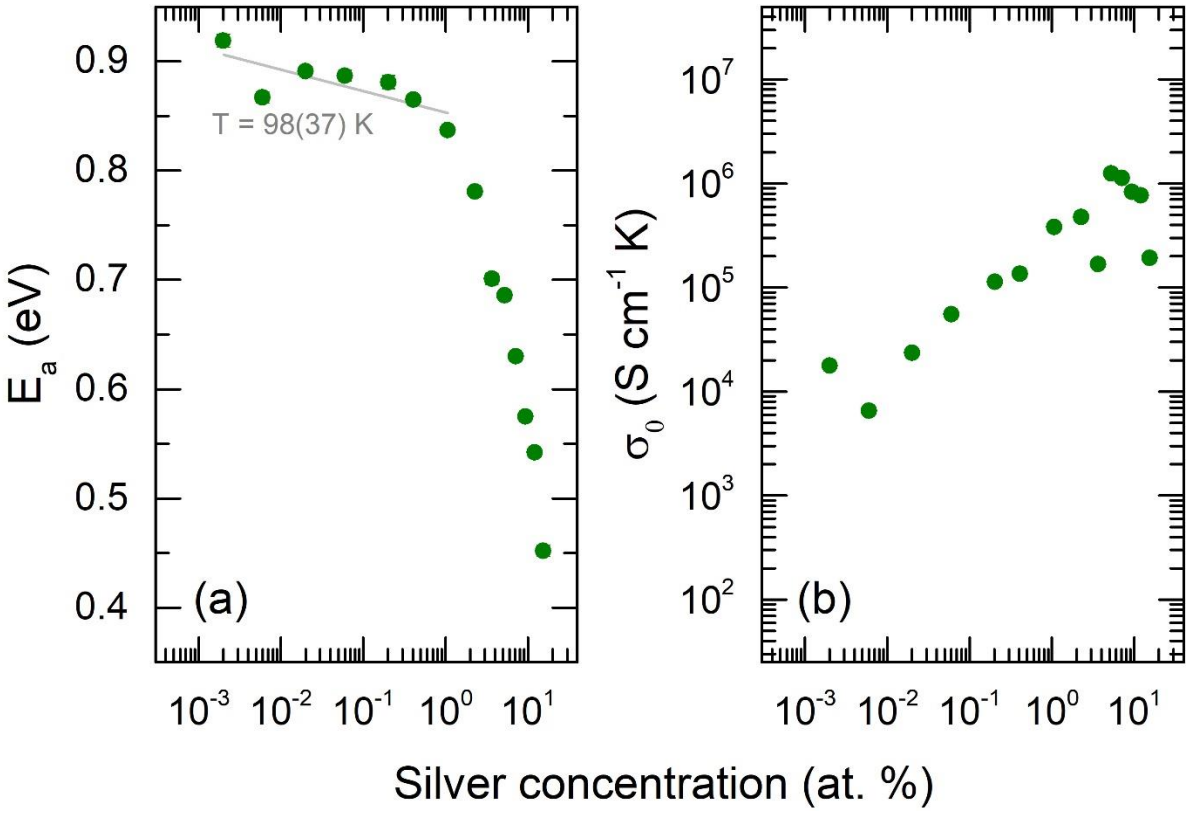

Figure II.24. (a) Conductivity activation energy E_a and (b) conductivity pre-exponential factor σ_0 of AgI-HgS-As_2S_3 glasses. The solid line represents a least-square fit of the E_a experimental data points in the critical percolation domain to Eq. (II.20).

Using the conductivity isotherms method, for the diluted glass compositions ($10^{-4} \leq x \leq 0.02$), we calculated the critical exponent $t(T)$ in the temperature range from 20 till 200 °C, then plotted the obtained results as a function of the reciprocal temperature T^{-1} in **Figure II.25**. A nearly perfect linear regression with a correlation coefficient, r = 0.9999 verifies Eq. (II.19). The values of T_0 and t_0 were found to be 68(1) K and 0.514(1) respectively. Using the activation energy data **(Figure II.24(a))**, T_0 was also calculated and the linear regression was consistent with Eq. (II.20). The line slope value of -0.019(7) yields a value of T_0 = 98(37) K.

The low values of T_0 compared to AgY-As_2S_3 glasses rises a question how the average matrix coordination number should be calculated. In case of As_2S_3, the $\langle n_0 \rangle$ =2.4 is well defined. A simultaneous doping with AgI/HgS = 1 yields two contrasting possibilities. (1) Silver and mercury distributions are independent from each other and in this case $\langle n_0 \rangle$ =2.4 since the probability to find a network forming mercury atom in the vicinity of silver cation is small for random distribution of both metallic species. (2) Silver and mercury distributions are correlated. At low

HgS concentrations, mercury is two-fold coordinated. As a result, the effective average matrix site coordination will vary between 2 and 2.4 depending on the number of Hg species in the vicinity of silver **(Figure II.31)**. Consequently, the low T_0 parameter may indicate correlated distributions of Hg and Ag.

In contrast, the critical temperature T_0 for $(AgI)_x(HgS)_{0.5-x/2}(As_2S_3)_{0.5-x/2}$ glasses is higher than that for AgY-As_2S_3 vitreous alloys. Assuming correlated distributions of mercury and silver and 30% of 4-fold coordinated mercury species in equimolar HgS-As_2S_3 matrix glass, the effective matrix site coordination is expected to vary between $2.29 < n_0 < 2.86$ in qualitative agreement with experimental data.

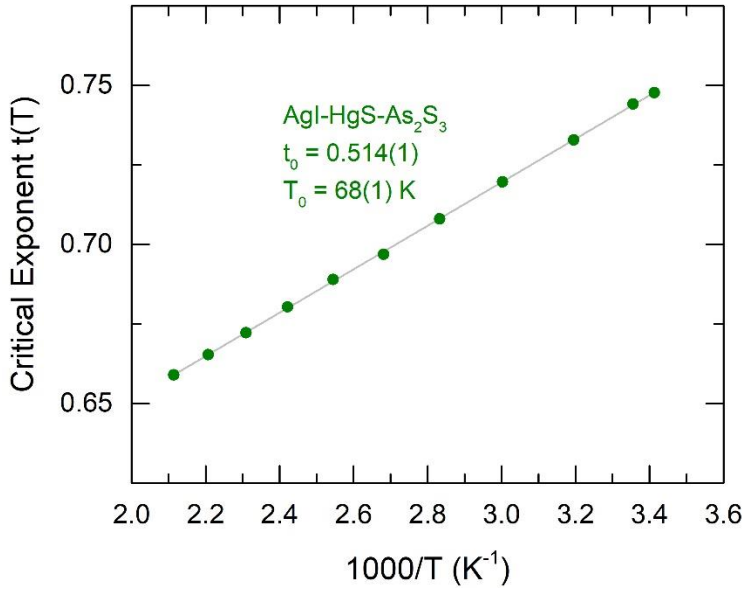

Figure II.25. Critical exponent, t, plotted versus T^{-1} for the AgI-HgS-As_2S_3 glass system. The solid line represent the result of a least-square fit of the experimental data points to Eq. (II.19).

II.3.2.b AgI-HgS-GeS_2 ternary system

As mentioned earlier (Chapter 1), the narrow glass-forming domain of the pseudo-ternary AgI-HgS-GeS_2 alloys is essentially centered around the $(AgI)_x(HgS)_{0.5-x/2}(GeS_2)_{0.5-x/2}$ composition line. Therefore, for this pseudo-ternary system, we will only focus on the study of the electrical conductivity of the glasses belonging to this line. **Figure II.26** shows the typical Cole-Cole impedance plots at 373 K for the AgI-poor (x =0.1) and AgI-rich (x = 0.5) glasses. The complex impedance spectrum corresponding to the AgI-poor glasses (x = 0.1) displays both a semi-circle

and a polarization tail in the low-frequency region. Meanwhile, for the AgI-rich composition glass (x = 0.5), the semi-circle almost disappears. The significant polarization tail present is typical for ion conducting samples in the cell with blocking electrodes.

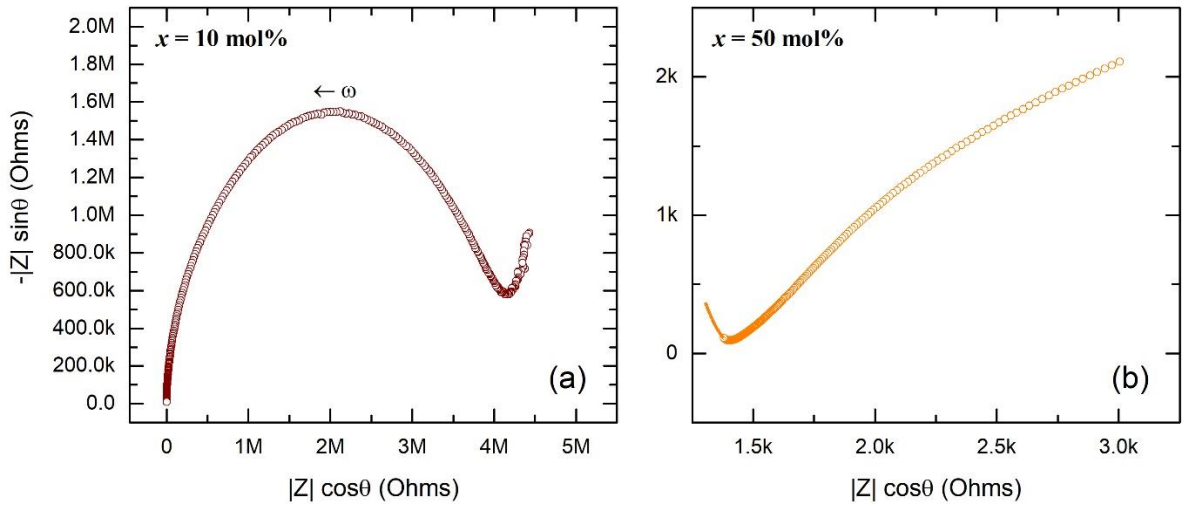

Figure II.26. Typical Cole-Cole impedance plots at 373 K for glasses (a) poor in AgI (10 mol %) and (b) rich in AgI (50 mol %) of the $(AgI)_x(HgS)_{0.5-x/2}(GeS_2)_{0.5-x/2}$ system measured in an electrochemical cell Au|glass|Au.

Typical conductivity temperature dependencies for the $(AgI)_x(HgS)_{0.5-x/2}(GeS_2)_{0.5-x/2}$ glasses, $10^{-4} \leq x \leq 0.6$, are shown in **Figure II.27**. They do not show any significant hysteresis effects and obey the Arrhenius law (Eq. (II.34)). The parameters σ_{298}, E_a and σ_0, calculated from the least fit squares of the data using Eq.(II.34), are represented in **Figure II. 28, Figure II.29** and **Table II.5**. The room temperature conductivity increases by 12 orders of magnitude from 4.5×10^{-15} S cm^{-1} (x = 0.0) to 1.99×10^{-3} S cm^{-1} (x = 0.6), **Figure II. 28** . This later conductivity value is obtained for the atomic silver concentration ≈27.27 at.% Ag. One could suggest that the saturation trend at higher x, reached for quasi-binary AgI-doped glasses seen earlier, continues for the current pseudo-ternary glasses regardless of the glass network former species.

The activation energy decreases drastically from ~0.96 eV to 0.25 eV **(Figure II.29(a))** and the pre-exponential factor values σ_0 do not change significantly varying between 10^4 and 10^6 S.cm^{-1} **(Figure II.29(b))**. However, the drop in σ_0 for high AgI-rich glasses could be attributed to the presence of micro- or nano-crystals in this region.

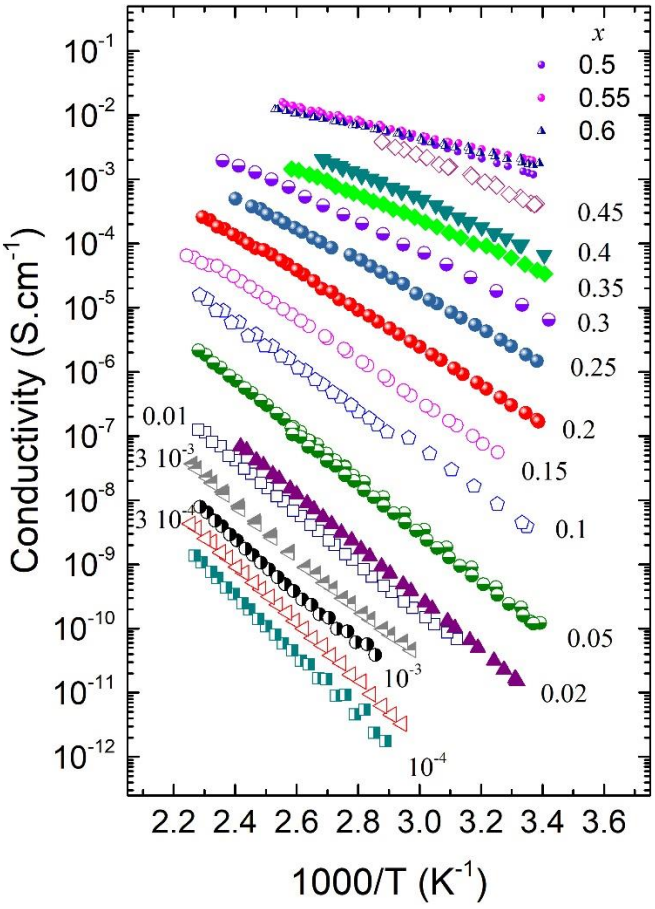

Figure II.27. Temperature dependences of the total electrical conductivity σ for the pseudo-ternary $(AgI)_x(HgS)_{0.5-x/2}(GeS_2)_{0.5-x/2}$ glass system. The numbers indicate the AgI molar fraction x.

The conductivity isotherms, displayed in **Figure II.28(a,b)**, shows four different concentration regions, i.e. (i) a low (≤ 2-5 at.% Ag), (ii) an intermediate ($5 < x \leq 12$ at.% Ag), (iii) a high ($12 < x \leq 22$ at.% Ag), and (iv) an extremely-high (> 22 at.% Ag) silver content region, and that the variation in the electrical conductivity between these four regions is clearly distinct. Therefore, analysis of the structure of glasses is necessary to shed light on the correlation between local network structure and Ag-ion conduction in new superionic conductors with prominent ionic transport properties. An overall look on the studied systems, one can see clearly that quasi-binary and pseudo-ternary silver halide-doped chalcogenide glasses behave similarly at low and high Ag concentrations. At least two marked ion transport regimes can be distinguished above the $x_c \approx 30$ ppm percolation threshold: (i) critical percolation regime at low x and (ii) modifier-controlled domain at high x.

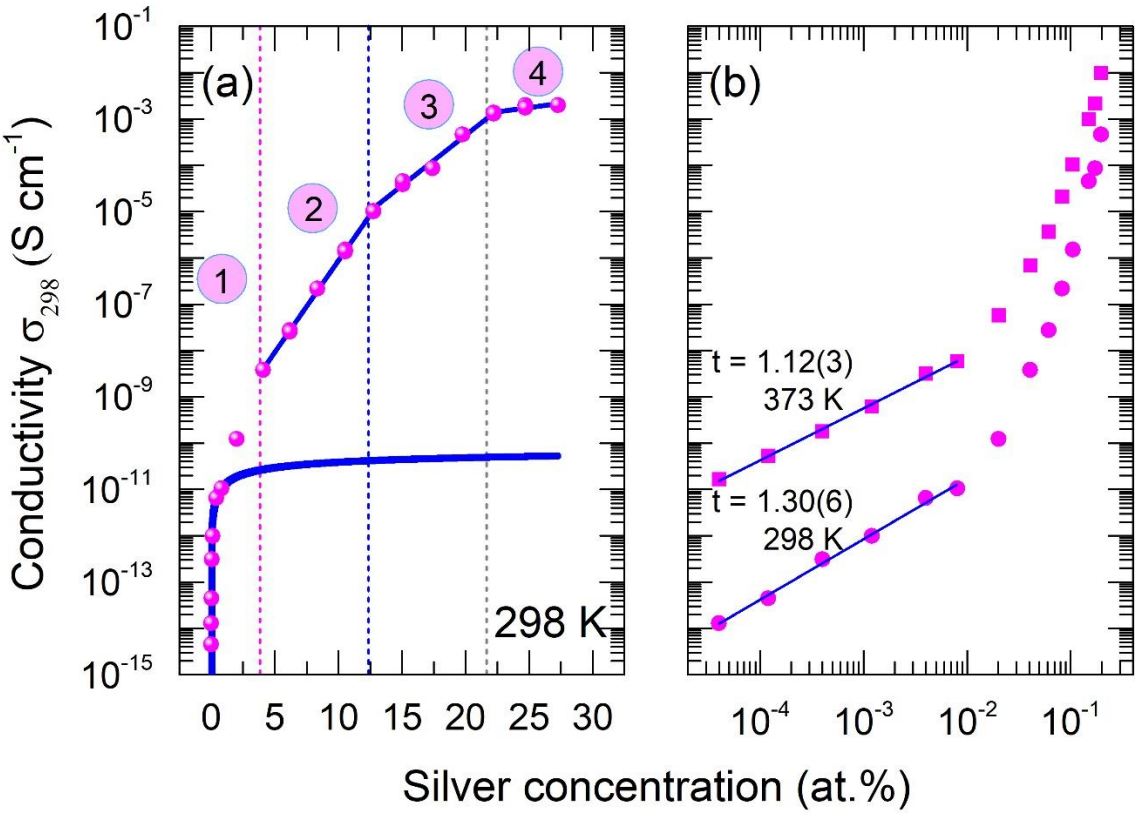

Figure II. 28. (a) Room-temperature conductivity of AgI-HgS-GeS_2 glasses plotted on a semi-logarithmic scale, and (b) conductivity isotherms of silver iodide mercury thiogermanate glasses at (●, solid circles) 298 K and (■, solid squares) 373 K plotted on a log-log scale. The solid lines represent a least-square fit of the experimental data points in the critical percolation domain to Eq. (II.17), with hypothetical conductivity data beyond the percolation domain; the bold lines in the modifier-controlled domain are drawn as a guide to the eye.

Table II.5. Electric characteristics of the glass system $(AgI)_x(HgS)_{0.5-x/2}(GeS_2)_{0.5-x/2}$.

x	[Ag] (at.%)	r_{Ag-Ag} (Å)	log σ_{298} (S cm^{-1})	E_a (eV)	log σ_0 (S cm^{-1} K)
0	0	-	-13.35	0.964	4.4
10^{-4}	0.004	108.7	-13.89	0.945	4.6
3×10^{-4}	0.012		-13.35	0.934	4.9
10^{-3}	0.040	50.2	-12.50	0.84	4.2
3×10^{-3}	0.120	34.9	-12.01	0.852	4.9
0.01	0.400	23.3	-11.19	0.819	5.1
0.02	0.803	18.4	-10.97	0.836	5.6
0.05	2.020	13.6	-9.91	0.813	6.3
0.10	4.081	10.8	-8.42	0.693	5.8
0.15	6.186	9.4	-7.56	0.654	6.0

0.20	8.333	8.5	-6.67	0.613	6.2
0.25	10.53	7.9	-5.82	0.528	5.6
0.30	12.77	7.4	-4.99	0.503	6.0
0.35	15.05	7.0	-4.35	0.426	5.3
0.40	17.39	6.7	-4.07	0.442	5.9
0.45	19.78	6.5	-3.33	0.419	6.2
0.50	22.22	6.2	-2.89	0.302	4.7
0.55	24.72	6.1	-2.76	0.239	3.7
0.60	27.27	5.9	-2.70	0.247	4.0

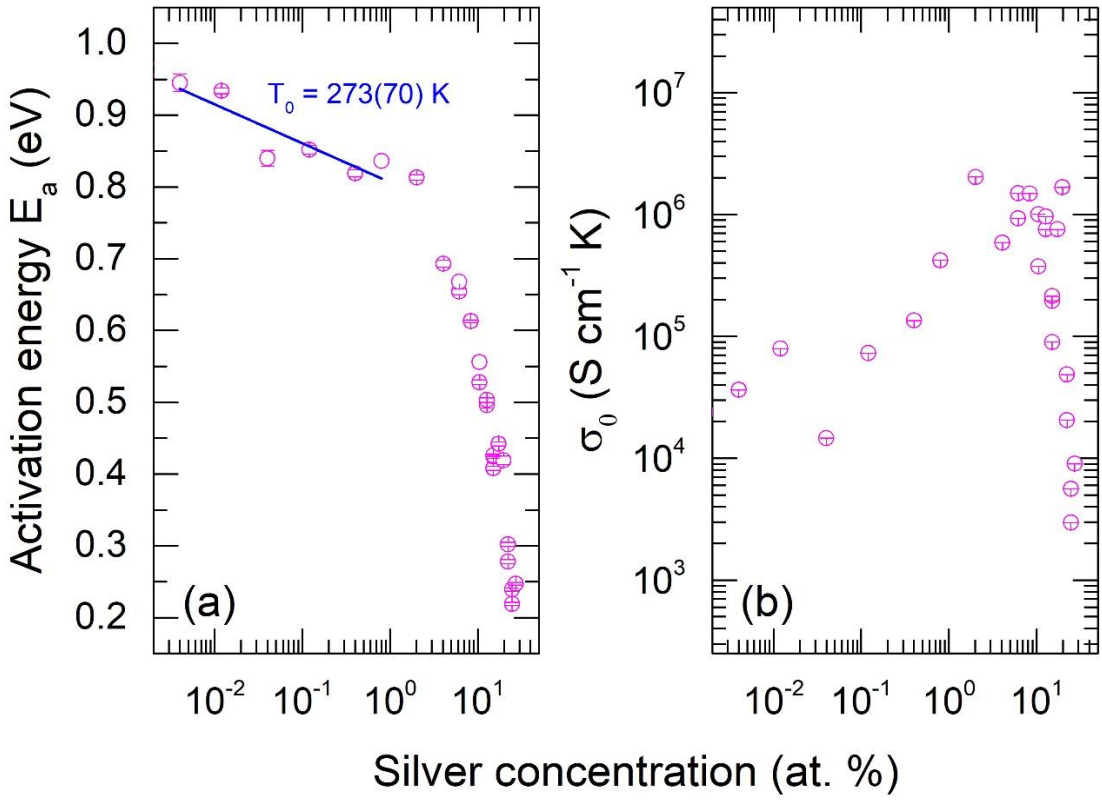

Figure II.29. (a) Conductivity activation energy E_a and (b) conductivity pre-exponential factor σ_0 of AgI-HgS-GeS_2 glasses. The solid line represents a least-square fit of the E_a experimental data points in the critical percolation domain to Eq. (II.20).

In a similar manner to what was presented earlier, the derived critical temperature T_0 = 272±9 K **(Figure II.30)** determined from the conductivity isotherms plotted on a log-log scale, **Figure II. 28(b)**, appears to be consistent with the one calculated using $E_a(x)$ composition dependence on a semi-logarithmic scale (Eq. (II.20)), T_0 = 273±70 K, **Figure II.29(a)**.

Assuming random distribution of silver between matrix sites with tetrahedral Ge, two-fold or four-fold mercury species, the derived critical temperature T_0 can be spread between $2.40 < n_0 < 3.20$ **(Figure II.31)**. The experimental T_0 for AgI-HgS-GeS_2 glasses crosses the $T_0\,(n)$ dependence at n_0 = 2.40, implying the preferential location of Ag cations in the vicinity of Ge and two-fold coordinated mercury.

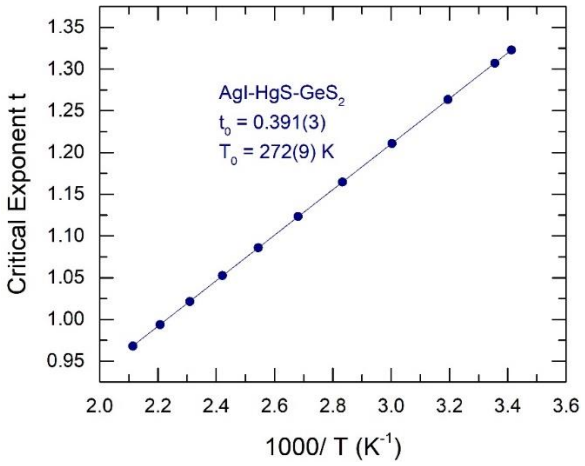

Figure II.30. The critical exponent $t(T)$ values calculated for AgI-HgS-GeS_2 glasses at $x \leq 2$ at.% Ag and plotted as a function of reciprocal temperature. The derived t_0 and T_0 parameters are also shown.

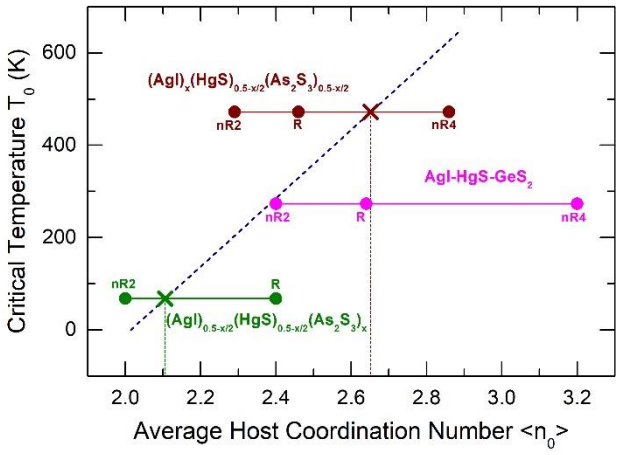

Figure II.31. Critical fictive temperature T_0 plotted as a function of the average local coordination number $\langle n_0 \rangle$ of the host matrix silver mercury ● thiogermanate and ●,● thioarsenate glasses. R stands for random; nR2 for non-random 2-fold coordinated Hg; and nR4 for 4-fold coordinated Hg.

II.4 Conclusions

The ionic conductivity σ_i measurements of AgY-As_2S_3 (Y = Br, I), AgI-HgS-As_2S_3 and AgI-HgS-GeS_2 glasses over 5 orders of magnitude in silver content have shown two ion transport regimes: (i) the critical percolation at $x \leq 2$ at.% Ag, and (ii) the modifier-controlled ionic motion at x > 7-10 at.% Ag. For the silver halide thioarsenate families, the chemically-invariant critical percolation, characterized by a power-law dependence of $\sigma_i(x,T) \propto x^{T_0/T}$, reveals identical ionic conductivity parameters within experimental uncertainty for AgY- and Ag_2S-As_2S_3 glasses. This behavior is fully reversed in the modifier-controlled region; the difference in σ_i approaches 4 orders of magnitude between AgI- and Ag_2S-As_2S_3 systems.

The electronic transport of the pseudo-binary HgS-GeS_2 and pseudo-ternary AgI-HgS-GeS_2 thiogermanate glasses have been studied. A non-monotonic change in the electronic transport properties of the HgS-GeS_2 insulating glasses (room temperature conductivity varies between 10^{-15} and 10^{-12}) was seen, which could be related to changes in the matrix structure. For the pseudo-ternary AgI-HgS-GeS_2 glasses, the room temperature conductivity increases by ~12 orders of magnitude from 4.5×10^{-15} S cm^{-1} (x = 0.0) to 1.99×10^{-3} S cm^{-1} (x = 0.6). However, it is accompanied by a drastic decrease in the activation energy from 0.96 eV to 0.25 eV. A notable superionic transport behaviour is observed in glasses with high silver concentrations (> 17 at.% Ag). The modifier controlled domain is divided into three distinct regions, indicating thus a difference in the local structure.

The critical temperature T_0 characteristic for the critical percolation domain and reflecting the connectivity of the host matrix exhibits the expected agreement with connectivity of g-As_2S_3, $\langle n_0 \rangle$ = 2.40, for the AgY-As_2S_3 glasses. For the ternary $(AgI)_{0.5-x/2}(HgS)_{0.5-x/2}(As_2S_3)_x$ and $(AgI)_x(HgS)_{0.5-x/2}(GeS_2)_{0.5-x/2}$ vitreous alloys, the derived T_0 parameters imply a correlated Ag location in the vicinity of two-fold coordinated mercury, while for the $(AgI)_x(HgS)_{0.5-x/2}(As_2S_3)_{0.5-x/2}$ glasses one suggests a predominant Ag distribution within 4-fold coordinated mercury and trigonal As sites.

II.5 References

[1] A. Helfen, “Elaboration et caractérisation d’un nouvel électrolyte solide pour les piles à combustible : δ-Bi_2O_3,” Université de Marne la Vallée, Paris, France, 2009.

[2] M. Filal, “Conductivité ionique de la zircone yttriée : rôle de la microstructure et effet composite,” Université de Picardie, Amiens, France, 1994.

[3] N. F. Mott and E. A. Davis, *Electronic processes in non-crystalline materials*. Oxford; New York: Clarendon Press; Oxford University Press, 1979.

[4] P. W. Anderson, “Absence of Diffusion in Certain Random Lattices,” *Phys. Rev.*, vol. 109, no. 5, pp. 1492–1505, Mar. 1958.

[5] A. I. Gubanov, *Quantum Electron Theory of Amorphous Conductors*. Springer US, 1965.

[6] L. Bányai and A. Aldea, “Theory of the Hall Effect in Disordered Systems: Impurity-Band Conduction,” *Phys. Rev.*, vol. 143, no. 2, pp. 652–656, Mar. 1966.

[7] N. F. Mott, “Electrons in disordered structures,” *Adv. Phys.*, vol. 50, no. 7, pp. 865–945, Nov. 2001.

[8] M. H. Cohen, H. Fritzsche, and S. R. Ovshinsky, “Simple Band Model for Amorphous Semiconducting Alloys,” *Phys. Rev. Lett.*, vol. 22, no. 20, pp. 1065–1068, May 1969.

[9] M. V. Minaev, “Glassy Semiconducting Alloys,” *Met Mosc*, 1991.

[10] Z. U. Borisova, “Structure, physico-chemical properties and applications of non-crystalline semiconductors,” *Kishinev*, vol. 10, pp. 55–61, 1980.

[11] A. Feltz, “Amorphous and Glassy Inorganic Solids,” vol. 12, p. 556, 1986.

[12] K. Weiser and H. Brodsky, “dc Conductivity, Optical Absorption, and Photoconductivity of Amorphous Arsenic Telluride Films,” *Phys Rev B*, vol. 1, no. 2, pp. 791–799, 1970.

[13] A. I. Borets, V. V. Khiminets, A. A. Turyanitsa, and D. G. Semak, “Complex Glassy Chalcogenides,” *Vysshaya Shkola L’vov*, 1987.

[14] K. Tanaka, “Encyclopedia of Materials: Science and Technology,” vol. 2, Elsevier, 2001, p. 1123.

[15] Z. U. Borisova, *Glassy Semiconductors*, Plenum Press New York. Springer, Boston, MA, 1981.

[16] A. Giridhar and S. Mahadevan, “Silver as a dopant and as a constituent in As-Ag-Te glasses: electrical conductivity,” *J. Non-Cryst. Solids*, vol. 197, no. 2, pp. 228–234, May 1996.

[17] B. Bilen, Y. Skarlatos, and G. Aktas, “Frequency-dependent conductivity in As_2Se_3 and As_2Te_3 thin films,” *J. Non-Cryst. Solids*, vol. 351, no. 27–29, pp. 2153–2158, Aug. 2005.

[18] M. Kitao, M. Senda, Y. Takano, and S. Yamada, “Effect of Tl additive on conductivity and absorption coefficient in glassy As_2Se_3,” *J. Non-Cryst. Solids*, vol. 127, no. 1, pp. 36–43, Jan. 1991.

[19] M. Bokova, I. Alekseev, and E. Bychkov, “^{204}Tl tracer diffusion and conductivity in thallium germanium sulphide glasses over a wide composition range,” *J. Electroceramics*, vol. 34, no. 1, pp. 63–68, Feb. 2015.

[20] M. Bokova, I. Alekseev, D. Kalyagin, V. Tsegelnik, Y. Ermolenko, and E. Bychkov, “^{204}Tl tracer diffusion and conductivity in thallium thiogermanate glasses,” *Solid State Ion.*, vol. 253, pp. 101–109, Dec. 2013.

[21] M. Bokova, A. Paraskiva, M. Kassem, I. Alekseev, and E. Bychkov, “Tl_2S-GeS-GeS_2 system: glass formation, macroscopic properties, and charge transport,” *J Alloys Compd. Press Accept. Manuscr.*, Nov. 2018.

[22] A. Pradel and M. Ribes, “Lithium chalcogenide conductive glasses,” *Mater. Chem. Phys.*, vol. 23, no. 1, pp. 121–142, Aug. 1989.

[23] E. Robinel, B. Carette, and M. Ribes, “Silver sulfide based glasses (I). Glass forming regions, structure and ionic conduction of glasses in GeS_2-Ag_2S and GeS_2-Ag_2S-AgI systems,” *J. Non-Cryst. Solids*, vol. 57, no. 1, pp. 49–58, Aug. 1983.

[24] M. Z. A. Munshi, *Handbook of Solid State Batteries & Capacitors*. World Scientific, 1995.

[25] E. Warburg, “Sodium ions migration through glass,” *Wiedemann Ann Phys*, vol. 21, pp. 622–24, 1884.

[26] H. L. Tuller, D. P. Button, and D. R. Uhlmann, “Fast ion transport in oxide glasses,” *J. Non-Cryst. Solids*, vol. 40, no. 1, pp. 93–118, Jul. 1980.

[27] D. P. Button, R. P. Tandon, H. L. Tuller, and D. R. Uhlmann, “Fast Li^+ ion conduction in chloro-borate glasses,” *J. Non-Cryst. Solids*, vol. 42, no. 1, pp. 297–306, Oct. 1980.

[28] F. A. Fusco, H. L. Tuller, and D. P. Button, “Lithium, sodium and potassium transport in fast ion conducting glasses: trends and models,” *Mater. Sci. Eng. B*, vol. 13, no. 2, pp. 157–164, Mar. 1992.

[29] Anderson O. L. and Stuart D. A., “Calculation of Activation Energy of Ionic Conductivity in Silica Glasses by Classical Methods,” *J. Am. Ceram. Soc.*, vol. 37, no. 12, pp. 573–580, Dec. 1954.

[30] D. Ravaine and J.-L. Souquet, “A thermodynamic approach to ionic conductivity in oxide glasses. Part 2. A statistical model for the variations of the chemical potential of the constituents in binary alkali oxide glasses,” *Phys. Chem. Glas.*, vol. 19, p. 115, Jan. 1978.

[31] R. Mercier, J. P. Malugani, B. Fahys, and G. Robert, “Superionic conduction in Li_2S - P_2S_5 - LiI - glasses,” *Solid State Ion.*, vol. 5, pp. 663–666, Oct. 1981.

[32] B. Carette, E. Robinel, and M. Ribes, “Ionic conduction of sulphide-based glasses in the systems M_2S-GeS_2-MI (M= Li, Ag),” *Glass Technol.*, vol. 24, no. 3, pp. 157–160, 1983.

[33] A. Pradel and M. Ribes, “Electrical properties of lithium conductive silicon sulfide glasses prepared by twin roller quenching,” *Solid State Ion.*, vol. 18–19, pp. 351–355, Jan. 1986.

[34] T. Minami, H. Nambu, and M. Tanaka, “Comparison of Ionic Conductivity Between Glassy and Crystalline Solid Electrolytes in the System AgI-Ag_2O-MoO_3,” *J. Am. Ceram. Soc.*, vol. 60, pp. 467–469, 1977.

[35] A. Schiraldi, “AgIAg oxysalt high conductivity glasses: a tentative approach to their structure,” *Electrochimica Acta*, vol. 23, no. 10, pp. 1039–1043, Oct. 1978.

[36] Y. Onodera, T. Furukawa, S. Hashimoto, T. Usuki, Y. Amo, and Y. Kameda, “Vitrification and transport properties in AgBr-doped chalcogenide systems,” *Solid State Ion.*, vol. 177, no. 26, pp. 2597–2599, Oct. 2006.

[37] T. Usuki *et al.*, “Structural and electrical properties of AgI dispersed As-chalcogenide glasses,” *J. Non-Cryst. Solids*, vol. 312–314, pp. 570–574, Oct. 2002.

[38] Y. M. Moustafa, “Electrical relaxation of superionic conducting glasses AgX-$AgPO_3$ (X=I, Br, Cl),” *J. Mater. Sci. Mater. Electron.*, vol. 6, no. 3, pp. 135–139, Jul. 1995.

[39] J. P. Malugani and G. Robert, “Conductivite ionique dans les verres $LiPO_3$LiX (X = I, Br, Cl),” *Mater. Res. Bull.*, vol. 14, no. 8, pp. 1075–1081, Aug. 1979.

[40] H. K. Patel and S. W. Martin, “Fast ionic conduction in Na_2S+B_2S_3 glasses: Compositional contributions to nonexponentiality in conductivity relaxation in the extreme low-alkali-metal limit,” *Phys. Rev. B Condens. Matter*, vol. 45, no. 18, pp. 10292–10300, May 1992.

[41] E. Bychkov, V. Tsegelnik, Y. Vlasov, A. Pradel, and M. Ribes, “Percolation transition in Ag-doped germanium chalcogenide-based glasses: conductivity and silver diffusion results,” *J. Non-Cryst. Solids*, vol. 208, no. 1–2, pp. 1–20, Nov. 1996.

[42] E. Bychkov, D. L. Price, C. J. Benmore, and A. C. Hannon, “Ion transport regimes in chalcogenide and chalcohalide glasses: from the host to the cation-related network connectivity,” *Solid State Ion.*, vol. 154–155, pp. 349–359, Dec. 2002.

[43] E. Bychkov, “Superionic and ion-conducting chalcogenide glasses: Transport regimes and structural features,” *Solid State Ion.*, vol. 180, no. 6–8, pp. 510–516, May 2009.

[44] E. Bychkov, A. Bolotov, V. Tsegelnik, Y. Grushko, and Y. Vlaso, “^{64}Cu Tracer Diffusion in Copper Chalcogenide Glasses,” *Defect Diffus. Forum*, vol. 194–199, pp. 919–924, Jan. 2001.

[45] E. Bychkov, A. Bychkov, A. Pradel, and M. Ribes, “Percolation transition in Ag-doped chalcogenide glasses: comparison of classical percolation and dynamic structure models,” *Solid State Ion.*, vol. 113–115, pp. 691–695, Dec. 1998.

[46] Y. Drugov, V. Tsegelnik, A. Bolotov, Y. Vlasov, and E. Bychkov, “^{110}Ag tracer diffusion study of percolation transition in Ag2S–As2S3 glasses,” *Solid State Ion.*, vol. 136–137, pp. 1091–1096, Nov. 2000.

[47] E. Bychkov, “Tracer diffusion studies of ion-conducting chalcogenide glasses,” *Solid State Ion.*, vol. 136–137, pp. 1111–1118, Nov. 2000.

[48] B. Roling, C. Martiny, and K. Funke, “Information on the absolute length scales of ion transport processes in glasses from electrical conductivity and tracer diffusion data,” *J. Non-Cryst. Solids*, vol. 249, no. 2, pp. 201–209, Jul. 1999.

[49] G. E. Murch, “The haven ratio in fast ionic conductors,” *Solid State Ion.*, vol. 7, no. 3, pp. 177–198, Oct. 1982.

[50] W. Weppner *et al.*, “Proceedings of the 6th International Conference on Solid State IonicsTransport properties of rapidly quenched glasses in the Z_2S_3−Ag_2S−AgI (Z=As, Sb) systems,” *Solid State Ion.*, vol. 28, pp. 792–798, Sep. 1988.

[51] T. Minami, “Glass Science and Technology Problems and Prospects for 2004 Fast ion conducting glasses,” *J. Non-Cryst. Solids*, vol. 73, no. 1, pp. 273–284, Aug. 1985.

[52] G. Chiodelli, A. Magistris, and M. Villa, “Ionic conductivity and glass transition of borophosphate glasses,” *Solid State Ion.*, vol. 18, pp. 356–361, Jan. 1986.

[53] G. Robert, J. P. Malugani, and A. Saida, “Fast ionic silver and lithium conduction in glasses,” *Solid State Ion.*, vol. 3, pp. 311–315, Aug. 1981.

[54] G. Robert, J. P. Malugani, and A. Saida, “Fast ionic silver and lithium conduction in glasses,” *Solid State Ion.*, vol. 3–4, pp. 311–315, Aug. 1981.

[55] J. M. Reau, B. Tanguy, J. J. Videau, J. Portier, and P. Hagenmuller, “Transport properties of rapidly quenched glasses in the Z_2S_3−Ag_2S−AgI (Z=As, Sb) systems,” *Solid State Ion.*, vol. 28–30, no. Part 1, pp. 792–798, Sep. 1988.

[56] J. L. Souquet, “Glasses as active materials in high-energy density cells,” *Solid State Ion.*, vol. 28–30, pp. 693–703, Sep. 1988.

[57] T. Minami, “Fast ion conducting glasses,” *J. Non-Cryst. Solids*, vol. 73, no. 1, pp. 273–284, Aug. 1985.

[58] J. C. Bachman *et al.*, “Inorganic Solid-State Electrolytes for Lithium Batteries: Mechanisms and Properties Governing Ion Conduction,” *Chem. Rev.*, vol. 116, no. 1, pp. 140–162, Jan. 2016.

[59] I. Alekseev *et al.*, “Ionic and electronic transport in AgI–As_2Te_3 glasses,” *Solid State Ion.*, vol. 253, pp. 181–184, Dec. 2013.

[60] Y. M. Ben-Shaban, “Ion Transport in AgY-Sb_2S_3 (Y = Cl, Br, I) Glasses,” Petersburg University, St. Petersburg, Russia, 1997.

[61] C. Näther and A. Beck, “Synthesis, Crystal Structure and Thermal Properties of Silver(I) Bromide Ethylenediamine Coordination Polymers,” *Z. Für Naturforschung B*, vol. 59, no. 9, pp. 992–998, 2014.

[62] A. Beck and C. Näther, “Crystal Structure of Poly[(μ3-iodo)(2-ethylpyrazine-N)-silver(I)] Containing a Novel AgX 63 Net,” *Z. Für Naturforschung B*, vol. 61, no. 5, pp. 517–520, 2014.

[63] E. Bychkov and D. L. Price, “Neutron diffraction studies of Ag_2S–As_2S_3 glasses in the percolation and modifier-controlled domains,” *Solid State Ion.*, vol. 136–137, pp. 1041–1048, Nov. 2000.

[64] I. T. Penfold and P. S. Salmon, “Glass formation and short-range order in chalcogenide materials: The $(Ag_2S)_x(As_2S_3)_{1-x}$ ($0 \leq x \leq 1$) pseudobinary tie line,” *Phys. Rev. Lett.*, vol. 64, no. 18, pp. 2164–2167, Apr. 1990.

[65] J. H. Lee and S. R. Elliott, "Isotopic-substitution neutron-diffraction studies of $(AgI)_{0.5}(AgPO_3)_{0.5}$ glass," *Phys. Rev. B Condens. Matter*, vol. 54, no. 17, pp. 12109–12114, Nov. 1996.

[66] J. H. Lee, A. P. Owens, A. Pradel, A. C. Hannon, M. Ribes, and S. R. Elliott, "Structure determination of Ag-Ge-S glasses using neutron diffraction," *Phys. Rev. B*, vol. 54, no. 6, pp. 3895–3909, Aug. 1996.

[67] J. Swenson, L. Börjesson, R. L. McGreevy, and W. S. Howells, "Structure of AgI-Ag_2O-$_2B_2O_3$ glasses: A neutron and x-ray-diffraction investigation," *Phys. Rev. B*, vol. 55, no. 17, p. 11236, 1997.

[68] C. J. Benmore and P. S. Salmon, "Structure of fast-ion conducting chalcogenide glasses: the Ag-As-Se system," *J. Non-Cryst. Solids*, vol. 156, pp. 720–724, May 1993.

[69] E. Bychkov, D. L. Price, and A. Lapp, "Universal trend of the Haven ratio in glasses: origin and structural evidences from neutron diffraction and small-angle neutron scattering," *J. Non-Cryst. Solids*, vol. 293, pp. 211–219, Nov. 2001.

[70] Z. U. Borisova, E. A. Bychkov, and Y. S. Tver'yanovich, *Interaction of Metals with Chalcogenide Glasses*. St. Petersburg: Petersburg University Press, 1991.

[71] K. L. Bhatia, M. Singh, and N. Kishore, "Electrical and optical properties of thermally evaporated thin films of $(As_2S_3)_{1-x}(PbS)_x$," *Thin Solid Films*, vol. 293, no. 1, pp. 303–309, Jan. 1997.

[72] P. K. Bhat, K. L. Bhatia, and S. C. Katyal, "Electrical conductivity and photoconductivity of As_2S_3-PbS glasses," *J. Non-Cryst. Solids*, vol. 27, no. 3, pp. 399–409, Mar. 1978.

[73] M. Kassem, S. Khaoulani, A. Cuisset, D. L. Coq, P. Masselin, and E. Bychkov, "Mercury thioarsenate glasses: a hybrid chain/pyramidal network," *RSC Adv.*, vol. 4, no. 90, pp. 49236–49246, Oct. 2014.

[74] A. K. Mahapatra and A. K. Dash, "α-HgS nanocrystals: Synthesis, structure and optical properties," *Phys. E Low-Dimens. Syst. Nanostructures*, vol. 35, no. 1, pp. 9–15, Oct. 2006.

[75] A. H. Kevshyn, V. V. Halyan, H. Y. Davydyuk, O. V. Parasyuk, and I. I. Mazurets, "Concentration dependence of the optical properties of glassy alloys in the $HgS–Ga_2S_3–GeS_2$ system," *Glass Phys. Chem.*, vol. 36, no. 1, pp. 27–32, Feb. 2010.

[76] V. Halyan, O. Parasyuk, and A. H. Kevshyn, "The structure of glassy HgS-GeS_2," Nov. 2017.

[77] K. L. Bhatia and S. C. Katyal, “Structure and photoelectric behavior of amorphous semiconductors in the system PbS-GeS-GeS_2,” *J. Non-Cryst. Solids*, vol. 50, no. 1, pp. 39–48, Jun. 1982.

[78] S. Khaoulani, M. Kassem, S. Fourmentin, and E. Bychkov, “The AgI-HgS-As_2S_3 glassy system: Macroscopic properties and Raman scattering studies,” *J. Alloys Compd.*, vol. 685, pp. 752–760, Nov. 2016.

[79] A. Paraskiva, “Développement de membranes pour les capteurs chimiques potentiométriques spécifiques aux ions Thallium et Sodium,” Université du Littoral Côte d’Opale, 15-Dec-2017.

[80] S. W. Martin, “An evaluation of the ionic conductivity in AgI-doped glasses: The graded-percolation model,” *Solid State Ion.*, vol. 51, no. 1–2, pp. 19–26, Mar. 1992.

Chapter III : Structural studies of the AgI-As_2S_3, AgBr-As_2S_3, HgS-GeS_2, and AgI-HgS-GeS_2 glasses

III.1 Introduction

The structural studies of disordered materials are very important because a detailed knowledge of the glass network organization at short and intermediate distances allows to anticipate certain macroscopic properties of glasses. The main problem is that these amorphous materials lack symmetry and periodicity. In other words, the efficient structural methods of the Rietveld type cannot be used. However, these difficulties can be partially solved using indirect spectroscopic methods and/or direct techniques using synchrotron radiation, nuclear reactors or spallation neutron sources. Advanced spectroscopic methods such as EXAFS « Extended X-ray Absorption Fine Structure » [1]–[4], Nuclear Magnetic Resonance (NMR) [5], [6], Nuclear Quadrupole Resonance (NQR) [7], [8], Mössbauer Spectroscopy [9], [10] and Raman spectroscopy [11], [12], have all proved to be effective in solving the local structure of chalcogenide glasses. However, in order to obtain structural information beyond the first coordination sphere, it is advisable to use high-energy X-ray diffraction and/or pulsed neutron diffraction [13]–[17].

Throughout this work, we have studied the structure of the AgY-As_2S_3 (Y = Br, I), HgS-GeS_2, AgI-HgS-As_2S_3 and AgI-HgS-GeS_2 systems by means of Raman spectroscopy, then we have completed these studies using high-energy X-ray diffraction and neutron diffraction experiments which additionally provide information on the short and intermediate range scale.

III.2 Raman spectroscopy

Raman spectra were collected at room temperature using a LABRAM HR spectrometer equipped with a triple monochromator, liquid nitrogen cooled CCD detector and a microscope. Raman scattering was excited by a 632.8 He-Ne laser and a 785 nm solid state laser over a spectral range from 80 to 1200 cm^{-1}. To avoid crystallization of the glassy samples, the laser power was set to 0.15 and 1.5 mW and the acquisition time was varied between 60 and 300 s. The spectrometer resolution was 1 cm^{-1}. Two to four spectra were recorded for each sample in different positions to verify the homogeneity of the sample and the absence of photo-induced phenomena.

III.3 Diffraction techniques

Fundamentally, neutrons and X-rays interact differently with matter. Therefore, neutron diffraction and high-energy X-ray diffraction techniques provide complementary information.

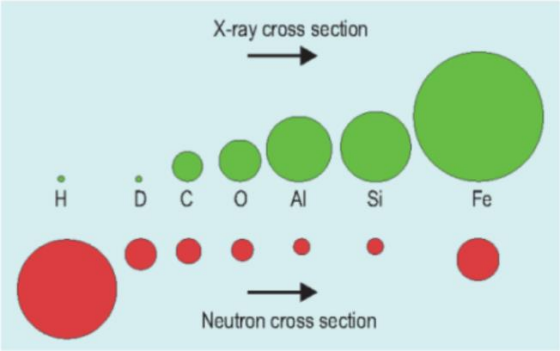

Figure III.1. Comparison of the sensitivities of some elements to neutrons and X-rays [18].

The scattering cross-sections presented in **Figure III.1** show that the sensitivity of the X-ray diffraction depends on the atomic number or number of electrons in the atom simplistically associated with the size of electronic cloud, while that of the neutron diffraction depends on the coherent neutron scattering length schematically shown as a relative size of the atomic nucleus.

The lack of periodicity, characteristic of amorphous materials, hinders significantly the precise determination of their atomic structure. However, complementary neutron and X-ray diffraction techniques allow obtaining a mean atomic arrangement around each atomic species.

Using hard X-rays of a synchrotron light source or pulsed neutrons, we can obtain diffraction pattern over a large range of the scattering vector, $Q = 4\pi sin\theta/\lambda$, where θ is the scattering angle and λ is the radiation wavelength. In fact, the larger is the range of scattering vector, the better is the resolution in real space. The pulsed neutrons (λ = 0.05-4 Å) and the hard X-rays ($0.1 \leq \lambda \leq 0.2$ Å) allow to reach Q values up to 50 Å^{-1}, which is very advantageous compared to the 7-10 Å^{-1} value obtained by diffractometers using copper K_α radiation.

The structure factor $S(Q)$ in Q-space and the real-space correlation functions $g(r)$ or $T(r)$ characterize the local order in the materials [19].

In the Faber-Ziman formalism [20], the structure factor is related to the coherent scattering intensity by the following equation:

$$S(Q) = \frac{I_{coh} - \langle |f(Q)|^2 \rangle}{|\langle f(Q) \rangle|^2} + 1 \qquad \text{(III. 1)}$$

where $|\langle f(Q)\rangle|^2 = |\sum_i c_i f_i|^2$ and $|\langle f(Q)\rangle^2| = \sum_i c_i |f_i|^2$ are respectively the square of the average and the square average of the atomic structure factor and $f_i = f_i^0(Q) + f_i'(E) + if_i''(E)$. Here, $\langle\ \rangle$ simplifies the average number of atoms *i* in the system.

In our calculations, the scattering factors f^0 are calculated using Waasmier and Kirfel tables [21] and the anomalous dispersion factors f' and f'' are obtained from the tables of Henke [22] or Sasaki [23].

It must be noted that the coherent intensity is not accessible directly from the scattering intensity which contains also many contributions:

- Air scattering
- Coherent scattering
- Incoherent scattering

In order to obtain the coherent intensity, it is necessary to make measurement corrections by taking into account these contributions and make a number of absorption corrections due to the geometry of the sample.

A software developed in the laboratory allows to carry out all these corrections and to obtain the pair correlation function. Such programs are based on the procedure described by Wagner [24].

$$I(2\Theta, Q) = I_p\big[A(2\Theta, E, E')P(2\Theta)I_{coh}(Q) + I_{mult}^{coh}(Q) + A(2\Theta, E, E')P(2\Theta)I_{incoh}(Q') + I_{mult}^{incoh}(Q)\big] \quad \text{(III. 2)}$$

where:

- $I_p =$ intensity of primary beam
- $I_x(Q) =$ coherent and incoherent scattering intensity
- $A(2\Theta, E) =$ attenuation coefficient
- $I_{mult} =$ multiple scattering
- $P(2\Theta, \mathrm{E}) =$ polarization factor
- $E' = E/(1 + 0.00392Esin^2(\Theta))$

The coefficient $A(2\Theta, E)$ is an attenuation coefficient which depends on the geometry of the sample. It is calculated by integrating the optical path of the X-ray beam onto the irradiated volume of the sample.

Practically, air scattering, important only at small angles is recorded during an experiment without sample and subtracted. Multiple scattering is removed analytically using the Warren and Mozzi procedure [25] and the Compton scattering intensity is calculated using the tabulated values by Balyuzi [26].

In the case of a system containing *n* components as it is always the case, the Faber-Ziman theory allows to define the total structure factor $S(Q)$ as the weighted sum of $n(n+1)/2$ of the partial structure factors S_{ij} corresponding to each of the atomic pairs present in the component:

$$S(Q) = \sum_{i,j} W_{ij} S_{ij}(Q) \qquad \text{(III. 3)}$$

The W_{ij} factors are the weights of the different partial structure factors and are calculated from the diffusion factors f_i and atomic concentrations c_i:

$$W_{ij} = \frac{c_i c_j f_i(Q) f_j^*(Q)}{|\langle f(Q)\rangle|^2} \qquad \text{(III. 4)}$$

When $Q \to \infty$, $I_{coh} \to \langle |f(Q)|^2 \rangle$ and $(S(Q) - 1) \to 0$. This allows to do the normalization for the curve at the high Q values.

When $Q \to 0$, $I_{coh} \to 0$ and $(S(Q) - 1 \to -\langle f(0)^2 \rangle / \langle f(0) \rangle^2$.

This value allows to verify that the normalization is correct at low Q values.

The structure of a sample can be described in real space in terms of its pair correlation function $g(r)$, which is proportional to the probability of finding an atom at a position *r* relative to a reference atom taken to be at the origin. The position of the peaks of $g(r)$ then allows to determine the interatomic distances. The functions $S(Q)$ and $g(r)$ are related by the Fourier transforms:

$$g(r) = 1 + \frac{1}{2\pi^2 \rho} \int_0^{Qmax} q[S(Q) - 1] \frac{\sin Qr}{r} M(Q) dQ \qquad \text{(III. 5)}$$

where ρ is the atomic number density calculated using the density of the sample. In practice, the finite maximum Q-value that is accessible in diffraction experiments, Q_{max}, leads to peak broadening in real space after Fourier transformation as well as to non-physical oscillations in g(r)

and in other r-space functions. Such 'truncation ripples' can be avoided via prudent modulation of the experimental $S(Q)$ by a damping function before Fourier transformation, being equivalent to a coarsening of the r-space resolution; it decreases slowly to 0 at Q_{max}. The modification function usually used is the Lorch function [27]:

$$M(Q) = \begin{cases} \dfrac{\sin\left({}^{Q\pi}/_{Q_{max}}\right)}{{}^{Q\pi}/_{Q_{max}}}, Q \leq Q_{max} \\ 0, Q \geq Q_{max} \end{cases} \quad \text{(III. 6)}$$

As for the structure factor, the total pair-correlation function $g(r)$ is a weighted sum of the partial pair-distribution functions. The radial distribution function (RDF or $N(r)$) is generally defined as:

$$N(r) = 4\pi r^2 \rho g(r) \quad \text{(III. 7)}$$

$N(r)dr$ has a direct physical interpretation, defined as the number of atoms in a range (r, r + dr) of any given atom [28], [29]. RDF can be integrated to obtain the average number of neighboring atoms C in a coordination shell (weighted average coordination number) existing between the distances r_1 and r_2 is thus:

$$C = \int_{r_1}^{r_2} N(r) d(r) \quad \text{(III. 8)}$$

For neutron and X-ray diffraction studies of glasses, one often defines the total correlation function, $T(r)$, as:

$$T(r) = \frac{N(r)}{r} = 4\pi r \rho g(r) \quad \text{(III.9)}$$

Because the peaks are symmetrical and allow easier modelling by Gaussian. The average coordination number is then given by:

$$C = \bar{r} \int_{r_1}^{r_2} T(r) dr \quad \text{(III. 10)}$$

where $\bar{r}$ being the position of the peak in $T(r)$.

III.3.1 High Energy X-Ray Scattering – Operating Mode

High energy X-ray diffraction measurements (HE-XRD) were conducted at the 6-D-ID beamline at APS (Argonne National Laboratory, USA). The X-ray energy was 100 keV, providing data at Q values up to 30 Å^{-1}. A 2D setup was used for data collection with a Perkin Elmer model 1621 X-Ray area detector **(Figure III.2)**. This detector has a good signal to noise ratio, a small pixel size (200 μm) and excellent resolution (2048 × 2048). The beam size was chosen to be 0.5 mm x 0.5 mm to allow a proper positioning of the beam on the various glass samples. The two-dimensional diffraction patterns were reduced using the Fit2D software [30]. The measured background intensity was subtracted, and corrections were for the different detector geometries and efficiencies, sample self-attenuation, and Compton-scattering using standard procedures [31], [32] giving the total X-ray structure factor $S_X(Q)$.

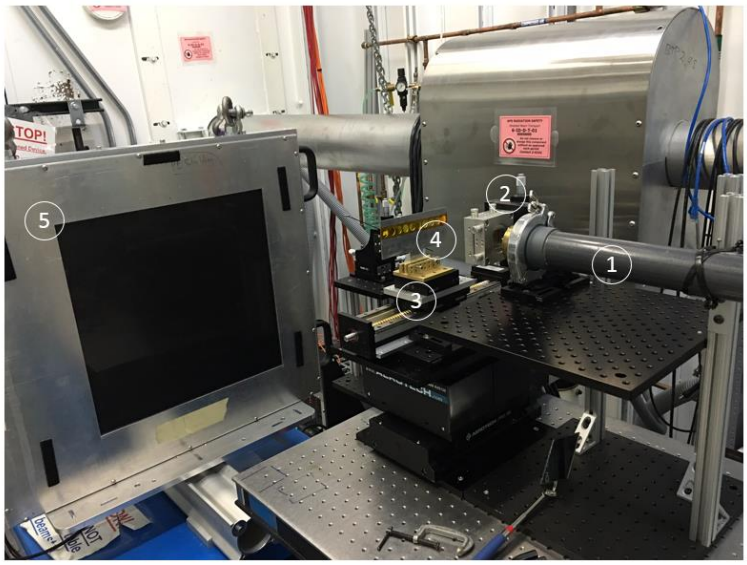

Figure III.2. (1) vacuum tube; (2) slit; (3) sample stage; (4) aluminum frame and (5) image plate detector.

III.3.2 Neutron diffraction – Operating mode

Neutron diffraction determines the atomic and/or the magnetic structure of a material. This technique can be applied to study crystalline structures, gases, liquids or amorphous materials. It is a kind of elastic scattering in which the neutrons emerging from the experiment have more or less the same energy as the incident neutrons. This technique is similar to X-ray diffraction, but different types of radiation give complementary information. In fact, it is a very well suited technique because the scattering power of a given nucleus is independent of the momentum

transfer, as consequence of the short range interaction between the neutron and the nucleus [33]. This scattering power is proportional to the square of the scattering lengths. A sample to be examined is placed in a beam of thermal or cold neutrons and the pattern of intensity around the sample gives information about the structure of the material.

Neutron diffraction experiments have been carried out at the ISIS spallation neutron source (Rutherford-Appleton laboratory, U.K.) and the Orphée reactor (Léon Brillouin Laboratory, CEA-Saclay). The 7C2 and GEM diffractometers provide diffraction data up to 20 and 40 $Å^{-1}$ respectively in reciprocal space (the scattering vector $Q = 4\pi \sin\theta/\lambda$, where 2θ is the scattering angle and λ the neutron wavelength). The glass samples were measured at room temperature using cylindrical vanadium containers. The neutron diffraction data were corrected for background, container scattering, self-attenuation, multiple scattering, inelasticity effects to obtain the total neutron structure factor $S_N(Q)$.

III.3.3 Small-angle neutron scattering

Small angle scattering techniques (SANS when using neutron beams or SAXS when using conventional X-ray radiation sources or synchrotron radiation) are experimental methods allowing the determination of structural features, such as size and volume fraction, of matrix inhomogeneities in a huge variety of materials. The order of magnitude of the size of objects that can be detected is in the approximate range $1\text{-}10^3$ nm.

Small-angle scattering (SAS) data are analyzed either using standard linear plots (such as Guinier or Porod plots) or using nonlinear least-squares fits to appropriate models [34]–[36]. The first method is easily performed and usually gives good estimates of ‘particle’ size (radius of gyration) and clues as to the nature of the scattering inhomogeneities through the Porod exponent; a Porod exponent d = 4 points to particles with smooth surfaces while d = 3 points to very rough surfaces. An exponent d = 2 can represent scattering from a two-dimensional structure (such as lamellae or platelets). An exponent d = 1 represents scattering from a stiff rod (or thin cylinder). Porod exponents less than 3 are for ‘mass fractals’ while Porod exponents between 3 and 4 are for ‘surface fractals’.

The PAXY small-angle neutron scattering instrument (Laboratoire Léon Brillouin, France) was used for mesoscopic (10 to 1000 Å) structural studies using different neutron wavelengths and

sample-to-detector distances: 5 Å/1.5 m, 5 Å/3.5 m, 8.5 Å/5 m, and 15 Å/6.7 m. Measurements have been carried out at room temperature and under atmospheric pressure. Standard corrections for sample volume, neutron beam transmission, empty beam signal subtraction, detector efficiency and subtraction of incoherent scattering were applied to get the scattered intensities on absolute scale. The data reduction has been done using the home-made software PASiNET [37].

(a) (b)

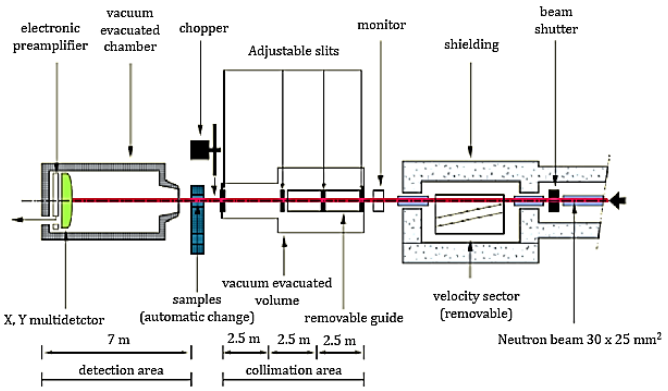

(c)

Figure III.3. (a) Schematic presentation of the G 2-3 PAXY-SANS instrument [38]; (b) a photo of the instrument; and (c) sample preparation.

Figure III.3 shows a schematic presentation of the G 2-3 PAXY-SANS instrument and related pictures. We have prepared samples with a diameter of 10 mm and a thickness of 1 mm. The samples were placed in a HELLMA cell between two glass plates before being measured at the PAXY platform.

III.4 Scanning electron microscopy

The principle of SEM is based on the electron-matter interactions. An electron gun bombards the material to be observed, and hence the sample will emit several types of radiation. Among the most currently used: X-rays for chemical analysis, backscattered electrons (between 1 and 200 nm

deep) for chemical contrast and secondary electrons (between 1 and 10 nm deep) for surface topography.

Images of the glass structures at various magnifications (200x – 2000x) were recorded using FE-SEM (JEOL JSM-7100F, acceleration voltage of 15 keV) equipped with an Xflash 6 | 30 backscatter electron (BSE) detector. X-ray microanalysis measurements were carried out with the aid of EDX Bruker QUANTAX 800 model unit to check the sample homogeneity.

III.5 Results and discussions

III.5.1 Glass homogeneity

Silver thioarsenate glasses Ag_2S-As_2S_3 appear to be phase-separated within the intermediate silver concentration range, $4 \leq x \leq 18$ at.% Ag, forming silver-rich and Ag-poor vitreous domains [39], [40]. Consequently, we have checked the homogeneity of $(AgY)_x(As_2S_3)_{1-x}$ glasses on mesoscopic level. Preliminary scanning electron microscopy (SEM) and small-angle neutron scattering (SANS) studies show that silver-poor glasses ($x \leq 0.2$ for AgY-As_2S_3, $x \leq 4$ at. % Ag for Ag_2S-As_2S_3) are homogeneous, while at intermediate and high silver concentrations ($x > 4$ at.% Ag), a mesoscopic phase separation was observed, **Figure III.4-6**.

The SEM images of the AgBr-As_2S_3 glasses are shown in **Figure III.4** and **Figure III.6**. As evidenced from the SEM images of the glasses, the introduction of Ag has a profound effect on the glass morphology at the micrometer spatial scale. The $x = 0.2$ sample appears to be uniform, while the $x > 0.2$ glass specimen exhibits multiple spherical objects of different sizes. The latter backscattered electron image contains also chemical information; brighter spherical particles are enriched with silver compared to darker glass matrix, confirmed also by energy dispersive x-ray (EDX) analysis.

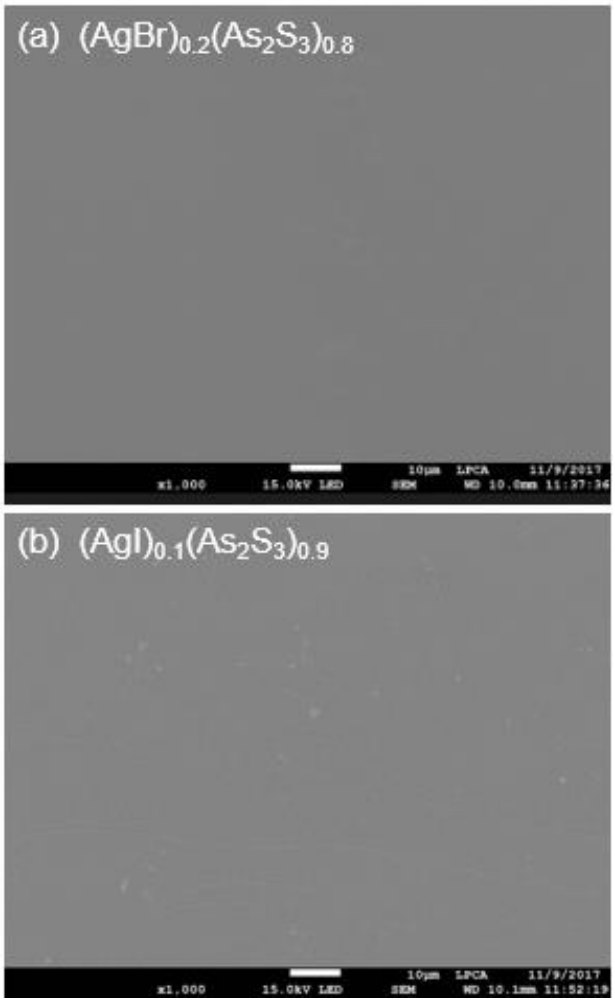

Figure III.4. Scanning electron microscopy images of $(AgY)_x(As_2S_3)_{1-x}$ glasses: (a) x = 0.2 (Y = Br), (b) x = 0.1 (Y = I). The secondary electron detection was used for these 2 samples.

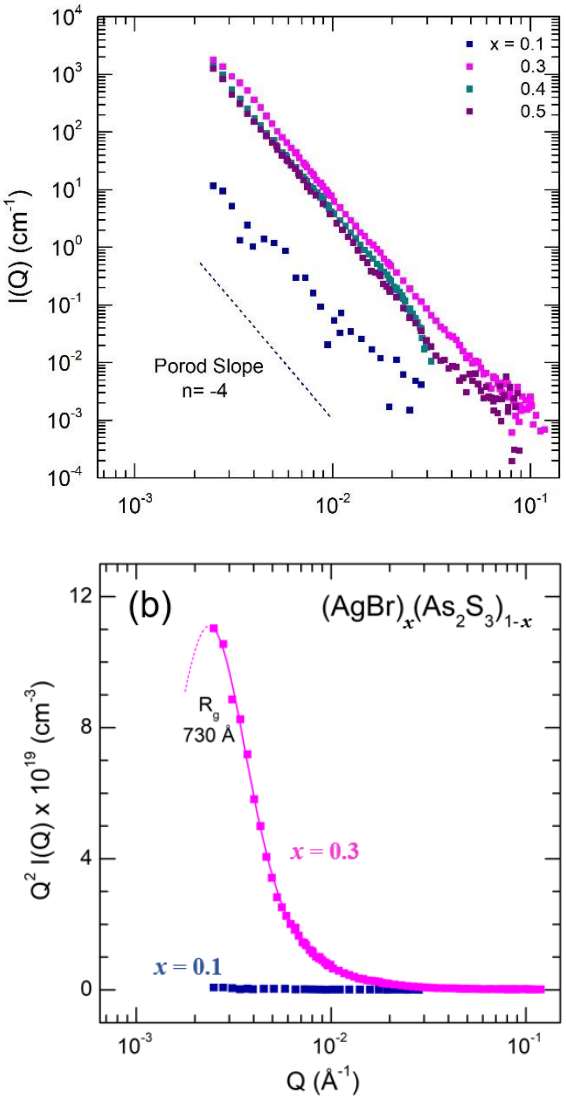

Figure III.5. Small-angle neutron scattering data for $(AgBr)_x(As_2S_3)_{1-x}$ glasses: (■,blue) x = 0.1, (■,magenta) x = 0.3, (■,cyan) x = 0.4, (■,purple) x = 0.5; (a) the normalized SANS intensity $I(Q)$ plotted on a log-log scale; (b) the Kratky plot: $Q^2\,I(Q)$ vs. Q. The Porod slope n = -4 is also shown.

Regarding glasses with x = 0.3, the Ag-poor phase is the dominant and the Ag-rich phase appears in the form of spherical droplets whose size account of few hundreds of nm (50 and 300 nm). For higher Ag concentrations, in particular for x = 0.5, the situation changes drastically and the Ag-rich phase becomes the dominant one. The larger Ag-rich domains, interestingly contain inclusions of Ag-poor phase of various sizes. In particular, when the Ag concentration exceeds ~7 at.% (x >

0.3) the initially continuous Ag-poor phase becomes fragmented and the Ag-rich phase percolates in the glass structure. The size of the Ag-poor droplets also spans a wide range in spatial scale. Increasing further the Ag content, with x = 0.6 causes the disintegration of the sizeable Ag-poor droplets to much smaller ones and the reduction of the size polydispersity; sizes of the Ag-poor droplets do not exceed 2–3 μm.

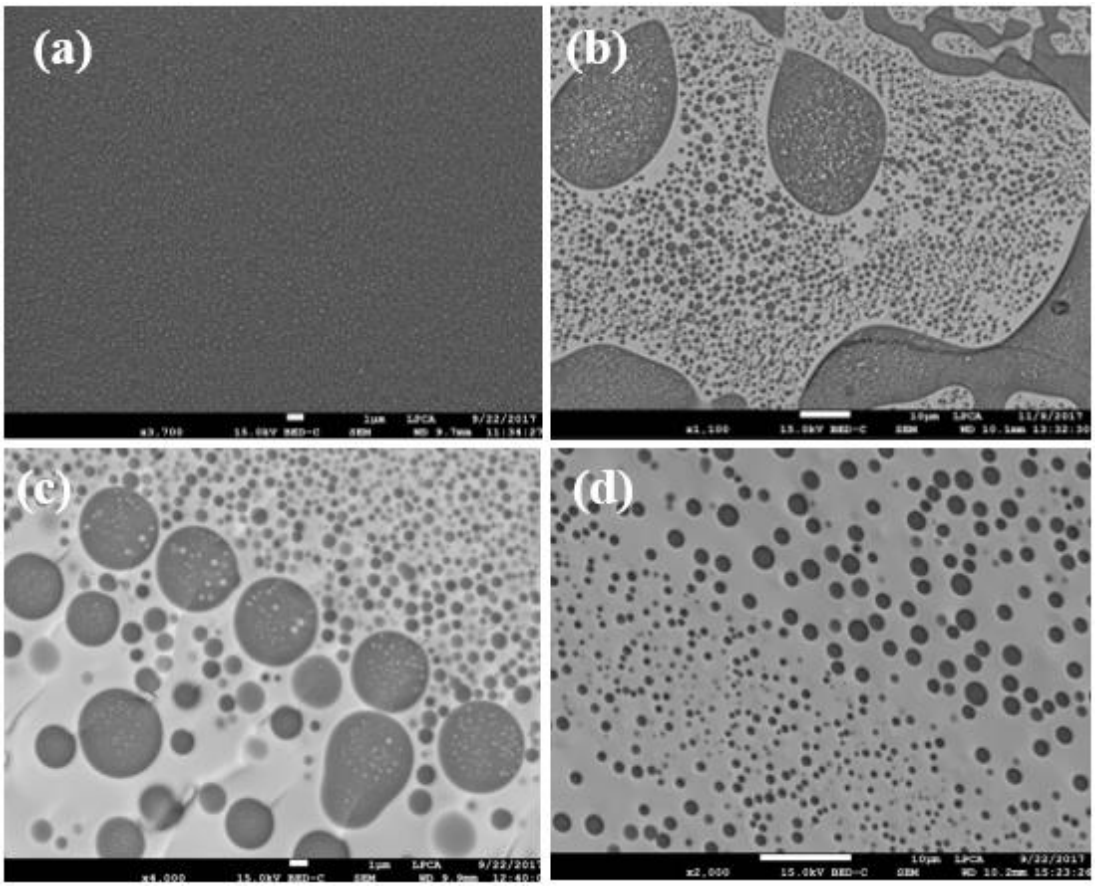

Figure III.6. Scanning electron microscopy images of $(AgBr)_x(As_2S_3)_{1-x}$ glasses: (a) x = 0.3, (b) x = 0.4, (c) x = 0.5 and (d) x = 0.6.

The SEM observations appear to be coherent with small-angle neutron scattering experiments, **Figure III.5**. The normalized SANS intensity $I(Q)$ of AgBr-As_2S_3 glass samples plotted on a log-log scale shows a remarkable difference of two orders of magnitude between the x = 0.1 and x = 0.3, 0.4 and 0.5 glasses. All scattering functions roughly follow a Porod law $I(Q) \propto Q^{-4}$ [41], [42]. Nevertheless, the slope $n = \partial \log I(Q)/\partial \log Q$ = -3.5±0.1 is lower for the Ag-poor glass. Moreover, the low SANS intensity and the $I(Q)$ shape for the x = 0.1 sample are typical for

homogeneous chalcogenide glasses with density fluctuations and rather well described by the Debye-Bueche model [43] with a characteristic correlation distance of ≈200 Å [39], [44], [45]. Much more intense $I(Q)$ for the y = 0.3 sample exhibits some positive deviations from the Porod slope n = -4 below 5×10^{-3} Å^{-1} with a subsequent slope decrease. However, the accessible Q-range ($Q > 2 \times 10^{-3}$ Å^{-1}) does not allow to follow the further evolution, presumably a Guinier regime [41], [42], n = -2, at lower Q. The Kratky plot, $Q^2\, I(Q)$ vs. Q, **Figure III.5(b)**, is often used to estimate a typical size of mesoscopic particles if the Guinier approximation is valid [46]. In this case, the function $Q^2\, I(Q)$ plotted versus the scattering vector Q shows a maximum. The position Q_{max} of this maximum and the Guinier radius of gyration R_g are related, $Q_{max} = \sqrt{3}/R_g$. Here again, the limited Q-range does not allow to observe a clear maximum. Nevertheless, a rough estimation of R_g = 730±200 Å is consistent with the SEM data.

Resuming, we conclude that silver-poor AgY-As_2S_3 glasses, $x \leq 0.2$, are homogeneous at mesoscopic scale showing only density fluctuations while the glasses with intermediate and high silver content, $x > 0.2$, are phase-separated. Further SEM and SANS studies of silver-rich AgY-As_2S_3 glasses are in progress.

III.5.2 Raman studies of Ag_2S-As_2S_3 and AgY-As_2S_3 (Y = Br, I) and DFT modelling

Several Ag-As-S and AgY crystalline references were synthesized and studied using Raman spectroscopy in order to compare their Raman spectra with the spectra of our glassy samples. In addition, we have used the results of DFT modelling of vibrational properties carried out by Prof. A. Cuisset and Dr. D. Fontanari for Raman mode assignments.

The DFT calculations have been carried out using Gaussian 16 software [47] associated with its graphical user interface GaussView. In order to find a compromise between the cost of the calculations and the accuracy of the results, structural optimization and harmonic vibrational frequency calculations were performed for size-limited clusters, i.e., Ag_2S or As_6S_6. The DFT calculations were carried out with the Becke [48] three parameters hybrid exchange functional and the Lee–Yang–Parr correlation functional (B3LYP) [49]. The small-core relativistic pseudo-potential basis set (cc-pVTZ-PP) [50] and the effective core potentials available in the Environment Molecular Science Library [51] were employed for cluster geometry optimization

and Raman intensity calculations. All the structures were optimized using the tight convergence option ensuring adequate convergence and reliability of computed wave numbers.

III.5.2.a Ag_2S-A_2S_3 crystal structures

The Ag-As-S system contains several thermodynamically stable compounds shown in **Figure III.7**.

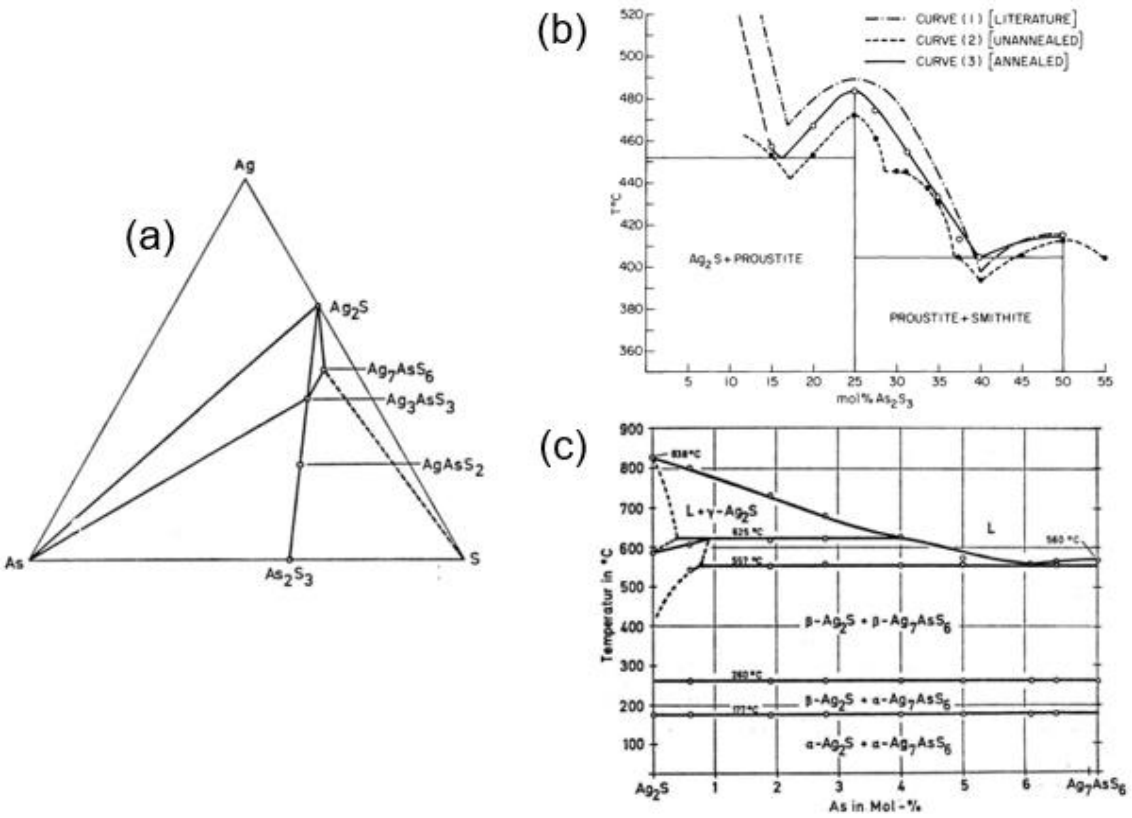

Figure III.7. (a) Phase equilibria in the Ag-As-S system [52]; phase diagram of (b) Ag_2S-A_2S_3 [53] and (c) Ag_2S-Ag_7AsS_6 [52].

III.5.2.b Synthesis and XRD analysis of Ag_2S, $AgAsS_2$, Ag_3AsS_3 and Ag_6AsS_7

Four Ag_2S, $AgAsS_2$, Ag_3AsS_3 and Ag_7AsS_6 crystalline compounds were synthesized from silver (Neyco, 99.999%), sulfur (Aldrich, 99.999%) and arsenic sulfide (synthesis described previously). The starting elements and compounds were weighed in stoichiometric proportions and introduced in silica tubes. After air vacuum and sealing, the silica tubes containing the different elements were placed in the furnace and were thermally treated slowly till 999 °C. Then the mixtures were cooled down slowly to room temperature in the turned off furnace. The $AgAsS_2$ compound was obtained

from the $(Ag_2S)_{0.5}(As_2S_3)_{0.5}$ glass by annealing at 275 °C for 3 days. XRD analysis **(Figure III.8)** confirms that the first three synthesized crystalline compounds in the Ag-As-S system correspond to their respective references. In contrast, the Ag_7AsS_6 composition does not show the Bragg peaks corresponding to this compound. The majority of reflections are related to low-temperature silver sulfide.

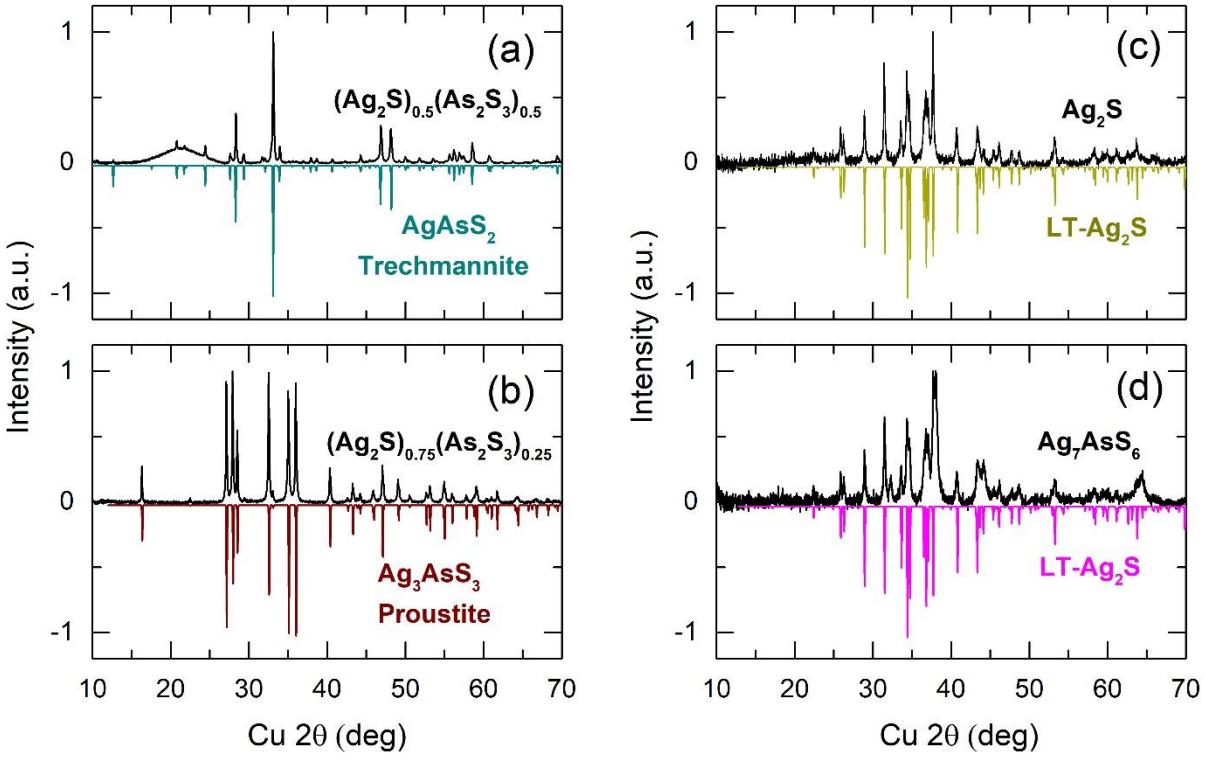

Figure III.8. XRD patterns of the following crystalline compositions: (a) $AgAsS_2$ annealed at 275 °C, (b) Ag_3AsS_3, (c) β-Ag_2S, and (d) Ag_7AsS_6 crystals.

III.5.2.c Raman spectra and DFT modelling of Ag_2S

β-Ag_2S

At room temperature and ambient pressure, β-Ag_2S has a monoclinic crystal structure with space group $P2_1/c$ and four formula units per primitive cell [54]. β-Ag_2S is known to be a semiconductor with a direct band gap of 1.3 eV. Its structure is based on a slightly distorted bcc lattice of sulfur atoms. The two structurally inequivalent silver atoms are equally distributed in positions close to the octahedral 6(*b*) (Ag1) sites with the shortest (Ag1)-S bond 2.47 Å, and tetrahedral 12(*d*) (Ag2) sites with the shortest (Ag2)-S bond 2.55 Å of the sulfur bcc array [55]. **Figure III.9** shows the

experimental Raman spectrum of the synthesized crystalline compound β-Ag_2S together with the results DFT modelling using triatomic cluster Ag_2S.

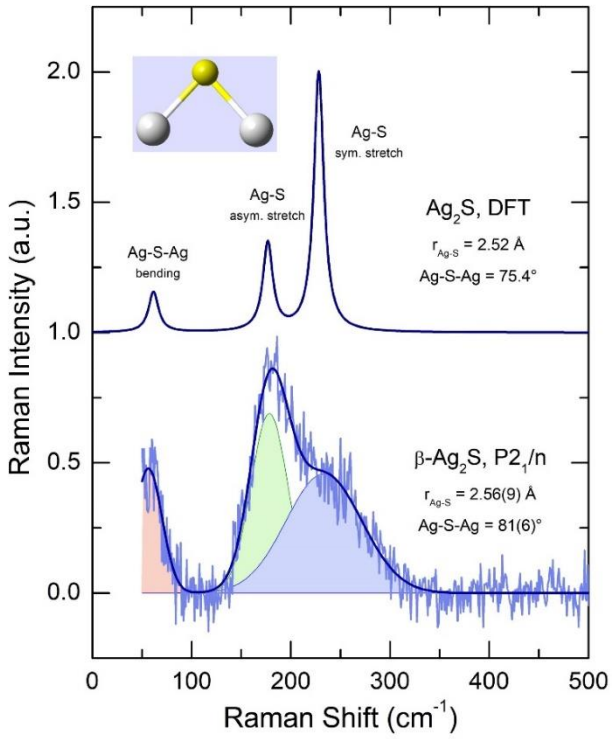

Figure III.9. DFT Raman spectra of Ag_2S compared to the experimental data for β-Ag_2S.

The Raman spectra of β-Ag_2S shows a broad intense unresolved peak between 100 and 350 cm^{-1}, and a low-frequency band at 55 cm^{-1}. A Gaussian fitting of the unresolved peak shows two intense bands at 180 and 240 cm^{-1}. The DFT Raman spectrum of Ag_2S cluster shows three bands similar to the experimental ones at 55, 180 and 240 cm^{-1} corresponding to Ag-S-Ag bending, Ag-S asymmetric and symmetric stretching, respectively.

III.5.2.d Raman spectra of $AgAsS_2$, Ag_3AsS_3 and Ag_6AsS_7

$AgAsS_2$

The Raman spectrum of $AgAsS_2$ shows very sharp distinct bands at 374 cm^{-1} and 320 cm^{-1} **(Figure III.10)**. The very strong band at 374 cm^{-1} is assigned to the symmetric vibrations, whereas the asymmetric stretching is represented by the medium intensity Raman band at 358 cm^{-1}. The band at 320 cm^{-1} and 291 cm^{-1} correspond to the symmetric and asymmetric bending vibrations of the pyramidal AsS_3 group, respectively. Other bands in the $AgAsS_2$ spectrum are attributed to the lattice vibrations [56].

Ag_3AsS_3

The Ag_3AsS_3 spectrum reveals two prominent bands at 364 and 332 cm^{-1}. The very strong band at 332 cm^{-1} corresponds to the symmetric As-S stretching mode, and the strong shoulder at 352 cm^{-1} to the asymmetric As-S stretching modes. The medium intensity band at 332 cm^{-1} is assigned to the symmetric S-As-S bending modes [56].

Ag_7AsS_6

The synthesized Ag_7AsS_6 essentially exhibit the Bragg peaks of silver sulfide. Consequently, its Raman spectrum is similar to that of β-Ag_2S.

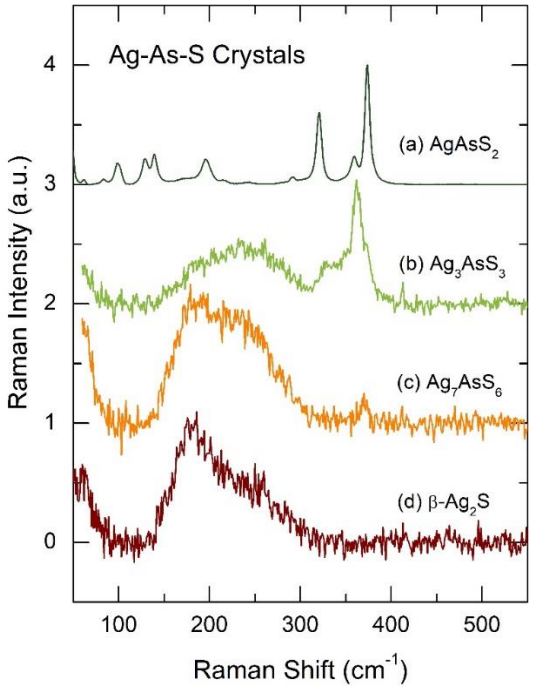

Figure III.10. Raman spectra of (a) $AgAsS_2$, (b) Ag_3AsS_3, (c) Ag_7AsS_6 and (d) β-Ag_2S crystals.

III.5.2.e The quasi-binary glasses: AgY-As_2S_3 (Y = Br, I)

The measured raw Raman spectra of the $(AgY)_x(As_2S_3)_{1-x}$ glasses show only a weak second-order Raman feature at ω ≈700 cm^{-1} in the high-frequency region. Thus, we will focus our attention on the 100–500 cm^{-1} domain. In order to quantitatively compare the Raman spectra obtained for the different glass compositions, a Voigt function was used to fit the spectral background and then

subtracted from the experimental data before normalizing the spectrum over the amplitude of the most intense peak.

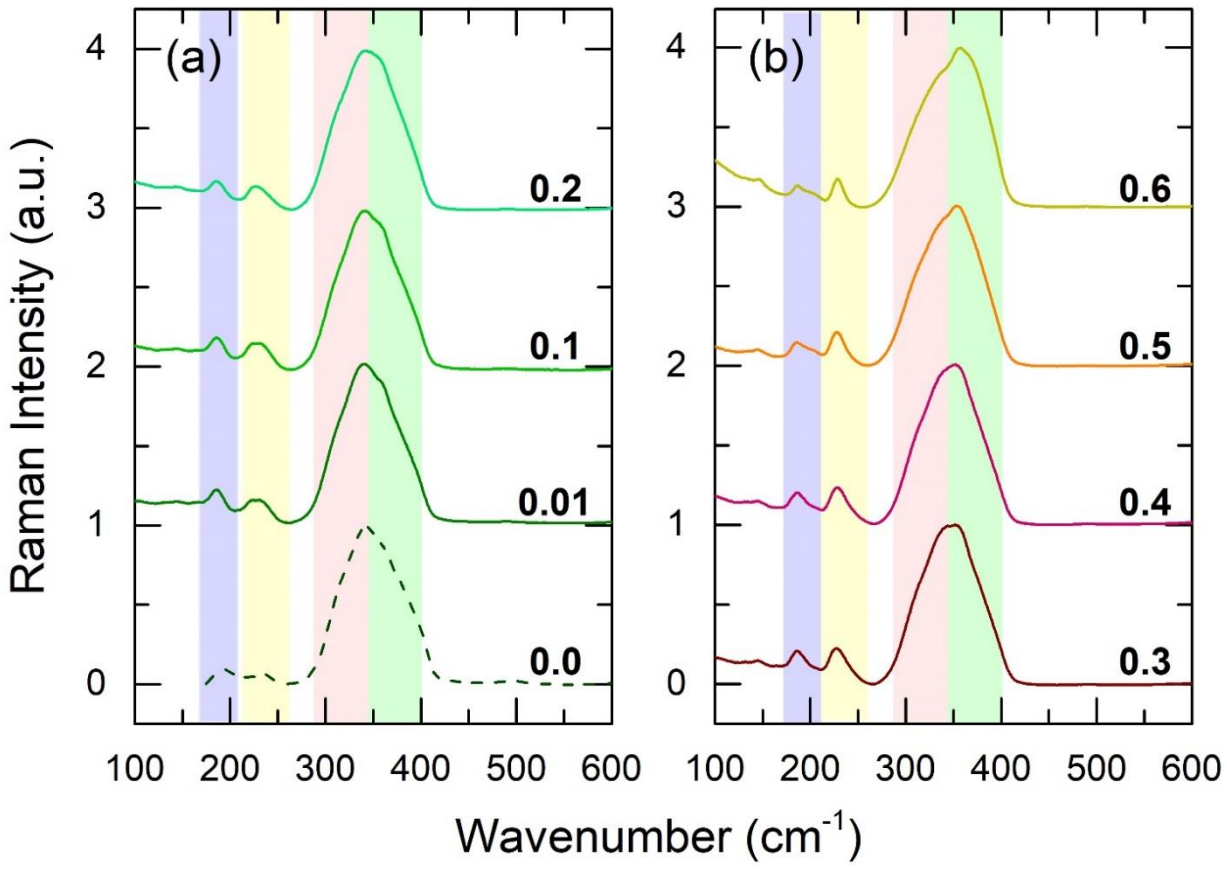

Figure III.11. Raman spectra of the quasi-binary $(AgBr)_x(As_2S_3)_{1-x}$ glasses with (a) low and (b) high AgBr content *x*.

The resulting Raman spectra of the AgY-As_2S_3 (Y=Br, I) glasses are shown in **Figure III.11** and **Figure III.15**. The glassy As_2S_3 (x = 0) has a broad poorly resolved multimodal feature centered at 340 cm^{-1}, corresponding to symmetric and asymmetric As–S stretching modes in corner-sharing $AsS_{3/2}$ pyramids and As–S–As bridges [11], [45], [57]–[60]. Two additional weak but distinct features at 230 cm^{-1} and 495 cm^{-1}, reported by many investigators, are related to As–As and S–S stretching modes respectively [59]–[63]. These modes come from different structural units having homopolar As–As or S–S bonds and indicate a small degree of chemical disorder in stoichiometric As_2S_3 glass (2–3% according to references [59], [62]). Doping with silver bromide or silver iodide does not change significantly the broad poorly resolved spectral envelope of glassy As_2S_3. However, starting from 1 mol.% AgBr, we observed more intense low-frequency features at 180

cm^{-1} and 230 cm^{-1}, corresponding to As-As stretching. The relative intensity of these features remains invariant compared to the As-S stretching at 340 cm^{-1}.

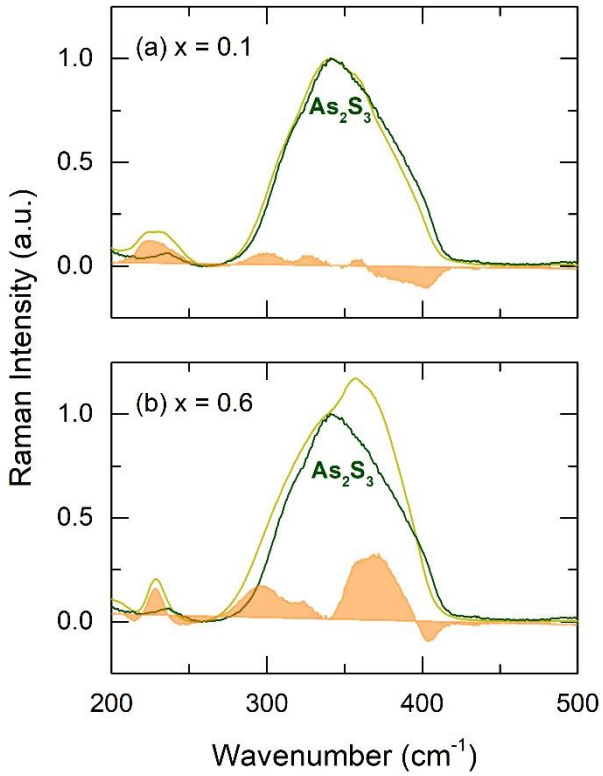

Figure III.12. Subtracting the scaled As_2S_3 spectral envelope from $(AgBr)_x(As_2S_3)_{1-x}$ glasses at (a) low x = 0.1 and (b) x = 0.6.

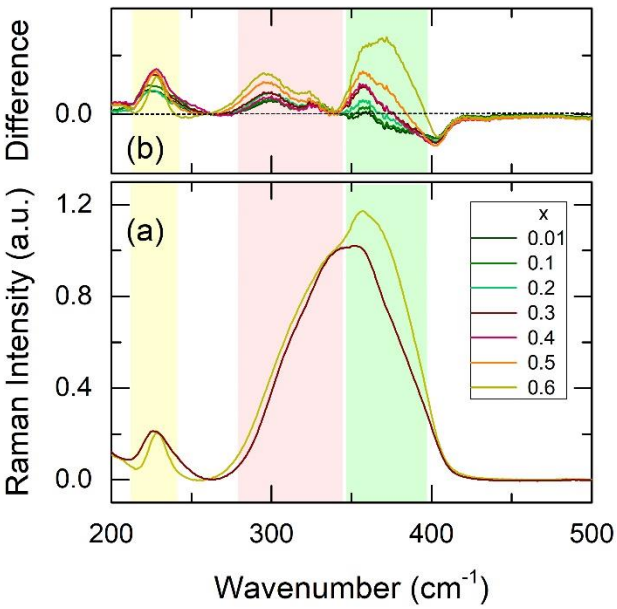

Figure III.13. Raman spectra of the x = 0.3 and x = 0.6 glasses, which belong to two composition domains with contrasting conductivity properties, superimposed on the same graph, and (b) a detail of the difference Raman spectra for the glasses.

Nevertheless, the shape of the main vibrational feature at 340 cm^{-1} changes with x and a distinct mode appears as a shoulder at ≈370 cm^{-1}. The direct adjustment of the poorly resolved Raman spectra represents a difficult task without a detailed DFT modelling of the vibrational properties. Consequently, we applied a subtraction of the scaled As_2S_3 spectral envelope to investigate these tiny vibrational signatures in more details, **Figure III.12** and **Figure III.13**. The difference spectra in the As-S stretching region (300-400 cm^{-1}) show, in addition to the 370 cm^{-1} mode, a broad feature at 300 cm^{-1} and negative amplitude at 400 cm^{-1}. All these features indicate changes in the intermediate range order of the As_2S_3 glassy matrix, in particular, a progressive decrease of the average size of As_nS_n rings, where $2 \leq n \leq 10$. The DFT calculations show a narrowing of the vibrational envelope with decreasing ring size n, **Figure III.14**. In particular, the negative peak at

400 cm^{-1} can be related to a decreasing population of As_6S_6 rings and a new mode at 370 cm^{-1} to more populated As_3S_3 rings of trechmannite type.

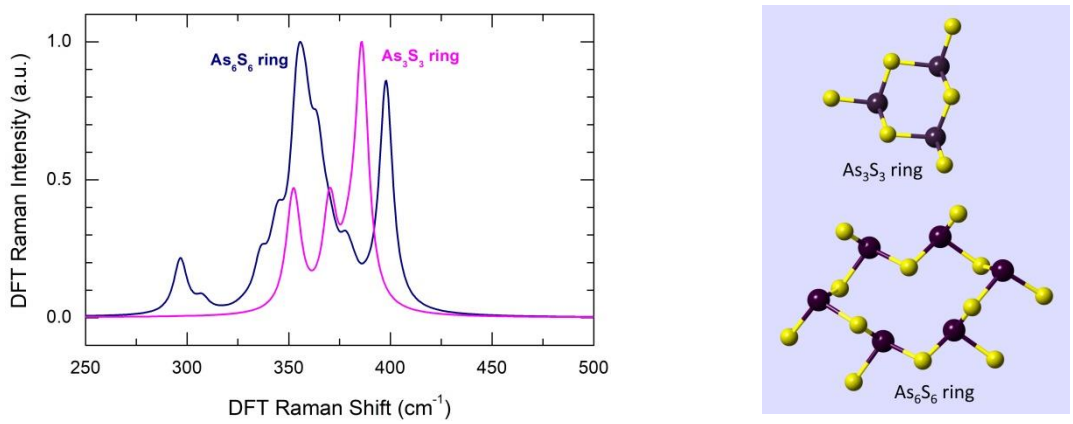

Figure III.14. (a) DFT Raman spectra of (b) As_6S_6 and As_3S_3 (trechmannite-type) rings with terminal sulfur atoms S_t in the As-S stretching spectral domain. The terminal hydrogen species are not shown and the H-related vibrations are removed.

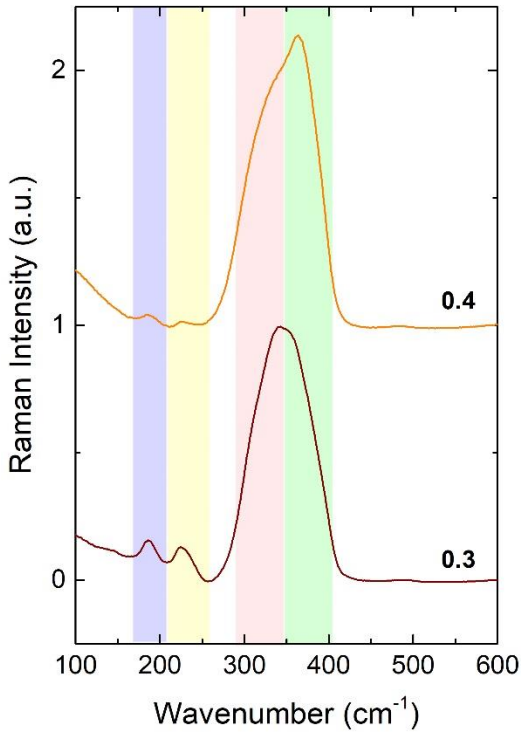

Figure III.15. Raman spectra of the quasi-binary $(AgI)_x(As_2S_3)_{1-x}$ glasses for x = 0.3 and 0.4.

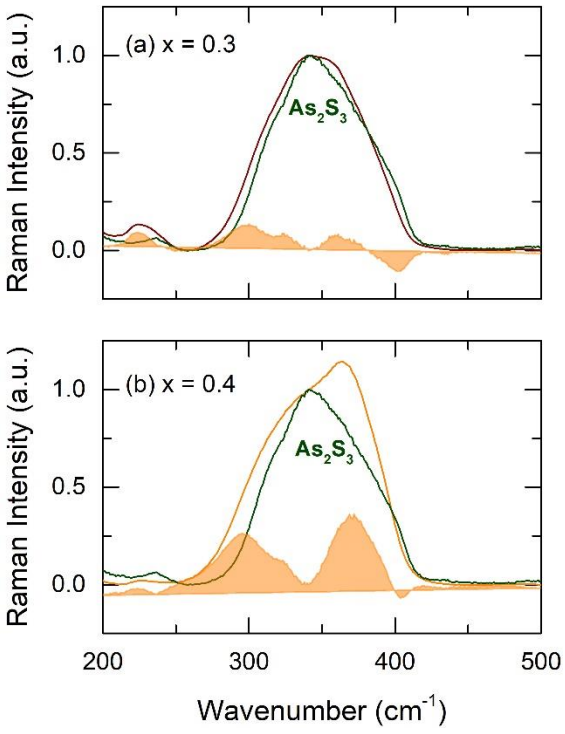

Figure III.16. Subtracting the scaled As_2S_3 spectral envelope from $(AgI)_x(As_2S_3)_{1-x}$ glasses for (a) x = 0.3 and (b) x = 0.4.

The observed structural changes appear essentially above $x > 0.3$ and also characteristic for AgI-As_2S_3 glasses, **Figure III.15** and **Figure III.16**.

The 370 cm^{-1} mode has been already observed in the silver-rich glasses Ag-AsS_2 [64], [65], and has been attributed to the As-S_t stretching of the terminal sulfur S_t in As_3S_3 rings similar to that observed in the $AgAsS_2$ trechmannite crystal. Similarly, Boidin *et al.* has observed a strong mode of this type in the Ag_2S-As_2S_3 glasses [66].

The two known crystalline structures of $AgAsS_2$ called smithite [67] and trechmannite [68] contain As_3S_6 cycles connected together with silver. The As_3S_6 group can have a C_{3v} [68] or a C_S symmetry [69]. The bridging As-S_b bonds in the ring have a bond length of 2.31±0.03 Å, while the terminal ones have a bond length of 2.22±0.02 Å. The main characteristic vibration in trechmannite appears at 375 cm^{-1}, at the same main energy band of $AgAsS_2$ glass, and is related to the shorter As-S_t bond compared to the average bond length of As-S_b in the As_2S_3 glass (2.26 Å [45]). However, the dominant peak of smithite appears at 364 cm^{-1}, slightly red-shifted from the trechmannite and the corresponding glass main bands. Therefore, it seems reasonable to assume that the intermediate-range structural order of our glasses is similar to what has been observed in trechmannite and $AgAsS_2$ glass.

The structure of trechmannite [68] and smithite [67] differs from crystalline orpiment As_2S_3; the latter contains 6-membered rings (As_6S_6) while the former is constituted of 3-membered rings (As_3S_3). Thus, the reduction of the average ring size in glasses can explain the observed changes of the main As-S stretching feature in AgY-As_2S_3 glasses.

However, we cannot exclude another possibility that in the AgY-As_2S_3 glasses may also appear isolated AsS_3 pyramids similar to that in As_3AsS_3 crystals [70]. The two crystalline forms of Ag_3AsS_3 are hexagonal proustite [71] and monoclinic xanthoconite [72]. The proustite structure is based on complex packing of isolated AsS_3 trigonal pyramids and Ag atoms. The crystal structure of xanthoconite is composed of double sheets consisting of interconnected AsS_3 pyramids pointing with their As apices outward, connected by two Ag atoms, while the third Ag atoms holding the sheets together. All the sulfur species are terminal in the two forms of Ag_3AsS_3 but the As-S_t average bond length is longer, 2.25±0.02 Å, than that in $AgAsS_2$. Our Raman measurements of proustite show a strong Raman mode at 363 cm^{-1}, **Figure III.10**, consistent with reported results

[56]. The observed vibrational feature may also be present in the difference spectra of AgY-As_2S_3 glasses.

Summarizing, the evolution of the Raman spectra indicates that silver cations are participating in transformations of the intermediate-range order in contrast to widely accepted point of view that metal halides leave intact the original glass structure. Since the AgY-rich glasses appear to be phase-separated, we suggest that the Raman spectrum at each *x* can be expressed as a linear combination of the Raman spectra of the Ag-poor and Ag-rich domains. Further structural information becomes available in diffraction experiments.

III.5.3 Raman spectroscopy of HgS-GeS_2 crystals and glasses

Before structural analysis of pseudo-ternary silver thiogermanate stoichiometric glasses, we have synthesized and carried out Raman spectroscopy measurements of the known crystalline compounds in the HgS-GeS_2 system. The obtained spectroscopic information appears to be useful for better understanding the structural features in glasses.

III.5.3.a HgS-GeS_2 crystals

Hg_4GeS_6 is the only incongruently melting compound at 996 K [1] and has a polymorphous transformation at 679 K[1], **Figure III.17**. The structure of LT modification is monoclinic (space group Cc) [1].

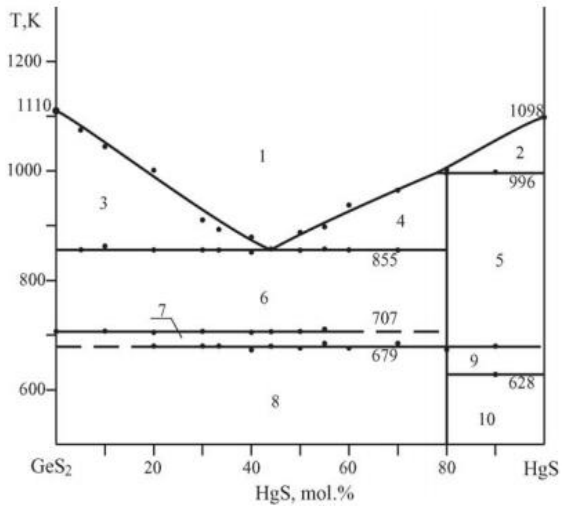

Figure III.17. Phase diagram of the HgS-GeS_2 quasi-binary system [73].

III.5.3.b Synthesis and XRD analysis of Hg_4GeS_6

The XRD analysis shows that only Hg_4GeS_6 was obtained as a single phase, low-temperature monoclinic polymorph, **Figure III.18**.

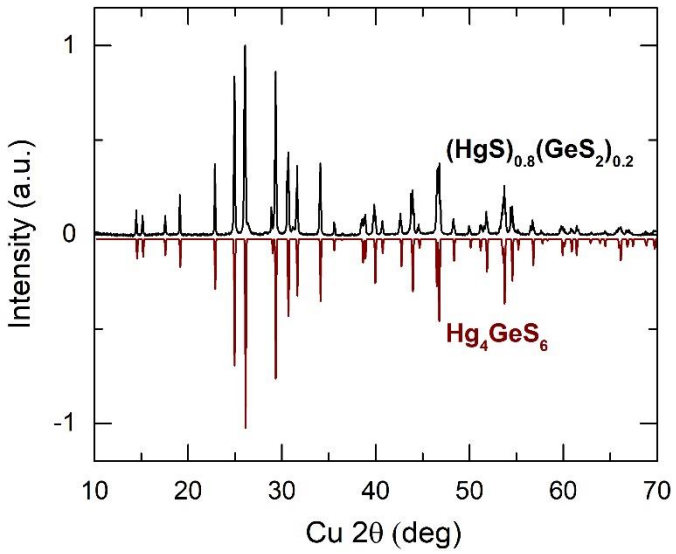

Figure III.18. XRD pattern of the crystalline $(HgS)_{0.8}(GeS2)_{0.2}$ sample compared to the monoclinic Hg_4GeS_6, space group Cc.

III.5.3.c Raman spectra of HgS-GeS_2 glasses

Before discussing the evolution of Raman features in the quasi-binary HgS-GeS_2 glassy system, it is useful to review the main structural motifs in glassy GeS_2, reflected by their characteristic vibrational modes and DFT replicas [74]. The GeS_2 stoichiometric glass exhibits well-known spectroscopic features consistent with neutron and X-ray diffraction results [45], [75], [76]:

1. ν = 344 cm^{-1}: corresponds to the A_1 symmetric in-phase breathing in CS-$GeS_{4/2}$ tetrahedra [77]–[79];
2. ν = 372 cm^{-1}: is related to symmetric breathing of ES-$GeS_{4/2}$ units [80];
3. ν = 400 cm^{-1}: contains contributions from both CS- and ES-tetrahedra as well as from ethane-like ETH-units [74], [81], [82];
4. ν = 436 cm^{-1}: is due entirely to the highest F_2 mode in the ES-$GeS_{4/2}$ tetrahedra [74], [81];

5. ν = 259 cm^{-1}: a weak asymmetric feature originating from Ge-Ge stretching in ethane-like ETH-$Ge_2S_{6/2}$ units [80], [82], [83].

Experimental Raman spectra of the $(HgS)_x(GeS_2)_{1-x}$, $0.0 \leq x \leq 0.6$, glasses are shown in **Figure III.19**. The spectra show subtle changes in the Raman intensity below 200 cm^{-1}, related to the bending and deformation modes. In the high frequency domain above 500 cm^{-1}, only a weak second-order Raman feature at ≈700 cm^{-1} appears to be visible. Therefore, we will focus our attention on the 200-600 cm^{-1} range.

The spectra show a new structural feature emerging at 300-320 cm^{-1} first as a shoulder, increasing in intensity with *x* and finally becoming the most intense Raman mode for HgS-rich vitreous alloys, $x > 0.3$. Similar feature was observed earlier in mercury thioarsenate glasses [84] and attributed to symmetric Hg-S stretching in $(HgS_{2/2})_m$ chain-like fragments, confirmed by DFT modelling.

Direct fitting of the multi-modal Raman spectra in the HgS-GeS_2 glass system unveils some structural aspects. The results of the Raman analysis are given in **Table III.1**, where the frequencies, the full width at half-maximum (FWHM) and the peak area are listed.

Table III.1 shows that the positions and FWHMs of the stretching modes typical for g-GeS_2 are practically unchanged but their intensity decreases with decreasing GeS_2 content. In particular, the stretching features related to ES-$GeS_{4/2}$ are decreasing faster than those for CS-$GeS_{4/2}$. On the contrary, the intensity and FWHM of the Hg-S stretching increases with *x*; however, its position shifts to lower frequencies from 328 cm^{-1} (x = 0.1) to 304 cm^{-1} (x = 0.6), **Figure III.20**.

We should also note a weak feature at ≈490 cm^{-1}; this mode is characteristic for S-S stretching in chalcogenide glasses and suggests the appearance of S-S homopolar bonds even in stoichiometric glasses. Possible Ge-Ge homopolar bonds characterized by a broad peak at ≈260 cm^{-1}, seem to be masked by Hg-S symmetric stretching centered at ≈300 cm^{-1}.

As a first approximation to reveal the structural role of mercury sulfide in the thiogermanate glasses, we have subtracted the scaled Raman signal corresponding to g-GeS_2 from the quasi-binary glasses, and normalized them to a constant GeS_2 spectral envelope. Typical subtraction procedure is shown in **Figure III.21(a)** and the resulting difference spectra are presented in **Figure III.21(b)**.

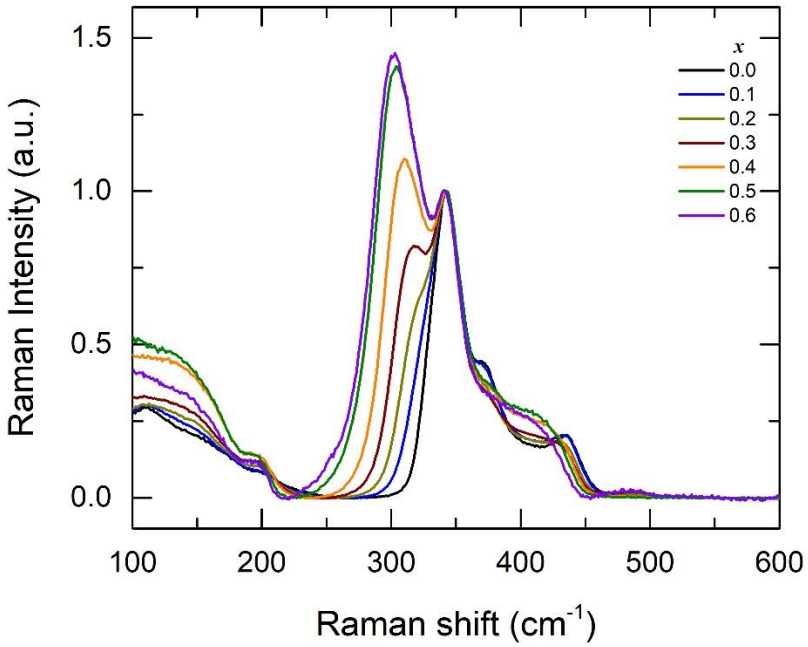

Figure III.19. Normalized and background corrected Raman spectra of the quasi-binary $(HgS)_x(GeS_2)_{1-x}$ glasses.

Table III.1. The scattering bands' parameters obtained by direct Gaussian fitting of the Raman spectra of the $(HgS)_x(GeS_2)_{1-x}$ glasses for $0.0 \leq x \leq 0.6$.

	1			2			3			4			5		
x	ν_1	FWHM	A_1	ν_2	FWHM	A_2	ν_3	FWHM	A_3	ν_4	FWHM	A_4	ν_5	FWHM	A_5
0.0				342.3	28.9	30.0	372.9	23.0	8.0	400.0	44.1	8.5	436.1	27.5	4.9
0.1	328.0	31.5	16.4	344.2	22.2	15.8	368.9	30.1	11.5	406.5	60.3	11.9	436.2	21.0	2.3
0.2	322.1	33.1	21.6	343.8	21.3	16.0	366.2	31.9	9.4	400.0	62.6	12.5	433.0	23.7	2.3
0.3	316.6	35.3	30.5	343.2	21.2	15.5	365.8	39.5	13.6	409.9	51.8	10.8	433.6	18.6	1.1
0.4	310.9	38.2	40.7	343.8	23.8	18.1	369.6	30.5	8.4	403.5	49.0	11.9	430.6	23.7	2.0
0.5	305.6	44.4	46.7	344.1	24.5	14.3	369.6	28.7	6.0	400.9	46.1	9.7	427.5	24.6	1.7
0.6	303.8	47.7	49.8	343.0	23.3	11.2	368.4	36.7	8.5	403.1	37.2	6.3	426.1	23.3	1.5

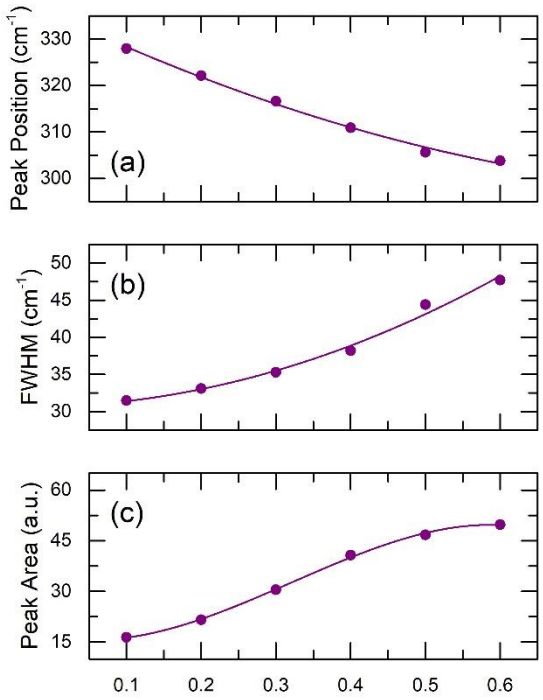

Figure III.20. (a) Peak position, (b) full width at half maximum (FWHM), and (c) relative area of the Hg-S stretching mode at 300-320 cm^{-1} in the $(HgS)_x(GeS_2)_{1-x}$ glasses. The solid lines are drawn as a guide to the eye.

The subtraction confirms the appearance of two major features at (i) 316±12 cm^{-1}, and (ii) ≈400 cm^{-1}. A monotonic increase in intensity of the symmetric in-phase Hg-S stretching at ≈316±12 cm^{-1} is clearly seen. Similarly to HgS-As_2S_3 glasses, the ≈316 cm^{-1} mode is accompanied by a less intense mode at ≈400 cm^{-1} related to asymmetric and/or out-of-phase symmetric Hg-S stretching [84]. The observed red shift of the Hg-S symmetric stretching is also common for the two glass systems. A quite significant difference should also be noted between HgS-As_2S_3 and HgS-GeS_2 glasses. In the former, one cannot see a lot of changes in the As_2S_3 spectral envelope, only a little bit different ring statistics. However, in the latter, we note a remarkable change in the CS/ES-$GeS_{4/2}$ ratio, i.e., ES-$GeS_{4/2}$ tetrahedra disappear very quickly, whereas CS-$GeS_{4/2}$ tetrahedra remain.

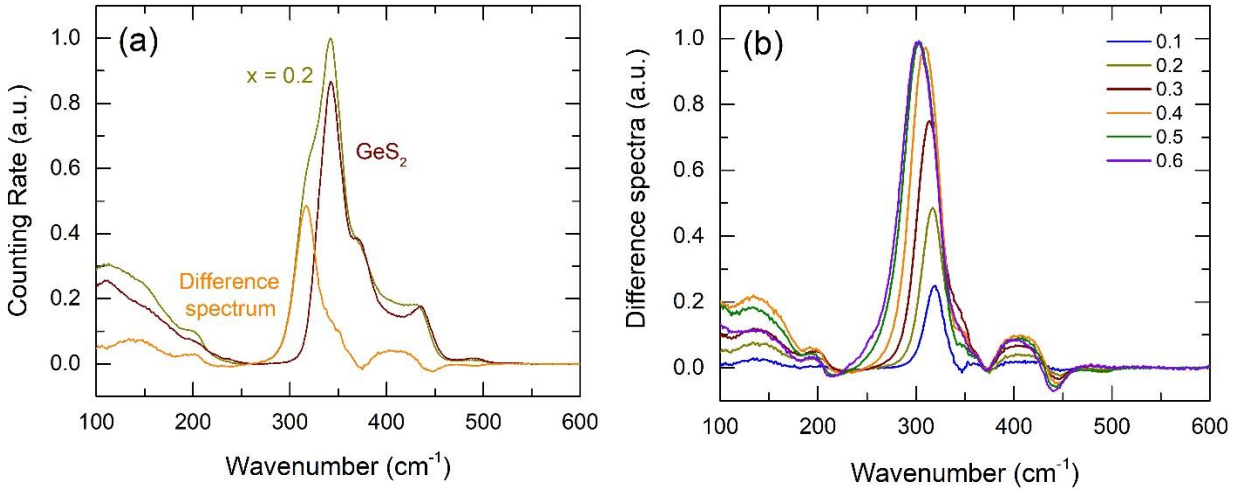

Figure III.21. (a) Subtraction procedure for the HgS-GeS_2 glass composition, x = 0.2, and the resulting difference spectrum $I_{x=0.2}(\omega) - k_{GeS2} \times I_{GeS2}(\omega)$; (b) the difference Raman spectra for the $(HgS)_x(GeS_2)_{1-x}$ glasses divided by k_{GeS2}, i.e., normalized to a constant GeS_2 spectral envelope. The numbers represent the mercury sulfide fraction in the glass.

A Gaussian fitting of the Raman spectra of some selected $(HgS)_x(GeS_2)_{1-x}$ glasses shown in **Figure III.22**, together with the Raman data for α-HgS, reflect both similarities and differences compared to crystalline mercury sulfide. Trigonal cinnabar over the 200-600 cm^{-1} spectral range is characterized by the most intense A_1 mode at 256 cm^{-1} and two weak LO/TO doublets of the E-modes at 290/283 cm^{-1} and 354/345 cm^{-1}, respectively. The intense high-frequency E-mode in α-HgS appears clearly in the $(HgS)_x(GeS_2)_{1-x}$ glasses at $x > 0.2$. The higher frequency of the Hg-S stretching in the glass can be related to hybrid Hg-S chain/Ge-S tetrahedral motifs. Another possible reason of the blue shift. First, the hybrid network implies the reduced average atomic mass of an Hg-hybrid oscillator, $m_{Hg} \propto \left(k_1 m_{Hg} + k_2 m_{Ge} + k_S m_S\right)$, where k_i is the weighting factor for the *i*-species, hence this increases the vibrational frequency, $\omega \propto {m_{Hg}}^{-1/2}$.

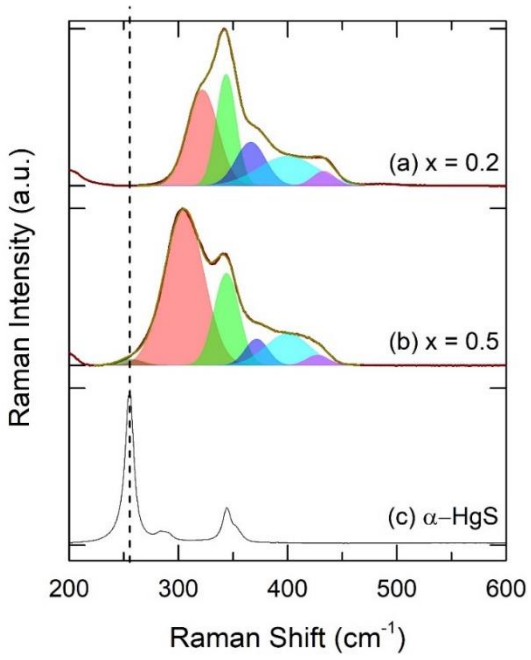

Figure III.22. Raman spectra for (a) x = 0.2 and (b) x = 0.5 HgS-GeS_2 glasses; (c) typical Raman spectrum for trigonal cinnabar α-HgS [84]. The dashed line at 256 cm^{-1} corresponds to the most intense A_1 symmetric mode in vibrational spectra of trigonal cinnabar.

III.5.4 Raman studies of AgI-HgS-GeS_2 glasses

Before discussing the effect of AgI on the glass structure, it is useful to review the structure and vibrational characteristics of g-GeS_2 vs. $(HgS)_{0.5}(GeS_2)_{0.5}$ glasses **(Figure III.23)**:

- New Hg-S stretching features, the most intense at ≈316 cm^{-1}, the A_1 symmetric Hg-S stretching.
- A significant decrease of ES-$GeS_{4/2}$ tetrahedra evidenced by a disappearance of the A_1^c companion mode at ≈370 cm^{-1}, and high-frequency F_2 asymmetric Ge-S stretching at ≈435 cm^{-1}.
- A very small red-shift of the A_1 in-phase Ge-S breathing mode in CS-$GeS_{4/2}$ at ≈340 cm^{-1}.

On the basis of the above discussion, the effect of AgI on the glass structure can now be elucidated. Experimental Raman spectra of the $(AgI)_x(HgS)_{0.5-0.5x}(GeS_2)_{0.5-0.5x}$ glasses are shown in **Figure III.24** in a normalized presentation. Characteristic changes in Raman spectra of $(AgI)_x(HgS)_{0.5-x/2}(GeS_2)_{0.5-x/2}$ glasses:

- Almost simultaneous increase of a new vibrational mode at ≈130 cm^{-1} and the A_1 in-phase Ge-S breathing mode in CS-$GeS_{4/2}$ at ≈340 cm^{-1} for Raman spectra normalized to the A_1 symmetric Hg-S stretching at ≈300 cm^{-1}.
- A significant low-frequency side broadening of the A_1 symmetric Hg-S stretching at ≈316 cm^{-1} assuming a new vibrational feature at about 270 cm^{-1}.
- Clearly visible red shift of the A_1 in-phase Ge-S breathing mode at ≈340 cm^{-1} with increasing AgI content.
- Some decrease of the high-frequency Ge-S stretching features (≳ 350 cm^{-1}) with increasing *x* for spectra normalized to the A_1 in-phase Ge-S breathing mode at ≈340 cm^{-1}.

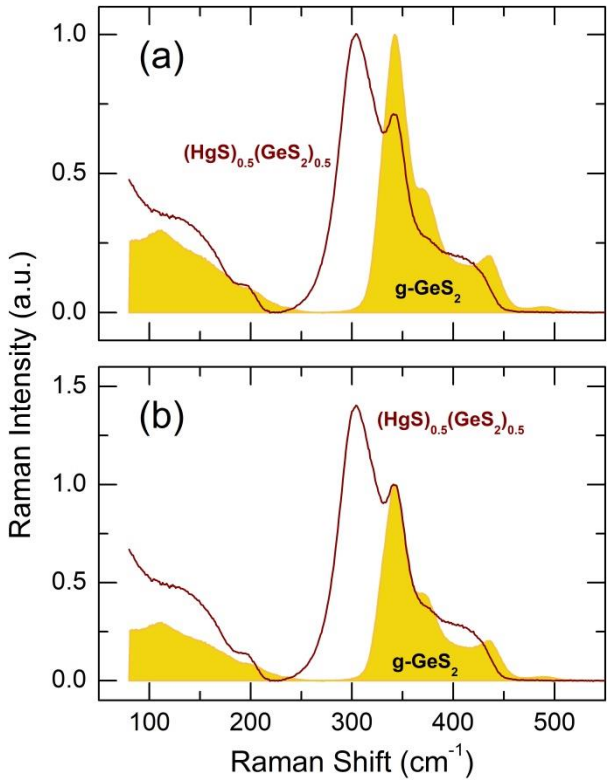

Figure III.23. Raman spectra of glassy host g-GeS_2 and $(HgS)_{0.5}(GeS_2)_{0.5}$; (a) normalized to the most intense vibration feature, (b) normalized to the A_1 in-phase Ge-S breathing mode in CS-$GeS_{4/2}$.

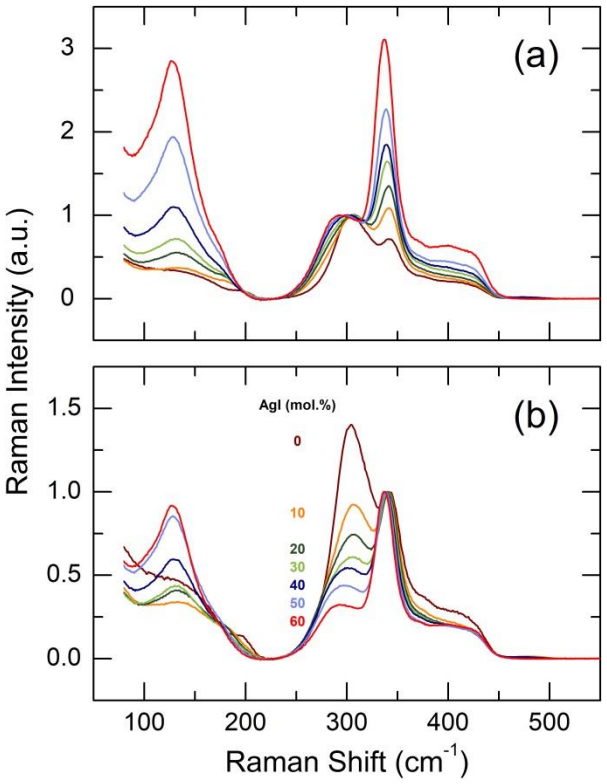

Figure III.24. Raman spectra of $(AgI)_x(HgS)_{0.5-x/2}(GeS_2)_{0.5-x/2}$ glasses with $0.0 \leq x \leq 0.6$; (a) normalized to the A_1 symmetric Hg-S stretching, (b) normalized to the A_1 in-phase Ge-S breathing mode in CS-$GeS_{4/2}$.

The new vibrational mode at ≈130 cm^{-1} increasing with silver iodide content is related to Ag-I stretching. First, the position of this mode is similar to that in crystalline β-AgI, **Figure III.25**. In

addition, DFT modelling of AgI monomer reproduces well the Ag-I stretching frequency at 121 cm^{-1} for the Ag-I interatomic distance of 2.80 Å.

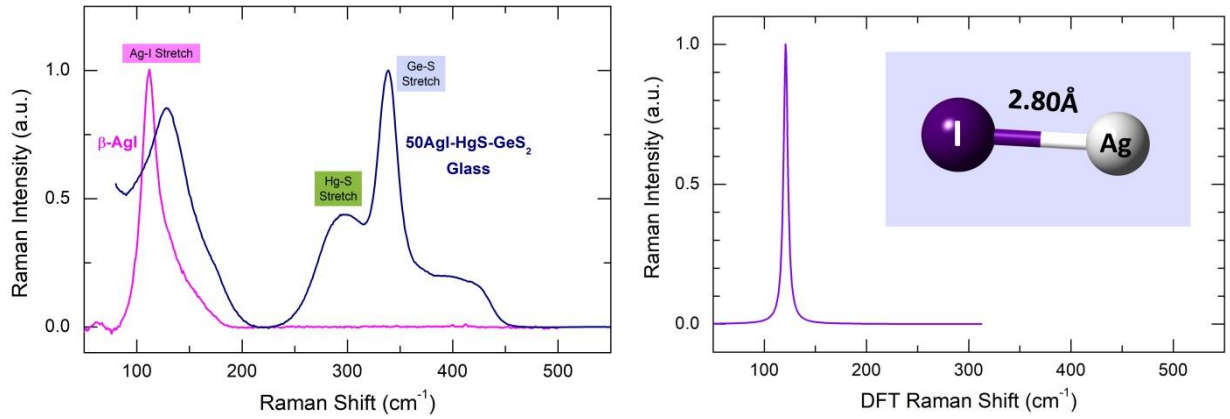

Figure III.25. (a) Raman spectra of crystalline β-AgI and glassy $(AgI)_{0.5}(HgS)_{0.25}(GeS_2)_{0.25}$, (b) DFT Raman spectra of AgI monomer.

The difference Raman spectra obtained by subtraction of the scaled Raman spectrum for $(HgS)_{0.5}(GeS_2)_{0.5}$ unveil interesting structural features, **Figure III.26**. We should precise that the difference spectra assume the subtraction of HgS-GeS_2 related vibrations, e.g. Ge-S and Hg-S stretching modes. The remaining vibrations should be related to AgI-based structural units and vibrational (structural) differences in the subtracted host, $(HgS)_{0.5}(GeS_2)_{0.5}$, with increasing silver iodide content. Consequently, a monotonic increase of the Ag-I stretching at ≈130 cm^{-1} in the difference spectra, normalized to a constant spectral envelope of the $(HgS)_{0.5}(GeS_2)_{0.5}$ host, is expected in accordance with the chemical composition of the ternary glasses, $(AgI)_x(HgS)_{0.5-0.5x}(GeS_2)_{0.5-0.5x}$. The 130 cm^{-1} spectral feature is, at least, bimodal; one observes a high-frequency shoulder at ≈180 cm^{-1}, whose relative intensity and position depends on *x*. The nature of this shoulder is not yet clear. The Ag-I stretching also exhibits a red shift with increasing *x*. An additional analysis is needed to quantify the observed changes.

In addition to the 130 cm^{-1} Ag-I stretching, a weak low frequency asymmetric feature at 280 cm^{-1} appears and grows up with AgI content. The 280 cm^{-1} feature is similar to that found in crystalline Ag_2S **(Figure III.9)** but shifted to higher frequencies and can be attributed to Ag-S stretching for short Ag-S separations of ≈2.43 Å. Similar peak has been observed in many Ag-rich glasses, increasing with silver content [12], [85]. The above results suggest mixed silver environment in AgI-HgS-GeS_2 glasses.

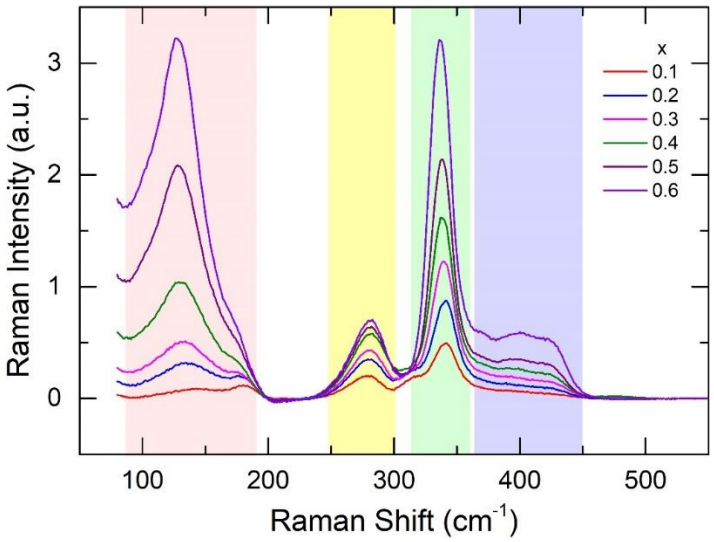

Figure III.26. The difference Raman spectra obtained by subtraction of the scaled Raman signal for 50HgS-50GeS_2 and normalized to a constant 50HgS-50GeS_2 spectral envelope.

The Ge-S stretching frequencies between 300 and 450 cm^{-1} are most difficult to discuss since they, in principle, should be subtracted. However, the A_1 in-phase Ge-S breathing in corner-sharing CS-$GeS_{4/2}$ tetrahedra at ≈340 cm^{-1} increases almost simultaneously with the Ag-I stretching at ≈130 cm^{-1}. It could be related to the fact that the mixed silver environment and additional Ge-S stretching modes are connected. They would appear simultaneously when silver iodide is dispersed at the molecular level in the host network approaching CS-$GeS_{4/2}$ tetrahedra and completing the existing Ag-I bonds by Ag-S-Ge linkages. The high-frequency Ge-S stretching (> 340 cm^{-1}) includes F_2 asymmetric vibrations of CS-$GeS_{4/2}$ tetrahedra and probably some indications of CS-Ge_2S_7 dimers at ≈400 cm^{-1}.

The A_1 Ge-S breathing mode at ≈340 cm^{-1} exhibits a significant red shift with increasing AgI content, **Figure III.27**. We note that in the HgS-GeS_2 binary glasses the red shift of the Ge-S breathing is much smaller. On the other hand, one observes very similar red shift in Ag_2S-GeS_2 binary glasses. This observation implies that the second neighbor of Ge is Ag and, consequently, silver has at least one sulfur nearest neighbor. Finally, we also note a strong red shift for Ag-I stretching coherent with the observed transport regimes in the AgI-HgS-GeS_2 glasses, **Figure III.28**.

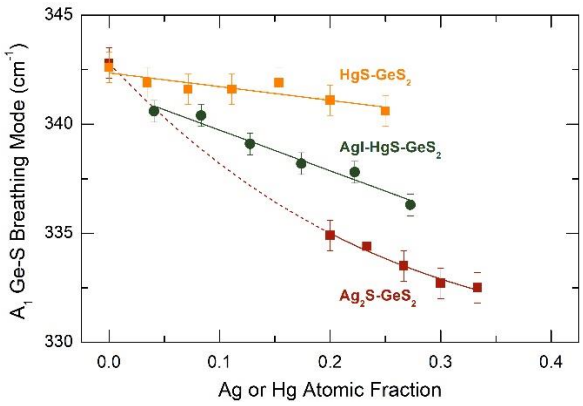

Figure III.27. Composition dependences of the A_1 Ge-S breathing mode in $HgS\text{-}GeS_2$, $Ag_2S\text{-}GeS_2$ and $AgI\text{-}HgS\text{-}GeS_2$ glasses. The solid and dotted lines are drawn as a guide to the eye.

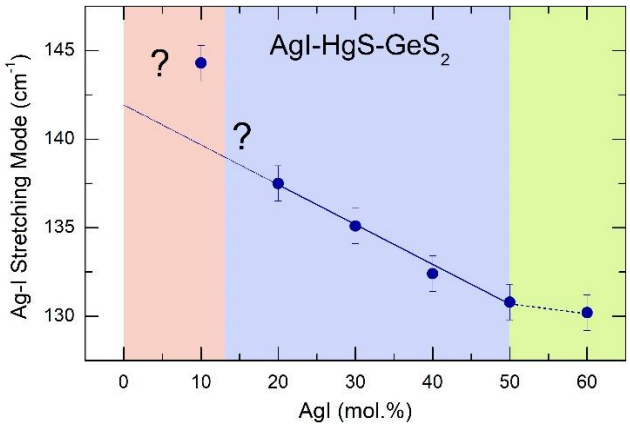

Figure III.28. Composition dependences of the Ag-I stretching mode in $AgI\text{-}HgS\text{-}GeS_2$ glasses. The question mark means missing Raman measurements.

III.5.5 Diffraction studies

The structural data obtained for the five-element glasses belonging to the ternary systems $AgI\text{-}HgS\text{-}As_2S_3$ and $AgI\text{-}HgS\text{-}GeS_2$ are particularly difficult to interpret. The presence of five $n = 5$ atomic species means that we would have $n(n+1)/2 = 15$ partial structural factors $S_{ij}(Q)$ in the reciprocal space or 15 total correlation functions $T_{ij}(r)$ in the real space. We discuss first the structural changes of the binary systems before considering the more complicated ternary ones. Thus, the obtained diffraction data are to be discussed in the following order:

A. The silver halide thioarsenate quasi-binary glasses
   (i) $(AgBr)_x(As_2S_3)_{1-x}$
   (ii) $(AgI)_x(As_2S_3)_{1-x}$
B. The mercury sulfide thiogermanate $(HgS)_x(GeS_2)_{1-x}$ quasi-binary glasses and crystals
C. The pseudo-ternary glasses:
   $(AgI)_x(HgS)_{0.5-x/2}(GeS_2)_{0.5-x/2}$

III.5.5.a The quasi-binary system: $AgBr\text{-}As_2S_3$

❖ ***Q-space functions***

Typical neutron $S_N(Q)$ and X-ray $S_X(Q)$ structure factors of $(AgBr)_x(As_2S_3)_{1-x}$ glasses are shown in **Figure III.29**. We note a significant transformation of both $S_N(Q)$ and $S_X(Q)$ for the binary glass. Oscillations are decreasing in amplitude with increasing AgBr content, and are shifting to lower Q; thus indicating an increase of average interatomic distances. The intense first sharp diffraction peak (FSDP) at Q_1 = 1.25 Å^{-1} for g-As_2S_3 is strongly reduced and shifted to higher Q. In contrast, the principle peak (PP) of the structural factor at Q_2 = 2.37 Å^{-1} grows substantially, shifts to lower scattering vectors (Q_2 = 2.25 Å^{-1} for x = 0.6 vs. 2.37 Å^{-1} for g-As_2S_3) and becomes the most intense feature in Q-space. In fact, the mean atomic volume in these glasses is decreasing (Chapter I) which means that the number density is increasing. Thus, increasing amplitude of PP is correlated with densification of glasses.

The FSDP is characteristic of intermediate-range order in oxide and chalcogenide glasses [86]. It is often observed for different silver chalcogenide glassy systems [87], [88], decreasing in intensity with increasing Ag concentration. As has been reported earlier, the changes in the FSDP are relatively small in the critical percolation domain in contrast to the modifier-controlled domain [87]. Anomalous X-ray scattering experiments on amorphous As-S showed that the FSDP is mainly caused by As-As correlations extended as far as 7 Å [89]. These correlations, characteristic of the host glassy matrix, disappear progressively with further increase of the silver content and are essentially absent in the modifier-controlled domain, indicating transformation and fragmentation of the As-S network [87].

The FSDP, isolated using a Voigt function, are presented in **Figure III.30**. The FSDP parameters: peak position Q_1, line width W_1 and area A_1, are collected in **Table III.2**. The position of the FSDP, corresponding to a correlation length $L_1 = 2\pi/Q \approx 5$ Å, remains essentially constant for the diluted and AgBr-poor glasses, and shifts to 1.27 Å^{-1} for the most concentrated glass (18.75 at.% Ag, x = 0.6). One observes a weak broadening of W_1 and a monotonic decrease of A_1 with increasing x. We should also note smaller FSDP amplitudes for hard X-rays compared to neutrons.

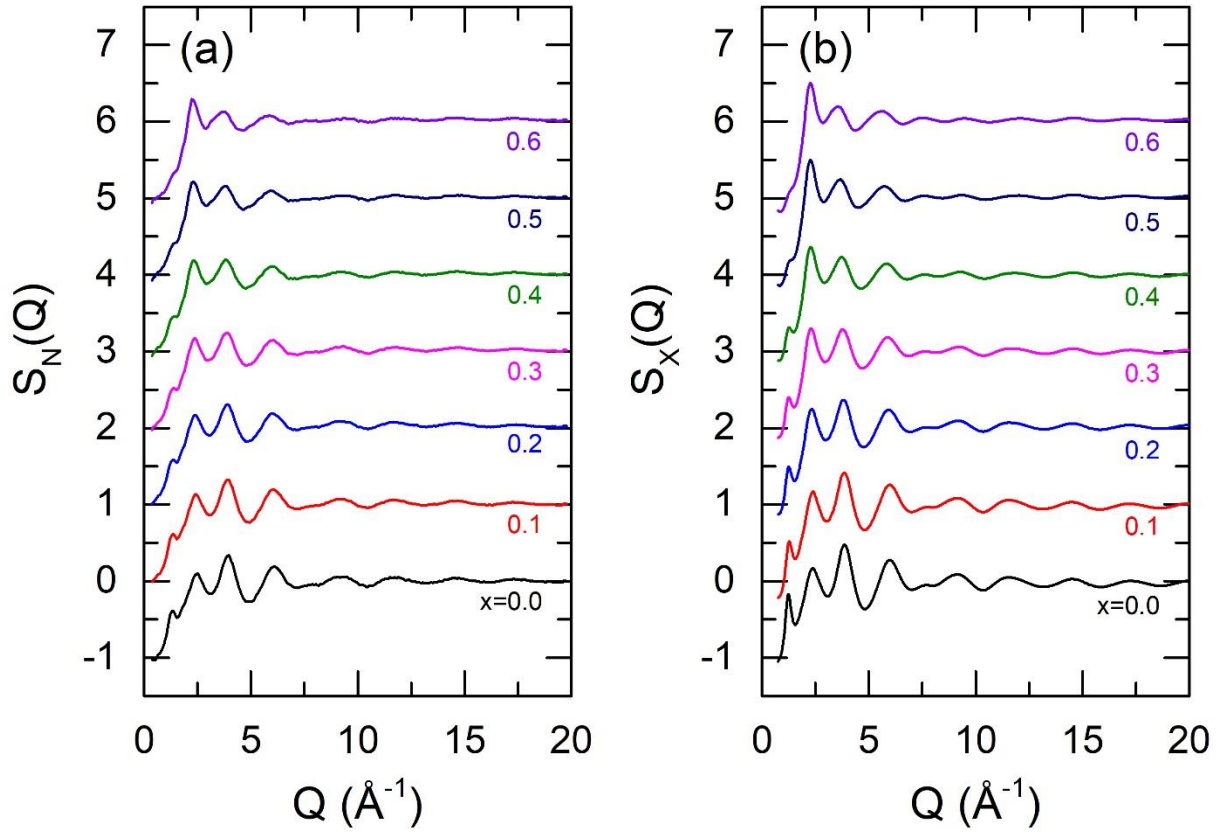

Figure III.29. (a) Neutron $S_N(Q)$ and X-ray $S_X(Q)$ structure factors for the $(AgBr)_x(As_2S_3)_{1-x}$ glasses, $0.0 \leq x \leq 0.6$.

Table III.2. FSDP parameters (position Q_1, full width at half maximum W_1 and area A_1) for quasi-binary $(AgBr)_x(As_2S_3)_{1-x}$ glasses.

AgBr fraction x	Hard X-rays				Neutrons			
	Q_1 (Å^{-1}) ± 0.017	W_1 (Å^{-1}) ± 0.06	A_1 ± 0.012	A_1/w_{AsAs} ± 0.05	Q_1 (Å^{-1}) ± 0.017	W_1 (Å^{-1}) ± 0.06	A_1 ± 0.012	A_1/w_{AsAs} ± 0.05
0.0	1.247	0.30	0.23	0.26				
0.1	1.260	0.30	0.19	0.24				
0.2	1.245	0.30	0.18	0.26	1.242	0.31	0.21	0.27
0.3	1.246	0.30	0.15	0.25				
0.4	1.261	0.30	0.11	0.23				
0.5	1.256	0.27	0.06	0.16	1.239	0.33	0.11	0.21
0.6	1.286	0.29	0.05	0.14				

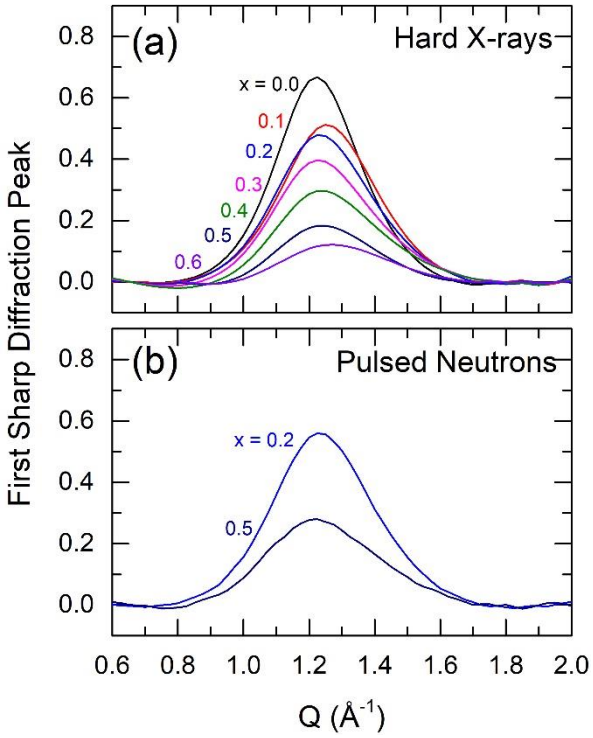

Figure III.30. FSDP isolated from (a) X-ray $S_X(Q)$ and (b) neutron $S_N(Q)$ structure factors for $(AgBr)_x(As_2S_3)_{1-x}$ glasses.

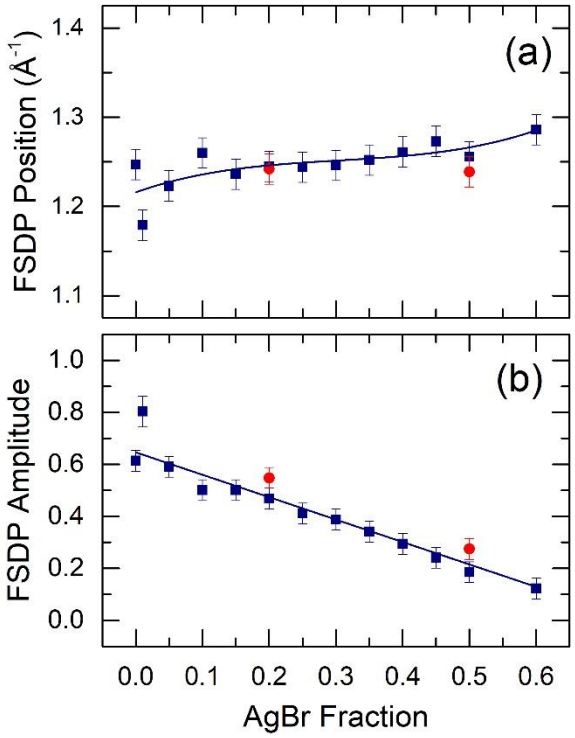

Figure III.31. FSDP (a) position Q_1 and (b) amplitude in neutron $S_N(Q)$ and X-ray $S_X(Q)$ structure factors of $(AgBr)_x(As_2S_3)_{1-x}$ glasses.

The observed increase of Q_1 with increasing *x*, **Figure III.31(a)**, suggests a slight decrease of the ring size *n*. Since the FSDP amplitude is related to As-As correlations, we could normalize A_1^i by dividing it by the neutron, w_{AsAs}^N, or the average X-ray, $\langle w_{\mathrm{AsAs}}^X(Q)\rangle$, As-As weighting factor, i.e., $A_1^N/w_{\mathrm{AsAs}}^N$. The resulting A_1/w_{AsAs} values, appear to be rather constant, 0.22±0.05 Å^{-1}, in remarkable contrast to the raw A_1^N or A_1^X parameters, **Table III.2**. As a result, we assume just a tiny change in the ring statistics for the AgBr-As_2S_3 glasses.

Figure III.32 shows that homogeneous glasses ($x \leq 0.2$), have no small-angle scattering, while non-homogeneous vitreous alloys ($x \geq 0.25$) exhibit an enhanced scattering at low Q. This information has already been observed in more details in the SANS measurements.

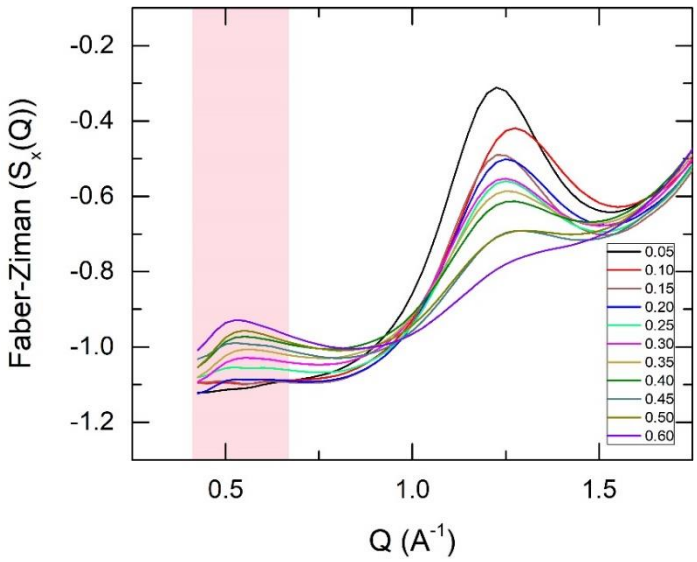

Figure III.32. X-ray $S_X(Q)$ structure factors for the $(AgBr)_x(As_2S_3)_{1-x}$ glasses at Q < 1.5 Å^{-1} showing enhanced scattering for $x \geq 0.25$, highlighted in pink.

❖ ***Real-space functions***

Typical neutron $T_N(r)$ and X-ray $T_X(r)$ total correlation functions for the AgBr-As_2S_3, $0.0 \leq x \leq 0.6$, glasses obtained from the corresponding $S_N(Q)$ and $S_X(Q)$ by Fourier transform using a Lorch window function, are shown in **Figure III.33**. They exhibit systematic changes with increasing AgBr content *x*, especially in the range 2 Å ≤ *r* ≤ 6 Å. One observes clearly three characteristic peaks at $r_1 \approx 2.3$ Å, $r_2 \approx 3.5$ Å and $r_3 \approx 5.2$ Å. The first peak of $T(r)$ at $r_1 \approx 2.3$ Å corresponds to As-S nearest-neighbor distance and the trigonal As coordination and two-fold coordinated sulfur species remain intact at *r*(As–S) = 2.27±0.01 Å **(Table III.3)**. The second peak at $r_2 \approx 3.5$ Å decreases in intensity with increasing *x*. It is related to As-As, S-S, and As-S second neighbor intra-layer correlations and shortest interlayer contacts as well as to Ag- and Br-related second neighbor correlations. One observes also broadening and reduction of As_nS_n ring center-center correlations at $r_3 \approx 5.2$ Å. However, the most distinguished difference compared to the As_2S_3 host glass are the additional correlations between 2.5 and 3.0 Å that are clearly increasing with the AgBr content. This region corresponds to Ag-Y first neighbor correlations, where Y = Br, S. Two types of silver-related nearest-neighbor distances, Ag-S (2.45-2.60 Å) and Ag-Br (2.67-2.77 Å), are known to exist in the above *r*-range in the vast majority of crystalline references and chalcohalide glasses.

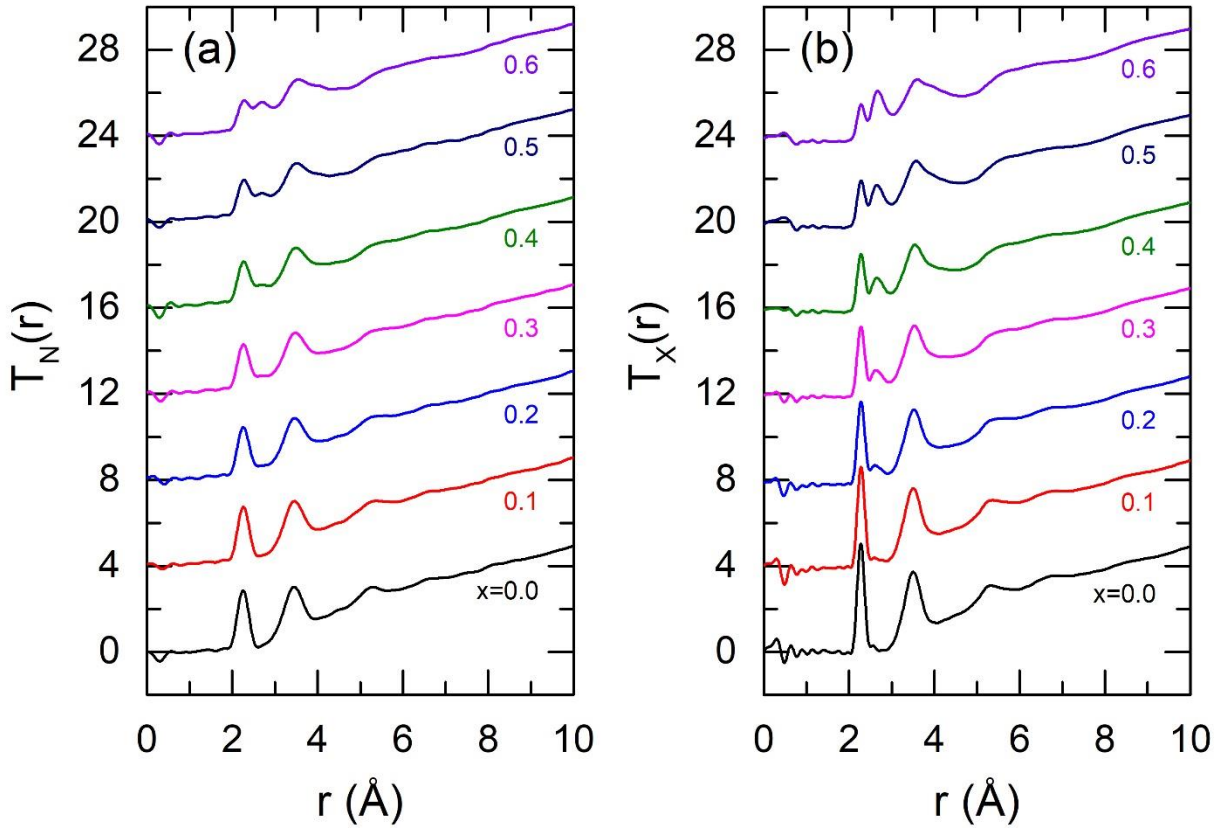

Figure III.33. (a) Neutron $T_N(r)$ and X-ray $T_X(r)$ total correlation functions for the $(AgBr)_x(As_2S_3)_{1-x}$ glasses, $0.0 \leq x \leq 0.6$.

The $T_X(r)$ of diluted glasses, especially for x = 0.01 or only 1 mol.% AgBr alloyed with g-As_2S_3, reveal unexpected changes between 2.5 and 3Å, **Figure III.34**.

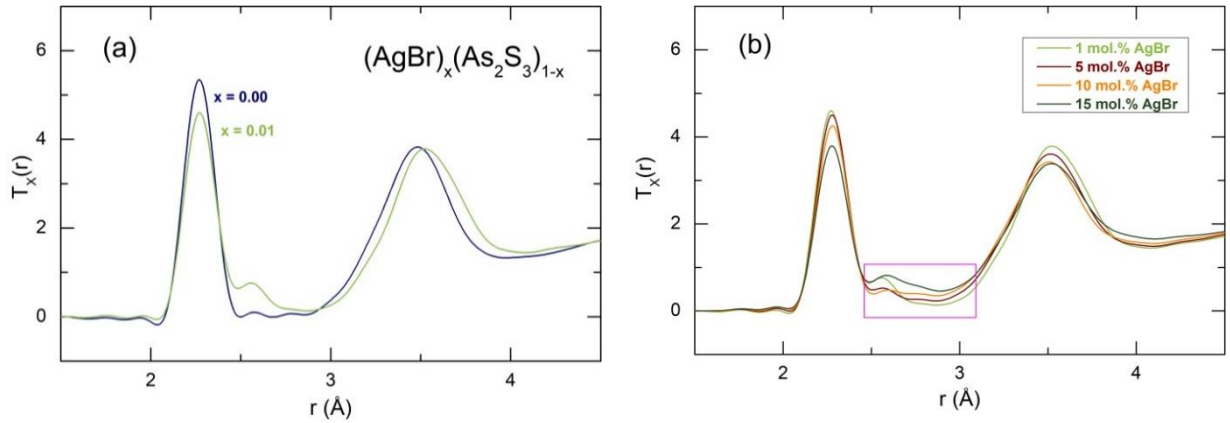

Figure III.34. (a) X-ray total correlation functions $T_X(r)$ for glassy As_2S_3 (blue) and $(AgBr)_{0.01}(As_2S_3)_{0.99}$ (light green) and (b) AgBr-As_2S_3 glasses containing 1, 5, 10 and 15% mol. % AgBr over a limited r-range, emphasizing structural features between 2.5 and 3.0 Å.

The As-S first neighbor peak at 2.27 Å has decreased in amplitude and a new feature emerges at ≈2.5 Å. This new contribution cannot be related to AgBr, since the corresponding Ag-X/Br-Y partial functions are very small for x = 0.01. The only reasonable hypothesis suggests the appearance of homopolar As-As bonds as a result of interactions between silver bromide and As-S glass network. A two-peak fitting confirms the trigonal arsenic coordination remains intact but about 10% of As form homopolar bonds. The XRD fitting results appear to be consistent with Raman data for AgBr-As_2S_3 glasses **(Figure III.35-37)** where the low-frequency features at 230 and 180 cm^{-1} are associated with As-As stretching. The chemical disorder exists in g-As_2S_3 but its magnitude (2-3 %) is at least by a factor of 3-4 smaller than that in glassy $(AgBr)_{0.01}(As_2S_3)_{0.99}$ (≈10%). The Raman data also indicate the magnitude of chemical disorder remains rather constant with increasing AgBr content. Consequently, further $T_N(r)$ and $T_X(r)$ analysis was carried out with the As-S and As-As coordination constraints.

Other diluted glasses, x = 0.05 and 0.10, have shown a systematic increase of r-space correlations in the vicinity of 2.75 Å, related to Ag-Br first neighbor contacts and a distinct threshold at about $x \approx 0.15$. We should, however, note that the Ag-Br coordination number appears to be low, $N_{Ag-Br} \lesssim 2$, implying mixed silver environment (Br + S) also suggested in Raman measurements and observed in MY-coordination polymers, where X = Cu, Ag and Y = Cl, Br, I [90]–[95]. Fitting the diluted glasses (x = 0.05 and 0.10) shows a better agreement with the 3:1 stoichiometry ratio (3S + 1Br nearest neighbors) while the concentrated vitreous alloys (x > 0.2) yield a better agreement with the 2:2 stoichiometry (2S + 2Br). The x = 0.15 glass shows an intermediate behavior. The fitting results are collected in **Table III.3** and presented in **Figure III.35-37**.

The use of two complementary data sets appears to be beneficial for $T(r)$ fitting in the $(AgBr)_x(As_2S_3)_{1-x}$ glasses. This is justified by the fact that neutron and X-ray weighting factors W_{ij} are distinctly different for these glasses (see, for example, **Figure III.36** representing the $T_X(r)$ and $T_N(r)$ analysis of $(AgBr)_{0.2}(As_2S_3)_{0.8}$ glass). The combined analysis of the two data sets allows reliably the mixed tetrahedral environment of Ag species to be determined **(Table III.3)**: the Ag-S nearest neighbors at 2.54±0.05 Å and Ag-Br atomic pairs at 2.71±0.02 Å. The multi-peak Gaussian fitting of $T(r)$ also shows a peak at ≈ 3.2 Å. The nature of this peak is not completely clear. In silver chalcogenide glasses the ≈3 Å peak is usually associated with short Ag-Ag correlations [87],

[88], [96], [97]. However, in our case this peak may contain many different contributions and its assignment to Ag-Ag second neighbor contacts is questionable.

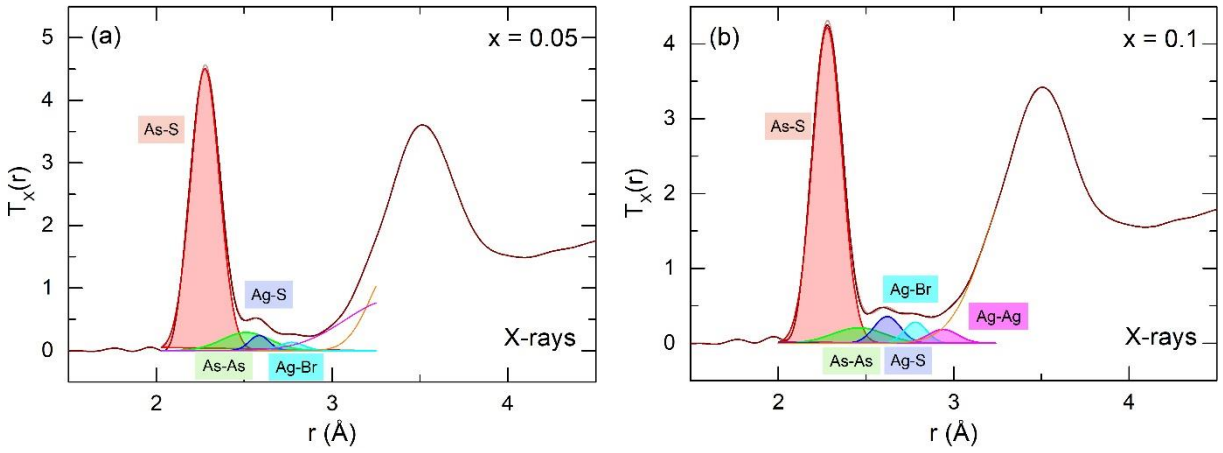

Figure III.35. Fitting X-ray $T_X(r)$ total correlation functions for the AgBr-As_2S_3 with x = 0.05 and 0.1 glass.

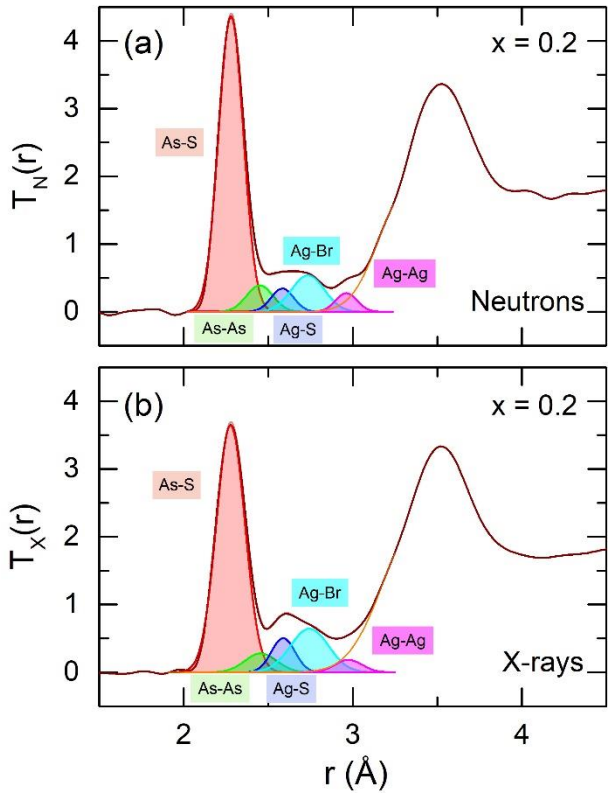

Figure III.36. Fitting (a) the neutron $T_N(r)$ and (b) X-ray $T_X(r)$ total correlation functions for the quasi-binary $(AgBr)_{0.2}(As_2S_3)_{0.8}$ glass.

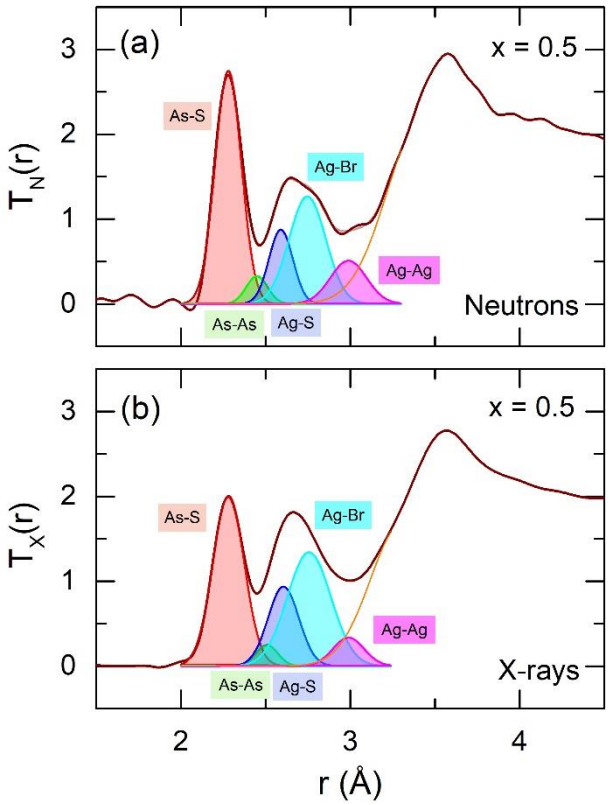

Figure III.37. Fitting (a) the neutron $T_N(r)$ and (b) X-ray $T_X(r)$ total correlation functions for the quasi-binary $(AgBr)_{0.5}(As_2S_3)_{0.5}$ glass.

Table III.3. Interatomic distances r_{ij} and coordination numbers N_{ij} for the $(AgBr)_x(As_2S_3)_{1-x}$ ($0.0 \leq x \leq 0.6$) glasses.

x	r(As-S) (Å)	N_{As-S}	r(As-As) (Å)	N_{As-As}	r(Ag-S) (Å)	N_{Ag-S}	r(Ag-Br) (Å)	N_{Ag-Br}
High-energy X-ray diffraction								
0.0	2.27	2.91			–	–	–	–
0.01	2.27	2.70	2.56	0.35				
0.05	2.27	2.75	2.51	0.31	2.58	3.05	2.77	1.01
0.10	2.27	2.75	2.45	0.25	2.62	3.05	2.78	0.98
0.15	2.27	2.76	2.52	0.25	2.59	2.53	2.74	1.48
0.20	2.27	2.73	2.45	0.24	2.58	1.99	2.74	2.00
0.25	2.27	2.74	2.52	0.25	2.60	2.03	2.75	2.03
0.30	2.27	2.74	2.56	0.25	2.58	1.98	2.75	2.00
0.35	2.28	2.75	2.52	0.25	2.60	2.02	2.75	2.00
0.40	2.28	2.76	2.51	0.25	2.61	2.03	2.76	2.01
0.45	2.28	2.75	2.51	0.25	2.61	2.03	2.76	2.00
0.5	2.28	2.76	2.50	0.25	2.60	2.03	2.75	2.00
0.6	2.28	2.76	2.52	0.25	2.61	2.04	2.75	2.00
Neutron diffraction								
0.0	2.25	3.03			–	–	–	–
0.1	2.24	2.75	2.39	0.24	2.58	2.95	2.77	0.99
0.2	2.24	2.74	2.41	0.24	2.58	2.00	2.77	2.02
0.3	2.24	2.74	2.41	0.24	2.52	1.95	2.74	1.99
0.4	2.24	2.74	2.38	0.24	2.51	1.96	2.73	1.99
0.5	2.24	2.75	2.38	0.24	2.51	1.99	2.72	1.98

0.6	2.24	2.74	2.38	0.24	2.52	2.00	2.72	1.98

Uncertainties in the As-S, As-As, Ag-S, Ag-I interatomic distances are ±0.01 Å, ±0.02 Å, ±0.02 Å, and ±0.03 Å, respectively. Uncertainties in the As-S, Ag-S, Ag-I coordination numbers are ±0.10, ±0.10, ±0.10, and ±0.15, respectively.

III.5.5.b The quasi-binary system: AgI-As_2S_3

❖ ***Q-space functions***

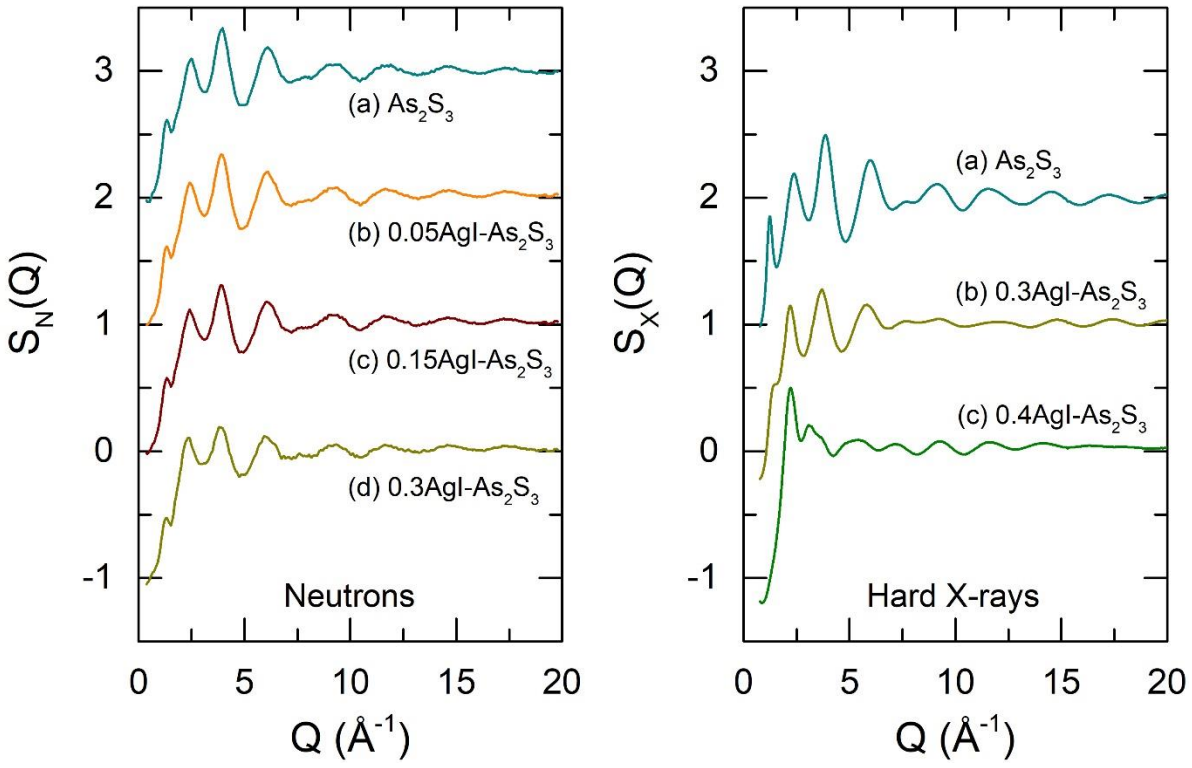

Figure III.38. Faber-Ziman (a) neutron $S_N(Q)$ and (b) X-ray $S_X(Q)$ structure factors for $(AgI)_x(As_2S_3)_{1-x}$ glasses, $0.0 \leq x \leq 0.4$.

Typical Faber-Ziman neutron $S_N(Q)$ and X-ray $S_X(Q)$ structural factors for the quasi-binary $(AgI)_x(As_2S_3)_{1-x}$ glasses, $0.0 \leq x \leq 0.4$, are shown in **Figure III.38**. They exhibit high-Q oscillations which are decreasing in amplitude with increasing AgI content, and shifting to lower Q. The FSDP Q_1 = 1.25 Å^{-1} decreases in intensity with increasing AgI concentration to disappear completely for x = 0.4. We should also note narrowing of the second peak in $S_X(Q)$ at ≈2.5 Å^{-1} and high-Q broadening of the peak at ≈3.85 Å^{-1} with the appearance of a distinct shoulder for x = 0.4 glass.

❖ ***Real-space functions***

Neutron and X-rays total correlation functions $T_N(r)$ and $T_X(r)$ of $(AgI)_x(As_2S_3)_{1-x}$ glasses, $0.0 \leq x \leq 0.4$, are shown in **Figure III.39**. They exhibit systematic changes with increasing AgI content x, especially in the range 2 Å $\leq r \leq$ 6 Å. As has been discussed for the AgBr-As_2S_3 glasses, the three characteristic peaks at $r_1 \approx 2.3$ Å, $r_2 \approx 3.5$ Å and $r_3 \approx 5.2$ Å are clearly identified. Similarly, the most distinguished differences compared to As_2S_3 host glass are the additional correlations between 2.5 and 3.0 Å, that are clearly increasing with silver iodide content. In this region, Ag-I and Ag-S first neighbor correlations exist, with the following nearest-neighbor distances: Ag-S (2.45-2.72 Å) and Ag-I (2.75-2.85 Å).

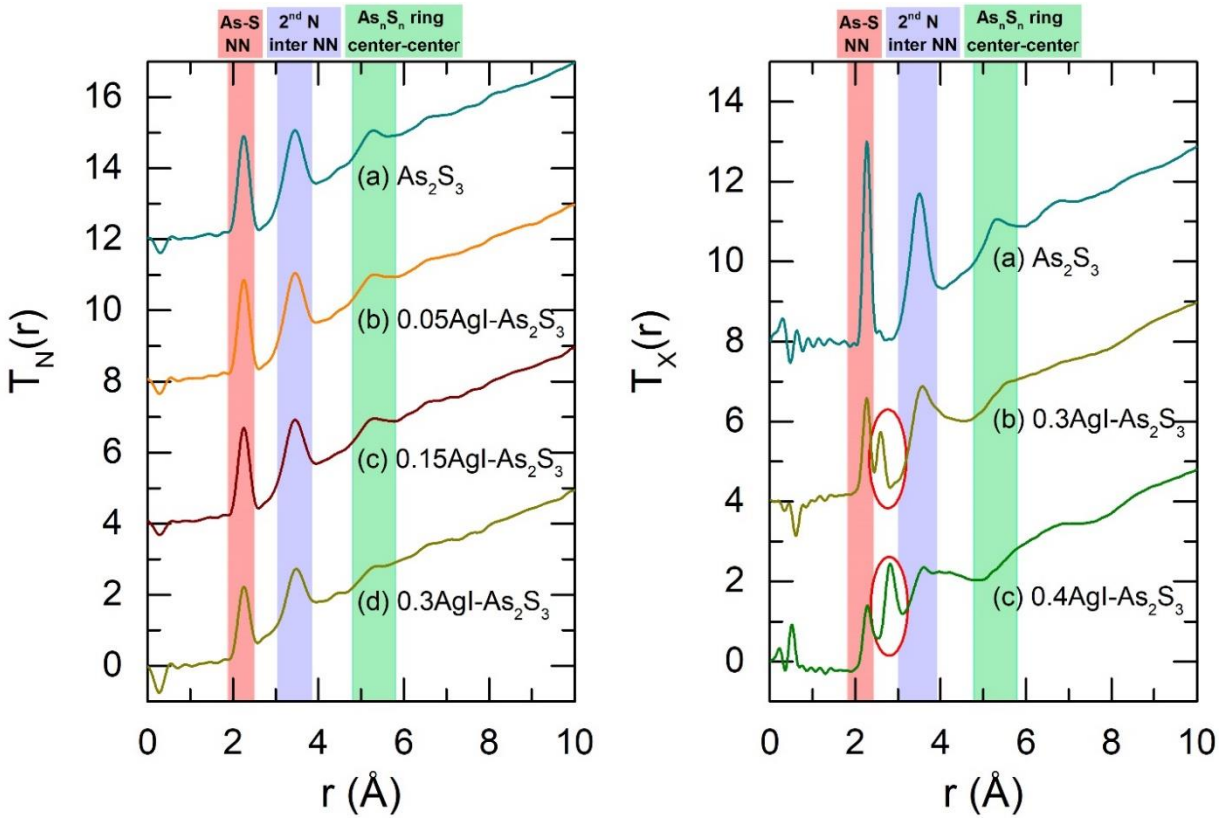

Figure III.39. Faber-Ziman (a) neutron $T_N(r)$ and (b) X-ray $T_X(r)$ total correlation functions for $(AgI)_x(As_2S_3)_{1-x}$ glasses, $0.0 \leq x \leq 0.4$.

The sensitivity of neutrons and X-rays to Ag-S correlations appears to be similar, W^X_{Ag-S}/W^N_{Ag-S} = 1.15, while X-rays are much more sensitive to Ag-I, W^X_{Ag-I}/W^N_{Ag-I} = 3.09, and to Ag-Ag correlations, W^X_{Ag-Ag}/W^N_{Ag-Ag} = 2.33. That's why, the Ag-I nearest neighbor contacts are more visible in $T_X(r)$. The combined analysis of the two data sets allows reliably identifying the mixed tetrahedral environment of sulfur and iodine around the Ag species **(Table III.4)**. The fitting

procedure was similar to that used in AgBr-As_2S_3 glasses. We also assume having 8-10% of As-As homopolar bonds. In this case, we have fixed As-S and As-As coordination numbers for all the concentrations, $N_{As-S} = 2.75$ and $N_{As-As} = 0.25$. Glass with x = 0.05 fits well with $N_{Ag-S} =$ 3 and N_{Ag-I}= 1. On the other hand, we tried 3 fittings for the glass with x = 0.15 in the intermediate region: N_{Ag-S}/N_{Ag-I} = 3/1, 2.5/1.5 and 2/2, and the first two are well fitted. However, for glasses in the modifier-controlled region, x = 0.30 and 40, we have fitted with N_{Ag-S}/N_{Ag-I} = 2:2.

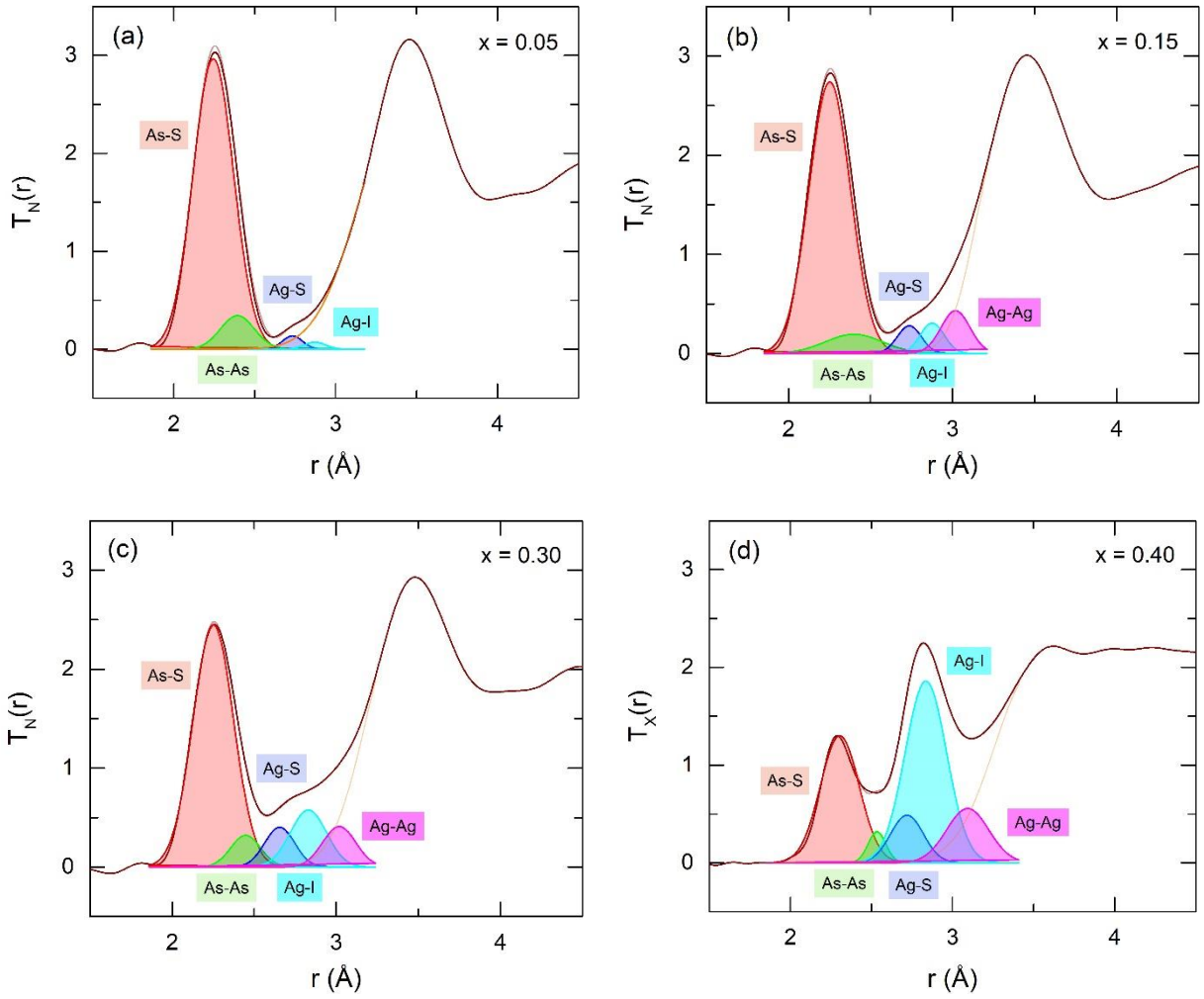

Figure III.40. Fitting (a) the neutron $T_N(r)$ and (b) X-ray $T_X(r)$ total correlation functions for the quasi-binary $(AgI)_x(As_2S_3)_{1-x}$ glass.

Table III.4. Interatomic distances r_{ij} and coordination numbers N_{ij} for the $(AgI)_x(As_2S_3)_{1-x}$ $(0.0 \leq x \leq 0.4)$ glasses.

x	r(As-S) (Å)	N_{As-S}	r(As-As) (Å)	N_{As-As}	r(Ag-S) (Å)	N_{Ag-S}	r(Ag-I) (Å)	N_{Ag-I}
High-energy x-ray diffraction								
0.40	2.30	2.76	2.53	0.25	2.71	2.00	2.83	2.02
Neutron diffraction								
0.05	2.24	2.71	2.39	0.25	2.73	3.14	2.87	1.01
0.15	2.25	2.74	2.39	0.24	2.73	2.46	2.87	1.53
0.30	2.25	2.74	2.44	0.25	2.65	2.02	2.83	2.02

III.5.5.c ab initio Molecular Dynamics Modelling AIMD of AgY-As_2S_3 glasses

In order to verify the main structural details of our HE-XRD and ND studies for AgY-As_2S_3 glasses, we started *ab initio* molecular dynamics simulations using a combined RMC/DFT approach [98], [99] carried out by Dr. A. Sokolov and Dr. D. Fontanari. As a first step, randomly generated initial configuration of 940 atoms for $(AgI)_{0.1}(As_2S_3)_{0.9}$ (critical percolation domain) or of 1050 atoms for $(AgBr)_{0.5}(As_2S_3)_{0.5}$ (modifier-controlled region) were optimized using RMC_POT++ code [100] to obtain a good agreement with neutron and high-energy X-ray diffraction results. Further optimization procedure has been carried out at 0K by DFT (Density Functional Theory) using CP2K 5.0 package [101] in a parallel environment. Calculations have been performed employing the GGA exchange-correlation functional PBEsol [102] and the consecutive basis sets SZV, DZVP and TZVP. The optimized DFT configurations were used for AIMD simulations which are running now above T_g (10 ps at 500 K for $(AgI)_{0.1}(As_2S_3)_{0.9}$ and 4 ps at 450 K for $(AgBr)_{0.5}(As_2S_3)_{0.5}$). The two simulations are expected to reach an equilibrium at high temperatures, presumably, after 30-50 ps. The simulation boxes will be then quenched to room temperature and equilibrated at 300 K. The current state of the simulations is briefly summarized below.

$(AgBr)_{0.5}(As_2S_3)_{0.5}$ simulation

Typical snapshot of a 1050-atom simulation box for $(AgBr)_{0.5}(As_2S_3)_{0.5}$ glass is shown in **Figure III.41**. The initial RMC configuration was completely random but the DFT modelling led to a phase separation clearly visible in **Figure III.41** and consistent with SANS and SEM results.

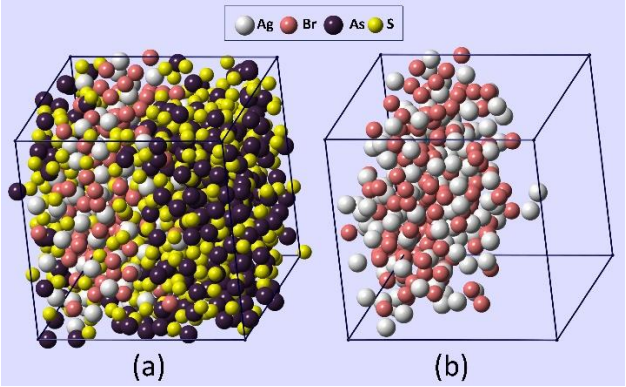

Figure III.41. (a) Typical snapshot of a AIMD simulation box showing a clear heterogeneity in atomic distributions for glassy $(AgBr)_{0.5}(As_2S_3)_{0.5}$; (b) simulation box but without As and S atoms.

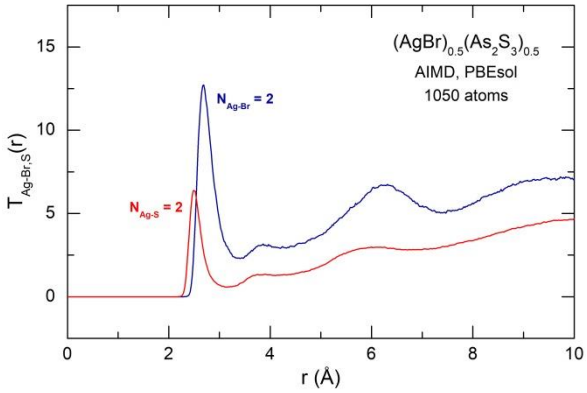

Figure III.42. The average total correlation functions $T_{Ag-Br,S}(r)$ calculated using a simulation box containing 1050 atoms.

The calculated Ag-Br and Ag-S partial correlation functions $T_{Ag-Br}(r)$ and $T_{Ag-S}(r)$, shown in **Figure III.42**, reveal mixed tetrahedral silver environment with 2Br and 2S nearest neighbors in accordance with the $T(r)$ analysis of the experimental ND and HE-XRD results.

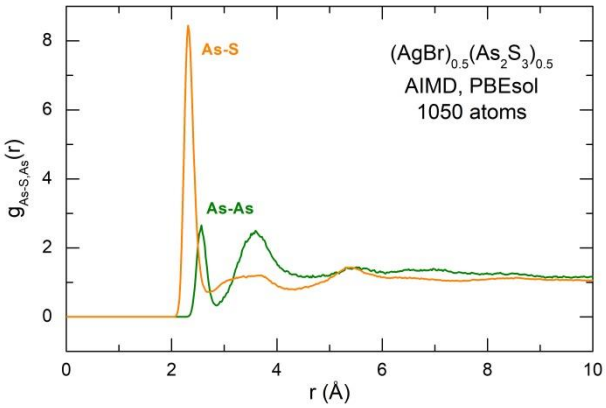

Figure III.43. Partial pair-distribution functions $g_{As-S}(r)$ and $g_{As-As}(r)$ for glassy $(AgBr)_{0.5}(As_2S_3)_{0.5}$.

We should also note the As-S and As-As partial pair-distribution functions confirm chemical disorder in glassy glassy $(AgBr)_{0.5}(As_2S_3)_{0.5}$ **(Figure III.43)**. The derived coordination numbers are, however, slightly different from the experimental values: N_{As-S} = 2.34 and N_{As-As} = 0.52.

(AgI)$_{0.1}$(As$_2$S$_3$)$_{0.9}$ simulation

The AIMD simulation box for glassy (AgI)$_{0.1}$(As$_2$S$_3$)$_{0.9}$ does not show any phase separation. The Ag- and As-related partials reveal some similarities and differences compared with those for glassy (AgBr)$_{0.5}$(As$_2$S$_3$)$_{0.5}$.

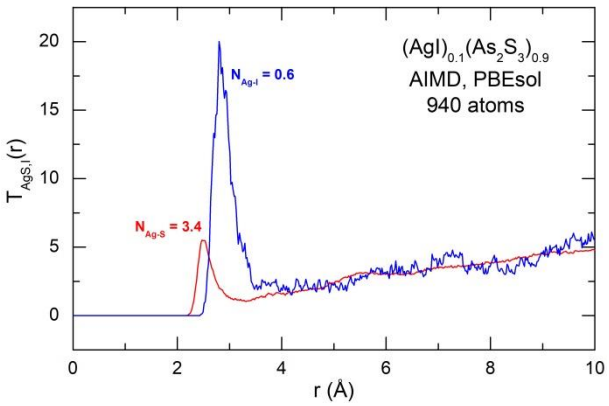

Figure III.44. The Ag-I and Ag-S partial correlation functions $T_{Ag-I}(r)$ and $T_{Ag-S}(r)$ for glassy (AgI)$_{0.1}$(As$_2$S$_3$)$_{0.9}$, derived using the initial steps in AIMD simulations.

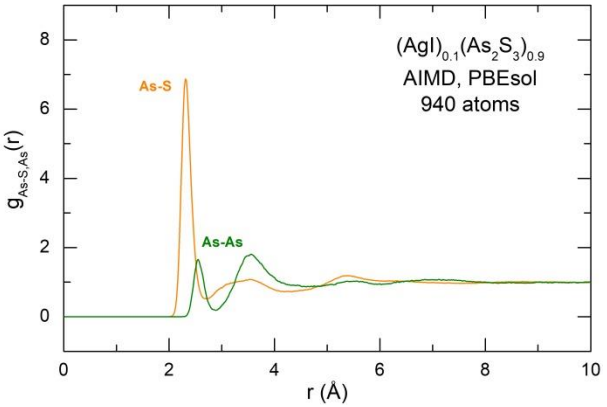

Figure III.45. The As-S and As-As partial pair-distribution functions $g_{As-S}(r)$ and $g_{As-As}(r)$ for glassy (AgI)$_{0.1}$(As$_2$S$_3$)$_{0.9}$, derived using the initial steps in AIMD simulations.

Silver also exhibits mixed tetrahedral environment but with different stoichiometry; N_{Ag-S} = 3.4 and N_{Ag-I} = 0.6, **Figure III.44**. These results are similar to the derived experimental values for diluted glasses. The remaining iodine atoms are mainly connected to arsenic. **Figure III.45** shows that the (AgI)$_{0.1}$(As$_2$S$_3$)$_{0.9}$ glass reveals identical chemical disorder to glassy (AgBr)$_{0.5}$(As$_2$S$_3$)$_{0.5}$: N_{As-S} = 2.33 and N_{As-As} = 0.49 and exceeds the experimentally determined As-As coordination number N_{As-As} ≈ 0.25-0.30. We should however emphasize that the AIMD simulations are not yet finished and the final results might be different from the above values.

III.5.5.d The quasi-binary system: HgS-GeS$_2$

- ***Q-space functions***

Typical neutron $S_N(Q)$ and X-ray $S_X(Q)$ structure factors of mercury thiogermanate glasses (HgS)$_x$(GeS$_2$)$_{1-x}$, 0.0 ≤ x ≤ 0.5, are shown in **Figure III.46**. We have chosen to work within the domain Q_{max} = 40 Å^{-1} for pulsed neutrons (GEM), and Q_{max} = 30 Å^{-1} for X-rays (APS). In both ND and HE-XRD, the $S(Q)$ for the vitreous matrix GeS$_2$ glass (x = 0.0) is very similar to that in

the literature [76]. One also observes a distinct high-Q oscillations and a pronounced FSDP at Q_1 ≈ 1.0 Å^{-1}.

In order to extract the FSDP parameters, a Voigt function was used to approximate the background underneath the FSDP in $S(Q)$ at low Q, allowing the FSDP to be isolated and fitted **(Figure III.47)**. The FSDP at Q_1 corresponds to Ge-Ge correlations at the characteristic distance $L_1 = 2\pi/Q_1 \approx$ 6 Å. Mercury sulfide additions to vitreous germanium sulfide change the GeS_2 structure factor. High-Q oscillations amplitude decreases with increasing *x*. However, the most distinguished changes occur in the low-Q region, < 2 Å^{-1}.

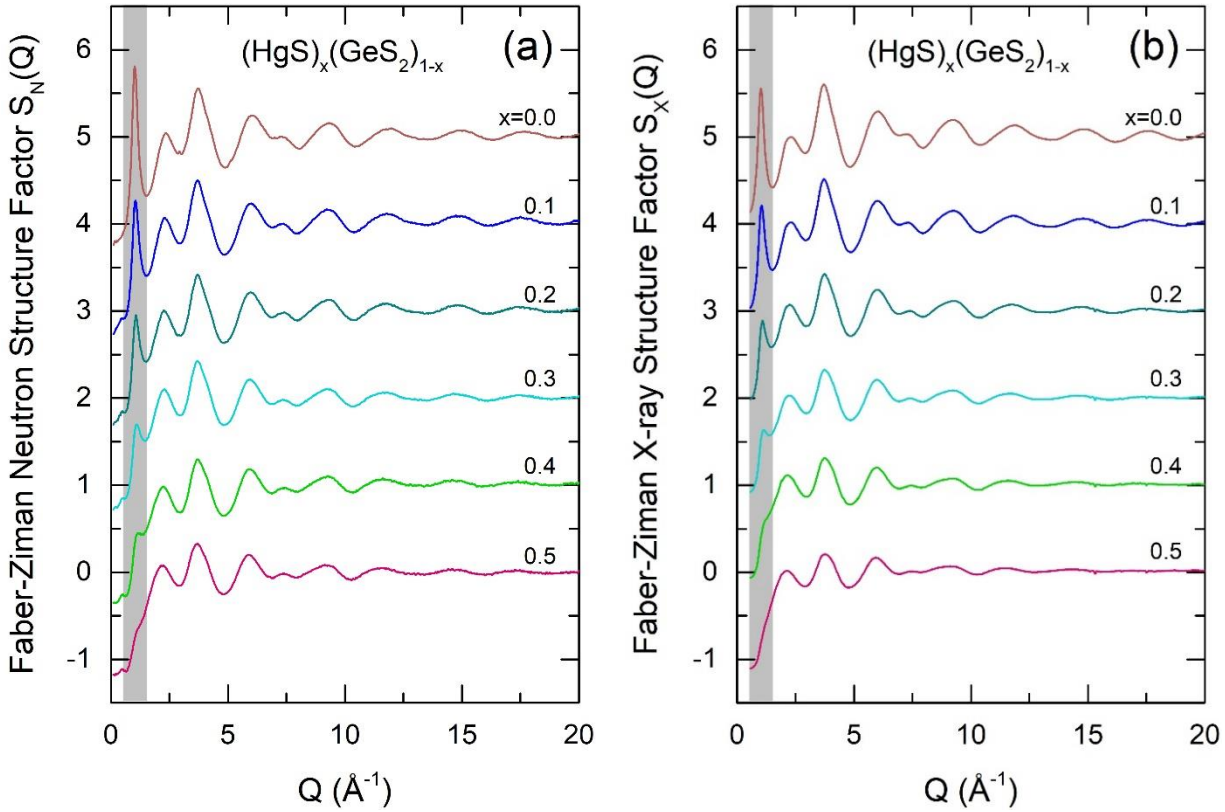

Figure III.46. Faber-Ziman (a) neutron $S_N(Q)$ and (b) X-ray $S_X(Q)$ structure factors for the quasi-binary $(HgS)_x(GeS_2)_{1-x}$ glasses, $0.0 \leq x \leq 0.5$.

The intensity of FSDP at $Q_1 \approx 1.0$ Å^{-1} decreases with increasing *x* **(Figure III.47)** and this is partly caused by the heavy element Hg (Z_{Hg} = 80) in the $(HgS)_x(GeS_2)_{1-x}$ glasses because the Ge-Ge weighting factor $w_{Ge\text{-}Ge}$ (Z_{Ge} = 32) decreases with increasing the average atomic number <*Z*>. The decrease in intensity is also coherent with the decrease in the glass transition temperatures for the $(HgS)_x(GeS_2)_{1-x}$ glasses with increasing *x* (Chapter I – **Figure I.21**).

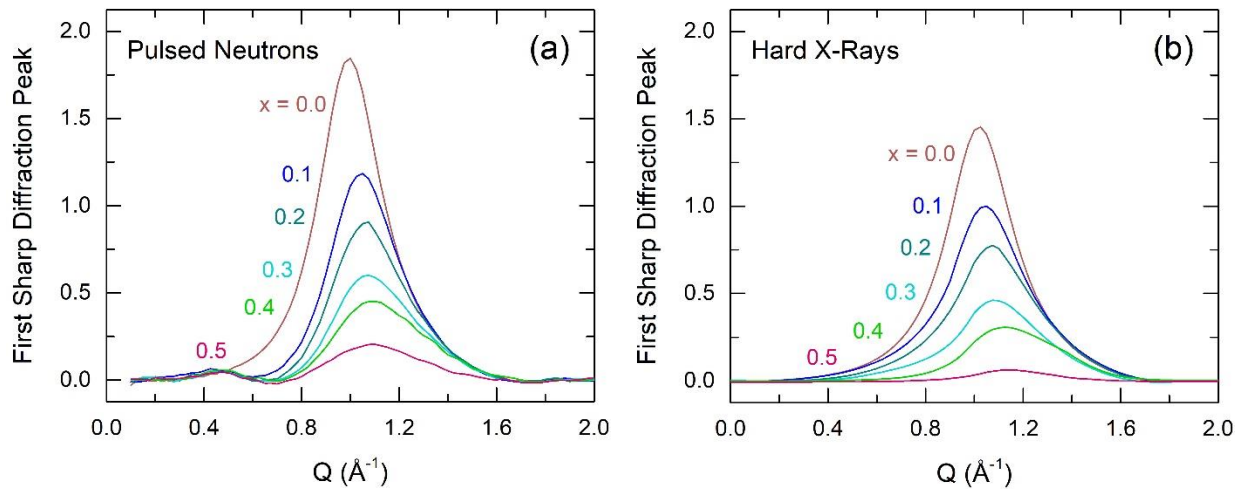

Figure III.47. Isolated FSDPs obtained with (a) pulsed neutron and (b) X-rays techniques for the $(HgS)_x(GeS_2)_{1-x}$ binary glasses, $0.0 \leq x \leq 0.5$.

Figure III.48(a,b) shows the position (Q_1) and area (A_1) of the FSDP for the quasi-binary $(HgS)_x(GeS_2)_{1-x}$ system, $0.0 \leq x \leq 0.5$, as a function of HgS fraction, respectively. The FSDP area A_1, related to Ge-Ge correlations, decreases linearly with increasing x. This indicates a gradual disappearance of the intermediate-range order in the HgS-GeS_2 glasses. Its amplitude in neutron data is slightly higher than that of X-rays, consistent with neutron and X-ray Ge-Ge weighting factors in the mercury thiogermanate glasses, $1.47 \leq \frac{W^N_{Ge-Ge}}{W^X_{Ge-Ge}} \leq 2.08$. The FSDP position ($Q_1$) increase with x from 1.03±0.005 Å^{-1} to 1.14±0.03 Å^{-1}.

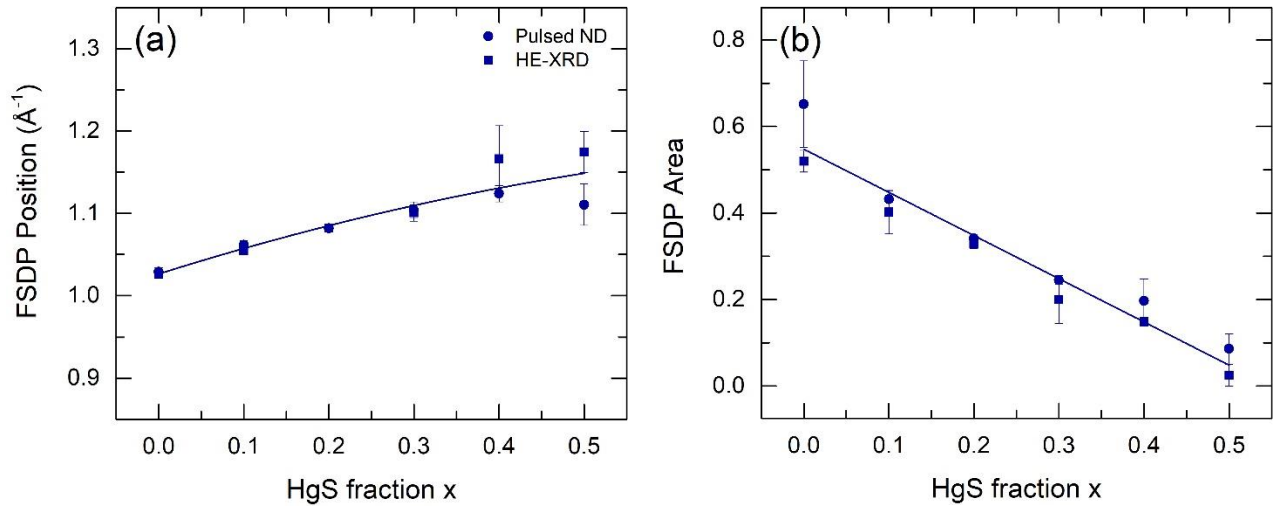

Figure III.48. FSDP (a) position (Q_1) and (b) area (A_1) obtained, with both (●) ND and (■) HE-XRD techniques, for the $(HgS)_x(GeS_2)_{1-x}$ binary glasses, $0.0 \leq x \leq 0.5$.

❖ ***Real-space functions***

Neutron and X-ray total correlation functions $T_N(r)$ and $T_X(r)$ were derived through the usual Fourier transform using the Lorch modification function. The results are shown in **Figure III.49**. The correlation functions for the vitreous matrix GeS_2 glass (x = 0.0), in both ND and HE-XRD, are comparable to those reported in literature [76].

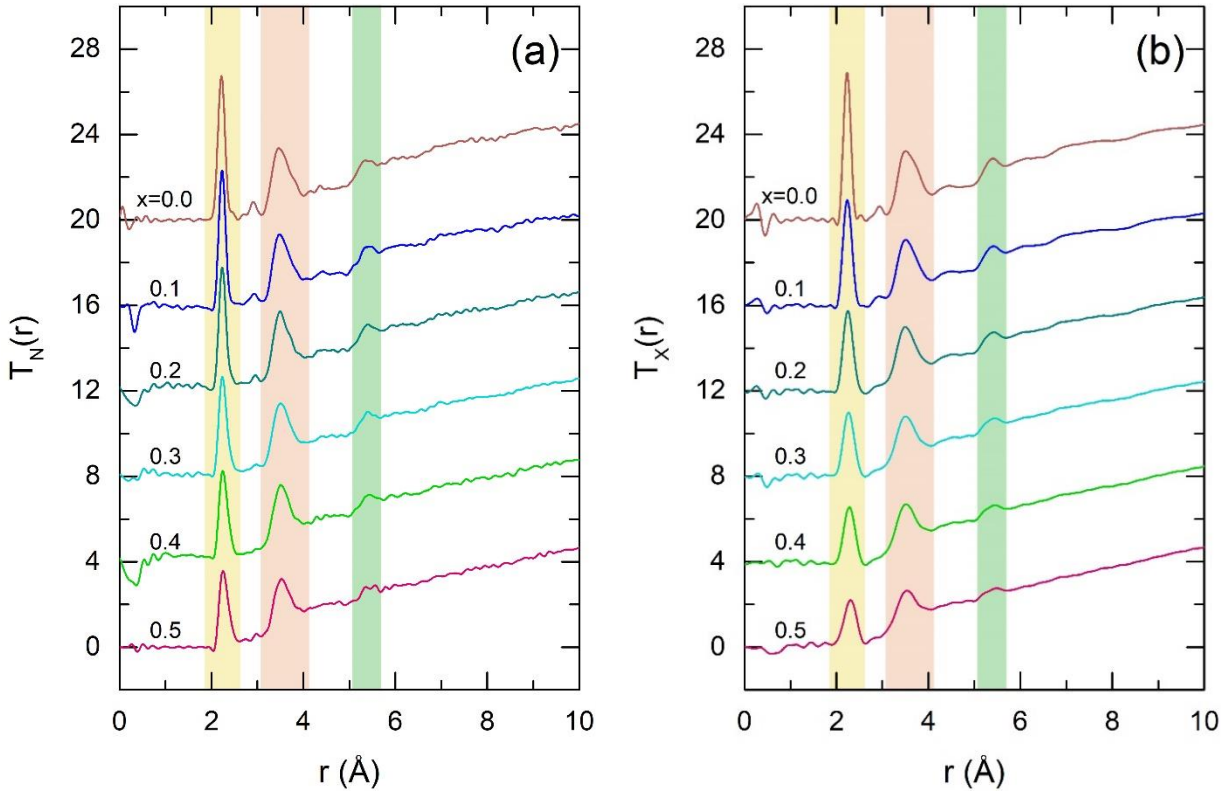

Figure III.49. (a) Neutron $T_N(r)$ and (b) X-ray $T_X(r)$ total correlation functions for the quasi-binary $(HgS)_x(GeS_2)_{1-x}$ glasses. The first neighbor peak ≈2.2, the second neighbor peak at ≈3.5, and the Ge_nS_n center–center correlations at ≈5.2 are highlighted in yellow, pink and green, respectively.

The first peak at ≈2.22 Å in glassy GeS_2 corresponds to Ge-S first neighbours. The peak at 2.90 Å is related to short Ge-Ge correlations in ES-$GeS_{4/2}$, and a broad feature at ≈3.5 Å reflects second-neighbour Ge-Ge contacts in CS-$GeS_{4/2}$, S-S and Ge-S correlations. More distant narrow peak at ≈5.4 Å and a broad bimodal feature at ≈7.2 Å are associated with the ring structure in g-GeS_2 [103].

The total correlation functions for binary glasses exhibit systematic changes with increasing HgS content x, especially in the range 2 Å ≤ r ≤ 5 Å. The peak at 2.22 Å decreases and distinct high-r broadening is observed with increasing x **(Figure III.49)**. This broadening is expected, since the

Hg-S distance in trigonal cinnabar α-HgS is 2.38 Å [104] and that in cubic metacinnabar β-HgS is 2.54 Å [105]. Also, with increasing HgS content, a broad and shallow feature appears at ≈4 Å. This change is expected, since the second neighbor correlations at 4 Å ≤ r ≤ 5 Å exist both in α- and β-HgS. Finally, the feature at 5.2 Å broadens and becomes less intense with increasing x.

Fitting the first peak in $T_N(r)$ and $T_X(r)$ with two Gaussians yields $N_{Ge-S} \approx 4$ and $N_{Hg-S} \geq 2$; the Hg-S coordination increases with x. In other words, the 4-fold coordination mercury species appear in the glass network. On the contrary, the tetrahedral germanium coordination remains intact. The fit quality was found to deteriorate with x since $r(\mathrm{Hg}_{4F} - \mathrm{S}) > r(\mathrm{Hg}_{2F} - \mathrm{S})$; 2.54 vs. 2.38 Å in crystalline β- and α-HgS, respectively. The derived fitting parameters, estimated to be too loose, dictated the addition of some constraints. Consequently, as for HgS-As_2S_3 glasses, a three-peak fitting **(Figure III.50)** was necessary with the following constraint on Hg_{2F}-S and Hg_{4F}-S peak areas:

$$2 - \frac{C_{Hg}^{2F}}{w_{\mathrm{Hg-S}}} = \frac{1}{2}\frac{C_{Hg}^{4F}}{w_{\mathrm{Hg-S}}}, \qquad \text{(III.11)}$$

where C_{Hg}^{2F} and C_{Hg}^{4F} are the peak areas corresponding to 2-fold and 4-fold coordinated mercury, $w_{\mathrm{Hg-S}}$ is the neutron or X-ray Hg-S weighting factor.

The obtained partial coordination numbers $N_{\mathrm{Hg-S}}^{2F}$ and $N_{\mathrm{Hg-S}}^{4F}$ were used to calculate the fraction of 4-fold coordinated mercury species f_{Hg}^{4F}:

$$f_{\mathrm{Hg}}^{4F} = \frac{N_{\mathrm{Hg-S}}^{4F}}{4} = 1 - \frac{N_{\mathrm{Hg-S}}^{2F}}{2} \qquad \text{(III.12)}$$

The f_{Hg}^{4F} fraction increases monotonically with mercury sulfide content **(Figure III.51)** reaching $f_{\mathrm{Hg}}^{4F} \approx 0.30$ for equimolar HgS/GeS_2 composition (x = 0.5). The two Hg-S distances decrease with increasing x: 2.30 Å ≤ $r(\mathrm{Hg}_{2F} - \mathrm{S})$ ≤ 2.33 Å, and 2.41 Å ≤ $r(\mathrm{Hg}_{4F} - \mathrm{S})$ ≤ 2.45 Å. Both distances distance appear to be distinctly shorter than $r(\mathrm{Hg}_{4F} - \mathrm{S})$ = 2.54 Å and $r(\mathrm{Hg}_{2F} - \mathrm{S})$ = 2.38 Å in cubic metacinnabar β-HgS and chain-like cinnabar α-HgS, respectively. Likewise, the Ge-S first neighbor separation decreases slightly with increasing x from 2.23 Å (x = 0.0) to 2.19 Å (x = 0.5). The fitting results are given in **Table III.5**.

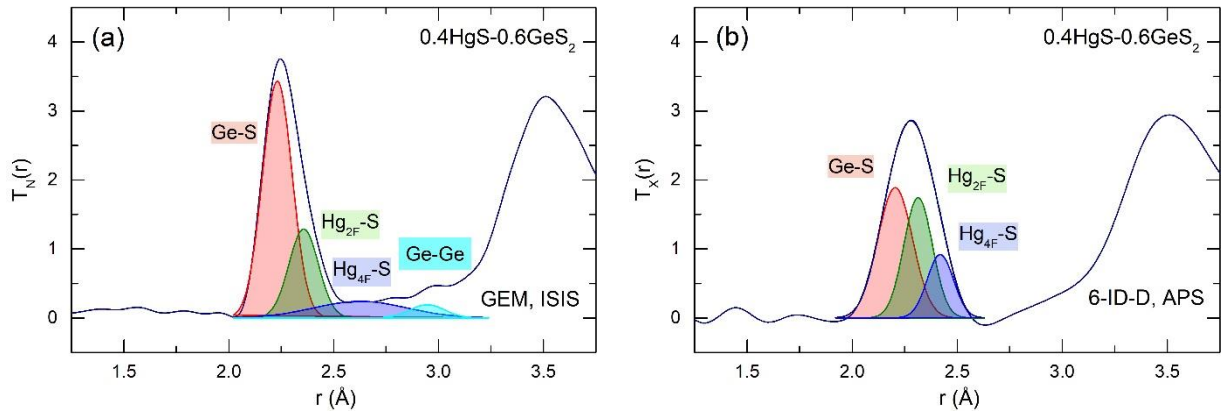

Figure III.50. Three-peak fitting of the first feature in (a) neutron $T_N(r)$ and (b) X-ray $T_X(r)$ total correlation functions for the $x = 0.4$ glass. The Ge–S, 2-fold Hg_{2F}–S, and 4-fold Hg_{4F}–S correlations are highlighted in red, green, and blue, respectively.

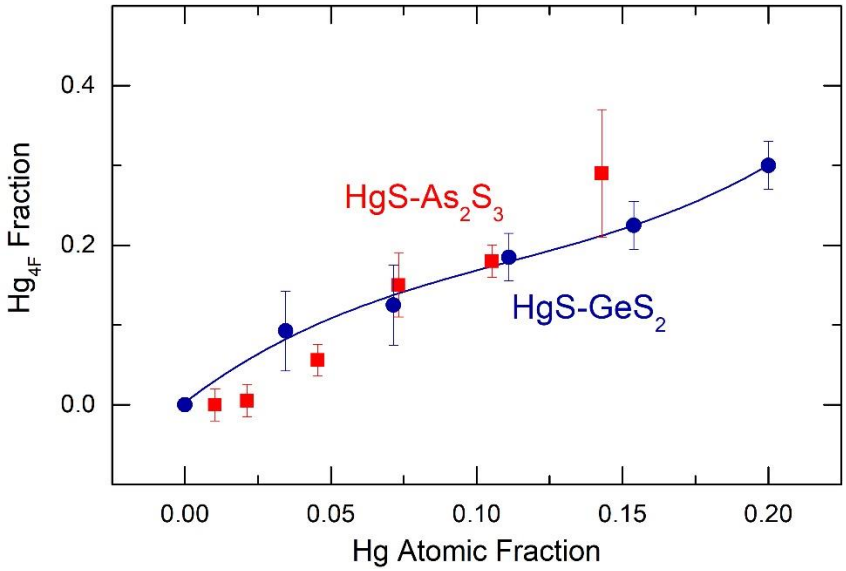

Figure III.51. Fraction of 4-fold coordinated mercury f_{Hg}^{4F} shown for neutrons and X-rays (average values) for HgS-GeS_2 glasses, together with HgS-As_2S_3 glasses plotted as a function of Hg atomic fraction. The line is drawn as a guide to the eye.

Table III.5. Interatomic distances r_{ij} and coordination numbers N_{ij} for the quasi-binary $(HgS)_x(GeS_2)_{1-x}$ glasses, $0.0 \leq x \leq 0.5$.

HgS Fraction x	$r(Ge-S)$ (Å)	$N_{\text{Ge-S}}$	$r(\text{Hg}_{2F}-\text{S})$ (Å)	$N_{\text{Hg-S}}^{2F}$	$r(\text{Hg}_{4F}-\text{S})$ (Å)	$N_{\text{Hg-S}}^{4F}$
Neutron diffraction						
0.0	2.22(1)	3.98(10)	-	-	-	-
0.1	2.23(1)	3.98(10)	2.37(1)	2.06(10)		
0.2	2.23(1)	4.01(10)	2.36(1)	1.70(10)	2.66(4)	0.61(10)
0.3	2.23(1)	3.93(10)	2.35(2)	1.60(10)	2.54(2)	0.78(10)
0.4	2.23(1)	3.96(10)	2.36(1)	1.51(10)	2.63(4)	0.99(10)
0.5	2.23(1)	3.89(10)	2.34(2)	1.40(10)	2.44(2)	1.17(10)
High-energy X-ray diffraction						
0.0	2.23(1)	4.00(10)	-	-	-	-
0.1	2.23(1)	3.89(10)	2.33(3)	1.80(10)	2.45(2)	0.38(10)
0.2	2.22(1)	3.96(10)	2.33(3)	1.83(10)	2.43(2)	0.40(10)
0.3	2.21(1)	3.88(10)	2.32(3)	1.67(10)	2.42(2)	0.68(10)
0.4	2.20(1)	3.88(10)	2.31(4)	1.62(10)	2.42(2)	0.82(10)
0.5	2.19(1)	3.89(10)	2.30(4)	1.46(10)	2.41(2)	1.26(10)

III.5.5.e Monoclinic Hg_4GeS_6 and crystallization of HgS-GeS_2 glasses

The monoclinic lattice of Hg_4GeS_6, space group Cc [106], consists of isolated $GeS_{4/2}$ tetrahedra connected via corner-sharing $HgS_{4/4}$ units, **Figure III.52**. One third of sulphur species are only connected to mercury similar to that in other crystals of argyrodite family [107]. Both $GeS_{4/2}$ and $HgS_{4/4}$ tetrahedra are distorted. The Ge-S units have three short, 2.101±0.022 Å, and one longer, 2.252±0.050 Å, Ge-S interatomic distances. The difference in the nearest-neighbor separations is even bigger for Hg-S atomic pairs: 2.46±0.04 Å (44%) vs. 2.69±0.12 Å (56%).

(a) (b)

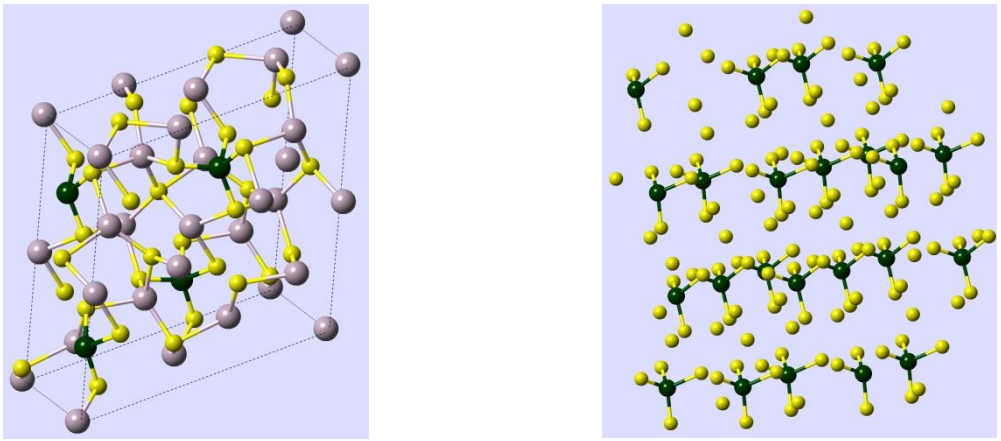

Figure III.52. (a) The elementary cell of monoclinic Hg_4GeS_6 [106], consisting of $GeS_{4/2}$ and $HgS_{4/4}$ tetrahedra. One third of sulphur species are only connected to mercury, as it is shown for (b) the Ge-S sublattice with omitted Hg species.

Glassy/crystalline $(HgS)_{0.6}(GeS_2)_{0.4}$ exhibits Bragg peaks, corresponding to monoclinic Hg_4GeS_6, **Figure III.53**. The PDF analysis of the corresponding X-ray structure factor shows a close resemblance between the two structures, **Figure III.54**.

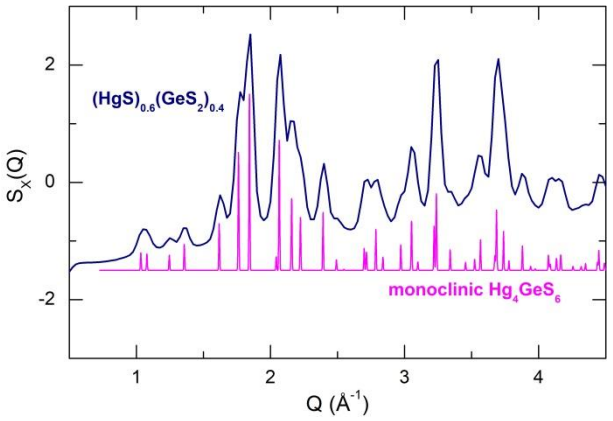

Figure III.53. A low-Q part of the X-ray structure factor for a $(HgS)_{0.6}(GeS2)_{0.4}$ glassy/crystalline alloy showing the Bragg peaks of monoclinic Hg_4GeS_6 [106].

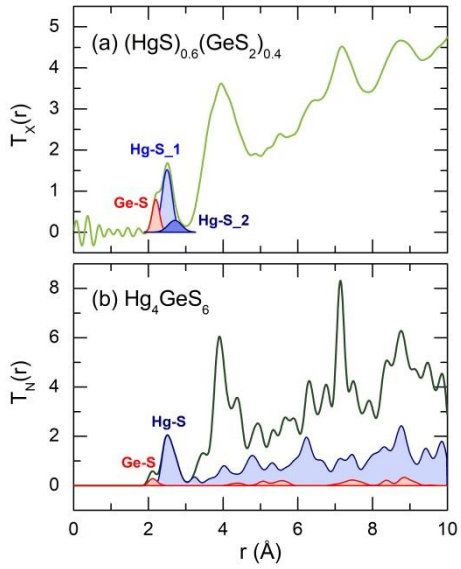

Figure III.54. (a) Derived $T_X(r)$ for $(HgS)_{0.6}(GeS2)_{0.4}$ and (b) calculated $T_N(r)$ for monoclinic Hg_4GeS_6 [106] using the XTAL program [108].

The most intense peaks in both derived $T_X(r)$ for $(HgS)_{0.6}(GeS2)_{0.4}$ and calculated $T_N(r)$ for monoclinic Hg_4GeS_6 [106] corresponding to Hg-Hg correlations are clearly visible at ≈4, ≈7 and ≈9 Å. The Ge-S (highlighted in red) and Hg-S (blue) first neighbor correlations are asymmetric for $(HgS)_{0.6}(GeS2)_{0.4}$ and Hg_4GeS_6, **Figure III.54**. Short (2.50 Å) and longer Hg-S (2.70 Å) contributions can be distinguished for $(HgS)_{0.6}(GeS2)_{0.4}$ in accordance with crystal data. The glassy/crystalline alloy shows essentially the 4-fold coordination for mercury species, $N_{\mathrm{Hg-S}}$ = 3.94±0.20, in contrast to $HgS\text{-}GeS_2$ glasses.

III.5.5.f The pseudo-ternary system: AgI-HgS-GeS₂

- ***Q-space functions***

The obtained Faber-Ziman X-ray $S_X(Q)$ structural factors for the pseudo-ternary $(AgI)_x(HgS)_{0.5-x/2}(GeS_2)_{0.5-x/2}$ glasses, $0.0 \leq x \leq 0.6$, are shown in **Figure III.55**. One observes essentially four changes with increasing silver iodide content *x*. (1) The high- and medium-Q oscillations shift to lower Q; thus indicating an increase of average interatomic distances. (2) The peak at 2.11 $Å^{-1}$ sharpens. (3) The amplitudes of the peaks at ≈ 2.11, 3.7 and 5.9 $Å^{-1}$ change non-systematically and shift strongly to lower Q. (4) The FSDP at Q_1≈ 1.0 $Å^{-1}$ characteristic for equimolar $HgS\text{-}GeS_2$ matrix glass (x = 0) disappears nearly completely with increasing AgI. It is related to Ge-Ge periodicity reflecting the intermediate-range order in the glass network formed by Ge_nS_n rings of different size *n* [86], [109], [110].

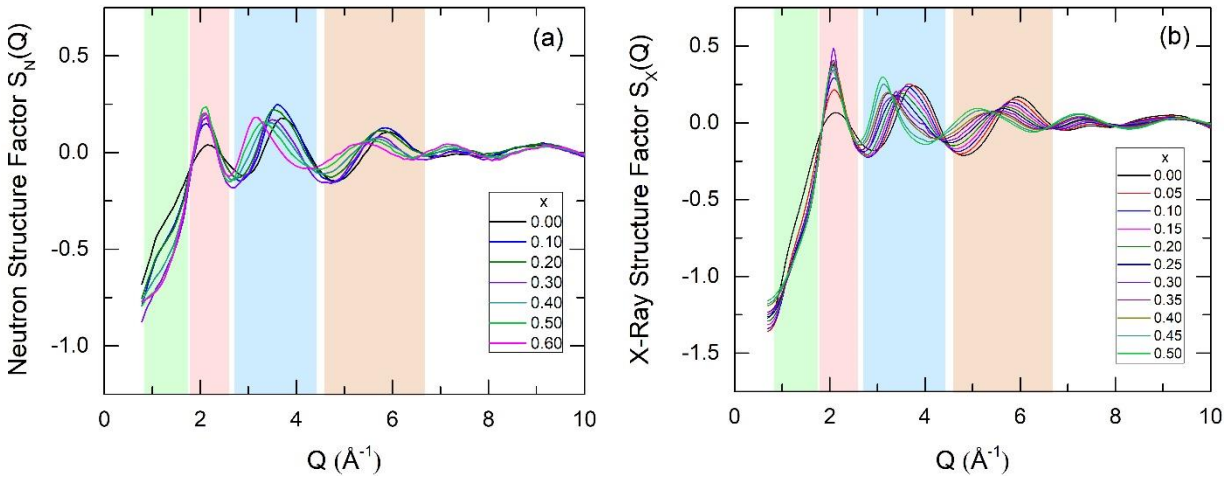

Figure III.55. Faber-Ziman (a) neutron $S_N(Q)$ and (b) X-ray $S_X(Q)$ structure factors for silver mercury thiogermanate glasses $(AgI)_x(HgS)_{0.5-x/2}(GeS_2)_{0.5-x/2}$, $0.0 \leq x \leq 0.6$, shown over a limited Q-range. Remarkable changes in the low-Q region below 2 Å^{-1} are highlighted in green.

❖ ***Real-space functions***

Typical total correlation functions $T_X(r)$ and $T_N(r)$ for the $(AgI)_x(HgS)_{0.5-x/2}(GeS_2)_{0.5-x/2}$ glasses are shown in **Figure III.56**. They exhibit a characteristic and systematic evolution as a function of the glass composition. With increasing silver iodide content *x*, one observes that (i) the broad unresolved first peak at ≈2.2 Å decreases rapidly in amplitude associated with the decreasing Ge content, shifts to higher interatomic distances with a simultaneous asymmetric broadening at high-*r* side, (ii) a new structural feature appears at ≈2.80 Å and grows monotonically, (iii) the second neighbor correlations (Ge-Ge contacts in corner-sharing CS-$GeS_{4/2}$ units, S-S and Ge-S separations) at ≈3.6 Å diminish, show a high-*r* broadening and finally develop broad features at ≈4.10 and 4.47 Å, and (iv) a broad band at ≈5.4 Å associated with the ring structure in g-GeS_2 disappear with increasing *x* confirming the fragmentation of the continuous Ge-S subnetwork.

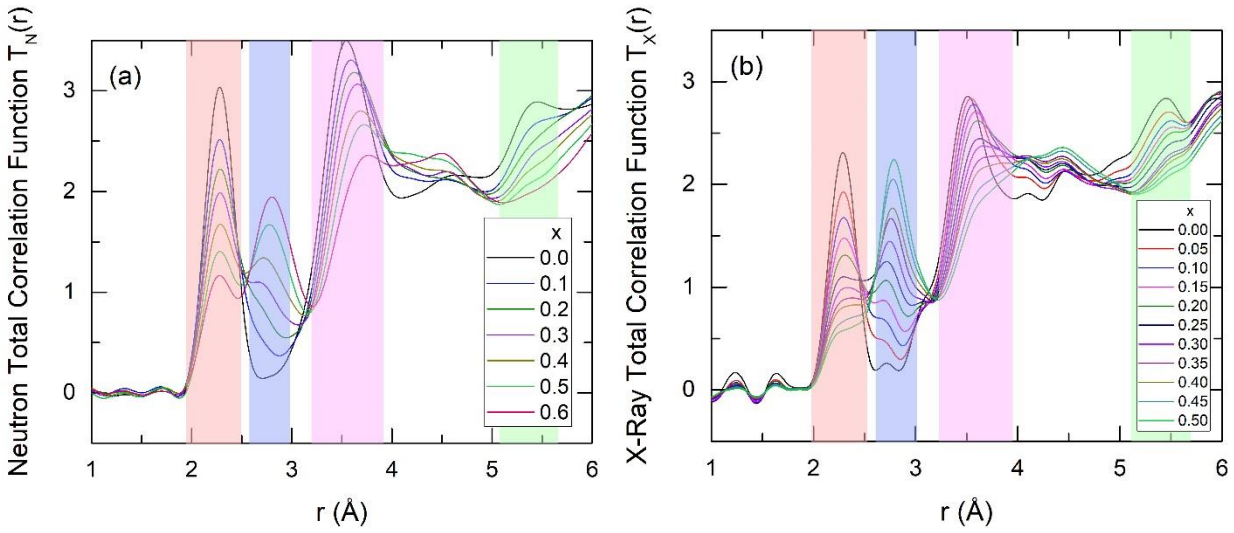

Figure III.56. Faber-Ziman (a) neutron $T_N(r)$ and (b) X-ray $T_X(r)$ total correlation functions for $(AgI)_x(HgS)_{0.5-x/2}(GeS_2)_{0.5-x/2}$ glasses, $0.0 \leq x \leq 0.6$.

Despite the apparent complexity of the first nearest neighbour correlations in a 5-component quasi-ternary glass, the structural knowledge of its quasi-binary parents allows the structural analysis to be realised rather smoothly. (A) The peak at $r_1 \approx 2.2$ Å which corresponds to Ge-S nearest neighbour correlations, highlighted in light pink in **Figure III.56**, remains intact over the entire glass-forming range. (B) The Hg-S nearest neighbor correlations appear at about $r_2 \approx 2.38$ Å and the Hg-S coordination number is expected to be $N_{Hg-S} \geq 2$. (C) The silver species form pure AgI_4 or mixed AgI_nS_{4-n} tetrahedra characterized by Ag-I and Ag-S distances highlighted in blue, $r_{Ag-I} \approx 2.8$ Å and $r_{Ag-S} \approx 2.5$ Å. Taking this structural hypothesis as a basis of $T_X(r)$ and $T_N(r)$ fitting, we have got consistent fitting results, characterized by excellent goodness-of-fit. (D) GeS_2 as well as the host matrix $(HgS)_{0.5}(GeS_2)_{0.5}$ reveal a peak at ≈ 2.9 Å associated with short Ge-Ge second neighbour correlations in edge-sharing ES-$GeS_{4/2}$ tetrahedra [76]. This peak disappears with increasing *x* and becomes substituted by a new emerging and growing peak at $r \approx 3.0$ Å related to Ag-Ag second neighbour contacts.

Typical fitting procedure of the total correlation functions is shown in **Figure III.57**, and the fitting results are summarized in **Table III.6**.

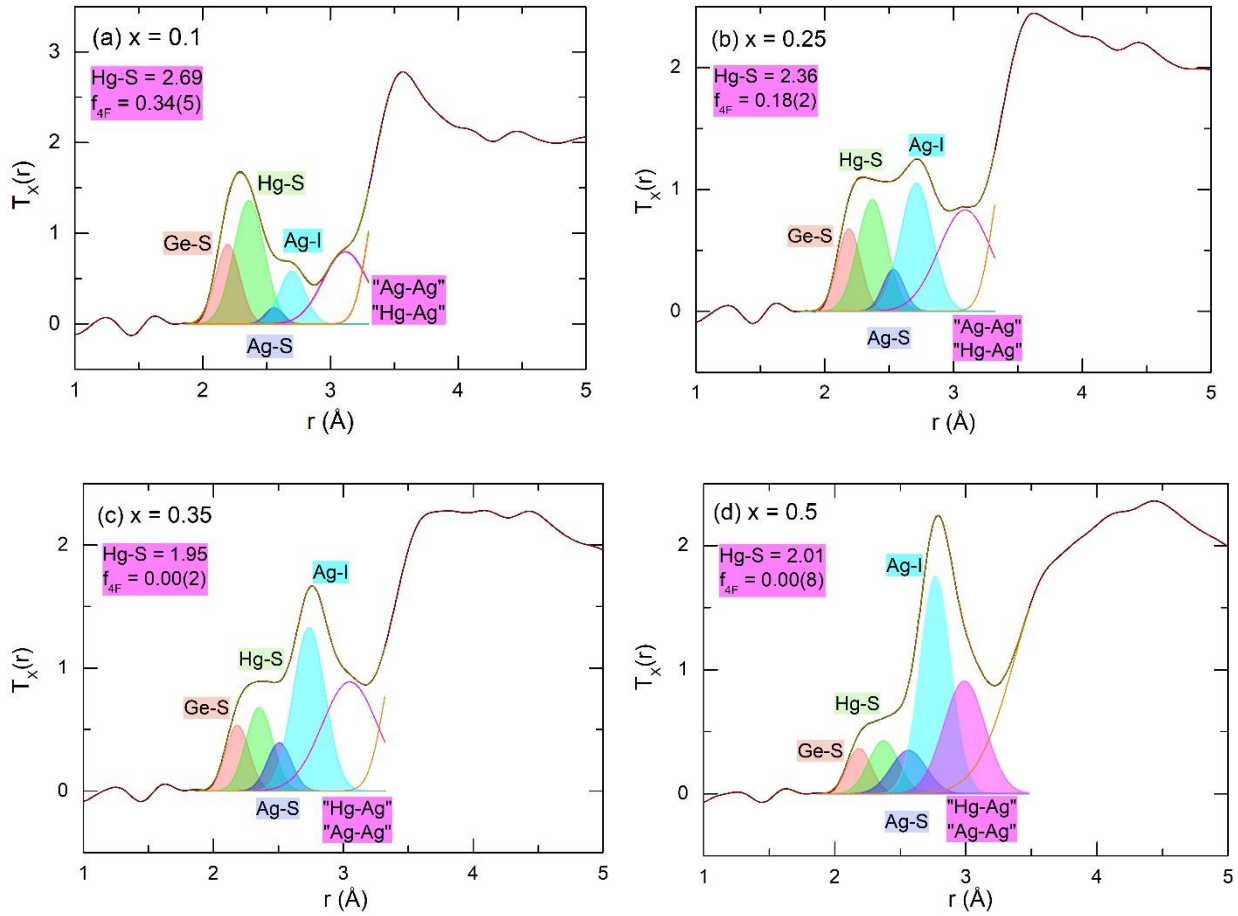

Figure III.57. Attribution of correlations in HE-XRD total correlation functions for the pseudo-ternary glasses, with (a) x =0.1, (b) x =0.25, (c) x =0.35, and (d) x =0.5. The boxes in magenta include the values of f_{Hg}^{4F}.

Table III.6. Interatomic distances r_{ij} and coordination numbers N_{ij} for the pseudo-ternary $(AgI)_x(HgS)_{0.5-x/2}(GeS_2)_{0.5-x/2}$ glasses, $0.0 \leq x \leq 0.5$.

AgI Fraction	Ge-S		Hg-S*		Ag-S		Ag-I	
	r_{ij} (Å)	N_{ij}	r_{ij} (Å)	N_{ij}	r_{ij} (Å)	N_{ij}	r_{ij} (Å)	N_{ij}
High-energy X-ray diffraction								
0.00	2.18	3.96			-	-	-	-
0.10	2.19	4.00	2.36	2.69	2.56	2.00	2.70	2.00
0.20	2.19	4.00	2.36	2.54	2.53	2.01	2.71	2.00
0.30	2.18	4.00	2.36	2.06	2.51	1.99	2.72	1.99
0.40	2.18	3.98	2.36	2.00	2.53	1.99	2.75	1.99
0.50	2.18	4.00	2.37	2.01	2.56	2.02	2.76	2.01
Neutron diffraction								
0.00								
0.10	2.25	4.04	2.45	2.73	2.73	2.18	2.87	2.09
0.20	2.23	4.02	2.45	2.47	2.66	2.06	2.81	2.03
0.30	2.23	4.01	2.43	2.05	2.65	2.05	2.79	2.06
0.40	2.22	4.01	2.41	1.97	2.62	2.05	2.79	2.00
0.50	2.21	3.99	2.41	1.99	2.65	2.07	2.81	2.01
0.6	2.21	3.97	2.40	1.99	2.659	2.07	2.83	2.02

Uncertainties in the Ge-S, Hg-S, Ag-S, Ag-I interatomic distances are ±0.01 Å, ±0.02 Å, ±0.02 Å, and ±0.03 Å, respectively. Uncertainties in the Ge-S, Hg-S, Ag-S, Ag-I coordination numbers are ±0.10, ±0.10, ±0.15, and ±0.10, respectively.

*average data for 2-fold and 4-fold coordinated mercury

Over the composition range $0.05 \leq x \leq 0.50$, the short-range of $(AgI)_x(HgS)_{0.5-x/2}(As_2S_3)_{0.5-x/2}$ glasses is formed by $GeS_{4/2}$ tetrahedra, $(HgS_{2/2})_n$ chains, $HgS_{4/4}$ and $AgI_{2/2}S_{2/2}$ tetrahedra **(Table III.6)**. Direct fitting the quasi-ternary glasses does not allow distinguishing between 2-fold and 4-fold coordinated mercury. Instead, an average structural feature is obtained whose peak area

reflects the 4-fold coordinated mercury fraction f_{Hg}^{4F}, if $N_{Hg\text{-}S}$> 2. In the quasi-binary $(HgS)_x(GeS_2)_{1-x}$ system, f_{Hg}^{4F} increases with increasing HgS content ($f_{Hg}^{4F} \approx 0.44$ for equimolar HgS/GeS_2 composition (x = 0.5)), suggesting the formation of agglomerated $HgS_{4/4}$ tetrahedral clusters for HgS-rich glasses at $x > 0.3$. The trend is reversed with increasing silver iodide content in the pseudo-ternary $(AgI)_x(HgS)_{0.5-x/2}(GeS_2)_{0.5-x/2}$ system. The coordination number $N_{Hg\text{-}S}$ decreases from 2.65 (x = 0.0) to 2.06 (x = 0.30), this is clearly related to the decrease of 4-fold coordinated mercury fraction f_{Hg}^{4F}. For $x \geq 0.3$, $HgS_{4/4\ 2}$ tetrahedra do not exist any longer. Yet, the atomic structure is governed by 2-fold coordinated mercury sulfide Hg_{2F}-S (helical $(HgS_{2/2})_n$ chains) like in HgS-poor glasses.

After identifying the short-range order in the $(AgI)_x(HgS)_{0.5-x/2}(GeS_2)_{0.5-x/2}$ glasses, the next question concerns the connectivity of AgI-related structural units. AIMD modelling of glassy $(AgI)_{0.1}(As_2S_3)_{0.9}$ **(Figure III.44)** shows that the major part of silver iodide exists as isolated AgI monomers in the glass, connected in average to three sulfur atoms of the host matrix. The Ag-related units are distributed more or less randomly in the glass network. For the pseudo-ternary $(AgI)_x(HgS)_{0.5-x/2}(GeS_2)_{0.5-x/2}$ glasses with $x \leq 0.1$ (AgI-poor glasses), we cannot clearly identify the connectivity of Ag-related units since the amplitude of Ag-Ag correlation at 3.1-3.2 Å, a key parameter for AgI-related connectivity, is strongly affected by Hg-related second neighbor correlations.

Nevertheless, the ternary AgI-rich glasses ($x \geq 0.3$) are fitted better with $N_{Ag\text{-}Ag} \geq 2$ than with $N_{Ag\text{-}Ag} = 1$, i.e., the previously isolated $AgI_{2/2}S_{2/2}$ mixed tetrahedra form $AgI_{2/2}S_{2/2}$-related chains above x = 0.2. The electrical conductivity measurements of these pseudo-ternary glasses as well as their transport regimes confirm our conclusion. The AgI-poor glasses ($x \leq 0.1$) in both systems belong to critical percolation domain. From structural point of view, the critical percolation regime is characterized by a random mobile cation distribution, and the diffraction data (isolated $AgIS_3$ monomers or ES-$Ag_2I_2S_{4/2}$ dimers) are consistent with ionic transport properties. At higher $x > 0.1$, the power-law compositional dependence of ionic conductivity, $\sigma_i(x) \propto x^{t(T)}$, changes to an exponential growth, $\sigma_i(x) \propto \exp(x)$, and a modifier-controlled regime. The modifier controlled regime is characterized by a non-random mobile cation distribution. The $AgI_{2/2}S_{2/2}$-related chains, forming preferential conduction pathways, seem to be a clear structural basis of this transport regime.

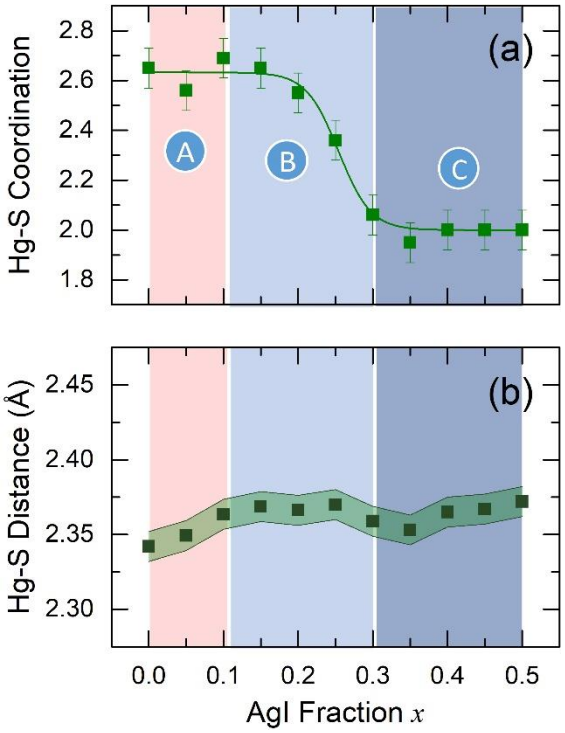

Figure III.58. (a) Total N_{Hg-S} mercury coordination number vs AgI fraction and (b) Hg-S interatomic distance in the AgI-HgS-GeS_2 glasses.

A new variable which we have mentioned previously and it is necessary to discuss further is the $N_{\text{Hg-S}}$. **Figure III.58(a)** shows that $N_{\text{Hg-S}}$ decreases as a function of AgI content, even though the Hg/Ge remains 1:1. And at $x \approx 0.3$, corresponding to a ratio of Hg/Ag ≈ 1, $N_{\text{Hg-S}}$ becomes roughly ≈2, i.e., a completely 2-fold coordinated Hg species (Hg_{2F}-S). This change is reflected in the (i) change of slope in ionic conductivity in the modifier-controlled region at $x \approx 0.3$, the conductivity increase continues but at a lower rate; and (ii) non-systematic changes in the structure factor and total correlation functions.

To sum up, the ionic conductivity measurements reveals four distinct composition trends: (i) the critical percolation below 2-4 at.% Ag, and (ii) the modifier-controlled regime at higher silver content, x > 4 at.% Ag, which is divided into three regions; they differ by their local structure. In the intermediate region ($5 < x \leq 12$ at.% Ag), there exists a mixed coordination of Hg (Hg_{2F}-S and Hg_{4F}-S). However, in the high-AgI region ($12 < x \leq 22$ at.% Ag), only chain structure of Hg exists. Finally, at the limit of glass-forming region, (x > 22 at.% Ag), it shows a plateau at the level of conductivity. One already notices here some fragile behavior because it is very sensitive to crystallization, evidenced by the appearance of AgI micro/nano-crystals in DSC measurements.

III.6 Structural differences between critical percolation and modifier-controlled domains and the structural role of silver halides in AgY-As_2S_3 glasses

III.6.1 Critical percolation vs modifier-controlled regime

The contrasting composition dependences of ionic conductivity in the critical percolation and modifier-controlled domains suggest structural differences in diluted and Ag-rich glasses. A random distribution of silver species at $x \leq 2$ at.% Ag looks reasonable, confirmed by small-angle neutron scattering of homogeneous Ag_2S-As_2S_3 glasses belonging to the both regions [39]. A common mesoscopic feature of the two glass series was density fluctuations with a characteristic Debye-Bueche correlation distance of 160±15 Å, similar to those observed for the $(AgBr)_{0.2}(As_2S_3)_{0.8}$ sample, **Figure III.5**. However, the Ag-related difference scattering functions[1], $\Delta I_{Ag}(Q)/\sum_i(x_i\bar{b}_i)^2$, appear to be different for Ag-poor and Ag-rich glasses, reflecting homogeneous silver distribution in the critical percolation domain and some Ag clustering in the modifier-controlled region [39]. A non-random silver distribution in Ag-rich glasses was observed in numerous diffraction studies of silver chalcogenide glasses, revealed by short Ag-Ag correlations at 3 Å [87], [88], [96], [97], [111]. This characteristic Ag-Ag separation appears to be shorter than that calculated assuming a random silver distribution, e.g. using a Wigner-Seitz type Eq. (II.26). Consequently, some local glass zones have higher silver content than the other, giving rise to a modified glass network [112], widely used for description of cation-rich vitreous alloys [113]–[116].

[1] The Ag-related difference scattering functions, $\Delta I_{Ag}(Q)/\sum_i(x_i\bar{b}_i)^2$, were obtained by subtraction of the weighted scattering function $I_{As_2S_3}(Q)/\sum_i(x_i\bar{b}_i)^2$ for the glassy host from the scattering functions $I_{Ag_2S-As_2S_3}(Q)/\sum_i(x_i\bar{b}_i)^2$ for the Ag_2S-As_2S_3 glasses. The experimental $I(Q)$'s before subtraction were normalized by the average coherent scattering cross-section $\sum_i(x_i\bar{b}_i)^2$, where x_i and $\bar{b}_i$ are the atomic fraction and neutron coherent scattering length of atom i, respectively.

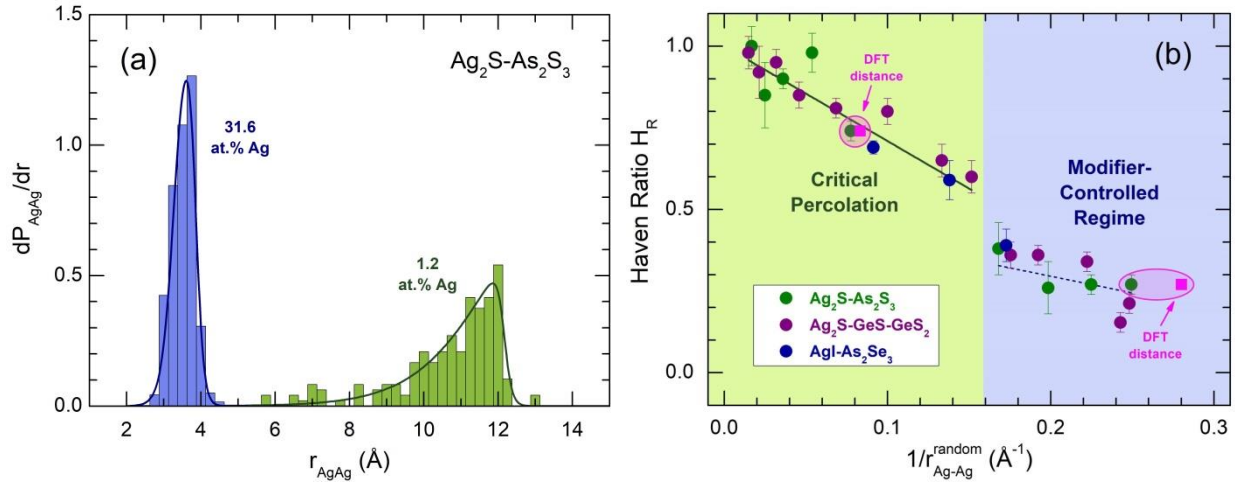

Figure III.59. (a) Connectivity analysis of Ag-Ag distributions in the x = 1.2 at.% Ag (critical percolation region) and x = 31.6 at.% Ag (modifier-controlled domain) glasses. The analyzed DFT data correspond to the average values of 10 simulation boxes containing either 988 (x = 1.2 at.% Ag) or 1007 (x = 31.6 at.% Ag) silver, arsenic and sulfur atoms. (b) The Haven ratio H_R in Ag_2S-As_2S_3, Ag_2S-GeS-GeS_2, and AgI-As_2Se_3 glasses [96], [117], [118] plotted as a function of reciprocal Ag-Ag distance, calculated assuming a random distribution of silver. The solid magenta squares show the H_R for the x = 1.2 and 31.6 at.% Ag glasses plotted using the derived Ag-Ag distances from DFT modelling. The solid line in **Figure III.59** (b) represents the result of a least-square fit of the experimental data points to Eq. (II.25) . All other lines are drawn as a guide to the eye.

We have used a DFT structural modelling of two Ag_2S-As_2S_3 glasses (unpublished results of Dr D Fontanari and Dr A Sokolov) to obtain quantitative estimations of Ag-Ag separation distances in the critical percolation domain (x = 1.2 at.% Ag) and modifier-controlled region (x = 31.6 at.% Ag). **Figure III.59(a)** shows a connectivity analysis of DFT simulation boxes for the two glasses. The derivative of the bound silver fraction, [2] $\partial P_{\mathrm{AgAg}}(r)/\partial r$, for the 1.2 at.% Ag glass is centered at ≈12 Å, indicating that the average derived Ag-Ag separation appears to be nearly identical to that calculated for a random silver distribution. In contrast, a $\partial P_{\mathrm{AgAg}}(r)/\partial r$ maximum for the 31.6 at.% Ag glass arises at shorter distances than expected for random distribution, in accordance with the reported diffraction data for silver-rich chalcogenide glasses [87], [88], [96], [97], [111] and recent *ab initio* MD modelling of $(Ag_2S)_{0.5}(As_2S_3)_{0.5}$ glass [119]. The derived DFT distances were used to plot the Haven ratio H_R of the two Ag_2S-As_2S_3 compositions. **Figure III.59(b)** shows the

[2] The bound silver fraction $P_{\mathrm{AgAg}}(r)$ is defined as a fraction of silver species having at least one nearest or distant neighbour at the distance r.

Haven ratio for Ag_2S-As_2S_3, Ag_2S-GeS-GeS_2 and AgI-As_2Se_3 glasses [96], [117], [118] plotted as a function of $(r_{Ag-Ag})^{-1}$, calculated assuming a random distribution of silver. The H_R in the critical percolation domain follows Eq. (II.25) while the transition to the modified-controlled region is accompanied by a step-like decrease of the Haven ratio from H_R = 0.5-0.6 to H_R = 0.3-0.4. This non-monotonic behavior was assumed to be related to a change in the silver distribution: (i) random in the critical percolation domain, and (ii) non-random in the modifier-controlled region. The Haven ratio for the 1.2 at.% Ag glass, plotted using the derived DFT distance, is located at the regression line following Eq. (II.25). On the contrary, the H_R for the 31.6 at.% Ag composition is shifted to higher $(r_{Ag-Ag})^{-1}$, since the derived Ag-Ag separation is shorter than that for random distribution. The latter result also raises a question whether Eq. (II.25) has a wider applicability. In other words, the change in H_R in the modifier-controlled region also follows Eq. (II.25) but it is related to real Ag-Ag distances which can be found using structural modelling.

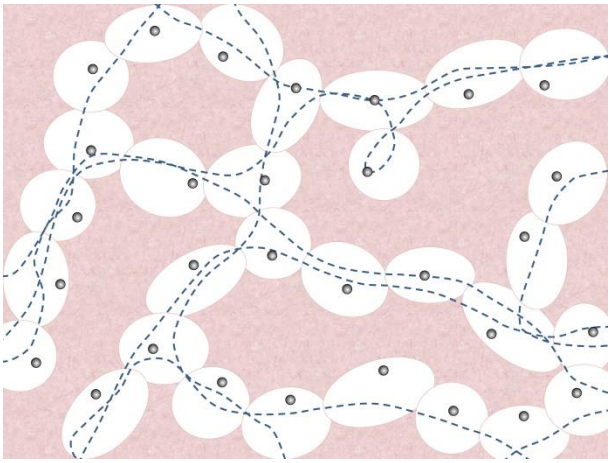

Figure III.60. Schematic representation of infinite percolation clusters in the critical percolation domain. Previously isolated allowed volumes of the glass containing mobile cations M^+ become connected at $x > x_c$ allowing the long-range diffusion. The dashed lines represent a limited number of simplified ionic migration trajectories. The majority of mobile cations are distributed randomly in the disordered network and do not have other cations as second neighbours, $\langle r_{M-M} \rangle$ > 7-8 Å.

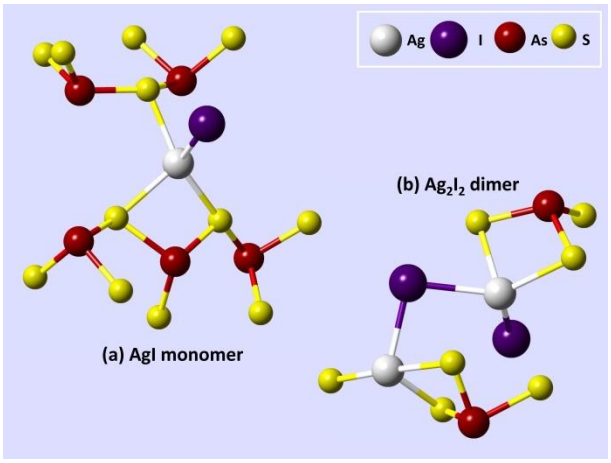

Figure III.61. Schematic representation of isolated AgY monomers or dimers in a disordered silver halide thioarsenate glass network in the critical percolation region based on initial RMC configuration of a $(AgI)_{0.2}(As_2S_3)_{0.8}$ glass.

The random silver distribution in the critical percolation domain is a key to explain the conductivity invariance for AgY- and Ag_2S-As_2S_3 glasses at $x \leq 2$ at.% Ag. The average Ag-Ag separation distance of 12 Å or more implies the absence of direct Ag-Ag contacts. It means the silver sites are isolated in a disordered glass network in the critical percolation domain as it is schematically shown in **Figure III.60**. When Ag^+ cation leaves its residence site and travels throughout the glass network via infinite percolation clusters, the memory of its original chemical form (sulfide or halide) vanishes rapidly with increasing the mean-square displacement.

Preliminary RMC modelling of neutron and high-energy X-ray diffraction data for the $(AgI)_{0.2}(As_2S_3)_{0.8}$ glass and AIMD simulations of glassy $(AgI)_{0.1}(As_2S_3)_{0.9}$ also shows that the major part of silver iodide is present in the glass as isolated AgI monomers, **Figure III.61**. The minority species are corner-sharing Ag_2I_2 dimers. Further evolution of structural motifs with increasing x suggests transformation of isolated oligomers into extended conduction pathways formed by corner- and edge-sharing silver chalcohalide units providing high ionic conductivity suitable for various applications.

III.6.2 Structural role of silver halides

The role of metal halide salts is quite different from that of oxides and chalcogenides when these salts are added to network glass-formers. It is well known that the addition of network-modifying metal oxides such as Na_2O, Li_2O [120] or metal chalcogenides such as Ag_2S [121], Li_2S [122] to an oxide (B_2O_3, P_2O_5, or SiO_2) or chalcogenide network (As_2S_3, GeS_2 or P_2S_5) results in breaking the continuous network, transforming part of the bridging oxygen or sulfur into non-bridging species. In this case, each metal cation (Ag, Na or Li) in the oxide or chalcogenide network will bond to oxygen or sulfur forming terminal bonds. In contrast, the widely accepted point of view implies that the alloying with metal halides (AgI, AgBr, AgCl, NaCl) leads to an expansion of the glass network and the resulting free volume $\Delta V = (V_d - V_m)/V_m$ appears to be a key parameter for high ionic conductivity, $\sigma/\sigma_0 \sim \Delta V^3$ [123], [124]. However, the cubic scaling of ionic conductivity with the free volume has limited applicability for chalcogenide glasses and, in particular, for our pseudo-binary glasses since the molar volume of AgY-glasses either remains constant (AgI-As_2S_3) or decreases (AgBr-As_2S_3), Chapter I.

Raman spectroscopy, neutron and high-energy X-ray diffraction results combined with preliminary AIMD simulations show that at least in AgY-As_2S_3 glasses the structural role of silver halides is different. First, AgY molecules interact with the host glass network. Mixed silver environment of either 3:1 (3S + 1Y) or 2:2 stoichiometry (2S + 2Y) is not consistent with a simple role of silver halides as chemically inert agents for glass network expansion. Just in opposite, in AgBr-As_2S_3 glasses the molar volume shrinks with increasing AgBr content while in AgI-As_2S_3 vitreous counterparts, in spite of large ionic radius of iodine, the molar volume appears to be invariant. Nevertheless, both AgBr- and AgI-As_2S_3 glasses become superionic conductors. Mixed silver environment in AgY-related units also indicates that interaction of silver cations with bridging sulfur appears to be reminiscent of usual interactions between silver sulfide and glassy host with the formation of non-bridging sulfur species. Raman spectra of AgY-As_2S_3 and Ag_2S-As_2S_3 glasses have several similar features associated with formation of non-bridging sulfur, in particular, a high-frequency As-S stretching mode at ≈370 cm^{-1}, typical for As_3S_3 rings in $AgAsS_2$ crystalline references, also observed in Ag-As-S glasses.

Looking on macroscopic molar volume of AgY-As_2S_3 glasses, a strong increase of the principal peak in neutron and X-ray structure factors, decrease in intensity and shift to higher Q of the FSDP, it appears to be difficult to avoid an apparent comparison with the effect of external high-pressure on the above mentioned parameters. In other words, the alloying with silver halides for glassy As_2S_3 seems to be equivalent to a densification of the host network but this is chemically-driven densification. Unusual and unexpected increase of chemical disorder in glassy As_2S_3 from 2-3 % to ≈10 % just adding 1 mol.% of AgBr is also evocative of high pressure. Liquid As_2S_3 at high temperature and pressures becomes unstable transforming into chemically-disordered forms: $As_2S_3 \leftrightarrows AsS + AsS_2$ with homopolar As-As and S-S bonds [125]–[127]. Similar results are achieved at room-temperature and applied high pressure $P > 10$ GPa [128]. Further studies and computer simulations are needed to clarify this situation.

III.7 Conclusions

Two silver halide thioarsenate AgY-As_2S_3 (Y = Br, I) families have been studied using Raman spectroscopy, neutron and high-energy X-ray diffraction completed by RMC/DFT and AIMD

structural modelling of the diffraction data. In addition, the known crystalline references in the $(Ag_2S)_x(As_2S_3)_{1-x}$ quasi-binary system have been synthesized and studied by Raman spectroscopy. Scanning electron microscopy and small angle neutron scattering measurements have been used to examine the glass homogeneity and mesoscopic features of these glasses.

Silver-poor glasses, $x \leq 0.2$, are homogeneous on mesoscopic scale showing only density fluctuations. In contrast, glasses with intermediate and high silver content, $x > 0.2$, are phase-separated. For AgBr-As_2S_3 glasses, at intermediate silver concentrations ($0.2 < x < 0.4$), the Ag-poor phase is predominant and the Ag-rich phase appears in the form of spherical droplets. However, for high silver concentrations ($x > 0.4$), the situation changes drastically and the Ag-rich phase becomes the dominant phase. This behavior could explain the non-monotonic change in room-temperature conductivity at $x = 0.4$.

The diffraction results of glassy AgY-As_2S_3 show two unusual features: (i) the enhanced chemical disorder characterized by the appearance of As-As homopolar bonds at ≈2.5 Å in these stoichiometric glasses, and (ii) mixed tetrahedral silver environment consisting of Ag-S and Ag-Y nearest neighbors. The both structural features are confirmed by Raman spectroscopy and preliminary AIMD modelling. The Raman spectra show low-frequency vibration modes at 180 and 230 cm^{-1} characteristic of As-As stretching. The intermediate steps in AIMD reveal both As-S and As-As nearest neighbors, and Ag-Y and Ag-S contacts. The mixed silver environment in AgY-related units indicates that interaction of silver cations with bridging sulfur appears to be reminiscent of usual interactions between silver sulfide and glassy host with the formation of non-bridging sulfur species. Raman spectra of AgY-As_2S_3 and Ag_2S-As_2S_3 glasses have several similar features associated with formation of non-bridging sulfur, in particular, a high-frequency As-S stretching mode at ≈370 cm^{-1}, typical for As_3S_3 rings in $AgAsS_2$ crystalline references, also observed in Ag-As-S glasses. Consequently, silver halides are participating in transformations of the intermediate range order in As_2S_3 glassy host in contrast to the widely accepted point of view that metal halides leave intact the original glass structure.

The stoichiometry of the mixed silver environment changes with increasing AgY content. Fitting the $T(r)$ of the AgY-diluted glasses ($x \leq 0.10$) shows a better agreement with the 3:1 stoichiometry ratio (3S + 1Y nearest neighbors) while the concentrated vitreous alloys ($x > 0.2$) yield a better agreement with the 2:2 stoichiometry (2S + 2Y). The $x = 0.15$ glass shows an intermediate

behavior. The AIMD simulations are consistent with the experimental findings. These structural results are also coherent with the conductivity data. Chemically invariant conductivity in the critical percolation domain ($x \lesssim 0.1$) is related to a random distribution of isolated AgY monomers, shown also in AIMD modelling of Ag_2S-As_2S_3 glass with small silver content (1.2 at.% Ag). The 2:2 stoichiometry implies a non-random silver distribution and formation of preferential conduction pathways related to Ag-S and Ag-Y chain-like structures.

AIMD modelling also shows a phase separation pattern for the $(AgBr)_{0.5}(As_2S_3)_{0.5}$ glass but not for $(AgI)_{0.1}(As_2S_3)_{0.9}$, in accordance with experimental results.

Pulsed neutron and high-energy X-ray diffraction measurements for mercury thiogermanate glasses show that both two-fold and 4-fold coordinated mercury species are present simultaneously starting from 10 mol. % HgS. The chain-like $(HgS_{2/2})_n$ structural fragments appear to be predominant; the tetrahedral mercury fraction $f_{Hg}^{4F}(x)$ increases with HgS content but reaches only $f_{Hg}^{4F}(x) \approx 0.3$ for equimolar $(HgS)_{0.5}(GeS_2)_{0.5}$ glass. In contrast, glassy/crystalline $(HgS)_{0.6}(GeS_2)_{0.4}$ alloys reveal Bragg peaks of monoclinic Hg_4GeS_6 and essentially tetrahedral mercury local coordination. The emerging, first as a shoulder, growing and finally the most intense vibrational mode at 316±12 cm^{-1}, related to symmetric Hg-S stretching, is consistent with the diffraction results.

Complementary structural experiments using Raman spectroscopy, neutron and high-energy X-ray diffraction allow a complex structure of 5-component $(AgI)_x(HgS)_{0.5-0.5x}(GeS_2)_{0.5-0.5x}$ glasses to be decoded. The analysis of real-space correlation functions $T_N(r)$ and $T_X(r)$ show tetrahedral Ge local coordination, mixed Hg_{2F}-S and Hg_{4F}-S mercury environment, and iodine/sulfur nearest neighbors around Ag cation sites. The S/I stoichiometry changes from 3:1 in AgI-diluted glasses ($x \lesssim 0.1$) to 2:2 for more concentrated vitreous alloys ($x > 0.2$), consistent with the critical percolation and modifier-controlled ion transport regimes. The tetrahedral mercury fraction $f_{Hg}^{4F}(x)$ decreases between 10 and 30 mol.% AgI from $f_{Hg}^{4F}(x) \approx 0.3$ to $f_{Hg}^{4F}(x) \approx 0$ and appears to be responsible for the change in ionic conductivity $\sigma_{Ag^+}(x)$ isotherm; the $\partial \log \sigma_{Ag^+}(x) / \partial x$ slope decreases by a factor of ≈2 at about 30 mol.% AgI.

III.8 References

[1] C. Y. Yang, M. A. Paesler, and D. E. Sayers, "Measurement of local structural configurations associated with reversible photostructural changes in arsenic trisulfide films," *Phys. Rev. B*, vol. 36, no. 17, pp. 9160–9167, Dec. 1987.

[2] D. A. Baker, M. A. Paesler, G. Lucovsky, and P. C. Taylor, "EXAFS study of amorphous $Ge_2Sb_2Te_5$," *J. Non-Cryst. Solids*, vol. 352, no. 9, pp. 1621–1623, Jun. 2006.

[3] T. Usuki, O. Uemura, S. Konno, Y. Kameda, and M. Sakurai, "Structural and physical properties of Ag–As–Te glasses," *J. Non-Cryst. Solids*, vol. 293–295, pp. 799–805, Nov. 2001.

[4] P. Armand, A. Ibanez, and E. Philippot, "Use of synchrotron techniques for a structural study of germanium chalcogenide glasses," *Nucl. Instrum. Methods Phys. Res. Sect. B Beam Interact. Mater. At.*, vol. 97, no. 1, pp. 176–179, May 1995.

[5] H. Eckert, J. H. Kennedy, A. Pradel, and M. Ribes, "Structural transformation of thiosilicate glasses: ^{29}Si MAS-NMR evidence for edge-sharing in the system Li_2S-SiS_2," *J. Non-Cryst. Solids*, vol. 113, no. 2, pp. 287–293, Dec. 1989.

[6] A. Pradel, G. Taillades, M. Ribes, and H. Eckert, "^{29}Si NMR structural studies of ionically conductive silicon chalcogenide glasses and model compounds," *J. Non-Cryst. Solids*, vol. 188, no. 1, pp. 75–86, Jul. 1995.

[7] M. Rubinstein and P. C. Taylor, "Nuclear quadrupole resonance in amorphous and crystalline As_2S_3," *Phys. Rev. B*, vol. 9, no. 10, pp. 4258–4276, May 1974.

[8] E. Ahn, G. A. Williams, and P. C. Taylor, "Nuclear quadrupole resonance study of local bonding in glassy As_xSe_{1-x}," *Phys. Rev. B*, vol. 74, no. 17, p. 174206, Nov. 2006.

[9] E. Bychkov and G. Wortmann, "^{121}-Sb Mössbauer study of insulating and ion-conducting antimony chalcogenide-based glasses," *J. Non-Cryst. Solids*, vol. 159, no. 1–2, pp. 162–172, Jun. 1993.

[10] E. A. Bychkov, Y. S. Grushko, and G. Wortmann, "^{129}I-Mössbaurer study of superionic glasses AgI−Sb_2S_3: Local structure and diffusion effects," *Hyperfine Interact.*, vol. 69, no. 1–4, pp. 709-712a, Apr. 1992.

[11] A. T. Ward, "Raman spectroscopy of sulfur, sulfur-selenium, and sulfur-arsenic mixtures," *J. Phys. Chem.*, vol. 72, no. 12, pp. 4133–4139, Nov. 1968.

[12] E. I. Kamitsos, J. A. Kapoutsis, G. D. Chryssikos, G. Taillades, A. Pradel, and M. Ribes, "Structure and Optical Conductivity of Silver Thiogermanate Glasses," *J. Solid State Chem.*, vol. 112, no. 2, pp. 255–261, Oct. 1994.

[13] D. L. Price, S. Susman, and A. C. Wright, "Probing medium-range order in chalcogenide glasses by neutron scattering and optical spectroscopy," *J. Non-Cryst. Solids*, vol. 97–98, pp. 167–170, Dec. 1987.

[14] D. L. Price, M. Misawa, S. Susman, T. I. Morrison, G. K. Shenoy, and M. Grimsditch, "The structure of phosphorus-selenium glasses I. Concentration dependence of the short- and intermediate-range order," *J. Non-Cryst. Solids*, vol. 66, no. 3, pp. 443–465, Aug. 1984.

[15] A. C. Barnes, M. A. Hamilton, P. Buchanan, and M.-L. Saboungi, "Combined X-ray and neutron diffraction from binary liquids and amorphous semiconductors," *J. Non-Cryst. Solids*, vol. 250–252, pp. 393–404, Aug. 1999.

[16] A. C. Hannon, "Results on disordered materials from the GEneral Materials diffractometer, GEM, at ISIS," *Nucl. Instrum. Methods Phys. Res. Sect. Accel. Spectrometers Detect. Assoc. Equip.*, vol. 551, no. 1, pp. 88–107, Oct. 2005.

[17] J. Neuefeind and K.-D. Liss, "Bond angle distribution in amorphous germania and silica," *Berichte Bunsenges. Für Phys. Chem.*, vol. 100, no. 8, pp. 1341–1349, Aug. 1996.

[18] Bill Kamitakahara, "A New Neutron Imaging Facility at BT-6 for the Non-Destructive Analysis of Working Fuel Cells." [Online]. Available: https://www.ncnr.nist.gov/AnnualReport/FY2003_html/RH2/. [Accessed: 18-Oct-2017].

[19] Y. Waseda, *The structure of non-crystalline materials: liquids and amorphous solids*. New York; London: McGraw-Hill International Book Co., 1980.

[20] J. M. Ziman, "A Theory of the Electrical Properties of Liquid Metals. I: The Monovalent Metals," *Philos. Mag.*, vol. 6, no. 68, pp. 1013–1034, 1961.

[21] D. Waasmaier and A. Kirfel, "New analytical scattering-factor functions for free atoms and ions," *Acta Crystallogr. A*, vol. 51, no. 3, pp. 416–431, May 1995.

[22] B. L. Henke, E. M. Gullikson, and J. C. Davis, "X-Ray Interactions: Photoabsorption, Scattering, Transmission, and Reflection at E = 50-30,000 eV, Z = 1-92," *At. Data Nucl. Data Tables*, vol. 54, no. 2, pp. 181–342, Jul. 1993.

[23] S. Sasaki, “Numerical tables of anomalous scattering factors calculated by the Cromer and Liberman’s method,” National Lab. for High Energy Physics, KEK--88-14, 1989.

[24] A. C. Wright, “Neutron scattering from vitreous silica. V. The structure of vitreous silica: What have we learned from 60 years of diffraction studies?,” *J. Non-Cryst. Solids*, vol. 179, pp. 84–115, Nov. 1994.

[25] B. E. Warren and R. L. Mozzi, “Multiple scattering of X-rays by amorphous samples,” *Acta Crystallogr.*, vol. 21, no. 4, pp. 459–461, Oct. 1966.

[26] H. H. M. Balyuzi, “Analytic approximation to incoherently scattered X-ray intensities,” *Acta Crystallogr. A*, vol. 31, no. 5, pp. 600–602, Sep. 1975.

[27] E. Lorch, “Neutron diffraction by germania, silica and radiation-damaged silica glasses,” *J. Phys. C Solid State Phys.*, vol. 2, no. 2, p. 229, 1969.

[28] S. Susman, K. J. Volin, D. G. Montague, and D. L. Price, “The structure of vitreous and liquid $GeSe_2$: a neutron diffraction study,” *J. Non-Cryst. Solids*, vol. 125, no. 1, pp. 168–180, Nov. 1990.

[29] J. H. Lee, A. P. Owens, A. Pradel, A. C. Hannon, M. Ribes, and S. R. Elliott, “Structure determination of Ag-Ge-S glasses using neutron diffraction,” *Phys. Rev. B*, vol. 54, no. 6, pp. 3895–3909, Aug. 1996.

[30] A. P. Hammersley, S. O. Svensson, M. Hanfland, A. N. Fitch, and D. Hausermann, “Two-dimensional detector software: From real detector to idealised image or two-theta scan,” *High Press. Res.*, vol. 14, no. 4–6, pp. 235–248, Jan. 1996.

[31] C. N. J. Wagner, “Direct methods for the determination of atomic-scale structure of amorphous solids (X-ray, electron, and neutron scattering),” *J. Non-Cryst. Solids*, vol. 31, no. 1, pp. 1–40, Dec. 1978.

[32] L. B. Skinner, C. J. Benmore, and J. B. Parise, “Area detector corrections for high quality synchrotron X-ray structure factor measurements,” *Nucl. Instrum. Methods Phys. Res. Sect. Accel. Spectrometers Detect. Assoc. Equip.*, vol. 662, no. 1, pp. 61–70, Jan. 2012.

[33] G. L. Squires, *Introduction to the Theory of Thermal Neutron Scattering*. Courier Corporation, 1978.

[34] A. Guinier and G. Fournet, *Small-angle scattering of X-rays*. New York: John Wiley & Sons, 1955.

[35] O. Glatter and O. Kratky, “Small-Angle X-ray Scattering, chapter 4,” London: Academic Press, 1982, pp. 155–156.

[36] L. A. Feigin and D. I. Svergun, *Structure Analysis by Small-Angle X-Ray and Neutron Scattering*. Springer US, 1987.

[37] “PASiNET: data treatment software for SANS spectrometers of LLB.” [Online]. Available: http://www-llb.cea.fr/Phocea/Page/index.php?id=84.

[38] F. Cousin, “G 2-3, Small Angle Neutron Scattering facility PAXY.” LLB edition, 2015.

[39] E. Bychkov, D. L. Price, and A. Lapp, “Universal trend of the Haven ratio in glasses: origin and structural evidences from neutron diffraction and small-angle neutron scattering,” *J. Non-Cryst. Solids*, vol. 293–295, pp. 211–219, Nov. 2001.

[40] A. Piarristeguy, M. Ramonda, N. Kuwata, A. Pradel, and M. Ribes, “Microstructure of Ag_2S–As_2S_3 glasses,” *Solid State Ion.*, vol. 177, no. 35, pp. 3157–3160, Nov. 2006.

[41] T. Li, A. J. Senesi, and B. Lee, “Small Angle X-ray Scattering for Nanoparticle Research,” *Chem. Rev.*, vol. 116, no. 18, pp. 11128–11180, Sep. 2016.

[42] W. Woo, M. Ohnuma, and X.-L. Wang, “Chapter 12 - Engineering Applications,” in *Experimental Methods in the Physical Sciences*, vol. 49, F. Fernandez-Alonso and D. L. Price, Eds. Academic Press, 2017, pp. 683–737.

[43] P. Debye and A. M. Bueche, “Scattering by an Inhomogeneous Solid,” *J. Appl. Phys.*, vol. 20, no. 6, pp. 518–525, Jun. 1949.

[44] P. Armand, A. Ibanez, E. Philippot, C. Williams, and D. Bittencourt, “Small angle X-ray scattering and the structure of Ge-S and GeS_2-Ag_2S glassy systems,” *J. Phys. IV*, vol. 03, pp. C8-389, Dec. 1993.

[45] E. Bychkov, M. Miloshova, D. L. Price, C. J. Benmore, and A. Lorriaux, “Short, intermediate and mesoscopic range order in sulfur-rich binary glasses,” *J. Non-Cryst. Solids*, vol. 352, no. 1, pp. 63–70, Jan. 2006.

[46] F. Fiori and F. Spinozzi, “Microstructural Investigations by Small Angle Scattering of Neutrons and X-rays,” in *Innovative Technological Materials*, Springer, Berlin, Heidelberg, 2010, pp. 35–78.

[47] Gaussian 16, Revision B.01, M. J. Frisch, G. W. Trucks, H. B. Schlegel, G. E. Scuseria, M. A. Robb, J. R. Cheeseman, G. Scalmani, V. Barone, G. A. Petersson, H. Nakatsuji, X. Li, M. Caricato, A. V. Marenich, J. Bloino, B. G. Janesko, R. Gomperts, B. Mennucci, H. P.

Hratchian, J. V. Ortiz, A. F. Izmaylov, J. L. Sonnenberg, D. Williams-Young, F. Ding, F. Lipparini, F. Egidi, J. Goings, B. Peng, A. Petrone, T. Henderson, D. Ranasinghe, V. G. Zakrzewski, J. Gao, N. Rega, G. Zheng, W. Liang, M. Hada, M. Ehara, K. Toyota, R. Fukuda, J. Hasegawa, M. Ishida, T. Nakajima, Y. Honda, O. Kitao, H. Nakai, T. Vreven, K. Throssell, J. A. Montgomery, Jr., J. E. Peralta, F. Ogliaro, M. J. Bearpark, J. J. Heyd, E. N. Brothers, K. N. Kudin, V. N. Staroverov, T. A. Keith, R. Kobayashi, J. Normand, K. Raghavachari, A. P. Rendell, J. C. Burant, S. S. Iyengar, J. Tomasi, M. Cossi, J. M. Millam, M. Klene, C. Adamo, R. Cammi, J. W. Ochterski, R. L. Martin, K. Morokuma, O. Farkas, J. B. Foresman, and D. J. Fox, Gaussian, Inc., Wallingford CT, 2016.

[48] A. D. Becke, "Density-functional thermochemistry. III. The role of exact exchange," *J. Chem. Phys.*, vol. 98, no. 7, pp. 5648–5652, Apr. 1993.

[49] C. Lee, W. Yang, and R. G. Parr, "Development of the Colle-Salvetti correlation-energy formula into a functional of the electron density," *Phys. Rev. B*, vol. 37, no. 2, pp. 785–789, Jan. 1988.

[50] K. A. Peterson, "Systematically convergent basis sets with relativistic pseudopotentials. I. Correlation consistent basis sets for the post-d group 13–15 elements," *J. Chem. Phys.*, vol. 119, no. 21, pp. 11099–11112, Nov. 2003.

[51] D. Feller, "The role of databases in support of computational chemistry calculations," *J. Comput. Chem.*, vol. 17, no. 13, pp. 1571–1586, Oct. 1996.

[52] R. Blachnik and U. Wickel, "Phase Relations in the System Ag-As-S and Thermal Behaviour of Ag7MX6 Compounds," *Z. Für Naturforschung B*, vol. 35, no. 10, pp. 1268–1271, 2014.

[53] F. H. Wehmeier, R. A. Laudise, and J. W. Shiever, "The system Ag_2S-As_2S_3 and the growth of crystals of proustite, smithite and pyrargyrite," *Mater. Res. Bull.*, vol. 3, no. 9, pp. 767–777, Sep. 1968.

[54] S. Miyatani, "On the Polarization of Silver Sulfide," *J. Phys. Soc. Jpn.*, vol. 10, no. 9, pp. 786–793, Sep. 1955.

[55] O. Alekperov, Z. Jahangirli, and R. Paucar, "First-principles lattice dynamics and Raman scattering in ionic conductor β-Ag_2S," *Phys. Status Solidi B*, vol. 253, no. 10, pp. 2049–2055, Oct. 2016.

[56] S. Kharbish, "Spectral-structural characteristics of the extremely scarce silver arsenic sulfosalts, proustite, smithite, trechmannite and xanthoconite: μ-Raman spectroscopy

evidence," *Spectrochim. Acta. A. Mol. Biomol. Spectrosc.*, vol. 177, no. Supplement C, pp. 104–110, Apr. 2017.

[57] G. Lucovsky, "Optic Modes in Amorphous As_2S_3 and As_2Se_3," *Phys. Rev. B*, vol. 6, no. 4, pp. 1480–1489, Aug. 1972.

[58] E. I. Kamitsos, J. A. Kapoutsis, I. P. Culeac, and M. S. Iovu, "Structure and Bonding in As−Sb−S Chalcogenide Glasses by Infrared Reflectance Spectroscopy," *J. Phys. Chem. B*, vol. 101, no. 51, pp. 11061–11067, Dec. 1997.

[59] T. Wágner, S. O. Kasap, M. Vlček, A. Sklenář, and A. Stronski, "The structure of As_xS_{100-x} glasses studied by temperature-modulated differential scanning calorimetry and Raman spectroscopy," *J. Non-Cryst. Solids*, vol. 227–230, Part 2, pp. 752–756, May 1998.

[60] P. Chen, C. Holbrook, P. Boolchand, D. G. Georgiev, K. A. Jackson, and M. Micoulaut, "Intermediate phase, network demixing, boson and floppy modes, and compositional trends in glass transition temperatures of binary AsxS1-x system," *Phys. Rev. B*, vol. 78, no. 22, p. 224208, Dec. 2008.

[61] M. Frumar, A. P. Firth, and A. E. Owen, "A model for photostructural changes in the amorphous As-S system," *J. Non-Cryst. Solids*, vol. 59, pp. 921–924, Dec. 1983.

[62] K. Shimakawa, A. Kolobov, and S. R. Elliott, "Photoinduced effects and metastability in amorphous semiconductors and insulators," *Adv. Phys.*, vol. 44, no. 6, pp. 475–588, Dec. 1995.

[63] F. Kyriazis and S. N. Yannopoulos, "Colossal photostructural changes in chalcogenide glasses: Athermal photoinduced polymerization in As_xS_{100-x} bulk glasses revealed by near-bandgap Raman scattering," *Appl. Phys. Lett.*, vol. 94, no. 10, p. 101901, Mar. 2009.

[64] F. Kyriazis *et al.*, "Effect of silver doping on the structure and phase separation of sulfur-rich As–S glasses: Raman and SEM studies," *J. Non-Cryst. Solids*, vol. 355, no. 37, pp. 2010–2014, Oct. 2009.

[65] K. S. Andrikopoulos, J. Arvanitidis, V. Dracopoulos, D. Christofilos, T. Wagner, and S. N. Yannopoulos, "Nanoindentation and Raman studies of phase-separated Ag-As-S glasses," *Appl. Phys. Lett.*, vol. 99, no. 17, p. 171911, Oct. 2011.

[66] R. Boidin, "Etude des propriétés de conduction et structurales des verres du système HgI_2-Ag_2S-As_2S_3 : application en tant que capteur chimique."

[67] E. Hellner and H. Burzlaff, “Die Struktur des Smithits $AgAsS_2$,” *Naturwissenschaften*, vol. 51, no. 2, pp. 35–36, Jan. 1964.

[68] T. Matsumoto and W. Nowacki, “The crystal structure of trechmannite, $AgAsS_2$* T. Matsumoto et W. Nowacki,” *Z. Für Krist.*, vol. 129, no. 1–4, pp. 163–177, 2010.

[69] E. Hellner and H. Burzlaff, “Die Struktur des Smithits $AgAsS_2$,” *Naturwissenschaften*, vol. 51, pp. 35–36, Jan. 1964.

[70] Z. U. Borisova and J. G. Adashko, *Glassy semiconductors*. Plenum Press New York, 1981.

[71] A. Ga¸gor, A. Pawłowski, and A. Pietraszko, “Silver transfer in proustite Ag_3AsS_3 at high temperatures: Conductivity and single-crystal X-ray studies,” *J. Solid State Chem.*, vol. 182, no. 3, pp. 451–456, Mar. 2009.

[72] P. Engel and W. Nowacki, “Die verfeinerung der kristallstruktur von proustit, Ag_3AsS_3, und pyrargyrit, Ag3SbS3,” *Neues Jahrb Miner. Monatsh*, pp. 181–184, 1966.

[73] I. D. Olekseyuk, I. I. Mazurets, and O. V. Parasyuk, “Phase equilibria in the $HgS–Ga_2S_3–GeS_2$ system,” *J. Alloys Compd.*, vol. 417, no. 1, pp. 131–137, Jun. 2006.

[74] P. Masselin, D. L. Coq, A. Cuisset, and E. Bychkov, “Spatially resolved Raman analysis of laser induced refractive index variation in chalcogenide glass,” *Opt. Mater. Express*, vol. 2, no. 12, pp. 1768–1775, Dec. 2012.

[75] I. Petri and P. S. Salmon, “A neutron diffraction study of glassy GeS_2,” *J. Non-Cryst. Solids*, vol. 293–295, pp. 169–174, Nov. 2001.

[76] A. Bytchkov, G. J. Cuello, S. Kohara, C. J. Benmore, D. L. Price, and E. Bychkov, “Unraveling the atomic structure of Ge-rich sulfide glasses,” *Phys. Chem. Chem. Phys.*, vol. 15, no. 22, pp. 8487–8494, May 2013.

[77] J. E. Griffiths, J. C. Phillips, G. P. Espinosa, J. P. Remeika, and P. M. Bridenbaugh, “Assignment of the Companion A Line in Ge_x (S, Se)$_{1–x}$ Glasses,” *Phys. Status Solidi B*, vol. 122, no. 1, pp. K11–K15, Mar. 1984.

[78] S. Sugai, “Stochastic random network model in Ge and Si chalcogenide glasses,” *Phys. Rev. B*, vol. 35, no. 3, pp. 1345–1361, Jan. 1987.

[79] K. Inoue, O. Matsuda, and K. Murase, “Raman spectra of tetrahedral vibrations in crystalline germanium dichalcogenides, GeS_2 and $GeSe_2$, in high and low temperature forms,” *Solid State Commun.*, vol. 79, no. 11, pp. 905–910, Sep. 1991.

[80] G. Lucovsky, F. L. Galeener, R. C. Keezer, R. H. Geils, and H. A. Six, "Structural interpretation of the infrared and Raman spectra of glasses in the alloy system Ge_{1-x} S_x," *Phys. Rev. B*, vol. 10, no. 12, pp. 5134–5146, Dec. 1974.

[81] S. Blaineau and P. Jund, "Vibrational signature of broken chemical order in a GeS_2 glass: a molecular dynamics simulation," *Phys. Rev. B*, vol. 69, no. 6, p. 064201, Feb. 2004.

[82] K. Jackson, A. Briley, S. Grossman, D. V. Porezag, and M. R. Pederson, "Raman-Active Modes of a-$GeSe_2$ and a-GeS_2: A First-Principles Study," *Phys. Rev. B*, vol. 60, no. 22, pp. R14985–R14989, Dec. 1999.

[83] I. Kotsalas and C. Raptis, "High-Temperature Structural Phase Transitions of Ge_xS_{1-x} Alloys Studied by Raman Spectroscopy," *Phys Rev B*, vol. 64, Sep. 2001.

[84] M. Kassem, S. Khaoulani, A. Cuisset, D. L. Coq, P. Masselin, and E. Bychkov, "Mercury thioarsenate glasses: a hybrid chain/pyramidal network," *RSC Adv.*, vol. 4, no. 90, pp. 49236–49246, Oct. 2014.

[85] C. Rau *et al.*, "Mixed cation effect in chalcogenide glasses Rb_2S-Ag_2S-GeS_2," *Phys. Rev. B - Condens. Matter Mater. Phys.*, vol. 63, pp. 1842041–1842049, Jan. 2001.

[86] S. C. Moss and D. L. Price, "Random Packing of Structural Units and the First Sharp Diffraction Peak in Glasses," in *Physics of Disordered Materials*, D. Adler, H. Fritzsche, and S. R. Ovshinsky, Eds. Boston, MA: Springer US, 1985, pp. 77–95.

[87] E. Bychkov and D. L. Price, "Neutron diffraction studies of Ag_2S–As_2S_3 glasses in the percolation and modifier-controlled domains," *Solid State Ion.*, vol. 136–137, pp. 1041–1048, Nov. 2000.

[88] J. H. Lee, A. P. Owens, A. Pradel, A. C. Hannon, M. Ribes, and S. R. Elliott, "Structure determination of Ag-Ge-S glasses using neutron diffraction," *Phys. Rev. B*, vol. 54, no. 6, pp. 3895–3909, Aug. 1996.

[89] W. Zhou, D. E. Sayers, M. A. Paesler, B. Bouchet-Fabre, Q. Ma, and D. Raoux, "Structure and photoinduced structural changes in a-As_2S_3 films: A study by differential anomalous x-ray scattering," *Phys. Rev. B*, vol. 47, no. 2, pp. 686–694, Jan. 1993.

[90] H.-J. Deiseroth, M. Wagener, and E. Neumann, "$(AgI)_2Te_6$ and $(AgI)_2Se_6$: New Composite Materials with Cyclic Te6 and Se6 Molecules Stabilized in the 'Solid Solvent' AgI," *Eur. J. Inorg. Chem.*, vol. 2004, no. 24, pp. 4755–4758, Dec. 2004.

[91] S. Reiser, T. Nilges, and A. Pfitzner, "$(CuBr)_3P_4Se_4$: A Low Symmetric Variant of the $(CuI)_3P_4Se_4$ Structure Type," *Z. Für Anorg. Allg. Chem.*, vol. 629, no. 3, pp. 563–568, Mar. 2003.

[92] A. Pfitzner, S. Reiser, and H.-J. Deiseroth, "$(CuI)P_4Se_4$: An Adduct of Polymeric P_4Se_4 with CuI," *Z. Für Anorg. Allg. Chem.*, vol. 625, no. 12, pp. 2196–2201, Dec. 1999.

[93] F. Schnieders and P. Boettcher, "Darstellung und Kristallstruktur von AgTeI," *Z. Für Krist. - Cryst. Mater.*, vol. 210, no. 5, pp. 323–327, 1995.

[94] A. Biegerl, C. Gröger, H. R. Kalbitzer, J. Wachter, and M. Zabel, "Investigation of the Coordination Behavior of P_4S_3 towards CuBr," *Z. Für Anorg. Allg. Chem.*, vol. 636, no. 5, pp. 770–774, Apr. 2010.

[95] A. Biegerl, E. Brunner, C. Gröger, M. Scheer, J. Wachter, and M. Zabel, "The Unexpected Versatility of P_4S_3 as a Building Block in Polymeric Copper Halide Networks: 2,3-P, 1,2,3-P and all-P Coordination," *Chem. – Eur. J.*, vol. 13, no. 33, pp. 9270–9276, Nov. 2007.

[96] E. Bychkov, D. L. Price, C. J. Benmore, and A. C. Hannon, "Ion transport regimes in chalcogenide and chalcohalide glasses: from the host to the cation-related network connectivity," *Solid State Ion.*, vol. 154–155, pp. 349–359, Dec. 2002.

[97] I. T. Penfold and P. S. Salmon, "Glass formation and short-range order in chalcogenide materials: The $(Ag_2S)_x(As_2S_3)_{1-x}$ ($0 \leq x \leq 1$) pseudobinary tie line," *Phys. Rev. Lett.*, vol. 64, no. 18, pp. 2164–2167, Apr. 1990.

[98] J. Akola *et al.*, "Experimentally constrained density-functional calculations of the amorphous structure of the prototypical phase-change material $Ge_2Sb_2Te_5$," *Phys. Rev. B*, vol. 80, no. 2, p. 020201, Jul. 2009.

[99] T. Matsunaga *et al.*, "From local structure to nanosecond recrystallization dynamics in AgInSbTe phase-change materials," *Nat. Mater.*, vol. 10, no. 2, pp. 129–134, Feb. 2011.

[100] O. Gereben, P. Jóvári, L. Temleitner, and L. Pusztai, "A new version of the RMC++ Reverse Monte Carlo programme, aimed at investigating the structure of covalent glasses," *J. Optoelectron. Adv. Mater.*, vol. 9, no. 10, pp. 3021–3027, Oct. 2007.

[101] "about [CP2K Open Source Molecular Dynamics]." [Online]. Available: https://www.cp2k.org/. [Accessed: 14-Nov-2018].

[102] J. P. Perdew *et al.*, "Restoring the Density-Gradient Expansion for Exchange in Solids and Surfaces," *Phys. Rev. Lett.*, vol. 100, no. 13, p. 136406, Apr. 2008.

[103] J. Akola, A. Sokolov, and E. Bychkov, “Combined RMC/DFT-MD study of Ge-S glasses,” unpublished results.

[104] T. Schleid, P. Lauxmann, and C. Schneck, “Roentgenographische Einkristalluntersuchungen an alpha-HgS (zinnober),” *Z Krist. Suppl*, vol. 16, p. 95, 1999.

[105] D. Rodic, V. Spasojevic, A. Bajorek, and P. Onnerud, “Similarity of structure properties of $Hg_{1-x}Mn_xS$ and $Cd_{1-x}Mn_xS$ (structure properties of HgMnS and CdMnS),” *J. Magn. Magn. Mater.*, vol. 152, no. 1, pp. 159–164, Jan. 1996.

[106] J. Serment, G. Perez, and P. Hagenmuller, “Les systèmes SiS_2 - MS et GeS_2 - MS (M =Cd, Hg) entre 800 et 1 000 °C,” *Bull. Soc. Chim. France*, pp. 561–566, 1968.

[107] O. Gorochov, “Les composes Ag_8MX_6 (M = Si, Ge, Sn et X = S, Se, Te),” *Bull. Soc. Chim. France*, pp. 2263–2275, 1968.

[108] A. C. Hannon, “XTAL: a program for calculating interatomic distances and coordination numbers for model structures,” Rutherford-Appleton Laboratory, Report RAL-93-063, 1993.

[109] S. R. Elliott, “Medium-Range Structural Order in Covalent Amorphous Solids,” *Nature*, vol. 354, pp. 445–452, Nov. 1991.

[110] M. Celino *et al.*, “First-principles molecular dynamics study of glassy GeS_2: Atomic structure and bonding properties,” *Phys. Rev. B*, vol. 88, no. 17, p. 174201, Nov. 2013.

[111] Y. Onodera, T. Usuki, T. Nasu, and S. Kohara, “Structure of silver bromide doped chalcogenide glasses,” *Solid State Ion.*, vol. 262, pp. 469–471, Sep. 2014.

[112] G. N. Greaves, “EXAFS and the structure of glass,” *J. Non-Cryst. Solids*, vol. 71, no. 1, pp. 203–217, May 1985.

[113] S. Adams and J. Swenson, “Determining Ionic Conductivity from Structural Models of Fast Ionic Conductors,” *Phys. Rev. Lett.*, vol. 84, no. 18, pp. 4144–4147, May 2000.

[114] C. Escher, T. Latychevskaia, H.-W. Fink, and D. W. Pohl, “Direct Evidence for Conduction Pathways in a Solid Electrolyte,” *Phys. Rev. Lett.*, vol. 97, no. 13, p. 136601, Sep. 2006.

[115] S. Adams and R. P. Rao, “Transport pathways for mobile ions in disordered solids from the analysis of energy-scaled bond-valence mismatch landscapes,” *Phys. Chem. Chem. Phys.*, vol. 11, no. 17, pp. 3210–3216, Apr. 2009.

[116] K. Mori *et al.*, “Visualization of conduction pathways in lithium superionic conductors: Li_2S-P_2S_5 glasses and Li7P3S11 glass–ceramic,” *Chem. Phys. Lett.*, vol. 584, pp. 113–118, Oct. 2013.

[117] E. Bychkov, V. Tsegelnik, Y. Vlasov, A. Pradel, and M. Ribes, “Percolation transition in Ag-doped germanium chalcogenide-based glasses: conductivity and silver diffusion results,” *J. Non-Cryst. Solids*, vol. 208, no. 1–2, pp. 1–20, Nov. 1996.

[118] Y. Drugov, V. Tsegelnik, A. Bolotov, Y. Vlasov, and E. Bychkov, “^{110}Ag tracer diffusion study of percolation transition in Ag_2S–As_2S_3 glasses,” *Solid State Ion.*, vol. 136–137, pp. 1091–1096, Nov. 2000.

[119] J. Akola *et al.*, “Structure, electronic, and vibrational properties of amorphous AsS_2 and $AgAsS_2$: Experimentally constrained density functional study,” *Phys. Rev. B*, vol. 89, no. 6, Feb. 2014.

[120] H. Jabraoui, E. M. Achhal, A. Hasnaoui, J.-L. Garden, Y. Vaills, and S. Ouaskit, “Molecular dynamics simulation of thermodynamic and structural properties of silicate glass: Effect of the alkali oxide modifiers,” *J. Non-Cryst. Solids*, vol. 448, pp. 16–26, Sep. 2016.

[121] A. Paraskiva, “Développement de membranes pour les capteurs chimiques potentiométriques spécifiques aux ions Thallium et Sodium,” Université du Littoral Côte d’Opale, 15-Dec-2017.

[122] A. Kato, M. Nose, M. Yamamoto, A. Sakuda, A. Hayashi, and M. Tatsumisago, “Mechanical properties of sulfide glasses in all-solid-state batteries,” *J. Ceram. Soc. Jpn.*, vol. 126, no. 9, pp. 719–727, Sep. 2018.

[123] T. Usuki, K. Nakajima, Y. Kameda, M. Sakurai, and T. Nasu, “Coordination environment and network structure in AgI doped As-chalcogenide glasses,” in *Superionic Conductor Physics*, 0 vols., WORLD SCIENTIFIC, 2007, pp. 103–112.

[124] J. Swenson and L. Börjesson, “Correlation between Free Volume and Ionic Conductivity in Fast Ion Conducting Glasses,” *Phys. Rev. Lett.*, vol. 77, no. 17, pp. 3569–3572, Oct. 1996.

[125] V. V. Brazhkin, M. Kanzaki, K.-I. Funakoshi, and Y. Katayama, “Viscosity behavior spanning four orders of magnitude in As-S melts under high pressure,” *Phys. Rev. Lett.*, vol. 102, no. 11, p. 115901, Mar. 2009.

[126] V. V. Brazhkin, Y. Katayama, M. V. Kondrin, A. G. Lyapin, and H. Saitoh, “Structural transformation yielding an unusual metallic state in liquid As_2S_3 under high pressure,” *Phys. Rev. B*, vol. 82, no. 14, p. 140202, Oct. 2010.

[127] N. B. Bolotina *et al.*, “High-pressure polymorphism of As_2S_3 and new AsS_2 modification with layered structure,” *JETP Lett.*, vol. 98, no. 9, pp. 539–543, 2013.

[128] E. Soignard, C. J. Benmore, and E. Bychkov, “Unpublished results of diamond anvil cell HE-XRD measurements at APS,” Jul. 2018.

Chapter IV : Development of Hg^{2+} chemical sensors based on chalcogenide glasses

IV.1 Introduction

The relation between the ionic transport and glass structure of the synthesized glasses are now well developed. Therefore, in this chapter, we would like to study the application of these glasses as chemical sensors.

Chalcogenide and chalcohalide glass membranes are new promising materials for the chemical detection of heavy metal ions (Hg^{2+}, Cu^{2+}, Cd^{2+}, Pb^{2+}, Cr^{6+}, Tl^{+}, etc.) and toxic anions (S^{2-}, CN^{-}, arsenite and arsenate ions). Compared with commercially available devices based on crystalline materials, chemical sensors based on chalcogenide glasses show:

1. Stability, reliability and much better chemical durability, which are extremely important for in situ and continuous measurements. Therefore, the developed sensors can be used for long periods without maintenance.
2. An almost unlimited ability to dope and modify the glasses in order to synthesize sensitive materials with better analytical properties and thus develop new sensors.
3. Higher ppb sensitivity and low detection limit.
4. Higher selectivity in the presence of many interfering species.

In **Table IV.1** we are presented the norm concerning certain heavy metals in industrial atmospheric emissions in France and the European Union.

Table IV.1. Heavy metal limit concentrations in industrial air emissions in France and the European Union [1].

Group number	Elements	Flow limit to start the control ($g.h^{-1}$)	Flow limit for in situ control ($g.h^{-1}$)	Concentration limit ($mg.Nm^{-3}$)
1	Cd, Hg, Tl	1	10 (Cd + Hg)	0.05 per metal 0.1 for the whole group 1
2	As, Se, Te	5	50	1
3	Pb	10	100	1
4	Sb, Cr, Co, Cu, Sn, Mn, Ni, V	25	500	5

The column (IV) shows the flow limits for in situ monitoring. Mercury is found in the first group, which is considered to be the most dangerous element from both environmental and health point of views. The ionic form of Hg^{2+} is graded among the most toxic.

IV.2 Bibliography

Mercury was known very long time ago already by Antique, Greek and Romans. That's why, the research on the physical and chemical properties of mercury had started at the same era. Mercury science has always been interdisciplinary. But scientists have started only recently to integrate a multi-tiered approach using chemistry, biology and human health sciences regarding the study of mercury pollution.

The following chapter's paragraphs include an overview of some main topics: (I) chemical and physical properties of mercury, (II) toxicity of mercury, (III) methods for analysis, and (IV) mercury-selective electrodes.

IV.2.1 Chemical and physical properties of mercury

Mercury is derived from the Latin name, hydragyrum, which means silver water. Elemental mercury is found in the earth's crust in only a limited number of regions in the world. Mercury in nature is found mostly like the mineral cinnabar (HgS), but also like calomel (Hg_2Cl_2), Livingstonite ($HgSb_4S_8$) and Tiemannite (HgSe) [2].

Mercury exists in three oxidation states:

- metallic mercury (Hg^0),
- mercurous ion (Hg_2^{2+}),
- mercuric ion (Hg^{2+}).

The principle chemical and physical properties of the mercury species are presented below. Redox reactions are at the origin of the conversions between the inorganic species of the oxidation states 0, +1 and +2 (discussed below).

IV.2.1.a Metallic mercury (Hg^0)

Hg^0, (elemental mercury), is a transition metal of group 12 of the periodic table being liquid at room temperature, and it has:

- atomic number of 80
- atomic mass of 200.59 g. mol^{-1}
- density (13.58 g. cm^{-3}) heavier than water
- melting point of -39˚C
- boiling point of 357˚C

Its exceptional combination of properties permits it to be useful for many applications, for instance, mercury batteries, vacuum pumps, barometers, thermometers, amalgamation, etc…

It possesses other unique properties [2], [3]:

- anomalously high vapor pressure for a heavy metal (14 mg m^{-1} at 20 °C),
- high Henry's law coefficient (729 at 20 °C),
- high surface tension (mercury-air: 486.5 mN m^{-1} at 20 °C),
- low electrical conductivity (1.1×10^6 S m^{-1}),
- low thermal conductivity (8 W m^{-1} K^{-1})
- high expansion coefficient (a volume expansion coefficient of 180×10^{-6} K^{-1} at 20 °C),
- capacity to form amalgams with noble metals (gold, silver, platinum and palladium)

Mercury can exist as well in the gaseous state in the environment. It is the dominant form in the atmosphere. Most of natural waters are nearly saturated, or supersaturated according to concentration of atmospheric Hg^0 [2].

IV.2.1.b Monovalent mercury (Hg_2^{2+})

The number of stable mercury (I) compounds is limited corresponding to the disproportionation reaction. The particularity of this ion is the absence of the hydroxide ion. In all monovalent (I) compounds, the mercury atoms are linked together by forming -Hg-Hg- group. All mercury (I) compounds are fairly strong reducing agents.

Mercury (I) chloride with the formula Hg_2Cl_2 is a mineral known as calomel. It is used for preparing the calomel reference electrodes in electrochemistry. This mineral has a particularity also that at heating, it sublimates.

Most mercury (I) compounds are not soluble in water. The three following salts are considered as an exception **(Table IV.2)**:

Nitrate → $Hg_2(NO_3)_2$

Chlorate → $Hg_2(ClO_3)_2$

Perchlorate → $Hg_2(ClO_4)_2$

Table IV.2. Solubility constants of mercury (I) compounds in water [4].

	Solubility in water (g/100g H_2O)									
	Temperature (C°)									
	0	8	20	30	35	40	50	60	70	99
$Hg_2(ClO_4)_2$	73.8	75.9	78.6	80.3	81.8	82	82.8	83.3	83.8	85.3
$Hg_2(NO_3)_2$	-	-	36 .76	-	-	-	-	-	-	-

These salts dissociate as well as all the alkaline salts; for example, $NaNO_3$. All mercury (1+) compounds are strong reducing agents.

Depending on the solubility products **(Table IV.3)**, we can say that monovalent mercury compounds are almost all insoluble with different levels of solubility.

Mercury (1+) is not predisposed to form complexes because of:

- the disproportionation reaction
- the creation of weak covalent coordination bonds.

Table IV.3. The solubility product of monovalent mercury compounds [5].

№	Compounds	pKsp = -logKsp
1	Hg_2Br_2	2.7
2	Hg_2CO_3	16.05
3	$Hg_2C_2O_4$	13
3	Hg_2Cl_2	17.88
4	Hg_2CrO_4	8.7
5	Hg_2I_2	28.35
6	$Hg_2(IO_3)_2$	13.71
7	Hg_2HPO_4	12.40
8	Hg_2O	22.8
9	Hg_2S	47.0
10	$Hg_2(SCN)_2$	19.52
11	Hg_2SO_3	27.0
12	Hg_2SO_4	6.17
13	Hg_2SeO_3	14.2
14	Hg_2WO_4	16.96

IV.2.1.c Bivalent mercury (Hg^{2+})

The most common oxidation state of mercury in nature is **2^+**. Inorganic and organic bivalent mercury compounds exist in gaseous, liquid and solid states. Their toxicity, solubility, vapor pressure and reactivity vary significantly. Bivalent mercury is much more prevailing in water medium than in the atmosphere.

It has a strong tendency to form complexes mainly with a coordination number 2 and 4. The compounds with coordination number 5 and 8 are rare. The most stable complexes are those formed with halides (for instance, $(HgX)^{2+}$, HgX_2, $(HgX_3)^-$ and $(HgX_4)^{2-}$), carbon, nitrogen, phosphorus and sulfur. And with cyanides and thiocyanates, we have $[Hg(CN)_4]^{2-}$ and $[Hg(SCN)_4]^{2-}$.

Mercury forms with halogens toxic compounds that are not dissociated in most cases. Mercury (II) iodide HgI_2 exists in two modifications: red (tetrahedral) and yellow (rhombohedral). The transition from the red modification to the yellow one takes place at a temperature of 126 °C;

however, the reverse transition is slow and needs cooling. Mercury (II) chloride $HgCl_2$ are transparent and toxic crystals [6].

Mercury (II) oxide HgO also exists in two modifications: red and yellow. Significant differences in electrical conductivity, dielectric permeability, and magnetic susceptibility of both modifications were found. It can be said that the difference in coloring is caused by the strong network distortion and the defect in the atomic distribution [6].

Mercury (II) sulfide HgS known as cinnabar is the main mercury ore widespread in nature. It exists in two modifications: red and black. HgS is soluble in aqua regia and hot nitric acid [6].

Most mercury salts (II) are soluble. They are as well dissociated as all the alkaline compounds of $NaNO_3$ type. Mercury (II) compounds have the course of positive solubility with increasing temperature **Table IV.3**.

In **Table IV.4**, we can find the stability constants of the mercury (II) complexes in aqueous solutions.

Table IV.4. Stability constants of mercury complexes Hg^{2+} (pK = -logK) [5] .

	pK_1	$pK_{1,2}$	$pK_{1,2,3}$	$pK_{1,2,3,4}$
NH_3	8.8	17.5	18.5	19.3
F^-	1.5	6	-	-
Cl^-	6.74	13.22	14.07	15.07
Br^-	9.05	17.33	19.74	21.00
I^-	12.87	23.82	27.6	29.83
OH^-	10.3	21.70	21.20	-
NO_3^-	0.35	0	-	-
NO_2^-	?	?	?	13.54
SCN^-	?	17.47	19.15	19.77
CN^-	18.0	34.7	38.53	41.51
SeO_3^{2-}	?	12.48	-	-
SO_4^{2-}	1.34	7.3	-	-
SO_3^{2-}	?	24.07	24.06	-
S_2O^{3-}	?	29.86	32.26	33.61
C_5H_5N	5.1	10.0	10.4	-

The most stable complexes are those formed with the ligands (Cl^-, Br^-, I^-) and cyanide (CN^-). Their stability varies from 10^{-18} for CN^- ligand to 10^{-2} for SO_4^{2-} ligand.

Generally, in the nature we distinguish two forms of mercury: waterborne and airborne. A number of mercury existing forms have not been directly analyzed. Actually, some fractions of mercury can be detected based on the collection methods and releasing the elemental mercury after. These forms are called operationally defined fractions. A simplified scheme of the forms of mercury that occurs in water and air is shown in **Figure IV.1** (the major operationally defined fractions are indicated with bold) [2].

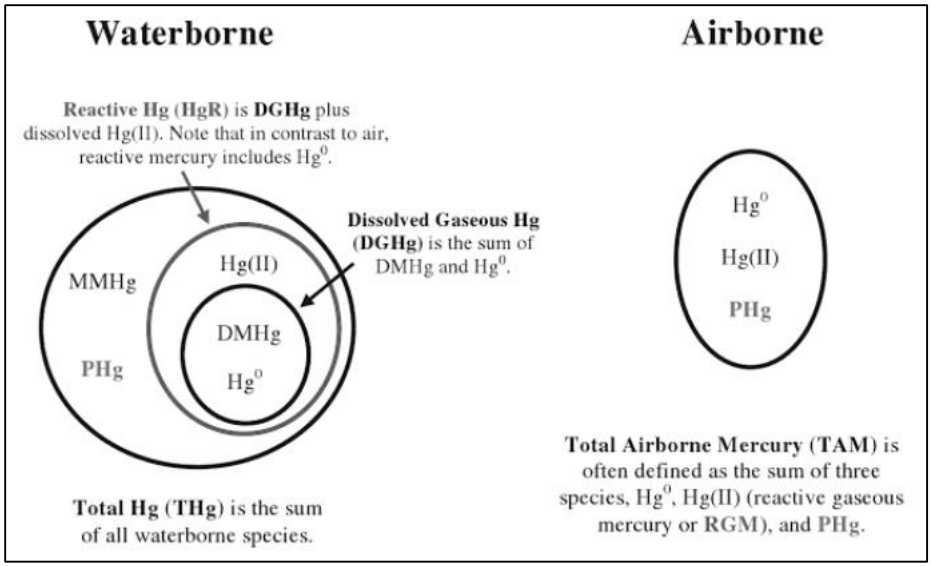

Figure IV.1. A simplified diagram presenting the major chemical forms of mercury found in water and air. DGHg = dissolved gaseous mercury, DMHg = dimethylmercury, HgR = reactive mercury, MMHg = monomethylmercury, PHg = particulate-bound mercury, RGM = reactive gaseous mercury, TAM = total airborne mercury, THg = total mercury [2].

IV.2.1.d Stability of mercury compounds in water

The potential-pH diagram of mercury (also known as the Pourbaix diagram) is presented in **Figure IV.2** (where total mercury concentration is 0.1 mol.L^{-1}). This diagram shows the areas of stable mercury species in aqueous solutions. We can observe four domains:

Domain I: metallic mercury (Hg^0)

Domain II: Hg_2^{2+} species

Domain III: Hg^{2+} species

Domain IV: mercury (II) oxide

All ion-selective electrodes are sensitive to ions, and in our case mercury selective electrodes are sensitive only to Hg^{2+} ions. Thus it is necessary to pay attention to the potential-pH diagram of mercury. It gives us information about the region of pH where mercury electrodes have a stable potential. This pH also avoids precipitation of HgO.

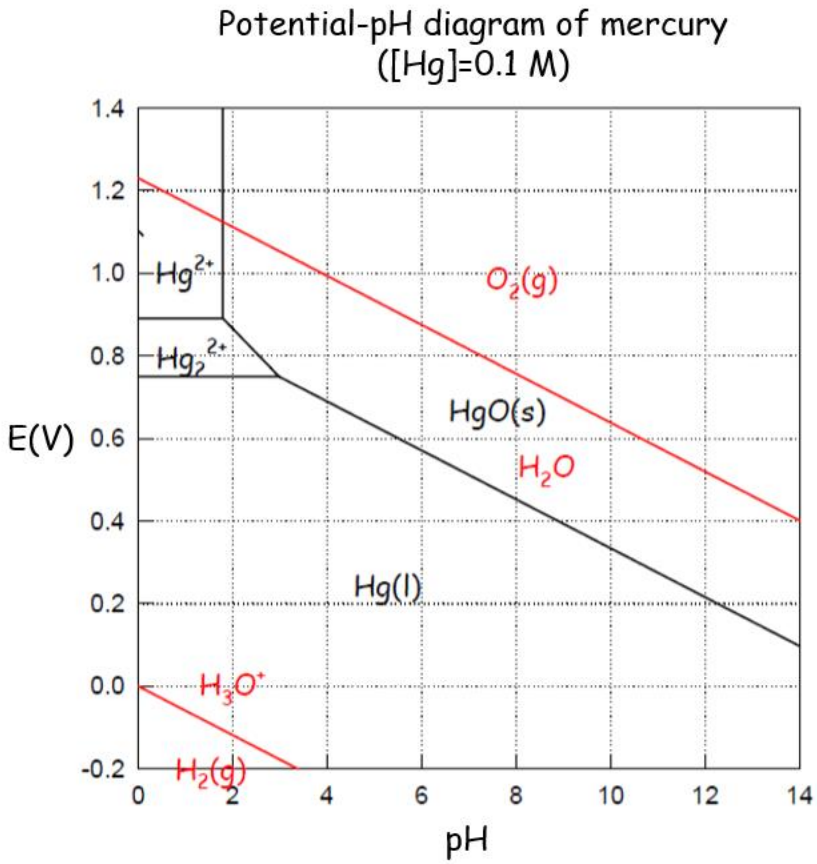

Figure IV.2. Potential - pH diagram of mercury ([Hg] = 0.1 mol.L^{-1}) [7].

An important factor to be taken into account while choosing a suitable analytical method is the recognition that mercury can exist in a wide variety of chemical forms that may or may not be liberated for analysis by the procedures adopted. The various fractions of inorganic Hg(II) that can exist in natural water systems are presented in **Figure IV.3**. The common aqueous species of inorganic Hg(II) in oxygenated freshwater are $Hg(OH)_2^0$ and $HgCl_2^0$. In seawater, the dominant inorganic forms are the chloride species ($HgCl_3^{2-}$, $HgCl_3^-$, etc). In suboxic to anoxic waters, polysulfide species can dominant (e.g. HgS^0) if sulfide concentration levels exceed Hg concentration levels. Hg(II) also strongly interacts with colloids and suspended particles in aqueous systems to form colloidal or particulate-bound Hg forms. Mercury also forms numerous stable complexes with well-defined organic ligands (e.g. ethylenediaminetertraacteic acid EDTA) and with dissolved organic mercury compounds. Biologic transformations can convert Hg(II) to gaseous elemental Hg and methylated Hg forms. In tissues, mercury can be present in both

inorganic and organo-Hg forms, with higher trophic level species, mercury tends to adsorb preferentially to carbon-based particles [2].

So, to perform a meaningful total Hg analysis, it is essential to perform a suitable preparation step to release the Hg from whatever metric or complexes in which it may reside. This removes any matrix interferences with the analysis that result in a biased determination that allows the detection method to quantify the mercury.

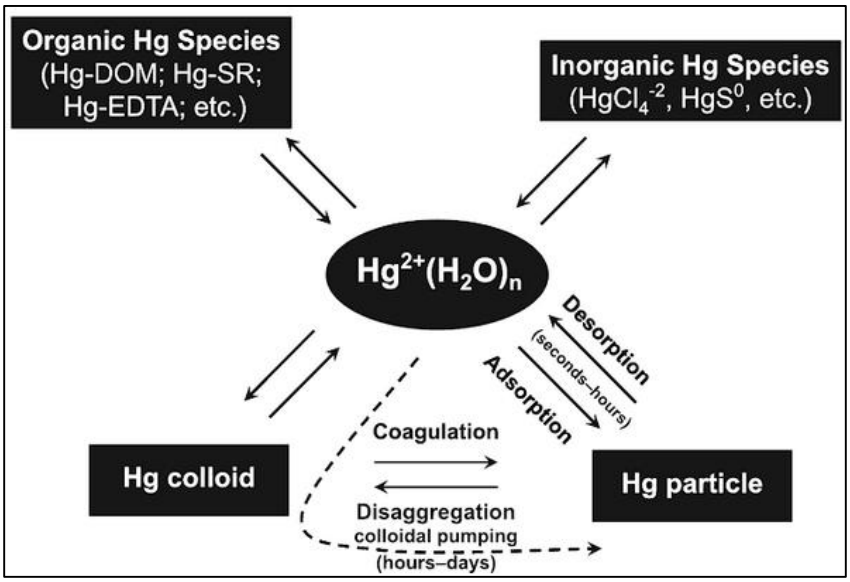

Figure IV.3. Competition for the partitioning of the free mercury ion into various fractions in natural waters [2].

IV.2.2 Toxicity of mercury

IV.2.2.a Natural processes mercury's emitter in the air

The natural processes that emit mercury to the atmosphere are presented in **Table IV.5**. Volcanoes, geothermal vents, and naturally enriched soils release mercury that originated in deep reservoirs, so can be considered purely natural emissions. Quantifying natural sources of mercury in the air is difficult because of the large range of source types, natural variability, concomitance with anthropogenic mercury and the global scale of the problem [2].

IV.2.2.b Anthropogenic sources of mercury in the air

Land emissions, forest fires and oceanic emissions are mixed sources because a significant fraction of their mercury was previously deposited. Anthropogenic sources are believed to emit approximately 2300 Mg/yr of mercury to the atmosphere **(Table IV.5)**. The largest sources, in order of importance, are:

1. coal combustion,
2. gold production,
3. nonferrous metal smelting,
4. cement production,
5. caustic soda manufacturing and
6. waste incineration

Coal combustion is the largest source globally and it is responsible for about 800 Mg/yr, which is nearly two thirds of the global anthropogenic total mercury [8]. In most first-world countries, coal combustion is carried out almost entirely in the industrial and power generation sectors [2].

Table IV.5. Natural and anthropogenic emission sources of mercury to the atmosphere in the world in 2008 [8].

Natural and anthropogenic mercury sources (Mg/yr)			
Natural sources		**Anthropogenic sources**	
Oceans	2682	Coal and oil combustion	810
Lakes	96	Non-ferrous metal production	310
Forests	342	Pig iron and steel production	43
Tundra/Grassland/Savannah/Prairie	448	Cement production	236
Desesrt/Metallifireous	546	Caustic soda production	136
Agricultural areas	128	Mercury production	50
Evasion after mercury depletion events	200	Artisanal gold mining production	400
Biomass burning	675	Waste disposal	187
Volcanoes and geothermal areas	90	Coal bed fines	32
		VCM production	24
		Other	65
Total	**~5207**	**Total**	**~2320**

IV.2.2.c Mercury cycle in nature

The mercury cycle in the environment is quite complex, but an extreme simplification allows describing it as follows [9]:

- In the atmosphere, mercury is predominantly as Hg(0)
- By precipitation, mercury is deposited as Hg^{2+} form in soils and water
- Under the action of microorganisms (sulfate-reducing bacteria) potentially present in lake sludge and rivers, mercury can be transformed by methylation to CH_3Hg^+.

Lake sediments cores and glacial ice cores have been used as historical records of preindustrial and anthropogenic deposition. Mercury's traces and hydrocarbon concentrations in cores reveal the impact of industrialization on air concentrations. They show the increasing deposition of pollutants to the earth and oceans.

A diagram of the simplified global mercury cycle is shown in **Figure IV.4**. The glacial and sediment records show that in the millennium before industrialization, mercury and other metals had relatively a steady deposition flux, i.e. the net flux coming into the atmosphere approximately equaled that deposited to the land and oceans.

The modern, industrial cycle of mercury differs from the preindustrial cycle because of the extraction and mobilization of mercury from deep reservoirs. Anthropogenic activities have greatly increased the mobilization of mercury from deep reservoirs. This enhanced mercury extraction is thought to have increased the total atmospheric burden of mercury by about a factor of 3, which has resulted in deposition to the land and ocean. Increased concentrations in the ocean and land surface have increased emissions back into the atmosphere. Thus, the amount of mercury cycling through the land surface, surface oceans and atmosphere has increased significantly.

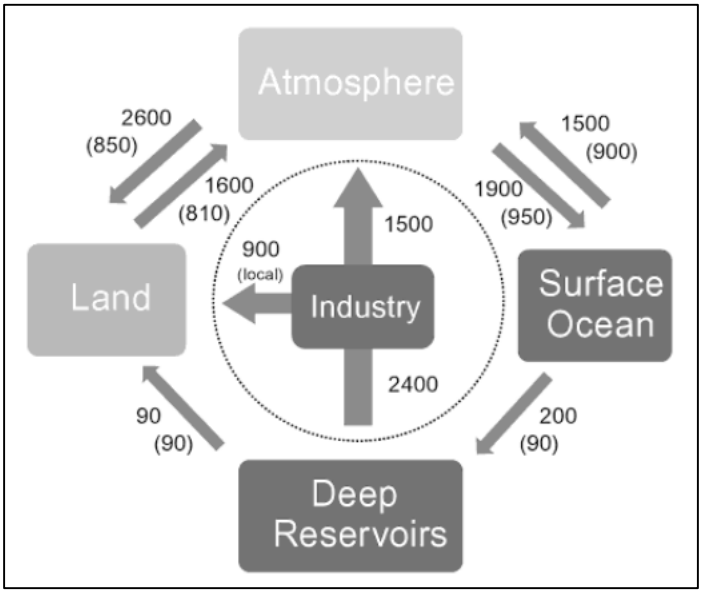

Figure IV.4. A simplified global geochemical mercury cycle. All values are tons per year. Preindustrial values are given in parentheses [2].

The transport and deposition of mercury from the atmosphere is a crucial pathway for contamination in remote ecosystems. Hydrologic transport also plays a role in redistributing mercury, but because of the slower movement and mixing of the oceans, this plays a small role in the enhancement of mercury in remote ecosystems [2].

1. *Aqueous transport*

Rivers play an important role in the transport of mercury from contaminated sites, but have a less significant role in the global cycle. About 1–2 % of the total sources to the ocean come from inputs from the rivers, with dissolved and particle bound mercury being the largest fractions. One study of fate and transport found out that over a course of several months, significant fractions of a newly deposited isotope ^{202}Hg were converted to MMHg and were transported below the water table and toward a neighboring lake by groundwater.

2. *Ocean settling and transport*

The world's oceans play an important role in transporting and redistributing heat throughout the globe, but they do not play as prominent a role for mercury. This is mainly due to (1) the much shorter intrahemispheric mixing time of the atmosphere as compared to the oceans (2) the shorter lifetime of Hg in the surface oceans.

3. *Atmospheric transport*

The majority of direct anthropogenic emissions are from point sources such as coal-fired power plants, municipal waste incinerators, metal refineries and others. The dispersion of these types of plumes are different. For example, gaseous elemental mercury (GEM) is largely unreactive. While reactive gaseous mercury (RGM) are deposited to particles and surfaces, and can be sequestered by cloud and rain drops. Particulate mercury can settle out of the atmosphere or become incorporated into rain and cloud drops. Depending on the ambient conditions and the chemistry of the emitted plumes, some of the RGM may be reduced to GEM.

4. *Continental export and long-range transport*

Large polluted air masses can be exported from their source region, and then transported and dispersed over thousands of kilometers in the jet stream through their interaction with a midlatitude cyclone. The studies conducted and modeling studies have confirmed the long-range transport of Hg seen in observations.

5. *Global transport*

Once polluted airmasses are lofted into the jet stream, they can circle the northern hemisphere in as little as 7-10 days and will generally be dispersed in the midlatitude pollution belt in 1-2 weeks. During transport, the airmasses tends to be stretched into long filaments and begin mixing into the global background.

IV.2.2.d Health risks of mercury exposure

All forms of mercury are toxic. Particularly problematic are the organic forms such as methylmercury, which diffuses easily through the biological membranes and it is a neurotoxin.

Monoatomic vapors of mercury diffuse through the lungs and they enter in the bloodstream. There, they interact with the proteins and form complexes. The last one makes serious changings in the central nervous system [9].

Acute mercury exposure can produce permanent damage to the nervous system. It results in various symptoms such as paresthesia, ataxia, sensory disturbances, tremors, blurred vision, slurred speech, hearing difficulties, blindness, deafness and death. In addition to neurotoxicity, mercury, in its inorganic and/or organic forms can affect other systems and sequentially cause adverse effects including renal toxicity, myocardial infraction, immune malfunction and irregular blood pressure [10]. Regular absorption of lower concentrations causes polyuria among adults and acrodynia among children, together with other symptoms such as irritability, insomnia, photosensitivity and redness [11].

Historically, one of the notorious poising episodes associated with the extremely high methylmercury exposures, that is, in Minamata, Japan where individuals were poisoned by MeHg through consumption of contaminated fish. This has resulted in the death of more than 1,000 people. Now this poisoning is known by the Minamata disease [12].

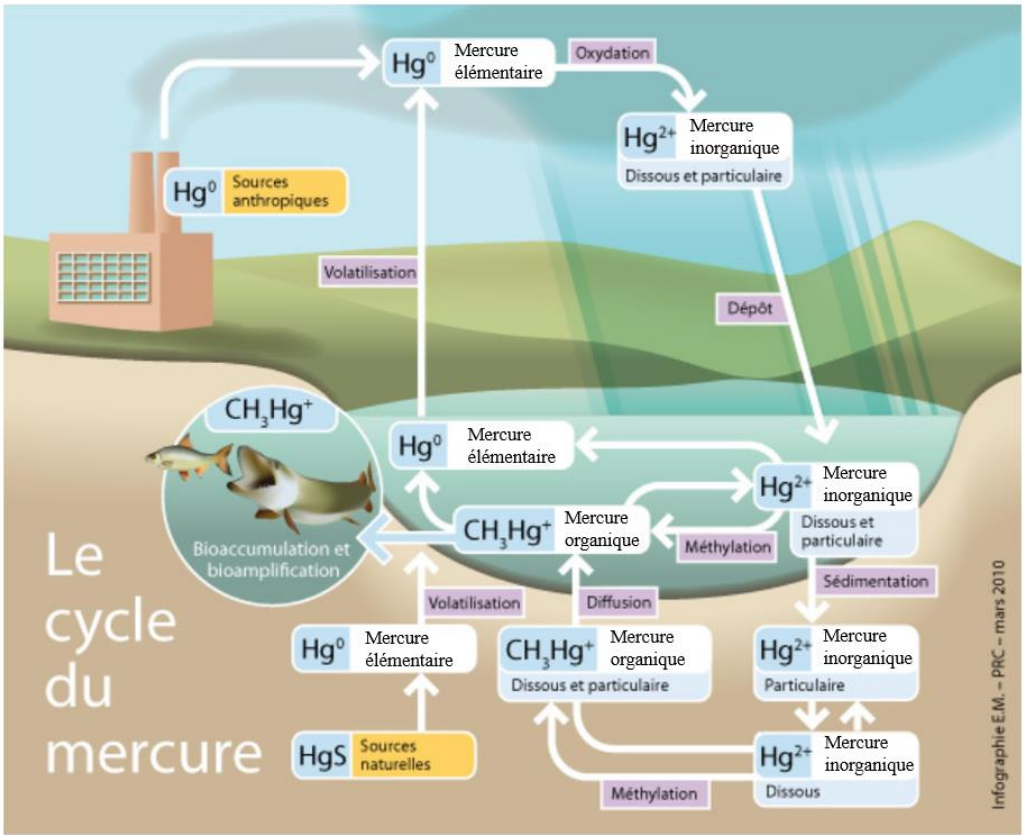

Figure IV.5. Mercury cycle in the environment [13].

The French Institute for Research and Safety (in French: Institut national de recherche et de sécurité, INRS) and French legislations define the threshold limit values (or « les valeurs moyennes d'expositions », VME) which are the limiting concentration values of the chemical agents to which a person may be exposed to, over the duration of a workstation (8h/day) [14] **(Table IV.6)**.

Table IV.6. Concentration limit values of mercury and its derivatives.

	Limit concentration ($mg.m^{-3}$),($ng.L^{-1}$),($mg.L^{-1}$),($\mu g.L^{-1}$)	**Notes**
Bivalent inorganic mercury compounds	0.02 $mg.m^{-3}$ [14]	
Alkyl compounds (of Hg)	0.01 $mg.m^{-3}$ [15]	
Aryl compounds (of Hg)	0.1 $mg.m^{-3}$ [15]	
Mercury in drinking water	1 $\mu g.L^{-1}$ [16]	5.0 x 10^{-9} $mol.L^{-1}$
Mercury in rainwater	0.05 to 0.5 $ng.L^{-1}$ [17]	
Mercury in industrial water	0.1 $mg.L^{-1}$ [18]	5.0 x 10^{-7} $mol.L^{-1}$

IV.2.3 Chemical and physio-chemical methods for the analysis of mercury

There are numerous analytical techniques for the analysis of mercury species in environmental and biological samples. The traditional and modern reported approaches to detect Hg^{2+} in aqueous samples can be listed as follows:

- Gravimetry
- Volumetry
- Colorimetry
- Spectroscopy
- Electrochemical analysis

The gravimetric methods for mercury determination are carried out by precipitation in the form of insoluble compounds:

1. Mercurous (I) compounds are in the form of calomel (Hg_2Cl_2 K_{sp} = 1.3 x 10^{-18}) [5]
2. Mercuric (II) compounds are in the form of sulfide (HgS K_{sp} = 1.6 x 10^{-52}) [5]

Mercuric sulfide HgS is about 3 times less soluble than mercuric chloride Hg_2Cl_2 so the detection limit of the second method is lower.

The precipitates obtained are very stable and can be easily dried and weighed. The minimum weight of sample weighed is 0.001 mg for balances with high accuracy (microbalances and ultra-microbalances).

The volumetric methods are realized by titration in the presence of a specific indicator [19]:

1. **Titrant**: potassium thiocyanate KCNS (0.1 M)
   Indicator: iron alum $KFe(SO_4)_2$
   The titration of the mercuric solution realized in acidic medium is carried out in the presence of the indicator until the appearance of stable pale brown color.
   1 ml of thiocyanate solution (0.1 M) corresponds to 10.03 mg of mercury.

2. **Titrant**: hydrochloric acid HCl (0.1 N)
   Indicator: phenolphtalein solution in alcohol (0.1%):
   $HgO\downarrow + 4KI + H_2O \rightarrow K_2[HgI_4] + 2KOH$ (1)
   $2KOH + 2HCl \rightarrow 2KCl + 2H_2O$ (2)

The titration is performed according to the chemical reactions (1 and 2). KOH is neutralized by HCl in the presence of phenolphtalein.

The colorimetric methods are carried out using a colored compound [19]:

1. One of the colorimetric methods is based on the reaction of mercury with the iodine solution in potassium iodide:

   $KI + J_2 \rightarrow$ solution (3)

   $Hg + J_2 \rightarrow HgJ_2$ (4)

   $HgI_2 + KI \rightarrow K_2[HgI_2]$ (5)

   $CuSO_4 + K_2[HgI_2] \rightarrow Cu_2[HgJ_4] + K_2SO_4$ (6)

   By using copper sulfate $CuSO_4$, a copper (I) tetraiodomercurate (II) complex salt is obtained with a red-pinkish color. The intensity of this coloration is compared with the standard colorimetric calibration measured in advance. The detection limit – 0.2 µg in volume measured in corresponding cuvette (ref).
2. Another method is based on the reaction between dithizone (0.001% solution in carbon tetrachloride CCl_4) and mercury ions in the presence of an acetate buffer solution (sodium acetate dissolved in acetic acid) and ethylenediamine tetra-acetic acid disodium salt. One obtains mercury dithiozionate complex of a yellow-orange color. The mercury content is calculated according to the calibration curve measured in advance. The detection limit - 0.05 mg/kg (ref).

The main disadvantages of these three methods of mercury dosing are their insufficient sensitivities and the impossibility to use them outside the laboratory.

The spectroscopic methods: The very often used analytical techniques in industry to determine the mercury content in natural waters at the picogram level are the spectroscopic techniques **(Table IV.7)** which are based on:

- Cold-vapor atomic absorption spectroscopy (CVAAS);
- Cold-vapor atomic fluorescence spectroscopy (CVAFS);
- Inductively coupled plasma-mass atomic emission spectrometry (ICP-AES);
- Inductively coupled plasma-mass spectrometry (ICP-MS);
- Atomic absorption spectroscopy (CVAAS).

Of these, CVAAS is the most widespread method; however, CVAFS is rapidly replacing CVAAS because of its superior detection limits [2].

Table IV.7. Selected methods for the analysis of mercury in water matrix [2].

Analyte	Detector	Reference or EPA method	Typical MDL (ng/L)
Total Hg	CVAAS	EPA method 245.1	5-10
Total Hg	CVAFS	EPA method 245.7	0.5-5
Total Hg	CVAFS	EPA method 1631	0.1-0.3
Total Hg	ICP-MS	EPA method 200.8	10
Total Hg	ICP-AES	EPA method 200.7	200
Elemental Hg	CVAFS	EPA method 1631	0.1-0.3
Reactive Hg	CVAFS	EPA method 1631	0.1-0.3
MMHg	CVAFS	EPA method 1630	0.01-0.05

The detection limits of the spectroscopic methods are quite low. However, they are limited in their extensive applications due to:

- the cost of the devices which is often very high;
- the impossibility to use them locally and continuously;
- complex sample pretreatment processes;
- the fairly substantial number of interferences including copper, sulfides or organic solvents.

Electrochemical methods:

There are three main categories of electrochemical methods: potentiometry, coulometry and voltammetry.

Regarding potentiometry, chemical sensors are widely used for the determination of different types of ions. Particularly, ion-selective electrodes with polycrystalline membrane are commercially available. **Table IV.9** presents the producers and types of membranes.

Table IV.8. Detection limits of some ion-selective electrodes [20]–[25].

	10^{-8} mol/L	**10^{-7} mol/L**	**10^{-6} mol/L**	**10^{-5} mol/L**
«Radiometer Analytical»	-	CN^-, F^-, S^{2-}	Br^-, Ca^{2+}, Cl^-, $Cu2^+$, I^-, K^+, Na^+, NH_4^+, NO_3^-, Pb_2^+	-
«Orion»	Cu^{2+}, I^-	NH_3, NH_4^+, Cd^{2+}, Ca^{2+}	Br^-, CN^-, F^-, BF_4^-, Pb^{2+},NO_3^-,NO_2^-,ClO_4^-, K^+, Na^+, SCN^-	Cl^-
«Radelkis»	-	I^-	Br^-, CN^-, F^-, S^{2-}, SCN^-, K^+, NH_4^+, Na^+	Ag^+, Cl^-, Ca^{2+}, NO_3^-
«Hach-Lange»	-	NH_3, F^-,	NH_4^+ , Cl-, NO_3^-, Na^+	-
«NICO 2000»	Cu^{2+}, Ag^+, S^{2-}	Ca^{2+}, Cd^{2+}, I^-	NH^{4+}, Ba^{2+}, Br^-, CN^-, F^-, Pb^{2+}, Hg^{2+}, NO_3^-, ClO_4^-, Na^+	Cl^-, NO_2^-, K^+, SCN^-
«Van London Co.»	Cu^{2+}	Cd^{2+}, I^-, Ag^+, S^{2-}	F^-, Pb^{2+}, K^+, Na^+,	NH_4^+, Br^-, Ca^{2+}, CN^- , NO_3^-, ClO_4^-, BF_4^-, NO_x

Table IV.9. Available commercial electrodes.

Ions	«Radiometer Analytical»	«Orion»	«Radelkis»	«Hach-Lange»	«NICO 2000»
	Type de membrane				
Ag^{2+}	-	-	AgS	-	AgS
Hg^{2+}	-	-	-	-	HgS/Ag_2S
Ba^{2+}	-	-	-	-	PVC
NH_3 CO_2 NO_2	-	Sensors sensitive to different gases	-	Sensors sensitive to NH_3	
Ca^{2+}	PVC	PVC	PVC	-	PVC
Cd^{2+}	CdS/Ag_2S	CdS/Ag_2S	-	-	CdS/Ag_2S
Br^-	$AgBr/Ag_2S$	$AgBr/Ag_2S$	$AgBr/Ag_2S$	-	$AgBr/Ag_2S$
Cl^-	$AgCl/Ag_2S$	$AgCl/Ag_2S$	$AgCl/Ag_2S$	$AgCl/Ag_2S$	$AgCl/Ag_2S$
CN^-	$AgCN/Ag_2S$	$AgCN/Ag_2S$	$AgCN/Ag_2S$	-	$AgCN/Ag_2S$
Cu^{2+}	CuS/Ag_2S	CuS/Ag_2S	-	-	CuS/Ag_2S
F^-	LaF_3(doped with Eu^{3+})	LaF_3(doped with Eu^{3+})	LaF_3(doped with Eu^{3+})	LaF_3(doped with Eu^{3+})	LaF_3(doped with Eu^{3+})
I^-	AgI/Ag_2S	AgI/Ag_2S	AgI/Ag_2S	-	AgI/Ag_2S
K^+	PVC	PVC	PVC	-	PVC
Na^+	Verre silicate	Verre silicate	Verre silicate	Verre silicate	PVC
NH_4^+	PVC	PVC	PVC	PVC	PVC
NO_3^-	PVC	PVC	PVC	PVC	PVC
NO_2 -	-	PVC	-	-	PVC
Pb^{2+}	PbS/Ag_2S	PbS/Ag_2S	-	-	PbS/Ag_2S
S^{2-}	Ag_2S	Ag_2S	Ag_2S	-	Ag_2S
BF_4^-	-	PVC	-	-	-
SCN-	-	$AgSCN/Ag_2S$	$AgSCN/Ag_2S$	-	$AgSCN/Ag_2S$
ClO_4^-	-	PVC	-	-	PVC

There is only one company which produces a commercial polycrystalline electrode for the detection of mercuric ions (Hg^{2+}). This membrane is based on the mixture of two compounds (Ag_2S+HgS) with a detection limit of 200 $\mu g.L^{-1}$ (1.0×10^{-6} $mol.L^{-1}$) [26]. The advantages of this technology are:

- the low cost (≈ 500 € for one piece);
- very simple fabrication.

The principle limitation of such electrodes is the detection limit.

Generally, all ion-selective electrodes have higher detection limits than many other techniques **(Table IV.8)**.

IV.2.4 Chemical sensors

The chemical sensors allow detecting ionic species in aqueous and non-aqueous mediums. The most important part of a sensor is the sensitive membrane. **Figure IV.6** shows the diagram of classification of ion-selective electrodes [27].

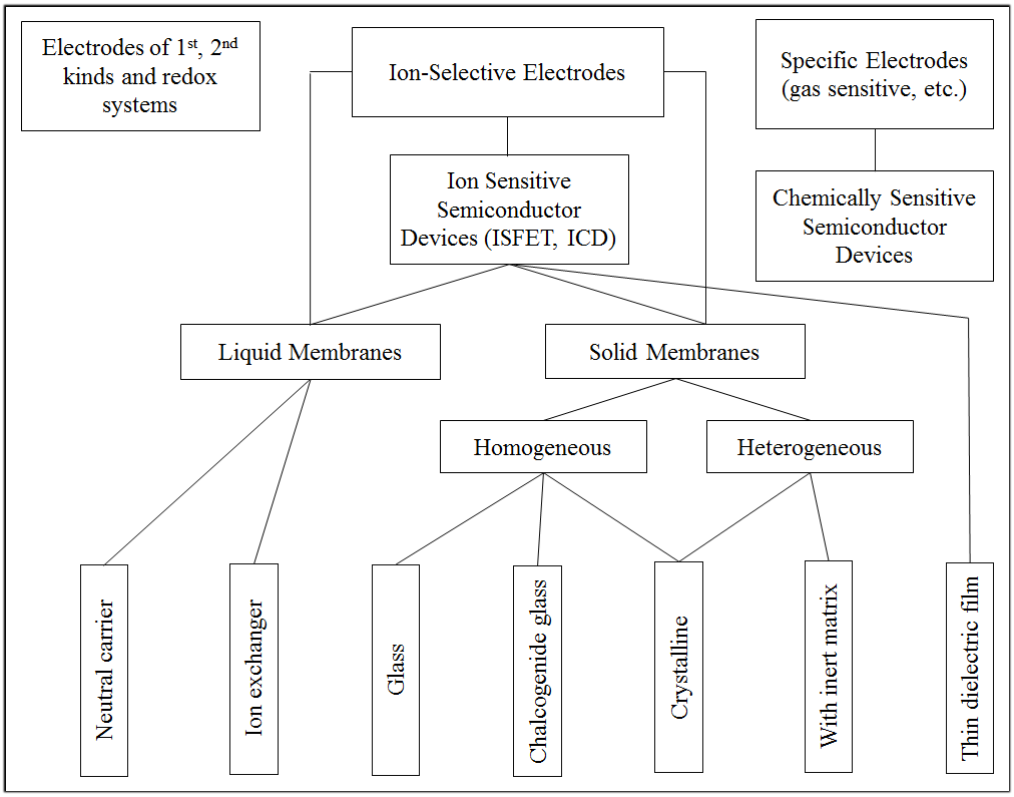

Figure IV.6. Scheme of the classification of chemical sensors [27].

IV.2.4.a Ion-selective electrodes

Membrane electrodes can be: (a) selective to ions and (b) selective to molecules.

The ion-selective electrodes can be subdivided into four major categories: liquids, solids, gases and thin films.

Liquid membranes can be neutral carriers and ion-exchangers. And solid membranes can be homogeneous and heterogeneous. In the group of homogeneous membranes, we can put glass, chalcogenide glass and crystalline. The heterogeneous group can be divided into crystalline and with inert matrix.

The working of ion-selective membranes is provided by the existence of electrical conductivity. The last one ensures the ion transport and ion-exchange, which explains the working mechanism.

1. Liquid membranes [28]

Liquid membrane electrodes are based on active substances generally some organic compounds (for instance, valinomycin sensitive to potassium ions K^+) which are dissolved in organic solvents and suitable polymers (polyvinylchloride (PVC)). Sensors with liquid membranes are generally divided into two groups depending on the type of active substance:

- ion exchanger and
- neutral carrier.

The detected ions are transported through the membrane to crown compounds. They have some weak points:

- not sufficiently good selectivity coefficients
- the leaching of the active substances
- possibility to work only in neutral pH.

2. Solid membranes

The solid membranes are divided into two subgroups, homogeneous and heterogeneous membranes. Unlike liquid membranes, solid membranes generally exhibit a little interference with other ions. Indeed, there will be interference only if the interfering ion can interact with the membrane or if a chemical reaction takes place between the membrane and the solution [29].

1- Homogeneous

Silicate glasses

The first ion-selective electrode was the pH electrode from the silicate glass [30]. This composition (72% of SiO_2, 21.3% of Na_2O, 6.4 % CaO) is the basic for the pH electrodes. But it does not work very well in all regions of pH, that's why it was changed many times to find the best composition for pH greater than 10.

There are many advantages of the glass electrodes such as:

- short response time,
- simplicity of calibration,
- reproducibility of the measurement,
- the possibility of use in oxidizing and reducing mediums,
- utilization in very small volumes,
- utilization at high temperatures.

However, there are some limitations; for instance, the electrode cannot be used in a hydrofluoric acid environment (glass attack), in a rigorously anhydrous medium (destruction of the hydrated thin ion exchange layer).

Chalcogenide glasses

The mechanism of detection of ion-selective electrodes with homogenous membranes from chalcogenide glasses are mostly the same as for the glass electrodes. Practically, a thin layer (5 to 100 nm) [31] is formed on the surface of the glass membrane when it is placed in the solution. The potential difference of the ionic exchange is measured. It corresponds to the thermodynamic activity of the ion.

There is not yet a chemical sensor with chalcogenide glass membrane in commerce. However, membranes based on chalcogenides and chalcohalides are promising materials for the detection of heavy metal ions (Hg^{2+}, Cu^{2+}, Cd^{2+}, Pb^{2+}, Tl^{+}, ..) and toxic anions (S^{2-}, CN^{-}, AsO_4^{3-}) compared to the commercially available devices due to several reasons:

- Ionic and/or electronic conductivity
- Stability
- Good selectivity coefficient

Crystalline

A well-known example of ion-selective electrodes with a homogeneous solid crystalline membrane is the fluoride ion selective electrode. The membrane consists of a single crystal of lanthanum fluoride (LaF_3) doped with europium fluoride (EuF_2), the last one creates gaps which facilitates the ionic transport in the crystal structure. This homogeneous crystal is an ionic conductor specific to fluoride ions whose diffusion involves successive jumps in the vacancies created. A fluoride salt solution is used as an internal reference solution. In this example, the main interfering ion is the OH^- ions because it reacts with the lanthanum to form lanthanum hydroxide. Therefore, these electrodes should be used in the presence of an acidic buffer solution to maintain a low concentration of OH^- ions [32], [33].

2- *Heterogeneous*

Crystalline

Ion-selective electrodes can be based on Ag_2S-MS or Ag_2S-AgX (X = halogen) [34]. In this case, the membrane is in the form of a polycrystalline heterogeneous pellet. It is used for the dosage of M^{2+} ions (for example, M = Cu, Pb, Cd, Hg). However, in these membranes, an oxidation of the electrode is observed over time.

Inert matrix

It is possible to make an ion-selective membrane by incorporating small crystals in an inert matrix (silicon rubber, polymer) whose role is to serve as a binder so that the heterogeneous membrane thus produced can be easily elaborated.

IV.2.5 Mercury-selective electrodes in the literature

So far, a quite number of studies have been carried out by various research groups on mercury ion-selective electrodes due to the inconveniences of the classical and spectroscopic methods (Section IV.2.3). We present below an overview of these studies **(Table IV.10)**.

IV.2.5.a Liquid membranes

Most of the work found in the literature concerns liquid membranes consisting of an organic molecule (neutral carrier or ion exchanger) embedded in a polymer, generally PVC. These sensors,

in general, all have common disadvantages: possess a short-life time which extends to a maximum of a few months and the presence of interfering ions.

Table IV.10. Different types of liquid membranes and their characteristics.

Membrane composition incorporating	Linear range (mol.L^{-1})	Sensitivity (mV/decade)	Detection limit (mol.L^{-1})	pH	Selectivity $K^{Pot}_{Hg,M}$	Lifetime (months)
organic molecule having diamine group [35]	1.25×10^{-5}–1.0×10^{-1}	25	8.9×10^{-6}	6.6–9.3	High selectivity over many M^{+}, M^{2+}, M^{3+} Ag^{+}, Cd^{2+}: no interference	4
***N,N′*-bis(salicylaldehyde)-phenylenediamine [36]**	3.2×10^{-7}–3.2×10^{-4}	58.8	1.5×10^{-7}	3.8–7.8	Good selectivity over M^{+}, M^{2+}, M^{3+} and heavy metals (10^{-1}–10^{-5})	-
Salicylaldehyde thiosemicarbazone [37]	1.78×10^{-6}–1.0×10^{-1}	29	1.0×10^{-6}	1.0–0.3	Good selectivity over alkali, alkaline and some heavy metals ions (10^{-3}–10^{-4})	2
poly-o-toluidine Zr(IV) phosphate [38]	1.0×10^{-6}–1.0×10^{-1}	30	1.0×10^{-6}	2–8	Selective in the presence of interfering cations	4
N,N-dimethylformamide-salicylacylhydrazone [39]	6.2×10^{-7}–8.0×10^{-2}	29.6	5.0×10^{-7}	1–4	Good selectivity over many cations	< 2
p-tert-butyl calix[4]crown with imine units [40]	5.0×10^{-5}–1.0×10^{-1}	27.3	2.24×10^{-5}	1.3–4.0	Good selectivity over alkali, alkaline and heavy metals ions ($10^{-1.69}$–$10^{-3.67}$) Ag^{+}: strong interference	-

IV.2.5.b Solid membranes

Earlier, solid membrane-based sensors were already produced for the detection of Hg^{2+}. However, in all the cases, the selected membrane is a chalcogenide glass containing mercury ions. For example, while Golikov *et al.* [41] designated a glass system of HgI_2-Ag_2S-As_2S_3, Tohge [42] and Guessous [43] chose the glass system $Ge_{0.2}Te_{0.3}Se_{0.5}$ and they respectively introduced HgS and

HgTe in it. The synthesized sensors present good selectivities, but a poor detection limit (5×10^{-6} M).

Although it was first admitted that the sensitive membrane should contain the ion to be detected, Vlasov has shown that Ag-As-Se glass system was sensitive to the Cu^{2+} ions [44]. Morf also indicated that crystalline AgX (X = Cl, Br, I) is sensitive to Hg^{2+}. Based on these findings, Pradel *et al.* [45] decided to test glasses based on the AgBr-Ag_2S-As_2S_3 system as sensitive membranes to Hg^{2+}. The Hg^{2+} sensing system with a thin film sensitive membrane from the system AgBr-Ag_2S-As_2S_3 exhibit very interesting performances with a very low detection limit (2 ppb), a very high sensitivity in the presence of interfering ions and a good stability. The potentiometric response of these membranes presents two domains with different slopes at low and high concentrations. ^{110}Ag tracer experiments show two different mechanisms of Ag^+ ion release at low and high silver concentrations, and therefore the two different potential-generating reactions govern the Hg^{2+} ion response. Based on the following observations, two different values of the power-law exponent (s), characterizing the dynamics of silver loss, and changes in the mercury concentration at the membrane surface at low (10^{-6} M) and high (10^{-5} M) Hg^{2+} concentrations. These are consistent with the change of the Hg^{2+} ion response slope above a critical concentration of ca. 3×10^{-6} M $Hg(NO_3)_2$. Below this threshold concentration, it is suggested that a simple ion-exchange process between the mercuric ions in the solution and the silver ions at the surface of the membrane (sensitivity of 30 mV/decade) governs the sensor response. In this concentration range, an ideal mixed (Hg, Ag) active phase is formed at the membrane surface.

Above the threshold concentration, two phases could coexist at the membrane surface due to chemical reactions between mercury and silver species (sensitivity = 100 mV/decade up to 10^{-3} M and 60 mV/decade above that). The lifetime of these sensors represent a major asset since they can operate for several years without special maintenance but with cleaning the membrane surface from time to time.

In this framework, **Table IV.11** shows the detection limit and sensitivity for some bulk silver halide-based sensors.

Table IV.11. Sensitivity and detection limit for some bulk silver halide-based sensors for Hg detection in the literature.

Sensors' compositions	DL (mol. L^{-1})	Sensitivity (mV/decade)		
		S1	S2	S3
$(HgI_2)_{20}(Ag_2S)_{40}(As_2S_3)_{40}$ [46]	1.0×10^{-7}	12		60
$(AgI)_{45}(HgS)_{27.5}(As_2S_3)_{27.5}$ [47]	1.0×10^{-8}	16	58	25
$(AgBr)_{60}(Ag_2S)_{25}(As_2S_3)_{15}$ [46]	5.0×10^{-7}	30	100	60
$(AgBr)_{60}(Ag_2S)_{20}(As_2S_3)_{20}$ [47]	6.16×10^{-6}		54	

IV.2.6 Basic principles of the potentiometric methods

In this paragraph, we will present some generalities about potentiometric methods.

IV.2.6.a Electrochemical cell

The measurement system which is simply an electrochemical cell **(Figure IV.7)** comprises:

a) A reference electrode which has a constant potential E_R whatever is the solution studied;
b) An indicator electrode (or a chemical sensor) whose potential E_M is as a function of the concentration (ionic activity) of the medium.

The requirements that should be met by the reference electrode and the indicator electrode are detailed below.

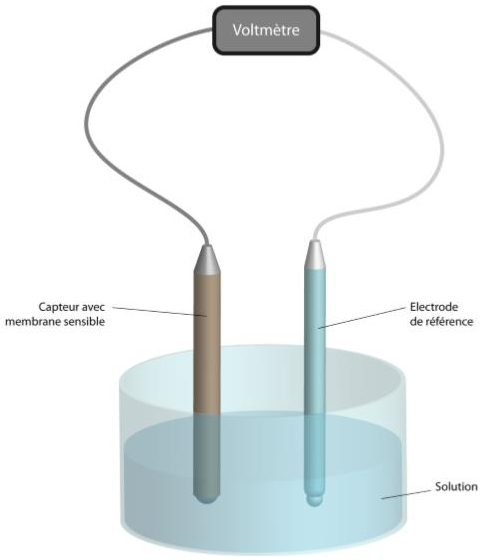

Figure IV.7. A simplified electrochemical cell.

The potential of the indicator electrode E_M can be written in terms of the activity of the ion to which it is responding by means of the Nernst equation:

$$E_M = E^0 \pm \frac{RT}{z_i F} \ln a_i \qquad \text{(IV.1)}$$

Where:

a_i the activity of the measured ionic species;
E^0 standard potential of the membrane;
R gas constant (8.314 $J.K^{-1}.mol^{-1}$);
T absolute temperature in Kelvins;
F Faraday's constant (96485 Coulomb);
z_i charge of the measured ionic species

By replacing the activity a_i of the ion i by the concentration c_i and the coefficient γ_i ($a_i = c_i \gamma_i$), we obtain:

$$E_M = E^0 \pm 2.303 \frac{RT}{z_i F} log(c_i \gamma_i) \qquad \text{(IV.2)}$$

In other words, the typical electrochemical cell can be represented as follows:

Ag, AgCl | KCl (s) || KNO_3 (0.1M) || sample | membrane| lq.cont. | Ag, AgCl,
E_{R1} E_{J1} E_{J2} E_M E_{R2}

Where:

Ag, AgCl | KCl (s)	Ag reference electrode
KNO_3 (0.1M)	liquid salt bridge
sample	analyzed solution
membrane|	mercury ion-selective electrode
lq.cont. | Ag,AgCl	Ag reference electrode in liquid contact

The total measured potential between the two electrodes of the cell is evidently composed from:

$$\boldsymbol{E = E_{R1} + E_{R2} + E_{J1} + E_{J2} + E_M} \qquad \text{(IV.3)}$$

Where:

E	cell potential (emf)
E_{J1}, E_{J2}	diffusion potentials
E_{R1}	potential of the reference electrode
E_{R2}	potential of the reference electrode (from the liquid contact)
E_M	membrane potential

Assuming that

$$E_{R1} + E_{R2} + E_{J1} + E_{J2} = constant \qquad \text{(IV.4)}$$

therefore, the overall potential difference becomes identical to that of equation (IV.2). However, one should not forget that the diffusion potential is not always constant.

Thus the emf of the cell reflects the three electrical potential contributions (diffusion potentials and membrane potential) that are influenced by the sample solution.

1. Liquid junction potential

The liquid junction potential results from contact between two liquids with different compositions and concentrations. This is the weak point of measurements with ion-selective electrodes.

The mechanism of formation of the liquid junction potential is schematized in **Figure IV.8**. When ions in zones A_1 and A_2 have different mobilities, then the activities a_1 and a_2 are different. In this case, we have uncompensated charges at the interface forming a liquid junction potential E_J.

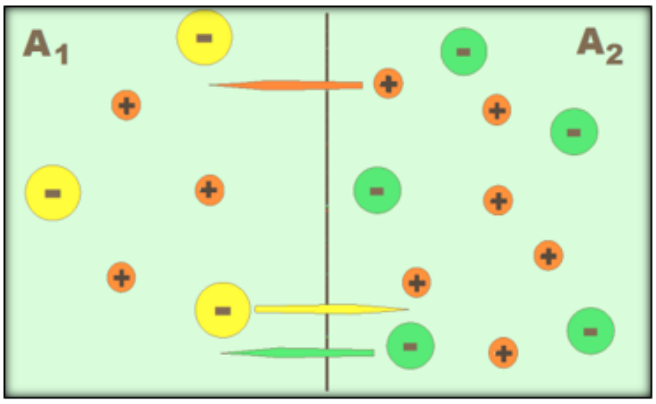

Figure IV.8. Schematization of the formation of liquid junction potential at the interface between two solutions A_1 and A_2.

The existence of a liquid junction potential on the border between two electrolytes often complicates the experimental measurements, because E_J can have significant and variable values. In other words, the global potential E is not described precisely by equation (IV.2) but by

$$E = E_R + E_{J1} + E_{J2} + E_0 + 2.303\frac{RT}{z_i F} log(c_i \gamma_i) \quad \text{(IV.5)}$$

For direct measurements of the liquid junction potential E_J, we must know the ion coefficient activity. But to measure the ion coefficient activity, we must know E_J. This is a thermodynamically indefinite situation. There are three possible solutions to solve this problem:

(a) Minimize the liquid junction potential by using the appropriate construction and appropriate solution of the salt bridge;
(b) Have a constant liquid junction potential using a support solution with ionic strength at least ten times higher than the concentration of the measured solution;
(c) Estimate the liquid junction potential using the Henderson equation:

$$E_J = -(RT/F)\int_1^2 \sum (t_i/z_i)\partial \ln a_i \quad \text{(IV.6)}$$

where t_i is the transport number of the i-th ion, 1 and 2 representing the two solutions forming the E_J.

We chose the (b) and as a support solution we use the potassium nitrate.

2. Reference electrode

The good results can be obtained when reference electrodes respond to the following conditions:

1. They have to be reversible. Their reversibility can be estimated by the value of the ion-exchange current between the reference electrode and the electrolyte, which should be very high.
2. They have to be reproducible, i.e. their potential should not change under the same conditions. The hysteresis phenomena should not exist.
3. The potential of the reference electrode has to be independent on the concentration of the ionic species present in the measured solution.
4. The stability of the potential on the long-term has to be high.

The commercial calomel electrode (Hg, Hg_2Cl_2 | KCl_{satd}), and the silver/silver chloride (Ag, AgCl | KCl_{satd}) correspond perfectly to all these conditions and can therefore be used as reference electrodes. In some cases, ion-selective electrodes which are very stable can be used as a reference electrode (this is the case of the fluoride ion-selective electrode).

3. Indicator electrode

The conditions imposed on the reference electrodes are also valid for the indicator electrodes, except the third point. The indicator electrode must be sensitive to the measured ionic species. There are several types of chemical sensors **(Figure IV.6)** as described previously. Our sensors possess a selective membrane based on chalcogenide glasses.

IV.2.6.b Hydrogen electrode

1. Determination of standard hydrogen electrode

The standard hydrogen electrode is a redox electrode that forms the basis of the thermodynamic scale of oxidation-reduction potentials. Its absolute electrode potential is estimated to be 4.44±0.02 V at 25 °C, but to form a reference for comparison with all other electrodes. Hydrogen's standard electrode potential (E^0) is declared to be zero volts only at 298 K [48]. Potentials of any other electrodes are compared with that of the standard hydrogen electrode at the same temperature. Hydrogen electrode is based on the redox half cell:

$$H^+(aq) + e \rightleftharpoons \frac{1}{2}H_2(g) \qquad \text{(IV.7)}$$

This redox reaction occurs at an inert but catalytically active metal surface consisting of a platinum electrode. The electrode is dipped in an acidic solution and pure hydrogen gas is bubbled through it. The concentration of both the reduced and oxidized forms is maintained at unity. That implies that the pressure of hydrogen gas is 1 bar (100 kPa) and the activity of hydrogen ions in the solution is unity. The activity of hydrogen ions is their effective concentration, which is equal to the formal concentration times the activity coefficient. These unit-less activity coefficients are close to 1.00 for very dilute water solutions, but usually lower for more concentrated solutions. The Nernst equation can be written as:

$$E = \frac{RT}{F} \ln \frac{a_{H^+}}{\sqrt{P_{H_2}/P^0}} \quad \text{(IV.8)}$$

$$E = -2.303 \frac{RT}{F} \text{pH} - \frac{RT}{2F} \ln\left(\frac{P_{H_2}}{P^0}\right) \quad \text{(IV.9)}$$

Where:

a_{H^+} activity of the hydrogen ions, $a_{H^+} = f_{\text{H}^+} C_{\text{H}^+} / C^0$

P_{H_2} partial pressure of the hydrogen gas, in pascals, Pa

R universal gas constant

T temperature, in kelvins

F Faraday constant (the charge per mole of electrons), equal to 9.6485309×10^4 C mol^{-1}

P^0 standard pressure, 10^5 Pa

2. *Difference between the normal hydrogen electrode (NHE) and the standard hydrogen electrode (SHE)*

During the early development of electrochemistry, researchers used the normal hydrogen electrode as their standard for zero potential. This was convenient because it could *actually be constructed* by immersing a platinum electrode into a solution of 1 N strong acid and bubbling hydrogen gas through the solution at about 1 atm pressure. However, this electrode/solution interface was later replaced by a theoretical electrode/solution interface, where the concentration of H^+ was 1 M, but the H^+ ions were assumed to have no interaction with other ions (a condition not physically attainable at those concentrations). Yet to differentiate this new standard from the previous one, it was called 'Standard Hydrogen Electrode' [49].

3. *Scheme of standard hydrogen electrode*

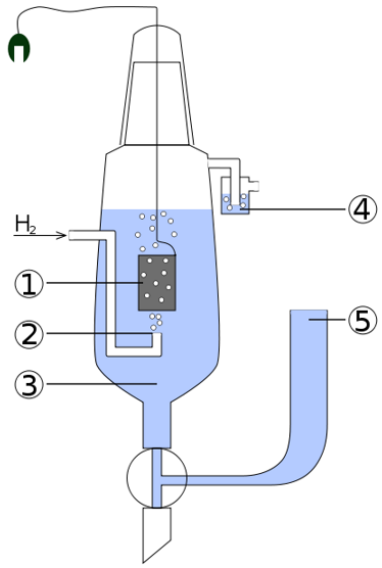

Figure IV.9. Standard hydrogen electrode [50].

The scheme of the standard hydrogen electrode is shown in **Figure IV.9** [50]. It consists of:

1. platinized platinum electrode
2. hydrogen blow
3. solution of acid with activity H^+ = 1 M.
4. hydroseal for prevention of the oxygen interference.
5. reservoir through which the second half-element of the galvanic cell should be attached. The connection can be direct, through a narrow tube to reduce mixing, or through a salt bridge, depending on the other electrode or solution. This creates an ionically conductive path to the working electrode of interest.

4. *Standard electrode potentials relative to the standard hydrogen electrode*

The data values of standard electrode potentials are given in **Table IV.12**, relative to the standard hydrogen electrode at 298 K [51].

Table IV.12. Standard reduction potentials at 298 K.

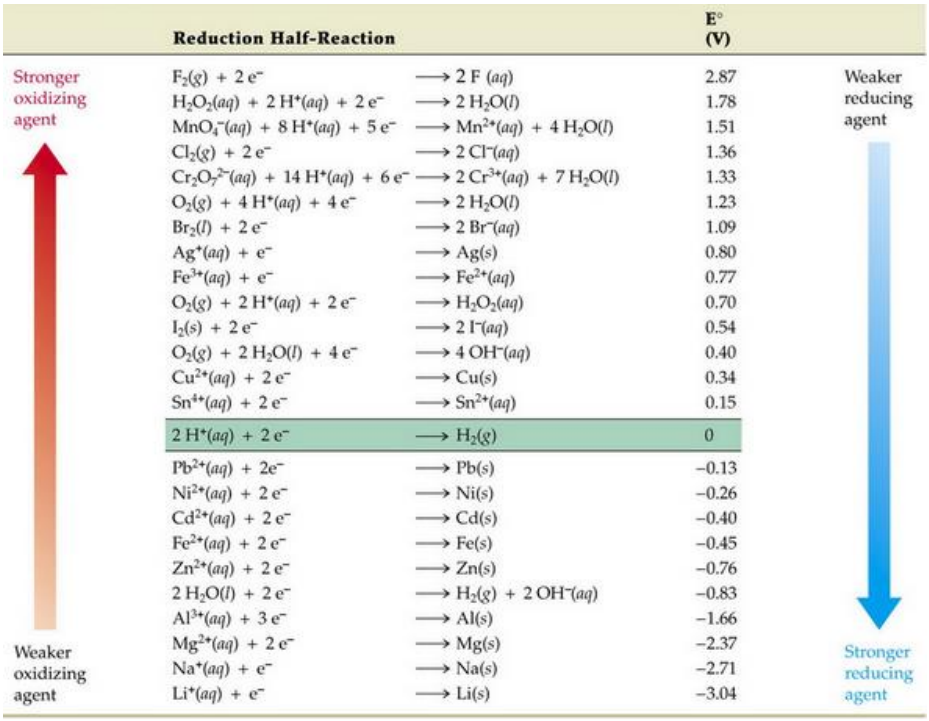

Reduction Half-Reaction		E° (V)
$F_2(g) + 2\,e^-$	$\longrightarrow 2\,F\,(aq)$	2.87
$H_2O_2(aq) + 2\,H^+(aq) + 2\,e^-$	$\longrightarrow 2\,H_2O(l)$	1.78
$MnO_4^-(aq) + 8\,H^+(aq) + 5\,e^-$	$\longrightarrow Mn^{2+}(aq) + 4\,H_2O(l)$	1.51
$Cl_2(g) + 2\,e^-$	$\longrightarrow 2\,Cl^-(aq)$	1.36
$Cr_2O_7^{2-}(aq) + 14\,H^+(aq) + 6\,e^-$	$\longrightarrow 2\,Cr^{3+}(aq) + 7\,H_2O(l)$	1.33
$O_2(g) + 4\,H^+(aq) + 4\,e^-$	$\longrightarrow 2\,H_2O(l)$	1.23
$Br_2(l) + 2\,e^-$	$\longrightarrow 2\,Br^-(aq)$	1.09
$Ag^+(aq) + e^-$	$\longrightarrow Ag(s)$	0.80
$Fe^{3+}(aq) + e^-$	$\longrightarrow Fe^{2+}(aq)$	0.77
$O_2(g) + 2\,H^+(aq) + 2\,e^-$	$\longrightarrow H_2O_2(aq)$	0.70
$I_2(s) + 2\,e^-$	$\longrightarrow 2\,I^-(aq)$	0.54
$O_2(g) + 2\,H_2O(l) + 4\,e^-$	$\longrightarrow 4\,OH^-(aq)$	0.40
$Cu^{2+}(aq) + 2\,e^-$	$\longrightarrow Cu(s)$	0.34
$Sn^{4+}(aq) + 2\,e^-$	$\longrightarrow Sn^{2+}(aq)$	0.15
$2\,H^+(aq) + 2\,e^-$	$\longrightarrow H_2(g)$	0
$Pb^{2+}(aq) + 2e^-$	$\longrightarrow Pb(s)$	−0.13
$Ni^{2+}(aq) + 2\,e^-$	$\longrightarrow Ni(s)$	−0.26
$Cd^{2+}(aq) + 2\,e^-$	$\longrightarrow Cd(s)$	−0.40
$Fe^{2+}(aq) + 2\,e^-$	$\longrightarrow Fe(s)$	−0.45
$Zn^{2+}(aq) + 2\,e^-$	$\longrightarrow Zn(s)$	−0.76
$2\,H_2O(l) + 2\,e^-$	$\longrightarrow H_2(g) + 2\,OH^-(aq)$	−0.83
$Al^{3+}(aq) + 3\,e^-$	$\longrightarrow Al(s)$	−1.66
$Mg^{2+}(aq) + 2\,e^-$	$\longrightarrow Mg(s)$	−2.37
$Na^+(aq) + e^-$	$\longrightarrow Na(s)$	−2.71
$Li^+(aq) + e^-$	$\longrightarrow Li(s)$	−3.04

IV.3 Experimental methods

The synthesis of membranes is summarized in **Table IV.13**. Here, we describe assembling of the sensors. The membranes were pasted to the PVC tube using the epoxy resin. After that, we realized liquid contact using Ag electrode covered with AgCl in a solution of $AgNO_3$ 10^{-1} M for silver-containing membranes, and a mixture (1:1) of $AgNO_3$ 10^{-1} M and $Hg(NO_3)_2$ 10^{-1} M for silver- and mercury-containing membranes **(Figure IV.10)**.

Table IV.13. Parameters used for the synthesis for the membranes.

Chemical composition	Tsynth. (°C)	T decr. before quenching	Quenching	Tanneal. (°C)
40%AgBr-As_2S_3	800	600	sand	100
50%AgBr-As_2S_3	800	600	sand	100
30%AgI-As_2S_3	850	700	sand	177
30%AgI-35HgS-35GeS_2	950	-	sand	-
45%AgI-27.5HgS-18As_2S_3-9.5GeS_2	950	875	sand	-
45%AgI-27.5HgS-9.5As_2S_3-18GeS_2	950	850	sand	-
30%AgI-35HgS-17.5As_2S_3-17.5GeS_2	950	875	sand	-

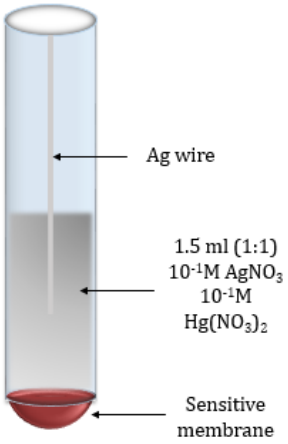

Figure IV.10. Chemical sensor with liquid contact.

And now we will describe the characteristics which we should measure for ion-selective electrodes.

IV.3.1 Characterization of the ion-selective electrodes

The performance of the sensors is characterized by the following parameters:

1. Sensitivity
2. Limit of detection
3. Selectivity in the presence of different interfering species
4. Influence of pH
5. Response time
6. Reproducibility
7. Life-time
8. Long-term stability

The first five parameters are presented in **Figure IV.11**.

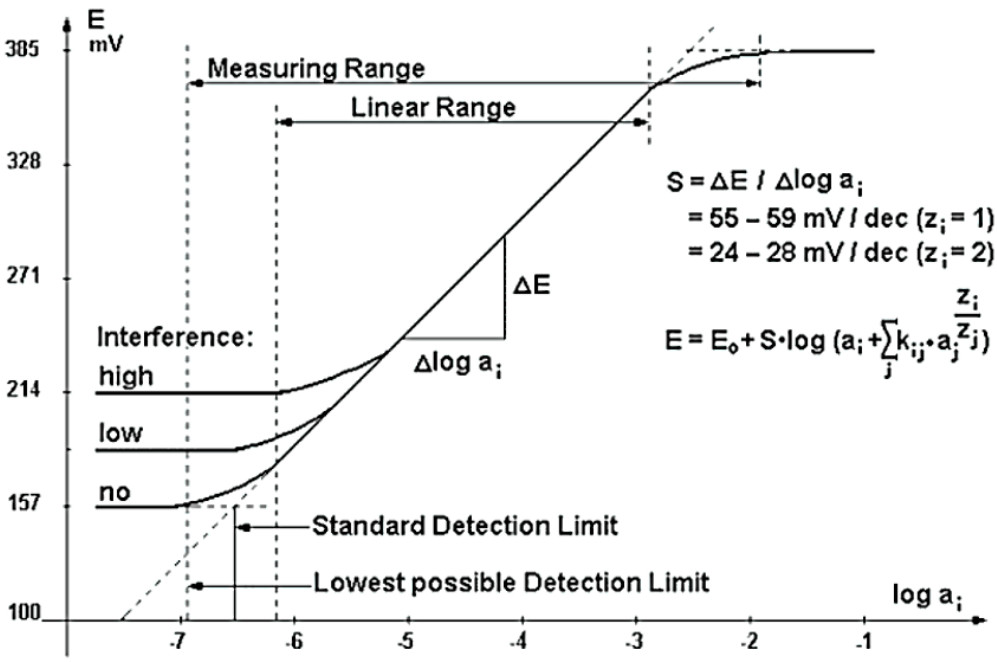

Figure IV.11. Typical example of ion-selective electrode calibration curve [52].

IV.3.1.a Sensitivity and detection limit

The most important parameter is the sensitivity. It defines the ability of the electrode to respond to certain ionic species in liquid medium. Always, we start with the sensitivity measurements, and these give us automatically the value of the detection limit. The second important characteristic is the limit of detection which corresponds to the concentration limit below which the sensor is no more sensitive to the measured ions. If these two parameters are good, we can pass to the other measurements. Calibrations were carried out in a concentration range of 10^{-8} mol.L^{-1} and 10^{-3} mol.L^{-1}. All the calibrations were performed using the titration method. All the additions are introduced into 100 ml of potassium nitrate KNO_3 solution with a concentration of 10^{-1} mol.L^{-1}. After introducing the additions, we should wait, to reach the equilibrium potential. The waiting time is normally about 2 minutes and potential does not change more than ± 2 mV in these 2 minutes.

The $Hg(NO_3)_2$ standard solutions were prepared by a method of successive dilutions. The support solution with a constant ionic strength was KNO_3 10^{-1} mol.L^{-1} with a pH = 1. This ionic strength allows us to use the concentration of the ions instead of their activity. In addition, it stabilizes the

liquid junction potential. In order to avoid contamination of the standard solutions by the Cl^- ions, a combined reference electrode has also been used, which contains a salt bridge. In this case, it was possible to minimize the liquid junction potential. A pH=1 was used to avoid the formation of precipitate HgO (**Figure IV.2**).

In the case of a bivalent ion M^{2+}, the theoretical sensitivity is 29 mV/decade at 20 °C in accordance with equation (IV.1).

The detection limit is defined as the intersection of the two straight lines corresponding to the first two parts of the graph (**Figure IV.11**).

IV.3.1.b Selectivity in the presence of interfering ions in standard solutions

Selectivity is a parameter which shows the possibility to use chemical sensors in the presence of different species in the measured solution. The lowest value of the selectivity coefficient shows that the ion-selective electrode can be used in the presence of this ion. Theoretically, the selectivity coefficient is given by Eisenman-Nicolsky equation [27]:

$$E = E_0 + \frac{RT}{z_x F} \ln(a_x + K_{x,y}\, a_y) \qquad \text{(IV.10)}$$

Where:

a_x activity of the primary species X detected by the sensor,

a_y activity of the interfering ion Y,

$K_{x,y}$ selectivity coefficient with respect to species X in the presence of Y ions,

z_x charge of the primary ionic species Y.

To determine the selectivity coefficient, we can use the method recommended by IUPAC [38]. This is the mixed solutions method with two versions:

1. Constant concentration of interfering ions and
2. Constant concentration of primary ions

The first method means that the concentration of the interfering ions has a constant concentration and used as the measuring solution. The concentration of the primary species is variable.

In the second method, the concentration of the primary ions is fixed and the concentration of the interfering species is changed. This version is usually used when the influence of the interfering ions is very strong in order to avoid possible contamination of the selective membrane by the interfering species. Normally, when the interference is strong, we work with a low concentration of interfering ions.

IV.3.1.c Influence of pH

The study of the pH influence is important in order to determine the optimal pH-working range in which we can use our sensors. The influence of pH on the response of the mercury ion-selective electrode is normally studied in a $Hg(NO_3)_2$ solution in the concentration range 10^{-7} mol.L^{-1} to 10^{-1} mol.L^{-1}. The change of pH is realized by adding nitric acid and potassium hydroxide solutions. Obtaining an equilibrium potential for each pH value requires a long time.

IV.3.1.d Response time

The response time is one of the important characteristics of ion-selective electrodes. It determines the sensor usability. All elf's measured should be realized in equilibrium. So, the time necessary to reach this equilibrium have to be determined. The response time is not a univocal parameter, i.e., it depends on the particular experimental conditions for each electrode, for instance such as concentration of the primary ion.

The Recommendations for Nomenclature of Ion-Selective Electrodes [53] adopted lately the following definition for response time: it is the time which passes between the instant at which an ion-selective electrode and a reference electrode (ISE cell) are brought into contact with a sample solution (or at which the activity of the ion of interest in a solution is changed) and the first instant at which the emf/time curve ($\Delta E/\Delta t$) becomes equal to a limiting value on the basis of the experimental conditions and/or requirements concerning the accuracy.

The response time may be studied using two experimental procedures:

1. The dipping method: the electrode is instantaneously immersed into a solution of known activity of the tested ion; simultaneously, the response record is started. In order to examine

the dependence of the response time on concentration, the operation must be repeated with a series of separate solutions. The response time is termed here the static response time.

2. The injection method: the electrode is kept immersed in one and the same supporting solution; after starting the response record, a measured aliquot of a concentrated solution of the tested ion is added. A continuous record of the response can be easily made from the initial conditioning in the supporting solution through stepwise additions that can encompass several orders of magnitude of concentration. The response time has been termed here the dynamic one.

Nevertheless, the response time can be measured also by decreasing concentration, either by transferring the electrode from a concentrated solution to diluted one using the first method, or by instantaneous dilution of the measured solution using the second method.

Only experimental potential versus time plots offer a comprehensive presentation of the response time **(Figure IV.12)**. The potential versus time plots must have a small time scale factor (time/length); thus analogical recording must be very fast, or digital sampling must be very frequent. An automatic operation, using PC and suitable homemade software, is exploited for calibrating an electrode and simultaneously determining $t(\Delta E/\Delta t)$.

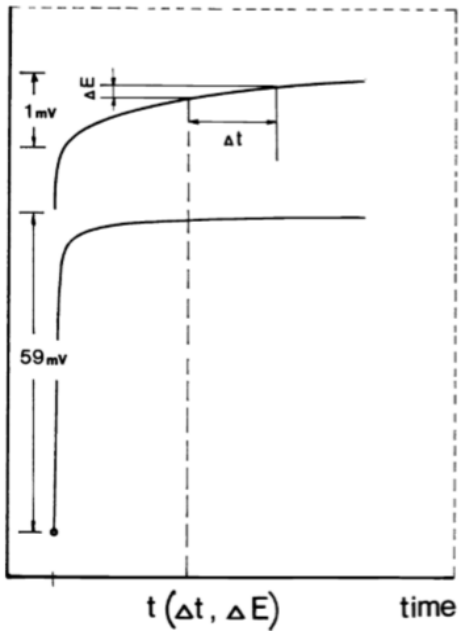

Figure IV.12. Definition and determination of response time [54].

IV.3.1.e Reproducibility in standard solutions

The reproducibility of the potential is an essential parameter which shows how precisely we realize our measurements. Reproducibility is studied using a series of consecutive measurements in standard solutions. The method used is as follows: the sensors are immersed in a solution for 2 minutes, their potential is noted, then they are placed in the open air also for 2 minutes, and this procedure is repeated ten times. After that, we plot the potential as a function of time. And thus, this is the reproducibility. The average value of the potential and, above all, the mean square deviation of this value gives a good estimate of the stability and reproducibility of the response of the sensors.

IV.3.1.f Long-term stability in standard solutions

Long-term stability is an important parameter because it is mainly linked to continuous measurements. Experimentally, this characteristic is studied in a well-closed hermetically electrochemical cell in order to avoid solvent evaporation and therefore the concentration change of the measured solution. The studies are to be carried out for at least one month. As part of this work, this measure has not been carried out.

IV.4 Discussion of the results

In this chapter, we will present the experimental results and their discussions. Basically, these discussions concern the choice procedure for the compositions of membranes. We have synthesized the following 9 compositions:

1. **25AgBr-75As_2S_3 = AgBr25 → 4 membranes**
2. **30AgBr-70As_2S_3 = AgBr30 → 4 membranes**
3. **40AgBr-60As_2S_3 = AgBr40→ 6 membranes**
4. **50AgBr-50As_2S_3 = AgBr50 → 6 membranes**
5. **30AgI-70As_2S_3 = AgI30 → 6 membranes**
6. **30AgI-35HgS-35GeS_2 = AgHg30 → 4 membranes**
7. **30AgI-35HgS-17.5GeS_2-17.5As_2S_3 = AH30 → 5 membranes**
8. **45AgI-27.5HgS-18GeS_2-9.5As_2S_3 = AG30 → 6 membranes**
9. **45AgI-27.5HgS-9.5GeS_2-18As_2S_3 = AA30 → 4 membranes**

So, for our research we have prepared 45 electrodes with 9 different compositions. The membranes have a size of ≈8 mm in diameter and a thickness of the order of 3 to 4 mm. The 8 electrodes with the first two compositions were eliminated after two days of calibrations because they didn't indicate any function. Below in **Figures IV.13, 17, 21, 25, 26, 30, 34** we can see the photos of the synthesized membranes after the calibrations. The photos show the states of the synthesized membranes. We could not say that our synthesis is completely successful. Nevertheless, we realize some calibrations because this is the first step in the usual procedure for choosing a suitable composition for membranes. It consists of the following steps:

1. synthesis of membranes,
2. assembling of ion-selective electrodes,
3. calibration,
4. estimation of selectivity and detection limit.

We look for a connection between the membranes' composition and sensitivity but also detection limits. This analysis gives us information how we can change composition to obtain a better sensitivity and a lower detection limit.

Below is shown in **Figure IV.13** the photos of the 40AgBr-60As_2S_3 composition.

40AgBr-60As_2S_3

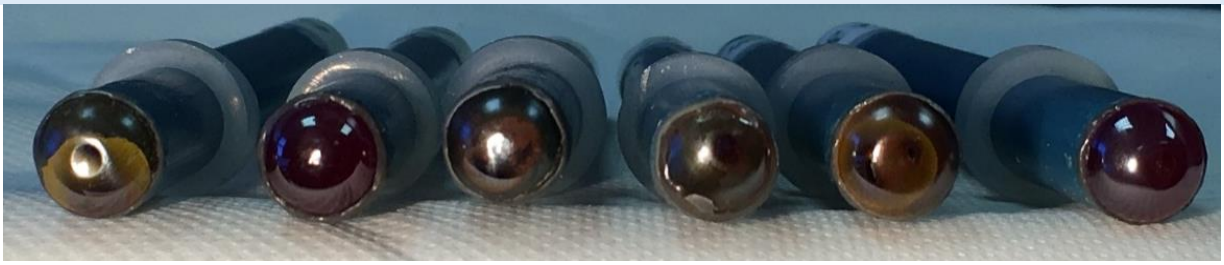

R1 **R2** **R3** **R5** **R6** **R7**

Figure IV.13. Photos showing the state of the synthesized membranes (40AgBr-60As_2S_3) after calibration.

From **Figure IV.13** we can see that some electrodes have a foxy color on the membranes' surfaces. From **Table IV.14**, we can see that after synthesis, we had only two shiny membranes and four matt. After calibration the shiny membranes did not change but all matt membranes obtained foxy color. Another important thing is that both shiny membranes do not have a good function.

In **Table IV.14**, we present the parameters of the electrodes AgBr40 (R1, R2, R3, R5, R6, R7).

Table IV.14. Parameters of the electrodes AgBr40 (R1, R2, R3, R5, R6, R7).

N°	Name	State after synthesis	State after calibration	Comment	E_{init} 15/03	S 15/03	DL 15/03
1	AgBr40R1	matt	foxy color		152	47	3.0×10^{-6}
2	AgBr40R2	shiny	shiny	not working	-	-	-
3	AgBr40R3	matt	foxy color		128	31	3.5×10^{-6}
4	AgBr40R5	matt	foxy color		128	30	3.4×10^{-6}
5	AgBr40R6	matt	foxy color		negative E		
6	AgBr40R7	shiny	shiny	bad function	-	-	-
				Average	**136**	**36**	**3.3×10^{-6}**

The next **Table IV.15** gives us calibrations in the time and experimental slopes.

Table IV.15. Calibrations in the time and experimental slopes for AgBr40 electrodes.

N°	Name	N° Calib.	Calibrations in the time										
			Jan.	S	Feb.	S	Mar.	S	April	May	S	June	S
1	AgBr40R1	20	22,26,30, 31	68–151	01–09	76–83	12–16	37–47	not measured			04–08	17–51
3	AgBr40R3	29	22,26,30, 31	88–132	01–09	60–76	12–16	30–43	26–30	02–04, 9,11,30	88/19	04–08	31–46
4	AgBr40R5	29	22,26,30, 31	60–125	01–09	45–61	12–16	23–33	26–30	02–04, 9,11,30	92/17	04–08	26–41
5	AgBr40R6	16	not yet synthesized				12–16	35–56	26–30	02–04, 9,11,30	41/18	04,05	-

* The red color means that electrode did not take part in discussion of results.

* The green color means that electrode has a negative potential.

We have to note that the highest value of the slope was in January (60-151 mV/decade). It constantly decreased in February (45-83 mV/decade) and March (23-47 mV/decade). In April and May, the electrodes did not work correctly. Finally, in June, they got better and showed a slope between 26 and 41 mV/decade.

Figure IV.14 shows typical calibration curves for composition 40AgBr-60As_2S_3 on 15/03/18.h. The best results present the AgBr40R3 electrode.

In **Table IV.14**, we find the initial potential, sensitivity and detection limit values for the AgBr40 electrodes (R1, R3, R5). The average value of the detection limit shows that it is sufficiently high (3.3×10^{-6} M). In this case, the ion-selective electrode cannot be used for the detection of mercury in the natural samples.

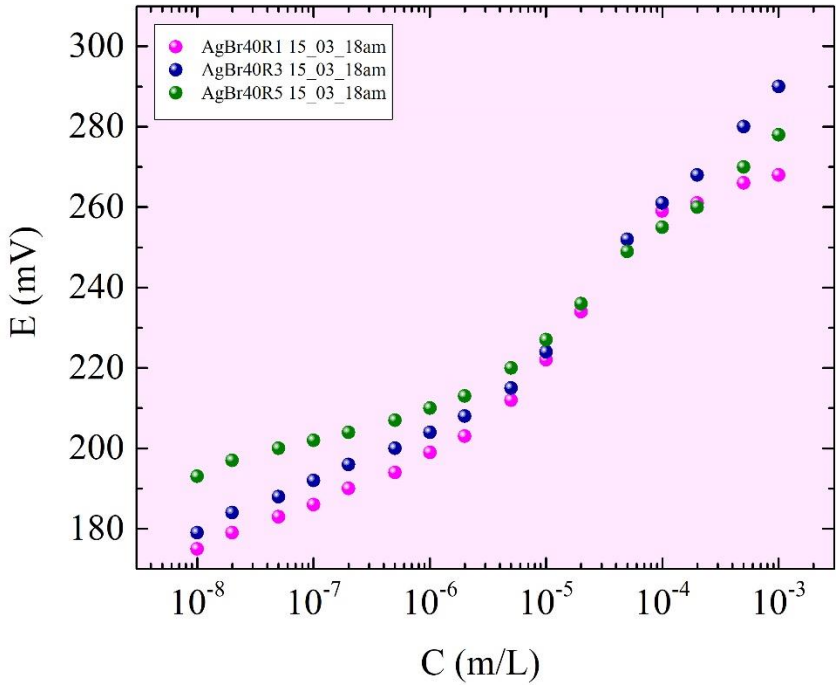

Figure IV.14. Calibration of AgBr40 (R1, R3, R5) electrodes on 15/03/18.

Figure IV.15 and **Figure IV.16** give us information on the stability of the initial potential for chemical sensors AgBr40 R3 and R5 between 30/01/2018 and 08/06/2018 (a.m. and p.m.).

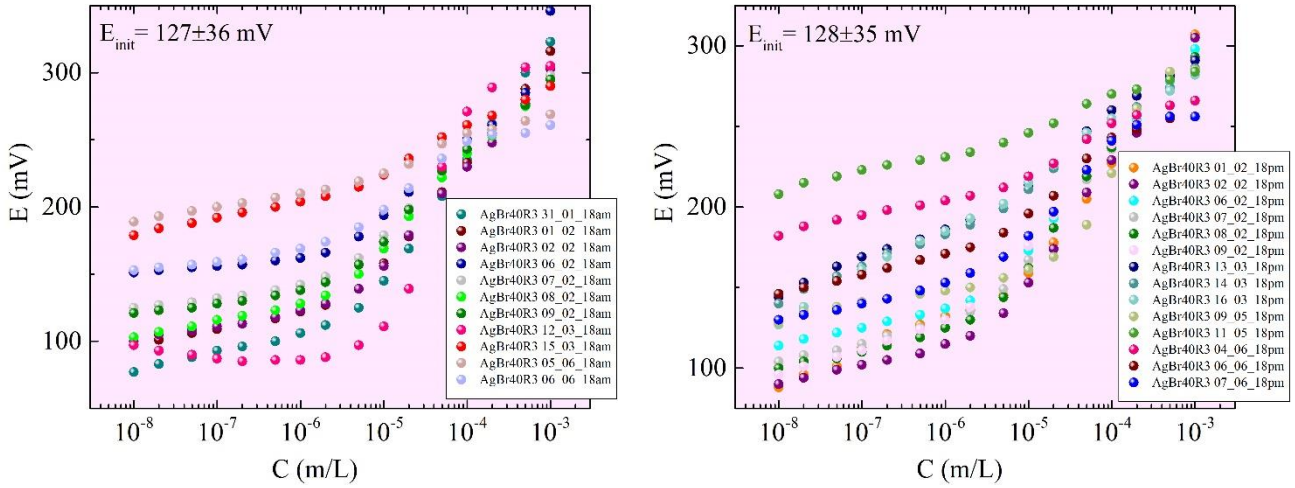

Figure IV.15. Calibration of AgBr40 R3 electrode from 30/01/2018 to 08/06/2018 (a.m. and p.m.).

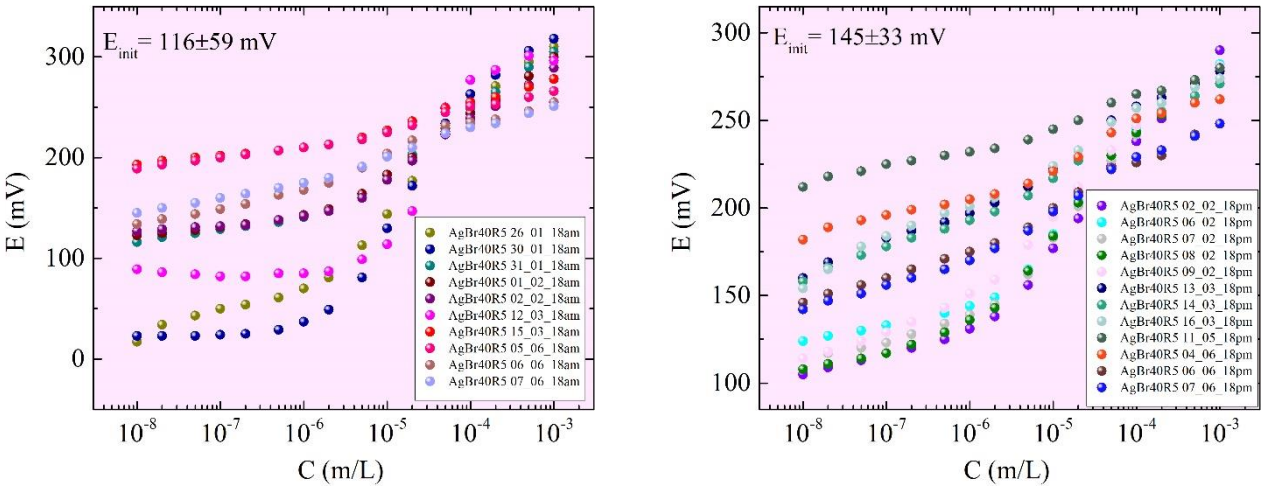

Figure IV.16. Calibration of AgBr40 R5 electrode from 30/01/2018 to 08/06/2018 (a.m. and p.m.).

Figure IV.15 and **Figure IV.16** show that both electrodes do not have at all good stability. We can see that the drift of potential is very consequent (±36, ±35, ±59 and ±33 mV) more than the value for slope for 2^+ charged inions. While a good ion-selective electrode must have a drift not more than ±5-10 mV. But if we have to choose between 2 electrodes R3 and R5, we can say that R3 is more stable than electrode R5. In case of R3, we have the almost the same initial potential in antemeridian and postmeridian (E_{init} = 127±36 mV and 128±35 mV). At the same time, for electrode R5 we can observe big difference in the initial potential (E_{init} = 116±59 mV and 145±33 mV).

Now, we pass to the fourth composition (50AgBr-50As_2S_3). From this composition was assembling six ion-selective electrodes.

50AgBr-50As_2S_3

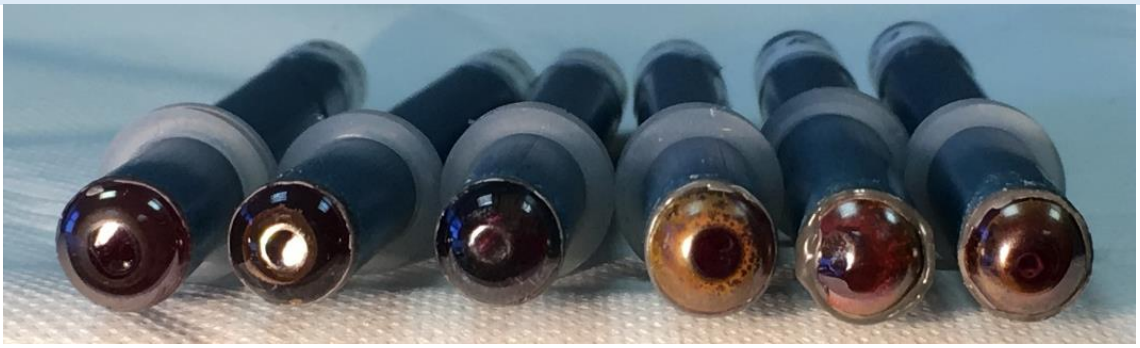

R1 **R2** **R3** **R4** **R6** **R7**

Figure IV.17. Photos showing the state of the synthesized membranes (50AgBr-50As_2S_3) after calibration.

Photos of the AgBr50 electrodes are shown in **Figure IV.17.** It was taken after several calibrations. From **Figure IV.17,** we can see that for some electrodes, i.e. AgBr50 (R2, R4, R6, R7), there are foxy colors on the membranes' surfaces. **Table IV.16** gives us information that after synthesis, we had three shiny membranes and three matt membranes. After calibration, all the matt membranes obtained foxy color but also one shiny membrane yet.

In **Table IV.16**, we present the parameters of electrodes AgBr50 (R1, R2, R3, R4, R6, R7).

Table IV.16. Parameters of the electrodes AgBr50 (R1, R2, R3, R4, R6, R7).

N°	Name	State after synthesis	State after calibration	E_{init} 08/02	S 08/02	DL 08/02
1	AgBr50R1	shiny	shiny	55	33	1.4×10^{-6}
2	AgBr50R2	shiny	foxy color	negative E		
3	AgBr50R3	shiny	shiny	84	41	1.7×10^{-6}
4	AgBr50R4	matt	foxy color	80	46	1.5×10^{-6}
5	AgBr50R6	matt	foxy color	not yet synthesized		
6	AgBr50R7	matt	foxy color			
			Average	**73**	**40**	**1.5×10^{-6}**

Table IV.17 shows calibrations in the time and experimental slopes for AgBr50 electrodes.

Table IV.17. Calibrations in the time and experimental slopes for AgBr50 electrodes.

N°	Name	N° Calib.	Calibrations in the time										
			Jan.	S	Feb.	S	Mar.	S	April	May	S	June	S
1	AgBr50R1	29	22,26,30,31	29–53	01–09	27–33	12–16	17	26–30	02–04, 9,11,30	-	04–07, 08	64
2	AgBr50R2	29	22,26,30,31	11–24	01–09	15–29	12–16	16–24	26–30	02–04, 9,11,30	-	04–07, 08	50
3	AgBr50R3	29	22,26,30,31	55–137	01–09	38–44	12–16	19–26	26–30	02–04, 9,11,30	-	04–07, 08	68
4	AgBr50R4	29	22,26,30,31	62–119	01–09	38–45	12–16	20–25	26–30	02–04, 9,11,30	-	04–06,07, 08	18–64
5	AgBr50R6	14	Not synthesized yet				12–16	21–48	26–30	02–04, 9,11,30	23	No function	
6	AgBr50R7	14					12–16	21–49	26–30	02–04, 9,11,30	27	04–08	20–60

* The red color means that electrode did not take part in discussion of results.

* The green color means that electrode has a negative potential.

Table IV.17 shows us that in January, the slope was the highest (≈58 mV/decade). It constantly decreased in February (15-45 mV/decade). But in March, April and May, most of the electrodes did not work correctly, and the ones which worked had a slope ≈25 mV/decade. Finally, in June, they started to work better and **S** varied between 18 and 64 mV/decade.

Figure IV.18 shows typical calibration curves for 50AgBr-50As_2S_3 composition on 08/02/18 for electrodes AgBr50 (R1, R3, R4). Here is difficult to say which one is the best because all three have not good function. In **Table IV.16**, we find the initial potential, sensitivity and detection limit values for the AgBr50 (R1, R2, R3, R4) electrodes. The average value of the detection limit is sufficiently high (1.5×10^{-6} M). In this case, the ion-selective electrode cannot be used for the detection of mercury in the natural samples.

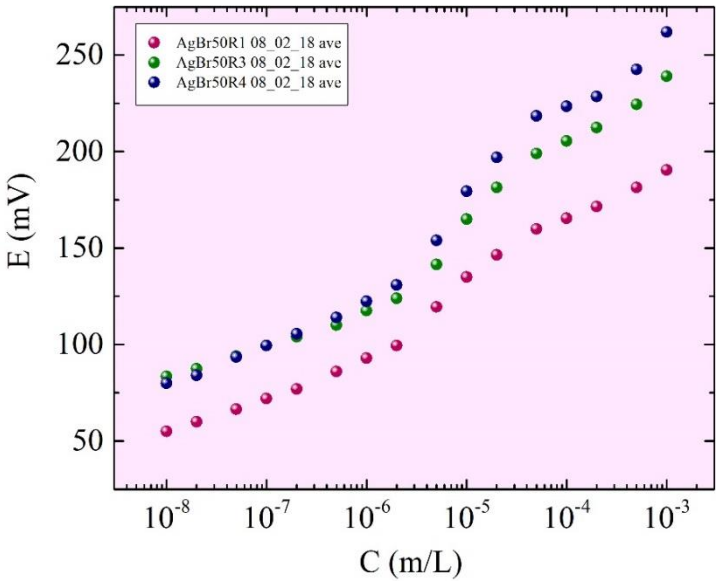

Figure IV.18. Calibration of AgBr50 (R1, R3, R4) electrodes on 08/02/18.

Figure IV.19 and **Figure IV.20** give us information on the stability of initial potential for ion-selective electrodes (AgBr50 R3 and R4) between 30/01/2018 and 08/06/2018. It can be concluded that both electrodes do not have a good stability. We can see that the drift of potential is between ±32 and ±47 mV. In case of R4, we have almost similar initial potential for antemeridian and postmeridian (E_{init} = 119±47 mV and 117±43 mV) measurements but also with high drift.

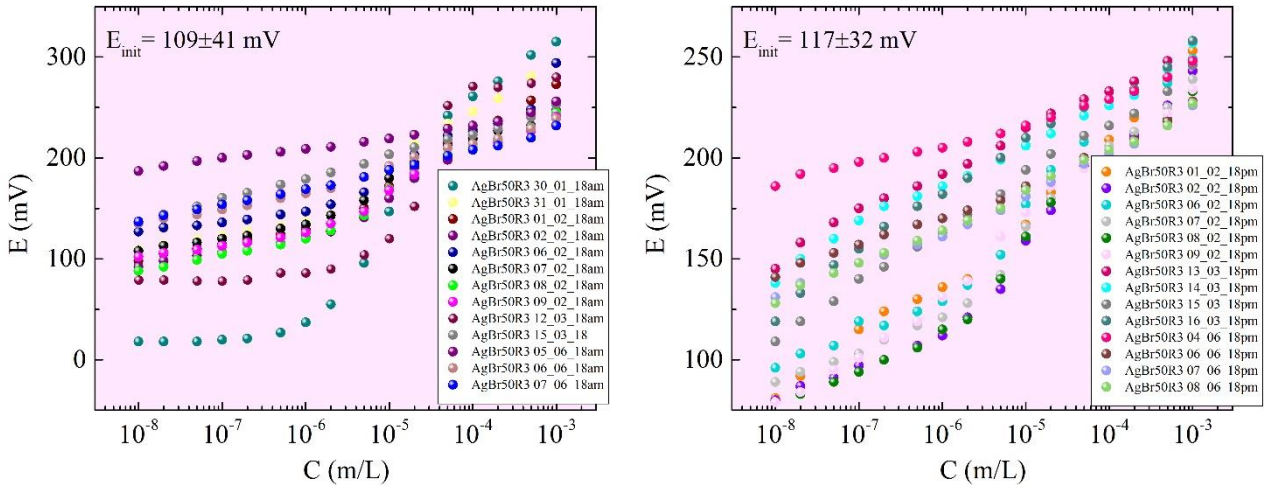

Figure IV.19. Calibration of AgBr50 R3 electrode from 30/01/2018 to 08/06/2018 (a.m. and p.m.).

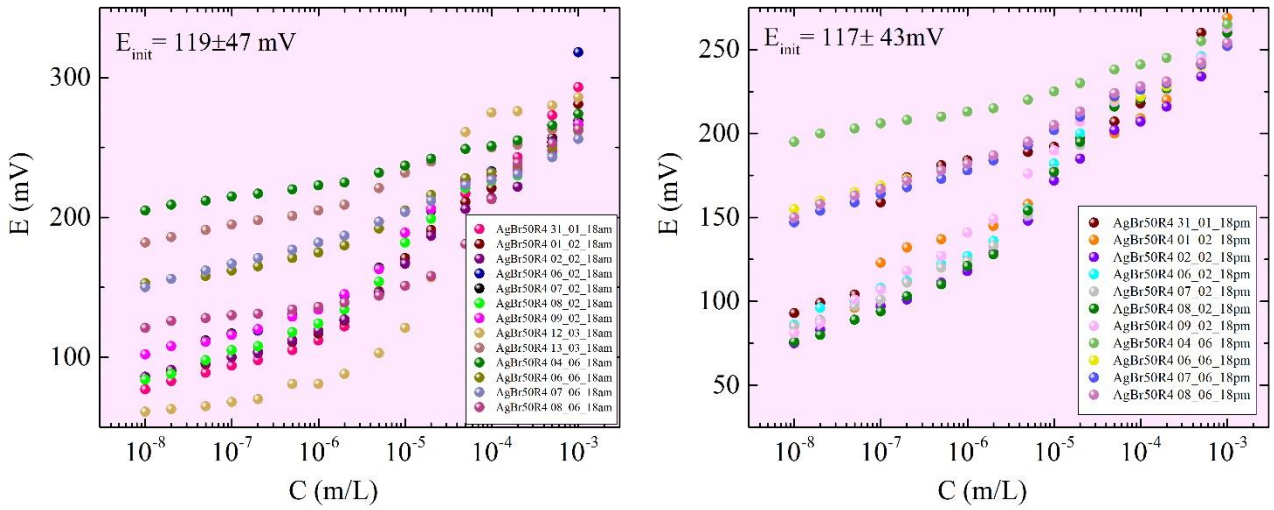

Figure IV.20. Calibration of AgBr50 R4 electrode from 31/01/2018 to 08/06/2018 (a.m. and p.m.).

Now, we pass to the fifth composition (30AgI-70As_2S_3). From this composition was assembling six ion-selective electrodes.

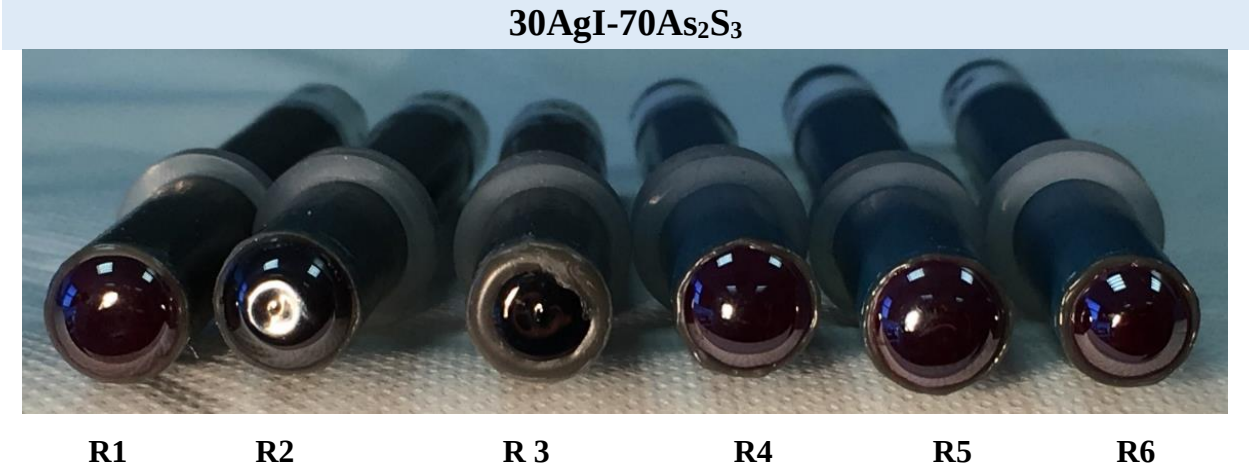

Figure IV.21. Photos showing the state of the synthesized membranes (30AgI-70As_2S_3) after calibration.

Figure IV.21 that all six AgI30 membranes have a shiny surface even after calibration and their look has not changed. In **Table IV.18**, we present the parameters of the AgI30 electrodes (R1, R2, R3, R4, R5, R6).

Table IV.18. Parameters of the electrodes AgI30 (R1, R2, R3, R4, R5, R6).

N°	Name	State after synthesis	State after calibration	E_{init} 15/03	S 15/03	DL 15/03
1	AgI30R1	shiny	shiny	192	25	1.1×10^{-6}
2	AgI30R2	shiny	shiny	197	28	1.5×10^{-5}
3	AgI30R3	shiny	shiny	204	27	2.0×10^{-5}
4	AgI30R4	shiny	shiny	182	22	1.5×10^{-5}
5	AgI30R5	shiny	shiny	185	22	1.4×10^{-5}
6	AgI30R6	shiny	shiny	190	19	8.4×10^{-6}
			Average	**192**	**23**	**2.6×10^{-6}**

The values presented for DL in the **Table IV.18** are relatively high (2.6×10^{-6} M). It means that we have the same situation like with the electrodes AgBr40 so we cannot use this composition for membrane of ion-selective electrode for the detection of mercury in the natural samples. E_{init} is not bad and they almost enter in the limit ±10 mV, the slope is close to theoretical for 2^+ charge ions but DL is always high (2.6×10^{-6} M). There is one more problem that the function is not good and it is very difficult to calculate DL.

Table IV.19. Calibrations in the time and experimental slopes for AgI30 electrodes.

N°	Name	N° Calib.	Calibrations in the time									
			Jan.	S	Feb.	S	Mar.	S	Apr.	May	June	S
1	AgI30R1	20	22,26,30,31	36–74	01–09	32–35	12–15,16	25–27	not measured		04–08	20–26
2	AgI30R2	20	22,26,30,31	33–68	01–09	32–36	12–15,16	27–31			04–08	18–25
3	AgI30R3	20	22,26,30,31	30–62	01–09	29–33	12–15,16	24–29			04–08	22–32
4	AgI30R4	19	not yet synthesized				12–15,16	20–22	26–30	02–04, 9,11,30	04–08	20–35
5	AgI30R5	19					12–15,16	20–24	26–30	02–04, 9,11,30	04–08	24–27
6	AgI30R6	19					12–16	18–24	26–30	02–04, 9,11	04–08	21–27

* The red color means that the electrode did not take part in discussion of results.

* The green color means that electrode has a negative potential.

Table IV.19 shows the calibrations in the time and experimental slopes for this series of sensors. Then, we can see that in January, the slope was significantly high (30-74 mV/decade), but in February, they decrease constantly to 29-36 mV/decade. This tendency was conserved in the

calibrations done in March (18-31 mV/decade). In April and May, the electrodes did not work correctly. Finally, in June they restored their behavior and a slope was between 18 and 32 mV/decade.

Figure IV.22 shows the calibration curves of the AgI30 (R1, R2, R3, R4, R5, R6) electrodes on 15/03/18. In **Table IV.18**, we find the initial potential, sensitivity and detection limit values for the six electrodes.

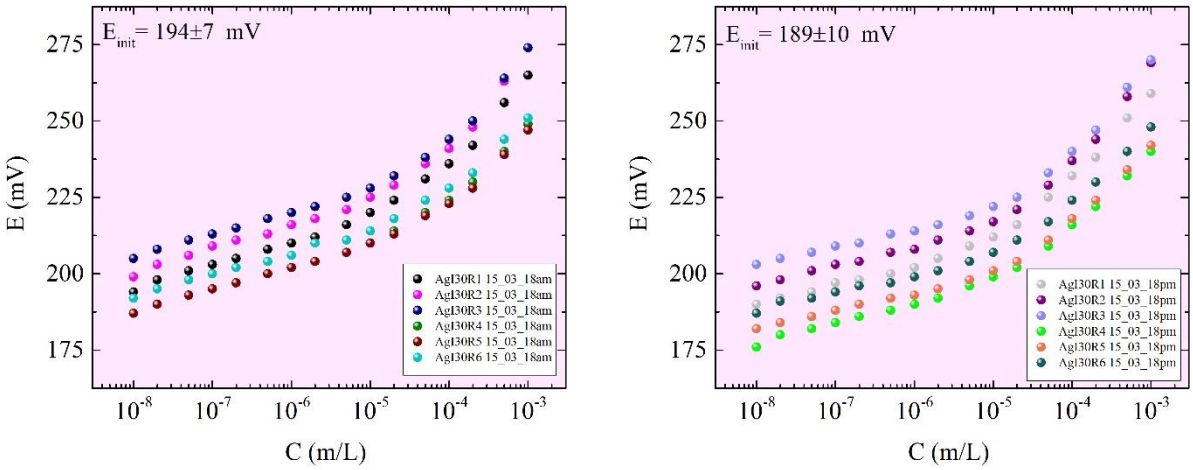

Figure IV.22. Calibration of AgI30 (R1, R2, R3, R4, R5, R6) electrodes on 15/03/18 (a.m. and p.m.).

Figure IV.23 and **Figure IV.24** show that AgI30 R1 and R2 electrodes have approximately the same initial potential between antemeridian and postmeridian (E_{init} = 157±31 mV and 157±27 mV for R1, E_{init} = 153±27 mV and 158±30 mV), but always with a notable drift.

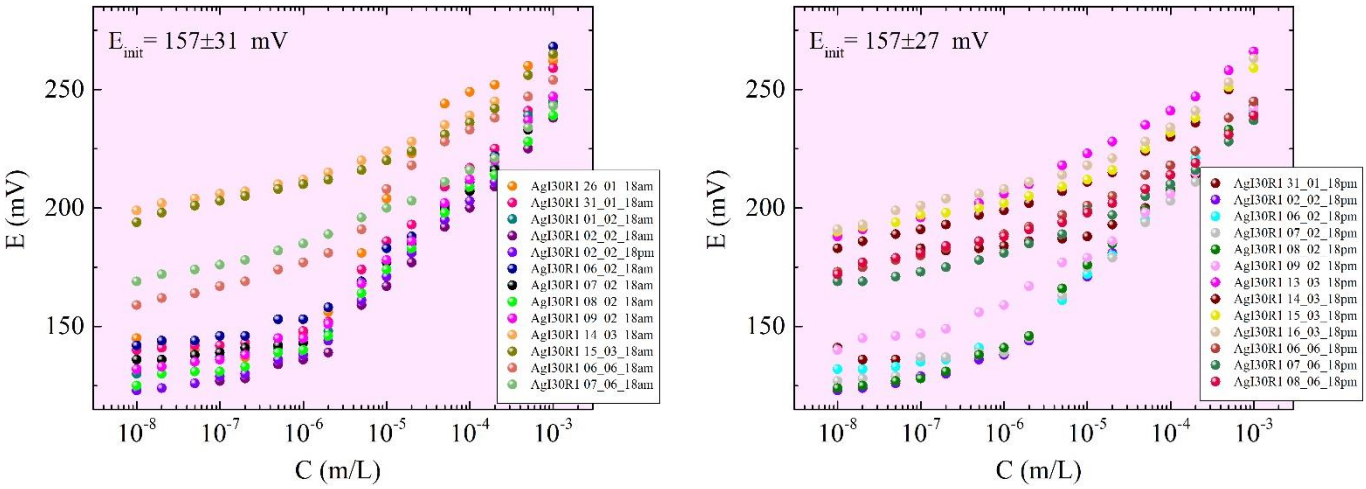

Figure IV.23. Calibration of AgI30 R1 electrode from 30/01/2018 to 08/06/2018 (a.m. and p.m.).

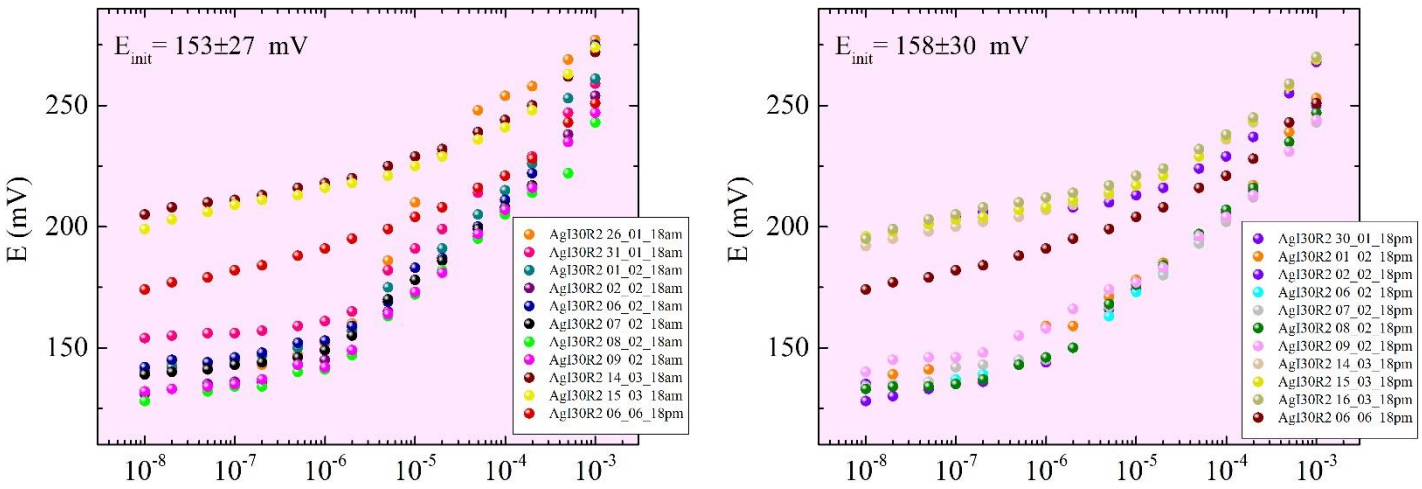

Figure IV.24. Calibration of AgI30 R2 electrode from 30/01/2018 to 08/06/2018 (a.m. and p.m.).

Here, we pass to the sixth composition (30AgI-35HgS-35GeS_2). From this composition was assembling four ion-selective electrodes.

30%AgI-35HgS-35GeS_2

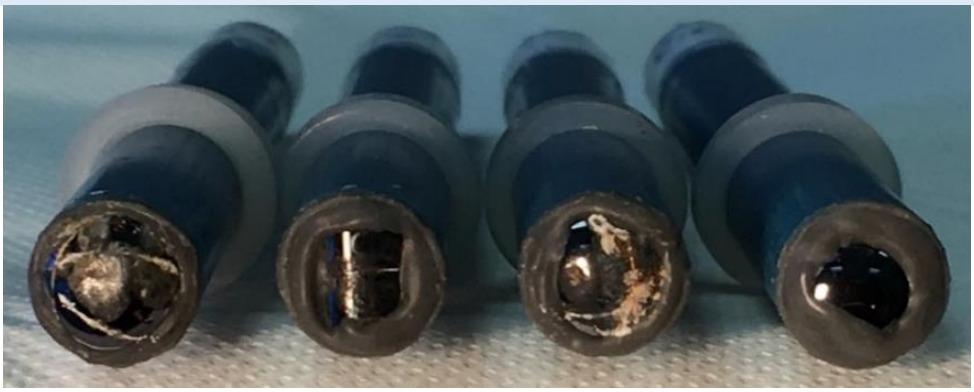

R1 **R2** **R3** **R4**

Figure IV.25. Photos showing the state of the synthesized membranes (30AgI-35HgS-35GeS_2) after calibration.

It seems that the membranes with the composition 30AgI-35HgS-35GeS_2 are the most fragile glasses among the synthesized glasses. After the first calibrations, big fissures appeared on the surface of AgHg30 (R1, R3) electrodes as can be seen in **Figure IV.25**. Also we find the traces of solution. Their defects are listed in **Table IV.20**. It is evident, that it is not possible to use them more.

Table IV.20. Parameters of the electrodes AgHg30 (R1, R2, R3, R4).

N°	Name	State after synthesis	State after calibration
1	AgHg30R1	shiny	2 big fissures with traces of solution
2	AgHg30R2	shiny	shallow fissure with traces of solution
3	AgHg30R3	shiny	big fissures with traces of solution
4	AgHg30R4	shiny (very small piece)	traces of solution

Subsequently, we pass to the seventh composition (45AgI-27.5HgS-18As_2S_3-9.5GeS_2). From this composition was assembling four ion-selective electrodes.

45%AgI-27.5HgS-18As_2S_3-9.5GeS_2

R1 **R2** **R3** **R4**

Figure IV.26. Photos showing the state of the synthesized membranes (45AgI-27.5HgS-18As_2S_3-9.5GeS_2) after calibration.

From **Figure IV.26,** we can see that the four AA45 membranes have a shiny surface. However, after several calibrations, R1 and R3 electrodes had big fissures in the middle of the membranes' surfaces. In **Table IV.21**, we present the parameters of the AA45 electrodes (R1, R2, R3, R4).

Table IV.21. Parameters of the electrodes AA45 (R1, R2, R3, R4).

N°	Name	State after synthesis	State after calibration	E_{init} 08/06	S 08/06	DL 08/06
1	AA45R1	shiny	fissure	not measured		
2	AA45R2	shiny	shiny	205	54	1.6×10^{-5}
3	AA45R3	shiny	fissure	not measured		
4	AA45R4	shiny	shiny	182	49	2.0×10^{-5}
			Average	**194**	**52**	**1.8×10^{-5}**

In **Table IV.21**, we find the initial potential, sensitivity and detection limit values for the electrodes AA45 (R2 and R4). The most important conclusion from this table is that the detection limit is extremely high ($\approx1.8\times10^{-5}$ M). So, AA45 electrodes are not appropriate to be used as ion-selective electrodes for the detection of mercury in the natural samples.

The next **Table IV.22** gives us calibrations in the time and experimental slopes. We can see that in April, the electrodes did not work correctly. In May and June, the sensors work only several days with a very varied slope between 16 and 60 mV/decade.

Table IV.22. Calibrations in the time and experimental slopes for AA45 electrodes.

N°	Name	N° Calib.	Calibrations in the time					
			April	S	May	S	June	S
1	AA45R1	11	13,16,17,26–30	35	02,03,04,11,30	19–25	not measured	
2	AA45R2	14	26–30	-	02–04,09,11,30	61	04, 05,06–08	18–58
3	AA45R3	9	26–30	-	02,03,04,09,11, 30	66/25	not measured	
4	AA45R4	14	26–30	-	02,03,04,09,11, 30	60	04, 05,06–08	16–58

* The red color means that the electrode did not take part in discussion of results.

Figure IV.27 presents typical calibration curves for electrodes AA45R2 and AA45R4 on 08/06/18. It confirms our conclusion about very high DL.

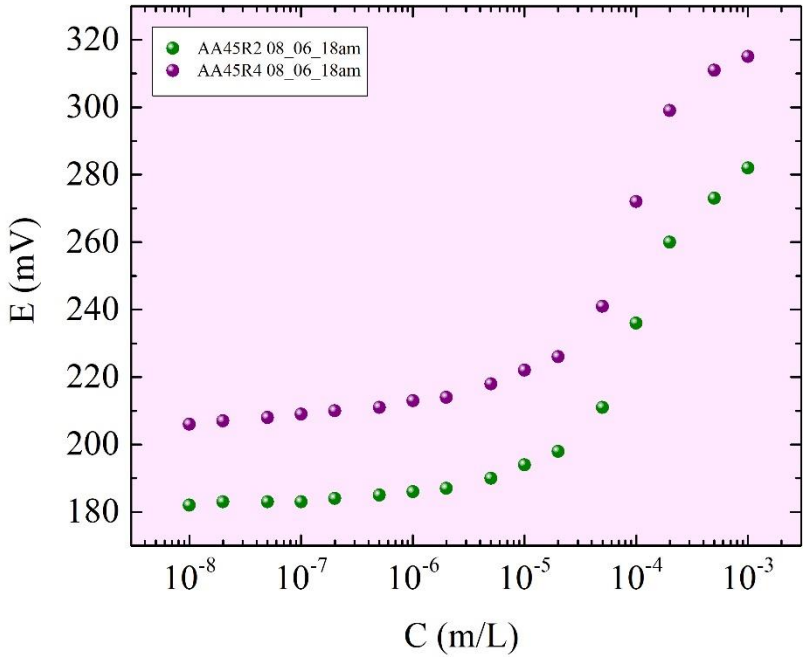

Figure IV.27. Calibration of AA45 (R2, R4) electrodes on 08/06/18.

Figure IV.28 and **Figure IV.29** show the initial potential of electrodes AA45 R2 and R4 on three consecutive days 06, 07 and 08/06/2018, but also the slope for postmeridian calibrations. And here we should note that both sensors start to behave similarly in postmeridian: E_{init}=213±3 mV and S_{pm}=19±1 mV/decade for AA45R2, E_{init}=242±4 mV and S_{pm}=17±3 mV/decade for AA45R4.

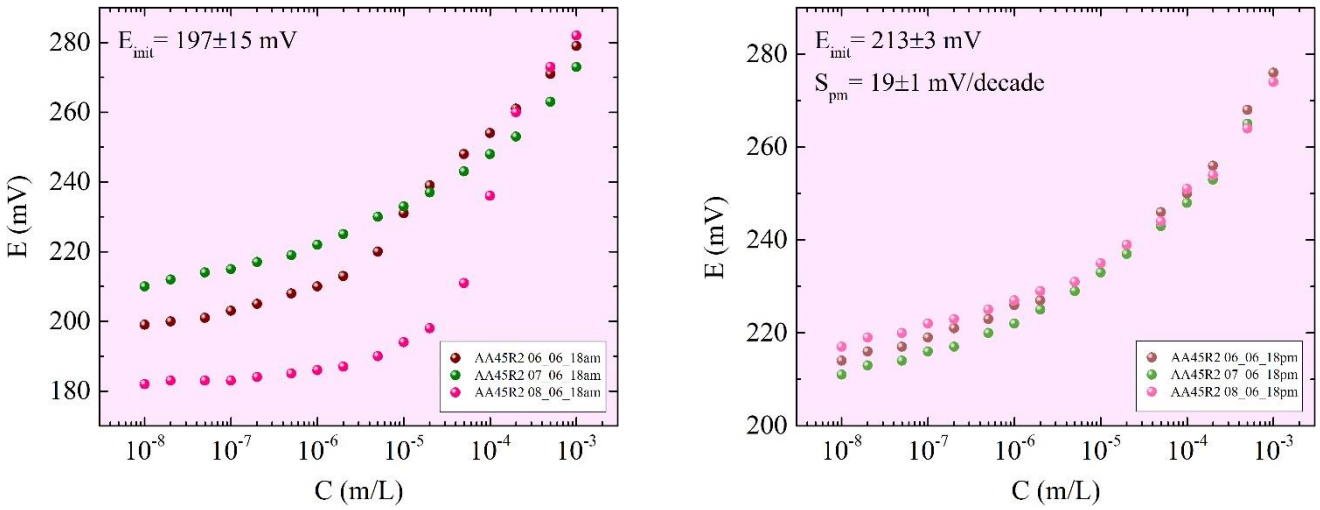

Figure IV.28. Calibration of AA45 R2 electrode 06, 07 and 08/06/2018 (a.m. and p.m.).

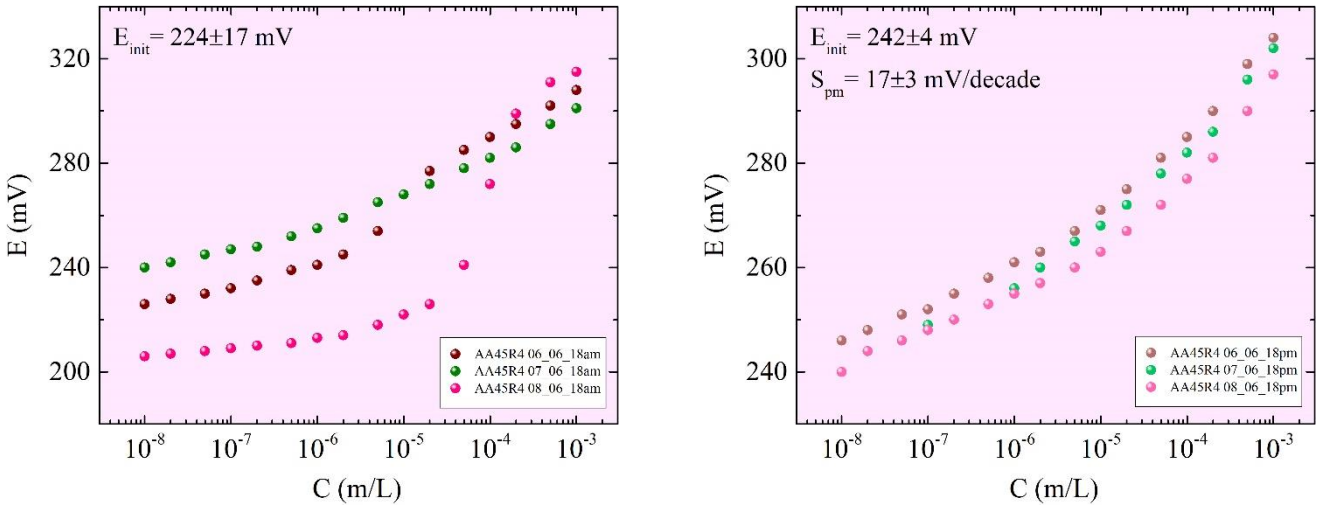

Figure IV.29. Calibration of AA45 R4 electrode between 06 and 08/06/2018 (a.m. and p.m.).

The results in the table below say that this composition can be used for membrane of ion-selective electrode when the surface will be treated in an appropriate way.

Table IV.23. E_{init} and S_{pm} for calibrations in postmeridian in the time between 06 and 08/06/2018.

№	Name of sensor	E_{init} mV	S_{pm} aver
1	AA45R2	213±3	19±1
2	AA45R4	242± 4	17±3

Next, composition (45AgI-27.5HgS-9.5As_2S_3-18GeS_2) is the eighth. From here we were assembling six ion-selective electrodes.

45%AgI-27.5HgS-9.5As_2S_3-18GeS_2

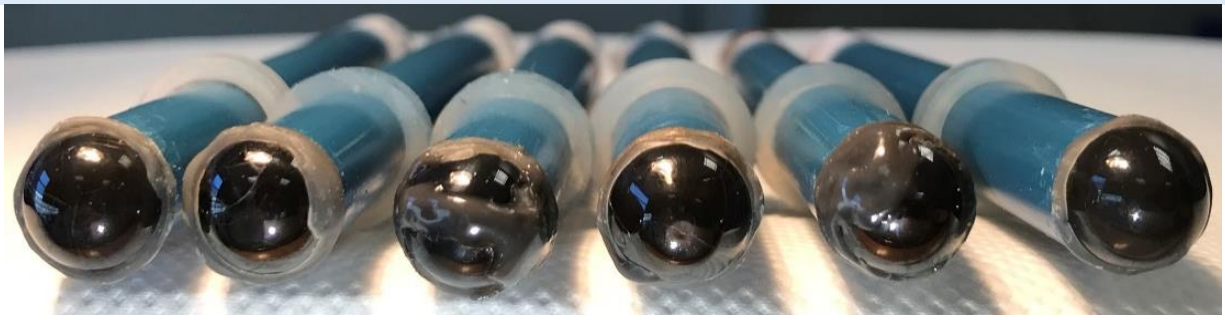

R1 **R2** **R3** **R4** **R5** **R6**

Figure IV.30. Photos showing the state of the synthesized membranes (45AgI-27.5HgS-9.5As_2S_3-18GeS_2) after calibration.

From **Figure IV.30,** we can see that all six AG45 membranes have a shiny surface. But, after few calibrations, all the AG45 electrodes (R1, R2, R3, R4, R5) except R6 exhibited superficial and/or deep fissures. However, we did some calibrations and tried to obtain the parameters: E_{init}, slope and detection limit.

In **Table IV.24**, we present the parameters of the AG45 electrodes (R1→R6) on 09/05/2018.

Table IV.24. Parameters of the electrodes (R1→ R6) obtained on 09/06/2018.

N°	Name	State after synthesis	State after calibration	E_{init} 09/05	S 09/05	DL 09/05
1	AG45R1	shiny	superficial fissures	154	65	1.7×10^{-5}
2	AG45R2	shiny	superficial fissures	199	44	1.8×10^{-5}
3	AG45R3	shiny	fissure	not measured		
4	AG45R4	shiny	fissure	185	56	1.6×10^{-5}
5	AG45R5	shiny	fissure	not measured		
6	AG45R6	shiny	shiny	148	83	1.8×10^{-5}
			Average	**172**	**62**	**1.5×10^{-5}**

In **Table IV.24**, we find the initial potential, sensitivity and detection limit values for the electrodes AG45 (R1→R6). The detection limit is high (5×10^{-5} m/L), it is worse than for the AA45 electrode

(10^{-5} m/L). We can suppose that composition with not very big quantity (may be not more than 10%) of GeS_2 could be perspective for membranes sensitive to Hg^{2+} ions. In **Table IV.25**, we present the calibrations in the time and experimental slopes for AG45 electrodes.

Table IV.25. Calibrations in the time and experimental slopes for AG45 electrodes.

N°	Name	N° Calib.	Calibrations in the time					
			April	S	May	S	June	S
1	AG45R1	12	13,16,17 26–30	16	02–04,09,11,30	65	not measured	
2	AG45R2	12	13,16,17 26–30	22–38	02–04,09,11,30	44		
3	AG45R3	11	13,16,17 26–30	-	02–04,11,30	-		
4	AG45R4	12	26–30	-	02–04,11,30	56		
5	AG45R5	13	26–30	-	02–04,11,30	20	04,05,06, 07,08	15–40
6	AG45R6	14	26–30	-	02–04,09,11,30	83,21	04–08	29–67

* The red color means that the electrode did not take part in discussion of results.

In April, only electrode AG45 R2 worked correctly with the slope between 16 and 38 mV/decade. We observed in May and June very high values of slope between 21 and 83 mV/decade.

Figure IV.31 exposes typical calibration curves for 45AgI-27.5HgS-9.5As_2S_3-18GeS_2 composition on 09/05/18.

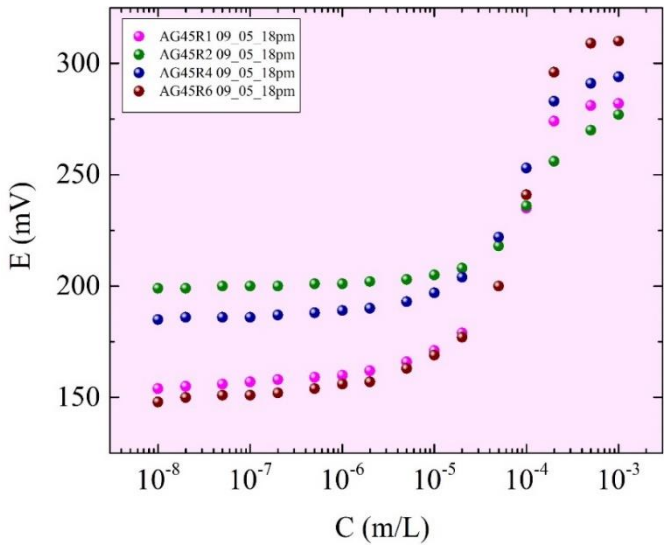

Figure IV.31. Calibration of AG45 (R1, R2, R4, R6) electrodes on 09/05/18.

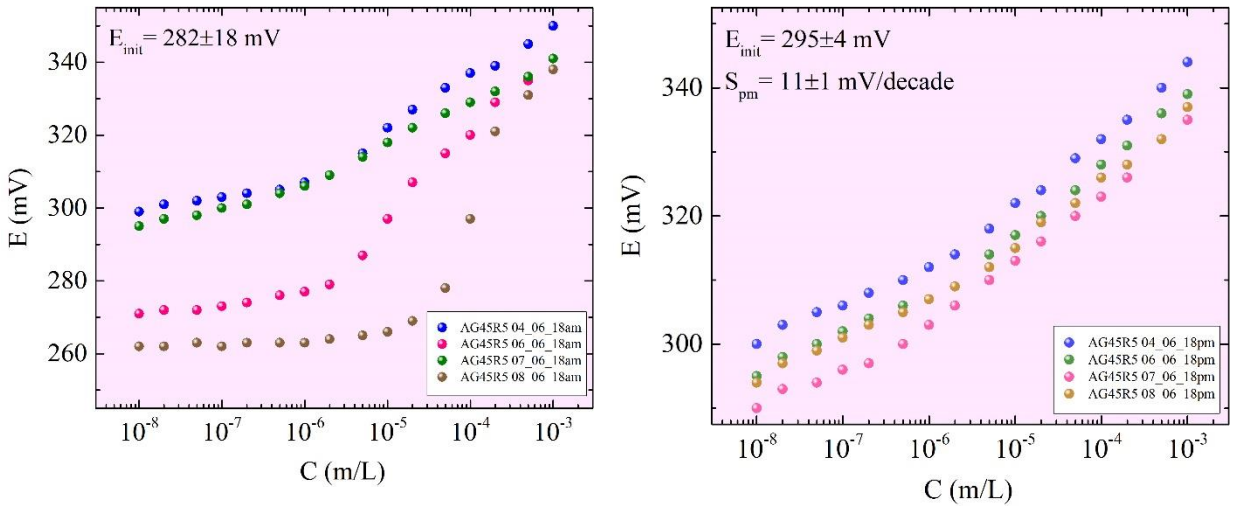

Figure IV.32. Calibration of AG45 R5 electrode on 13/04/2018 to 08/06/2018 (a.m. and p.m.).

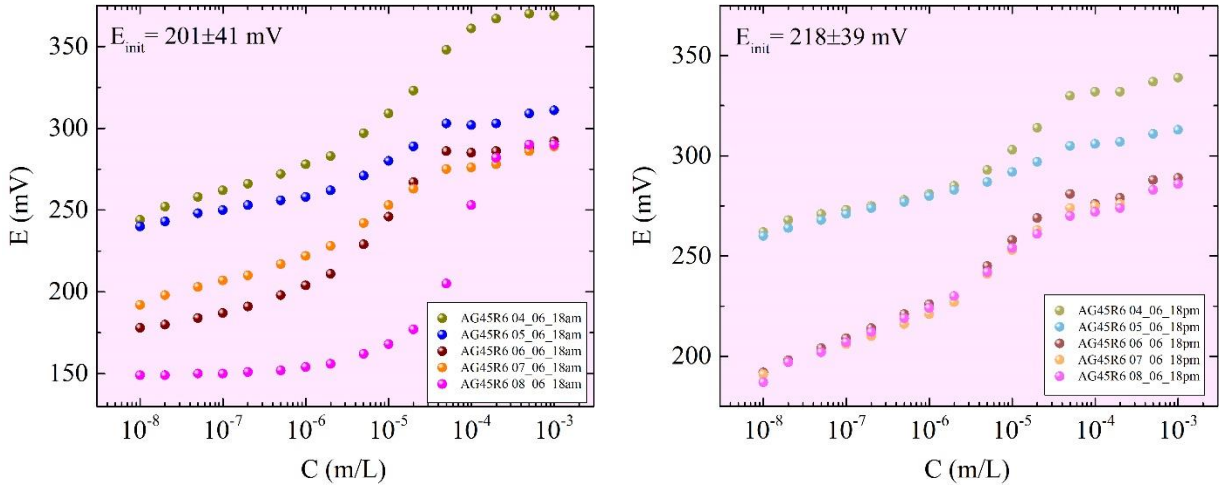

Figure IV.33. Calibration of AG45 R6 electrode from 13/04/2018 to 08/06/2018 (a.m. and p.m.).

Figure IV.32 and **Figure IV.33** show the stability of ion-selective electrodes R5 and R6 in the time. In the case of AGR5 we were observing the same phenomena like in the case of AA45R2 and R4, so very close initial potential E_{init} = 295±4 mV. But for the electrode AGR6, we cannot say that it was in good condition at those times.

Table IV.26. E_{init} and S_{pm} for calibrations in postmeridian in the time between 06 and 08/06/2018.

№	Name of sensor	E_{init} mV	S_{pm} aver
1	AG45R5	295±4	11±1

The results in the table above show that this composition can be used for membrane of ion-selective electrode when the surface will be treated in an appropriate way.

Now, we pass to the ninth composition (30AgI-35HgS-17.5As_2S_3-17.5GeS_2). From this composition was assembling five ion-selective electrodes.

30%AgI-35HgS-17.5As_2S_3-17.5GeS_2

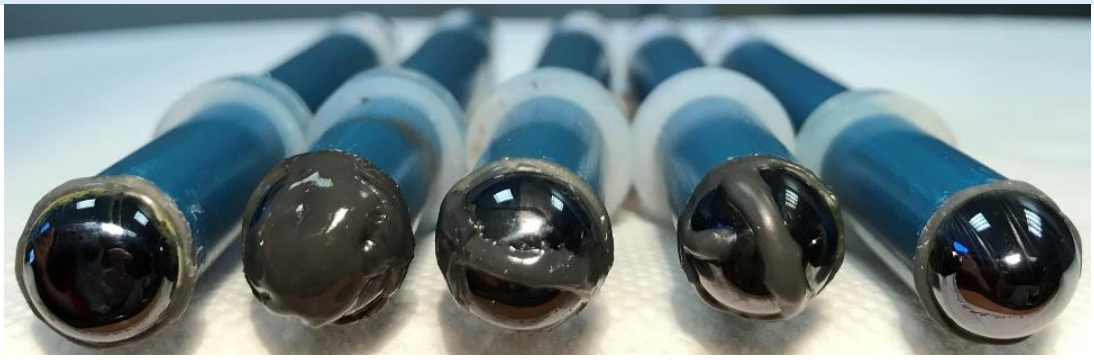

1 **2** **3** **4** **5**

Figure IV.34. Photos showing the state of the synthesized membranes (30AgI-35HgS-17.5As_2S_3-17.5GeS_2) after calibration.

From **Figure IV.34,** we can see that AH30 membranes have a shiny surface. However, after few calibrations, some of the electrodes, i.e. AH30 R2, R3, R4 exhibited deep fissures on their surfaces. On the other hand, electrodes AH30 R1 and R5 present little defects (yellow spots or scratches).

In **Table IV.27**, we present the parameters of the AH30 electrodes (R1, R2, R3, R4, R5).

Table IV.27. Parameters of the electrodes AH30 (R1, R2, R3, R4, R5).

N°	Name	State after synthesis	State after calibration	E_{init} 08/06	S 08/06	DL 08/06
1	AH30R1	shiny	yellow color on the edge	201	51	3.1×10^{-5}
2	AH30R2	shiny	big fissure	not measured		
3	AH30R3	shiny	fissure			
4	AH30R4	shiny	fissures			
5	AH30R5	shiny	shiny + scratches	238	42	3.3×10^{-5}
			Average	**220**	**47**	**3.2×10^{-5}**

In **Table IV.27**, we find the initial potential, sensitivity detection limit values for the electrodes AH30 (R1, R5). The average detection limit is too high (3.2×10^{-5} M). In this case, this composition is not suitable to be used as an ion-selective electrode for the detection of mercury in natural samples.

Table IV.28 shows the calibrations in the time and experimental slopes for AH30 electrodes.

Table IV.28. Calibrations in the time and experimental slopes for AH30 electrodes.

N°	Name	N° Calib.	Calibrations in the time					
			April	S	May	S	June	S
1	AH30R1	17	13,16,17 26–30	28	02–04,09,11,30	36	04, 05,06–08	18–51
2	AH30R2	10	13,16,17 26–30	19	02–04,11,30		not measured	
3	AH30R3	10	13,16,17 26–30	19	02–04,11,30			
4	AH30R4	8	26–30		02–04,09,30	47		
5	AH30R5	14	26–30		02–04,09,11,30	22	04, 05,06,07,08	19/42

In April and May, we made many calibrations about 15 but only 7 were good for treatment. They had the slope between 19 and 47 mV/decade. The situation with June is similar.

Figure IV.35 shows typical calibration curves for 30AgI-35HgS-17.5As_2S_3-17.5GeS_2 composition on 08/06/18.

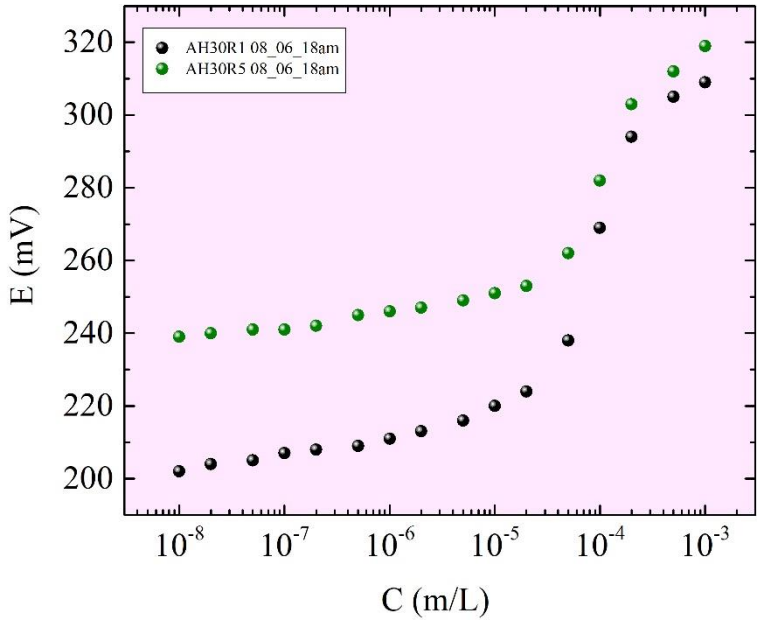

Figure IV.35. Calibration of AH30 (R1,R5) electrodes on 08/06/18.

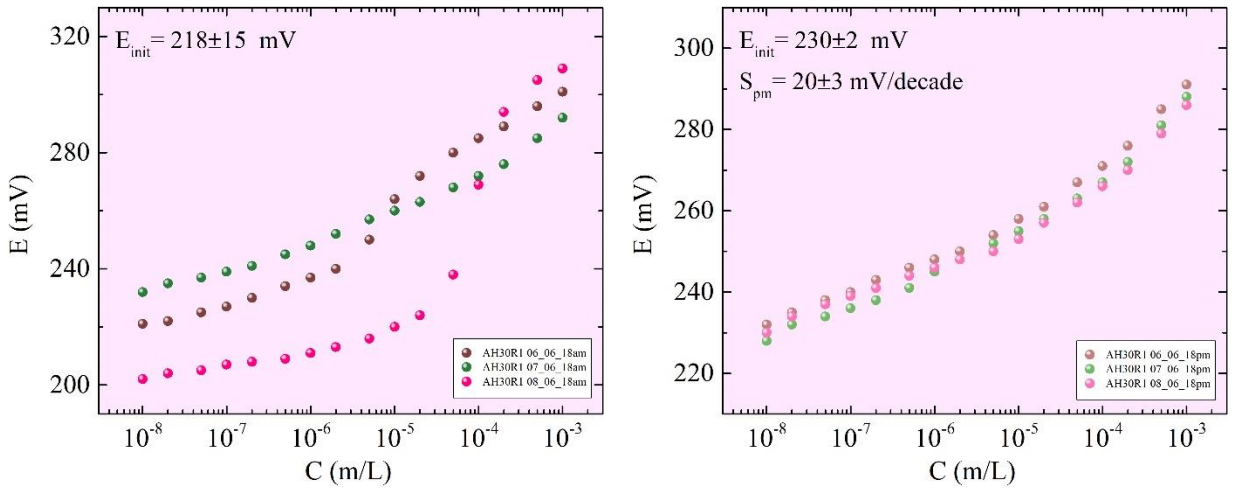

Figure IV.36. Calibration of AH30 R1 electrode on 06, 07 and 08/06/2018 (a.m. and p.m.).

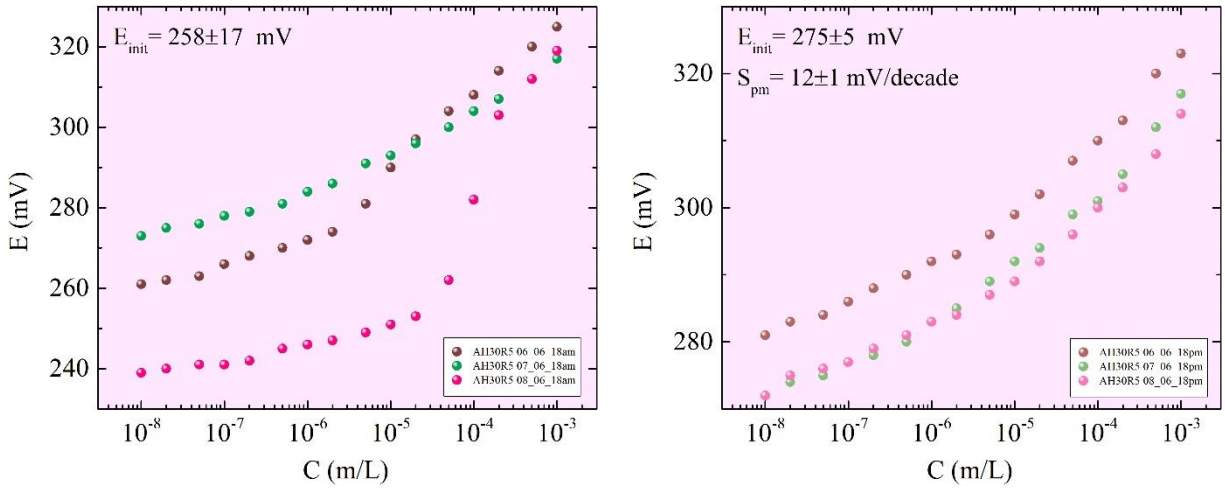

Figure IV.37. Calibration of AH30 R5 electrode between 06 and 08/06/2018 (a.m. and p.m.).

Figure IV.36 and **Figure IV.37** show the initial potential of electrodes AH30 R1 and R5 on three consecutive days 06, 07 and 08/06/2018, but also the slope for pm calibrations. And here we should note that both sensors start to behave similarly in postmeridian: E_{init}=230±2 mV and S_{pm}=20±3 mV/decade for AH30R1, E_{init}=275±5±4 mV and S_{pm}=12±1 mV/decade for AH30R5.

Table IV.29. E_{init} and S_{pm} for calibrations in postmeridian in the time between 06 and 08/06/2018.

№	Name of sensor	E_{init} mV	S_{pm} aver
1	AH30R1	230±2	20±3
2	AH30R5	275±5	12±1

The results in the above table show that this composition can be used for membrane of ion-selective electrode when the surface will be treated in an appropriate way.

We saw that the last three compositions containing mercury sulfide present the similar results of calibration in postmeridian with very good initial potential which respect the rules that should be not more than 10 mV. We can conclude that all three compositions can be used for membranes for mercury ion-selective electrodes with one condition that we must develop at first an appropriate procedure for surface treatment.

IV.5 Conclusions

1. This work has to be considered preliminary. As a result, the real parameters of the studied glasses which can be used as chemical sensors have not yet been fully exploited.
2. There were two groups of systems investigated:
   a. The systems free of the Hg content: $40AgBr\text{-}60As_2S_3$
      $50AgBr\text{-}50As_2S_3$
      $30AgI\text{-}70As_2S_3$
   b. The systems with the Hg content: $30AgI\text{-}35HgS\text{-}35GeS_2$
      $45AgI\text{-}27.5HgS\text{-}18As_2S_3\text{-}9.5GeS_2$
      $45AgI\text{-}27.5HgS\text{-}9.5As_2S_3\text{-}18GeS_2$
      $30AgI\text{-}35HgS\text{-}17.5As_2S_3\text{-}17.5GeS_2$
3. The systems from group (free of the Hg content), we cannot recommend like composition which can be used for membrane of ion-selective electrode sensitive to Hg^{2+}. But it will be to good make more rapt research with them.
4. The second group demands special serious investigations because these glasses show a tendency for very stable potential.
5. Special attention must be payed to development of the procedure for treatment of membrane surface. This is the key to obtain good parameters like sensitivity, DL, selectivity.
6. Should be ascertained the presence of HgS for stability of potential.

IV.6 References

[1] Arrêté du 2 février 1998 relatif aux prélèvements et à la consommation d'eau ainsi qu'aux émissions de toute nature des installations classées pour la protection de l'environnement soumises à autorisation.

[2] M. S. Bank, Mercury in the Environment: Pattern and Process. University of California Press, 2012.

[3] "Conductive Materials or Metal Conductivity - TIBTECH innovations -." [Online]. Available: http://www.tibtech.com/conductivity.php. [Accessed: 17-Jun-2018].

[4] A. B. Zdanovsky, Handbook of solubilization, vol. 1. 1954.

[5] Y. Y. Lure, Handbook of Analytical Chemistry. Moscow: Khimia, 1971.

[6] H. Remy, Lehrbuch der anorganishen chemie, vol. 2. 1966.

[7] C. Legein, "Cours de chimie des solutions en ligne," Universite du Maine.

[8] N. Pirrone et al., "Global Mercury Emissions from Natural and Anthropogenic Sources," p. 5.

[9] R. Perraud and C. Bliefert, Chimie de l'environnement. Air, eau, sols, déchets, De Boeck. 2001.

[10] G. Liu, Y. Cai, and N. O'Driscoll, Environmental Chemistry and Toxicology of Mercury. John Wiley & Sons, 2011.

[11] F.-X. Reichl, Guide pratique de toxicologie, De Boeck. 2004.

[12] G. Mance, Pollution Threat of Heavy Metals in Aquatic Environments. Springer Science & Business Media, 2012.

[13] "Prévention du risque chimique - Le mercure, cycle et toxicité." [Online]. Available: http://www.prc.cnrs.fr/spip.php?article75&lang=fr. [Accessed: 04-Apr-2017].

[14] "Mercure et composés minéraux (FT 55) - Fiche toxicologique - INRS." [Online]. Available: http://www.inrs.fr/publications/bdd/fichetox/fiche.html?refINRS=FICHETOX_55. [Accessed: 05-Apr-2017].

[15] "Le mercure-Prévention de l'hydrargyrisme-Brochure-INRS," INRS - Santé et sécurité au travail. [Online]. Available: http://www.inrs.fr/media.html?refINRS=ED%20546. [Accessed: 21-Jan-2018].

[16] "Version électronique authentifiée publiée au JO du 06/02/2007 | Legifrance." [Online]. Available:

https://www.legifrance.gouv.fr/jo_pdf.do?numJO=0&dateJO=20070206&numTexte=00017&pageDebut=00017&pageFin=. [Accessed: 05-Apr-2017].

[17] “Service des eaux-Seine-Normandie, « Le mercure dans l’eau ».” [Online]. Available: http://www.eau-seine-normandie.fr/fileadmin/mediatheque/Expert/Etudes_et_Syntheses/etude_2008/Guide_toxique/fiche_indiv/mercure.pdf. [Accessed: 05-Apr-2017].

[18] “L’Office national de l’eau et de l’assainissement (ONEA).” [Online]. Available: http://oneabf.com/espace-clients/44-les-reglements/129-les-eaux-usees-industrielles.html. [Accessed: 05-Apr-2017].

[19] G. Charlot, Les méthodes de la chimie analytique: analyse quantitative minérale. Masson, 1966.

[20] “Radelkis Ltd.” [Online]. Available: http://www.radelkis.hu/en/elekt/ion/frames.html. [Accessed: 10-May-2018].

[21] “Servilab, vente de consommable et matériel pour le laboratoire.” [Online]. Available: https://www.servilab.fr/. [Accessed: 10-May-2018].

[22] “Hach.” [Online]. Available: https://www.hach.com/ra/en_meterlab_ion_electrodes.asp. [Accessed: 10-May-2018].

[23] “HACH LANGE SENSORS (VAULX EN VELIN) Chiffre d’affaires, résultat, bilans sur SOCIETE.COM - 954506002.” [Online]. Available: https://www.societe.com/societe/hach-lange-sensors-954506002.html. [Accessed: 10-May-2018].

[24] “Nico Scientific - Products.” [Online]. Available: http://www.nicosensors.com/Level_1/products.htm. [Accessed: 10-May-2018].

[25] “Ion Selective - Van London - pHoenix.” [Online]. Available: http://www.vl-pc.com/default/index.cfm/custom/ion-selective. [Accessed: 10-May-2018].

[26] “ELIT Ion Selective Electrodes and other sensors for measuring Ions, pH, DO,ORP, conductivity in aqueous solutions.” [Online]. Available: http://www.nico2000.net/datasheets/electrodes.html. [Accessed: 10-May-2018].

[27] Y. G. Vlasov, E. A. Bychkov, and A. V. Bratov, “Ion-selective field-effect transistor and chalcogenide glass ion-selective electrode systems for biological investigations and industrial applications,” Analyst, vol. 119, no. 3, pp. 449–454, Jan. 1994.

[28] D. Patranabi, Sensors and Transducers. PHI Learning Pvt. Ltd., 2003.

[29] R. A. Durst, Ion-selective electrodes. [Gaitherssburg, Md.] : U.S. National Bureau of Standards; for sale by the Supt. of Docs., U.S. Govt. Print. Off. ; Washington, 1969.

[30] R. G. (Roger G. Bates, Determination of pH; theory and practice. New York, Wiley, 1964.

[31] E. A. Bychkov, M. Bruns, H. Klewe-Nebenius, G. Pfennig, W. Hoffmann, and H. J. Ache, "Cu^{2+}-selective thin films for chemical microsensors based on sputtered copper-arsenic-selenium glass," Sens. Actuators B Chem., vol. 25, no. 1–3, pp. 733–736, Apr. 1995.

[32] M. S. Frant and J. W. Ross, "Electrode for Sensing Fluoride Ion Activity in Solution," Science, vol. 154, no. 3756, pp. 1553–1555, Dec. 1966.

[33] E. Kissa, "Determination of fluoride at low concentrations with the ion-selective electrode," Anal. Chem., vol. 55, no. 8, pp. 1445–1448, Jul. 1983.

[34] V. Young, "Electronic conductivity of Ag_2S/AgX(X = Cl, Br) ion selective electrode membranes: Effect of silver incorporation," Solid State Ion., vol. 25, no. 1, pp. 21–25, Oct. 1987.

[35] V. K. Gupta, S. Chandra, and H. Lang, "A highly selective mercury electrode based on a diamine donor ligand," Talanta, vol. 66, no. 3, pp. 575–580, Apr. 2005.

[36] H. M. Abu-Shawish, "A mercury(II) selective sensor based on N,N′-bis(salicylaldehyde)-phenylenediamine as neutral carrier for potentiometric analysis in water samples," J. Hazard. Mater., vol. 167, no. 1–3, pp. 602–608, Aug. 2009.

[37] R. K. Mahajan, I. Kaur, and T. S. Lobana, "A mercury(II) ion-selective electrode based on neutral salicylaldehyde thiosemicarbazone," Talanta, vol. 59, no. 1, pp. 101–105, Jan. 2003.

[38] A. A. Khan, null Inamuddin, and T. Akhtar, "Organic-inorganic composite cation-exchanger: poly-o-toluidine Zr(IV) phosphate-based ion-selective membrane electrode for the potentiometric determination of mercury," Anal. Sci. Int. J. Jpn. Soc. Anal. Chem., vol. 24, no. 7, pp. 881–887, Jul. 2008.

[39] G. Ye, Y. Chai, R. Yuan, and J. Dai, "A mercury(II) ion-selective electrode based on N,N-dimethylformamide-salicylacylhydrazone as a neutral carrier," Anal. Sci. Int. J. Jpn. Soc. Anal. Chem., vol. 22, no. 4, pp. 579–582, Apr. 2006.

[40] R. K. Mahajan, R. Kaur, I. Kaur, V. Sharma, and M. Kumar, "Mercury(II) ion-selective electrodes based on p-tert-butyl calix[4]crowns with imine units," Anal. Sci. Int. J. Jpn. Soc. Anal. Chem., vol. 20, no. 5, pp. 811–814, May 2004.

[41] D. Golikov, St Petersburg University, 1990.

[42] N. Tohge and M. Tanaka, “Chalcogenide glass electrodes sensitive to heavy metal ions,” J. Non-Cryst. Solids, vol. 80, no. 1, pp. 550–556, Mar. 1986.

[43] A. Guessous, P. Papet, J. Sarradin, and M. Ribes, “Thin films of chalcogenide glass as sensitive membranes for the detection of mercuric ions in solution,” Sens. Actuators B Chem., vol. 24, no. 1, pp. 296–299, Mar. 1995.

[44] Y. G. Vlasov, E. A. Bychkov, and A. M. Medvedev, “Copper ion-selective chalcogenide glass electrodes: Analytical characteristics and sensing mechanism,” Anal. Chim. Acta, vol. 185, pp. 137–158, 1986.

[45] A. Pradel et al., “Electrochemical microsensors for the detection of heavy ions in solutions,” Electrochem. Soc. Proc., vol. 22–95, pp. 76–86, 1995.

[46] R. Boidin, “Etude des propriétés de conduction et structurales des verres du système Hgl_2-Ag_2S-As_2S_3 : application en tant que capteur chimique.”

[47] S. Khaoulani, “Traitement d’eaux usées par adsorption sur des polymères de cyclodextrine et développement de capteurs chimiques à base de membranes de verres de chalcogénures destinées à la détection des ions Hg^{2+},” Université du Littoral Côte d’Opale, 16-Dec-2015.

[48] IUPAC, Compendium of Chemical Terminology, 2nd ed. (the "Gold Book"). 1997.

[49] R. W. Ramette, “Outmoded terminology: The normal hydrogen electrode,” J. Chem. Educ., vol. 64, no. 10, p. 885, Oct. 1987.

[50] “Standard hydrogen electrode,” Wikipedia. 03-Nov-2018.

[51] “Chapter 17 Electrochemistry, Chemistry: McMurry and Fay,” 6th Edition., Pearson Prentice Hall, Inc., 2008.

[52] C. C. Rundle, “A Beginners Guide to Ion-Selective Electrode Measurements,” Jan. 2000.

[53] R. P. Buck and E. Lindner, “Recommendations for nomenclature of ionselective electrodes (IUPAC Recommendations 1994),” Pure Appl. Chem., vol. 66, no. 12, pp. 2527–2536, 1994.

[54] I. Uemasu and Y. Umezawa, “Comparison of definitions of response times for copper(II) ion selective electrodes,” Anal. Chem., vol. 54, no. 7, pp. 1198–1200, Jun. 1982.

GENERAL CONCLUSION

The work realized in this thesis can be divided into three main parts:

1. Synthesis and characterization of silver and/or mercury thioarsenate and thiogermanate glasses (chapter I);
2. Study of conduction and structural properties of the glassy systems (chapters II and III);
3. Potential evaluation of the new glasses as sensitive membranes (chapter IV).

The first studies presented in the manuscript concern the physical and thermal characteristics of AgY-As_2S_3 (Y = Br, I), HgS-GeS_2, AgI-HgS-As_2S_3 and AgI-HgS-GeS_2 glassy systems. Density measurements show monotonic increase with increasing the silver halide content. Yet, this densification of glass is reflected by the increase of the principal peak PP in $S(Q)$.

The characteristic glass temperatures measured using DSC show an overall decrease of the glass transition temperatures with the addition of silver halides. This can be explained by the fragmentation of the As–S or Ge–S glass networks. Silver halide thioarsenate glasses exhibit two T_g at intermediate and high silver concentrations. This implies that they are phase-separated, forming Ag-rich and Ag-poor vitreous domains as evidenced from the SEM images of the glasses. Thus, the introduction of Ag has a profound effect on the glass morphology.

The ionic conductivity σ_i measurements of AgY-As_2S_3 (Y = Br, I) glasses over 5 orders of magnitude in silver content have shown two ion transport regimes: (i) the critical percolation at $x \leq 2$ at.% Ag, and (ii) the modifier-controlled ionic motion at $x >$ 7-10 at.% Ag. The chemically-invariant critical percolation, characterized by a power-law dependence of $\sigma_i(x,T) \propto x^{T_0/T}$, where T_0 is the critical temperature, reveals identical ionic conductivity parameters within experimental uncertainty for AgY- and Ag_2S-As_2S_3 glasses. The ionic conductivity diverges in the modifier-controlled region, and the difference in $\sigma(x)$ between AgI- and Ag_2S-As_2S_3 glasses approaches 4 orders of magnitude.

DFT structural modelling of two Ag_2S-As_2S_3 glasses belonging either to the critical percolation (1.2 at.% Ag) or modifier-controlled (31.6 at.% Ag) domains confirms previous structural hypothesis that silver distribution is random at low x. The observed conductivity invariance for the critical percolation is directly related to the average Ag-Ag separation distance of 12 Å or

more. When silver cation leaves its residence site and travels throughout the glass network, the memory of its original chemical form (sulfide or halide) disappears rapidly with increasing the mean-square displacement. Chemically-invariant ionic conductivity seems to be a common feature of any disordered system with random distribution of mobile ions having similar size of charge carriers.

Important structural results have been obtained in the quasi-binary AgY-As_2S_3 glasses which have multiple phases. AIMD modelling reveals a quite unexpected but interesting results for the $(AgBr)_{0.5}(As_2S_3)_{0.5}$ glass. It shows a quite compact phase separated structure, which was observed in SANS experiment, but also in HE-XRD measurements in the low-Q part. We should note the absence of random distribution of silver, bromine and sulfur in the simulation box. They form the connected pathways resembling the preferential conduction pathways which ensure the high ionic conductivity in Ag-chalcogenide glasses. Another interesting result shown by AIMD simulations is the presence of a mixed tetrahedral environment around silver, and this seems to be coherent with the Gaussian fitting of $T(r)$ in ND and HE-XRD measurements. The mixed silver environment implies some kind of chemical interaction with the host network leading to formation of As–As bonds, evidenced in Raman spectra and diffraction results. Consequently, silver halides are participating in transformations of the intermediate range order in contrast to the widely accepted point of view that metal halides leave intact the original glass structure.

The study of the electronic transport properties of HgS-GeS_2 glasses shows a non-monotonic change which could be related to changes in the matrix structure. This is supported by the appearance and changes in the population of S–S homopolar bonds in Raman measurements. We have to note that crystalline mercury sulfide exists in two drastically different polymorphic forms: red chain-like insulator α-HgS, stable below 344 °C, and black tetrahedral narrow-band semiconductor β-HgS, stable at higher temperatures. Using pulsed neutron and high-energy X-ray diffraction, we show that both are present simultaneously in mercury thiogermanate glasses starting from 10 mol% HgS. These glasses, similar to the HgS-As_2S_3 system, show a composition dependence of the tetrahedral mercury fraction $f_{Hg}^{4F}(x)$.

The room temperature conductivity isotherm plotted on a semi-logarithmic scale for AgI-HgS-GeS_2 glasses show four different concentration regions. In addition to the critical percolation domain, the modifier-controlled region is divided into three distinct composition ranges,

distinguished by their local structure. From Raman measurements, ones observe a very similar red shift of A_1 Ge-S breathing mode at ≈340 cm^{-1} to that in Ag_2S-GeS_2 binary glasses. This indicates that the second neighbor of Ge is Ag and, consequently, silver has at least one sulfur nearest neighbor. We also note a strong red shift for Ag-I stretching coherent with the observed transport regimes in the AgI-HgS-GeS_2 glasses. It is important to mention that a new variable appears and seems to be responsible for the conductivity changes; this is the Hg–S coordination number N_{Hg-S}. It decreases as a function of AgI content, even though the Hg/Ge ratio remains 1:1. At $x \approx 0.3$, corresponding to a ratio of Hg/Ag ≈ 1, N_{Hg-S} becomes roughly ≈2, i.e., a completely 2-fold coordinated Hg species (Hg_{2F}-S). This change is reflected (i) in the change of the slope of ionic conductivity in the modifier-controlled region at $x \approx 0.3$, the conductivity increase continues but at a lower rate; and (ii) in non-systematic changes in the structure factor and total correlation functions.

The critical temperature T_0 , a primordial parameter to describe the percolation phenomena in glass and reflecting the connectivity of the host matrix, exhibits the expected agreement with connectivity of g-As_2S_3, $\langle n_0 \rangle = 2.40$, for the AgY-$As_2S_3$ glasses. However, for the ternary $(AgI)_{0.5-x/2}(HgS)_{0.5-x/2}(As_2S_3)_x$ and $(AgI)_x(HgS)_{0.5-x/2}(GeS_2)_{0.5-x/2}$ vitreous alloys, the derived T_0 parameters imply a correlated Ag location in the vicinity of two-fold coordinated mercury, while for the $(AgI)_x(HgS)_{0.5-x/2}(As_2S_3)_{0.5-x/2}$ glasses one suggests a predominant Ag distribution within 4-fold coordinated mercury and trigonal As sites.

Finally, the application part was dedicated to the development of new chemical sensors for the detection of Hg^{2+} ions. We synthesized and tested 9 compositions. Calibrations show the existence of sensitivity towards Hg^{2+}. However, a deep research and appropriate treatment are necessary for the development of such sensors.

ABSTRACT

The aim of the thesis is to study the physicochemical properties of the silver halide doped chalcogenide glasses for the possibility to use them as chemical sensors for quantitative analysis of Hg^{2+} ions.

First, the macroscopic properties of AgY-As_2S_3 (Y = Br, I), HgS-GeS_2, AgI-HgS-As_2S_3 and AgI-HgS-GeS_2 glassy systems such as the densities and the characteristic temperatures (T_g and T_c) were measured and analyzed according to the glass compositions.

Second, the transport properties were studied using complex impedance and dc conductivity. Measurements show that the silver halide doped chalcogenide glasses exhibit two drastically different ion transport regimes above the percolation threshold at $x_c \approx 30$ ppm: (i) critical percolation, and (ii) modifier-controlled regimes.

Third, to unveil the composition/structure/property relationships, various structural studies were carried out. Raman spectroscopy, high-energy X-ray diffraction, neutron diffraction and small-angle neutron scattering experiments, together with RMC/DFT and AMID modelling were employed.

Finally, the last part was a preliminary study of the characteristics of new chemical sensors. It was devoted to study the relationship between the membranes' composition and sensitivity but also detection limits.

Keywords: chalcogenide glasses, conductivity, critical percolation and modifier-controlled ion transport regimes, phase-separation, HgS dimorphism, network connectivity, chemical sensors.

RESUME

Le but de ce travail de thèse consiste à étudier les propriétés physico-chimiques des verres chalcogénures afin de pouvoir les utiliser comme membranes de capteurs chimiques destinés pour le dosage des ions Hg^{2+}.

Dans un premier temps, les propriétés macroscopiques des systèmes vitreux $AgY\text{-}As_2S_3$ (Y = Br, I), $HgS\text{-}GeS_2$, $AgI\text{-}HgS\text{-}As_2S_3$ and $AgI\text{-}HgS\text{-}GeS_2$, telles que les densités et les températures caractéristiques (T_g and T_c) ont été mesurées et analysées selon les compositions des verres.

Puis dans un second temps, les propriétés de transport ont été étudiés à l'aide de la spectroscopie d'impédance complexe d'une part, ou d'autre part, par des mesures de la résistivité. Ces dernières montrent que les verres des chalcogénures dopés à l'halogénure d'argent présentent deux différents régimes de transports au-dessus du seuil de percolation $x_c \approx 30$ ppm: (i) domaine de percolation critique, et (ii) domaine contrôlé par modificateur.

Vient ensuite la troisième partie, elle consiste à déchiffrer les relations composition/structure/propriété grâce à plusieurs études structurales. Des mesures par spectroscopie Raman, par diffraction de neutrons et de rayons X haute énergie, par diffusion des neutrons sous petits angles (SANS), ainsi que des modélisations RMC/DFT et AMID ont été réalisées.

Enfin, la dernière partie de ce travail était une étude préliminaire des caractéristiques des nouveaux capteurs chimiques. Il a été consacré à l'étude des relations entre la composition et la sensibilité des membranes ainsi qu'aux limites de détection qui les définissent.

Mots-clés : verres chalcogénures, conductivité, domaine de percolation critique, domaine contrôlé par modificateur, séparation de phases, dimorphisme HgS, connectivité réseau, capteurs chimiques.